UNCLASSIFIED

AD NUMBER

AD530206

NEW LIMITATION CHANGE

TO

Controlling DoD Organization: Chief of Naval Research [ONR-411], Arlington, VA 22217

FROM

Distribution authorized to U.S. Gov't. agencies only; Test and Evaluation; 31 MAR 1972. Other requests shall be referred to Chief of Naval Research [ONR-411], Arlington, VA 22217.

AUTHORITY

Office of Naval Research ltr dtd 15 Mar 1979

THIS PAGE IS UNCLASSIFIED

~~SECRET~~

REPORT MDC A2658
10 MAY 1974

QUIET ATTACK AIRCRAFT (U)

TECHNICAL REPORT
VOLUME II

By C.A. Mohr, et al.

This research was sponsored by the Office of Naval Research under USN Contract N00014-72-C-0222, ONR Task NR 212-210.

MCDONNELL AIRCRAFT COMPANY
Box 516, Saint Louis, Missouri 63166

MCDONNELL DOUGLAS CORPORATION

~~SECRET~~

Unclassified
SECURITY CLASSIFICATION OF THIS PAGE (When Data Entered)

REPORT DOCUMENTATION PAGE		READ INSTRUCTIONS BEFORE COMPLETING FORM
1. REPORT NUMBER	2. GOVT ACCESSION NO.	3. RECIPIENT'S CATALOG NUMBER
4. TITLE (and Subtitle) Quiet Attack Aircraft (U) Volume II		5. TYPE OF REPORT & PERIOD COVERED Annual Technical Report 15 March 1973-31 Dec 1973 6. PERFORMING ORG. REPORT NUMBER MDC A2658, Volume II
7. AUTHOR(s) Charles A. Mohr, et al.		8. CONTRACT OR GRANT NUMBER(s) N00014-72-C-0222
9. PERFORMING ORGANIZATION NAME AND ADDRESS McDonnell Aircraft Company McDonnell Douglas Corporation P. O. Box 516 St. Louis, Missouri 63166		10. PROGRAM ELEMENT, PROJECT, TASK AREA & WORK UNIT NUMBERS ONR Task NR 212-210
11. CONTROLLING OFFICE NAME AND ADDRESS Chief of Naval Research ONR-411 Arlington, Virginia 22217		12. REPORT DATE 10 May 1974 13. NUMBER OF PAGES 231
14. MONITORING AGENCY NAME & ADDRESS(if different from Controlling Office)		15. SECURITY CLASS. (of this report) SECRET 15a. DECLASSIFICATION DOWNGRADING SCHEDULE GDS-Exempt 3

16. DISTRIBUTION STATEMENT (of this Report)

[redacted]

17. DISTRIBUTION STATEMENT (of the abstract entered in Block 20, if different from Report)

18. SUPPLEMENTARY NOTES

19. KEY WORDS (Continue on reverse side if necessary and identify by block number)

Quiet	IR Signature	Signature Reduction
Attack Aircraft	Radar Cross Section	Aircraft Detectability
Carrier Based	Covert Operation	Tip Driven Fans
Noise	Weapon Delivery	Visual Signature

20. ABSTRACT (Continue on reverse side if necessary and identify by block number)

(U) Volume I, Program Overview, and Volume II, Technical Report, cover the studies performed for the Office of Naval Research during the contract extension period from 15 March 1973 to 31 December 1973 on a quiet attack carrier based aircraft having low signatures. Studies performed during the initial contract period from 15 March 1972 to 15 March 1973 were discussed in two volumes of Report MDC A1659, Volume I being "Quiet Attack Aircraft - Program Overview" (DDC #AD525774-L) and Volume II was "Quiet Attack Aircraft - Technical Report" (DDC #AD524801-L). Techniques are described for achieving significant

DD FORM 1 JAN 73 1473 EDITION OF 1 NOV 65 IS OBSOLETE

Unclassified
SECURITY CLASSIFICATION OF THIS PAGE (When Data Entered)

20.

reduction in acoustic noise, infrared signature in both the 1.7-5 and the 8-14 micron spectral bands, radar cross section, and visual signature. At all speeds up to maximum in the high subsonic region, propulsion noise is made less dominant than aerodynamic noise by the use of a high bypass tip-driven fan propulsion system with duct acoustic treatment. The benefits of low signatures in reducing enemy capabilities are discussed. Weapon delivery is analyzed and shown to be feasible for a wide range of speed and payload. Design is based on near term technology.

FOREWORD

(U) This technical report summarizes research performed for the Office of Naval Research, Arlington, Virginia under USN Contract N00014-72-C-0222, modification No. P00001, identified as ONR Task NR 212-210.

(U) The USN Scientific Officer is CDR W. F. Greene, Vehicle Warfare Technology, Code ONR-411.

(U) The specific effort reported herein includes all tasks performed in the contract extension period from 15 March 1973 to 31 December 1973. Volume I, Program Overview, provides a summary of principal program findings, and Volume II, Technical Report, presents a detailed discussion of all phases of the program during this contract extension period.

(U) The tasks performed in the initial contract period from 15 March 1972 to 15 March 1973 were discussed in two volumes of Report MDC A1659, Volume I being the "Quiet Attack Aircraft-Program Overview" (DDC #AD525774-L) and Volume II was the "Quiet Attack Aircraft-Technical Report" (DDC #AD524801-L).

(U) Quiet Attack Aircraft program activities are conducted within the McDonnell Aircraft Company (MCAIR) Advanced Systems Concepts project. This project is directed by Mr. C. V. Dresser, Manager of Advanced Systems Concepts, and is an element of MCAIR Advanced Engineering, directed by Mr. H. D. Altis, Director, Advanced Engineering. The Quiet Attack Aircraft study team is managed by Mr. C. A. Mohr, Assistant Project Engineer.

(U) Other principal contributors for the program elements reported here are: J. E. Augustus-Weights, R. W. Holzwarth-Design, H. S. Littlepage-Aerodynamics, R. H. Livingstone-Visual Signature, G. C. Matlock-Acoustic Noise, D. S. McCormack-Infrared Signature, J. G. Rose-Radar Cross Section, and N. F. Sullivant-Propulsion.

ABSTRACT

(U) Volume I, Program Overview, and Volume II, Technical Report, cover the studies performed for the Office of Naval Research during the contract extension period from 15 March 1973 to 31 December 1973 on a quiet attack carrier-based aircraft having low signatures. Studies performed during the initial contract period from 15 March 1972 to 15 March 1973 were discussed in two volumes of Report MDC A1659, Volume I being "Quiet Attack Aircraft - Program Overview" (DDC #AD525774-L) and Volume II was "Quiet Attack Aircraft - Technical Report" (DDC #AD524801-L). Techniques are described for achieving significant reduction in acoustic noise, infrared signature in both the 1.7-5 and the 8-14 micron spectral bands, radar cross section, and visual signature. At all speeds up to maximum in the high subsonic region, propulsion noise is made less dominant than aerodynamic noise by the use of a high bypass tip-driven fan propulsion system with duct acoustic treatment. The benefits of low signatures in reducing enemy capabilities are discussed. Weapon delivery is analyzed and shown to be feasible for a wide range of speed and payload. Design is based on near term technology.

TABLE OF CONTENTS

TABLE OF CONTENTS (Continued)

List of Pages

LIST OF ILLUSTRATIONS

LIST OF ILLUSTRATIONS (Continued)

LIST OF ILLUSTRATIONS (Continued)

LIST OF ILLUSTRATIONS (Continued)

LIST OF ABBREVIATIONS AND SYMBOLS

Abbreviation/Symbol	Definition
A	Area
AAA	Anti-Aircraft Artillery
Accel	Acceleration, Accelerating
AGL	Above Ground Level
AR	Wing Aspect Ratio
AZ	Azimuth
b	Wing Span
C_D	Drag Coefficient
cd ft^{-2}	Candles Per Square Foot
C_L	Wing Lift Coefficient
C_{Lmax}	Wing Maximum Lift Coefficient
cm^2	Square Centimeters
cps	Cycles Per Second (Hertz)
C_R	Root Chord
C_T	Tip Chord
CVA-59	Forrestal Class Aircraft Carrier
dB	Decibels
dBSM	Decibels Referenced to One Square Meter
DDC	Defense Documentation Center
deg	Degrees
DI	Noise Directivity Index
ECM	Electronic Countermeasures
EL	Elevation

LIST OF ABBREVIATIONS AND SYMBOLS (Continued)

Abbreviation/Symbol	Definition
f/f_{PRIME}	Sound Spectrum Band Center Frequency over Peak Frequency
FAC	Forward Air Controller
FLIR	Forward Looking Infrared
fps	Feet Per Second
frag	Fragments
ft^2	Square Feet
fus	Fuselage
FWD	Forward
g	Acceleration of Gravity
GHz	Giga-Hertz (Billions of Cycles Per Second)
GP	General Purpose (bomb)
h	Distance from Aircraft to Observer
HUD	Head-Up Display
hr	Hour
Hz	Hertz (Frequency in Cycles Per Second)
IR	Infrared
J/S	ECM Jamming to Signal Ratio
°K	Degrees Kelvin (°C + 273.16)
KHz	Kilo-Hertz (Thousands of Cycles Per Second)
kt	Knots
KW	Kilowatts

LIST OF ABBREVIATIONS AND SYMBOLS (Continued)

Abbreviation/Symbol	Definition
LDGP	Low Drag General Purpose (bomb)
LGB	Laser Guided Bomb
log	Logarithm to Base 10 of . . .
LOS	Line of Sight
M	Mach Number
M^2	Square Meters
Ml17Al	750 Lb Bomb
MAX	Maximum
MCAIR	McDonnell Aircraft Company
min	Minutes
MK81	250 Lb Bomb
MK82	500 Lb Bomb
MK83	1000 Lb Bomb
MK84	2000 Lb Bomb
mm	Millimeters
Nz	Structural Load Factor
nm	Nautical Miles
OAPWL	Sound Overall Power Level
OASPL	Overall Sound Pressure Level
ONR	Office of Naval Research
PNdB	Perceived Noise Decibels
psf	Pounds Per Square Foot

LIST OF ABBREVIATIONS AND SYMBOLS (Continued)

Abbreviation/Symbol	Definition
q	Dynamic Pressure
QAA	Quiet Attack Aircraft
°R	Degrees Rankine (°F + 460)
R_{85}	Radar Range for 85% Cumulative Probability of Detection
R_N	Reynolds Number
R_S	Radar Screening Range
RAM	Radar Absorbing Material
RCS	Radar Cross Section
re	Referenced To . . .
ref	Reference
S, S_W	Wing Area
S_{FILLET}/S_{REF}	Ratio of Wing Fillet Area to Wing Reference Area
SAM	Surface-to-Air Missile
SEA	Southeast Asia
sec	Seconds
SFC	Specific Fuel Consumption
SLS	Sea Level Static
S/N	Signal to Noise Ratio
SPL	Sound Pressure Level
t/c	Airfoil Thickness to Chord Ratio
TOGW	Takeoff Gross Weight

LIST OF ABBREVIATIONS AND SYMBOLS (Continued)

Abbreviation/Symbol	Definition
V	Velocity in Feet Per Second
V_{KT}	Velocity in Knots
$V_{PA_{min}}$	Minimum Power Approach Speed
VRS	Visual Radiation Source
V_{STALL}	Stall Speed at Maximum Lift Coefficient
WOD	Wind Over Deck
W/S	Wing Loading
wt	Weight
WWI	World War I
WWII	World War II
α	Wing Angle of Attack
Δ	Incremental Increase or Decrease
ϵ	Infrared Emissivity
Λ	Wing or Tail Sweep Angle
λ	Wing or Tail Taper Ratio
μ	Microns (Wavelength in Meters x 10^{-6})
σ	Radar Cross Section

(Page xvi is blank)

1. INTRODUCTION AND SUMMARY

(U) The objective in this program has been to explore the initial technical feasibility and potential operational values of a covert quiet attack carrier based aircraft for Navy/Marines Corps missions, which minimizes detectable acoustic, infrared, radar, and visual signatures with minimum compromises in size, weight, performance, and carrier suitability. Emphasis has been on a practical aircraft with significantly lower signatures which can effectively perform its mission, rather than the unrealistic objective of absolute minimum signatures.

~~(C)~~ During the initial contract period, as reported in Reference (1), a design evolution took place, Figure 1-1, to arrive at the Model 226-454A quiet attack aircraft. This aircraft had a 400 ft^2 wing of aspect ratio 8 to reduce wing loading for low aerodynamic noise, and the propulsion system consisted of a scaled GE 1/10 gas generator powering two tip driven fans to reduce propulsion noise as well as 3-5 micron IR signature. Radar cross section was reduced by such techniques as exterior shaping and the use of radar absorbing material (RAM) in the inlet and exhaust ducts.

~~(C)~~ FIGURE 1-1
DESIGN EVOLUTION

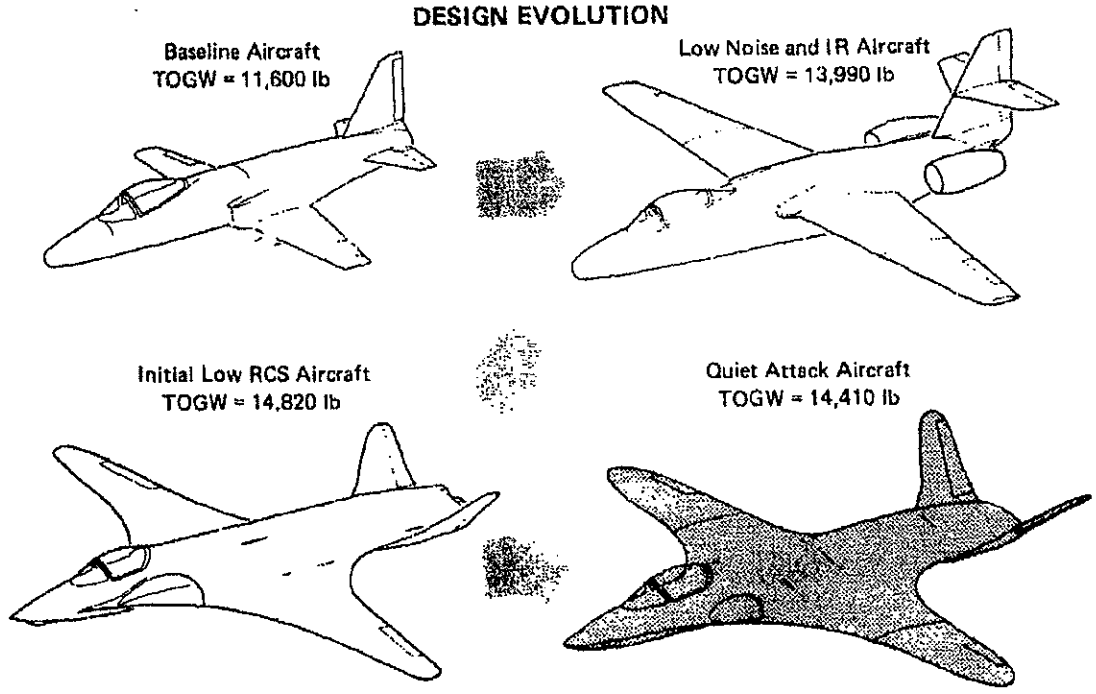

(C) In the contract extension period reported herein the specific objectives have been:

- Design refinement to increase wing lift and to use existing hardware for the propulsion gas generator
- Analysis of the feasibility of weapon delivery at low quiet speed at low altitude
- Alternate mission capabilities with large external bomb payloads and ferry flight
- Reduction of visual signature and IR signature in the 8-14 micron band used by ground-based FLIR sensors.

(C) The current quiet attack aircraft resulting from these latest studies is Model 226-458, illustrated by Figure 1-2. In outward size and appearance this aircraft is nearly identical to the previous Model 226-454A, except that Visual Radiation Source (VRS) lights have been added to the wing and tail leading edges and the fuselage nose, Figure 1-3, to reduce visual signature. Internally, two tip-driven fans are still used in the propulsion system but the gas generator is now the core from the TF-34 turbofan currently in production for the S-3A and other aircraft.

(C) FIGURE 1-2
QUIET ATTACK AIRCRAFT
Model 226-458

Two Tip-Driven Fans
TOGW ..... 16,630 lb
Wing Area ..... 400 ft^2
Takeoff Thrust/Weight 0.36

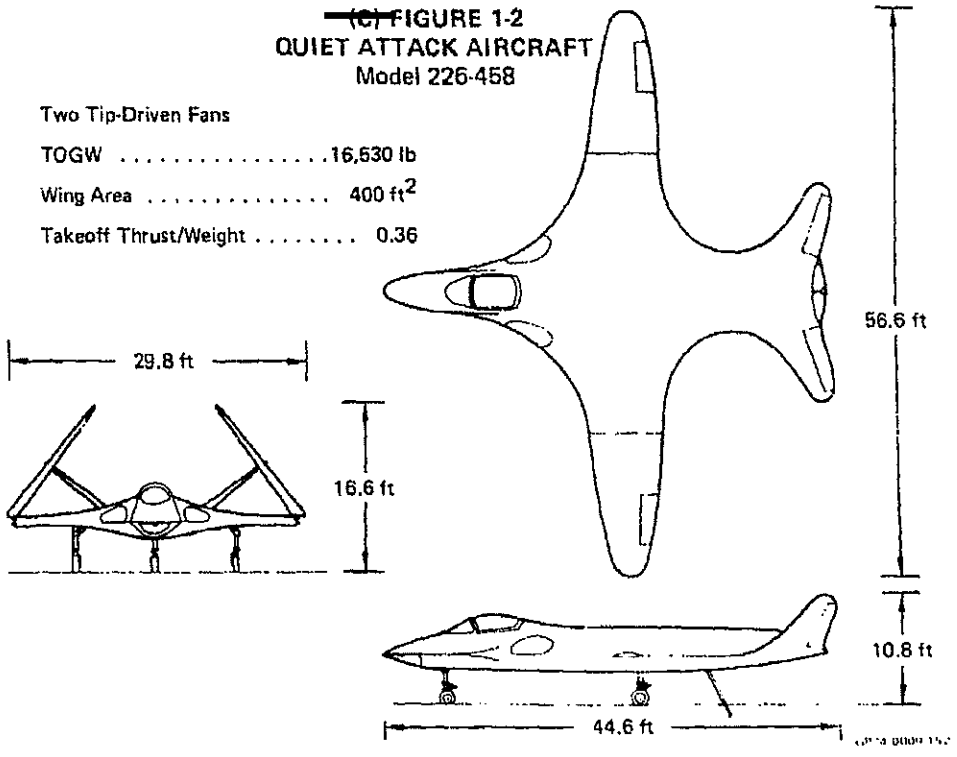

~~(S)~~ FIGURE 1-3
POSSIBLE VRS ELEMENT LOCATIONS

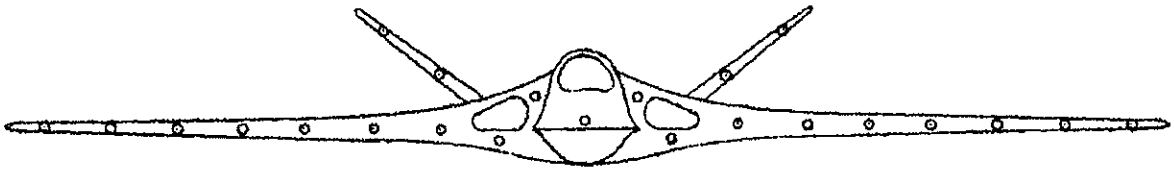

~~(C)~~ Attempts were made to increase the maximum lift coefficient of the wing by using a high lift airfoil developed by Dr. Liebeck of Douglas Aircraft, but it was found that the drag would be prohibitive at low lift coefficients. However, wind tunnel tests by NASA Langley and others show that wing maximum lift coefficient is appreciably increased when the leading edge is continued forward along the fuselage side as a strake. This is similar to the cusps or fillets which are used to blend the wing into the fuselage nose of the quiet attack aircraft to reduce radar cross section. Further analysis and data correlation has now shown that the quiet attack aircraft also experiences a similar maximum lift coefficient increase, which amounts to an increment of 0.4 without flaps over a conventional wing planform for the same airfoil section. Because of the higher lift coefficient available, the use of a smaller 350 ft^2 wing was investigated. but after performance and signature comparisons the 400 ft^2 wing was retained. Thus the external shaping concept of Figure 1-2 produces both radar cross section and aerodynamic benefits, and also could be applied to other aircraft.

~~(C)~~ On Model 226-458 the internal fuselage bomb bay has been retained for carrying two 500 lb bombs on a quiet mission, but provisions have also been made for carrying eight 1000 lb bombs or six 2000 lb bombs externally under the wings on conventional missions where low signatures are not as critical. The aircraft's weights and performance are tabulated in Figure 1-4 for the quiet mission, conventional missions, and ferry flight. The mission profiles used for the quiet (design) mission and the conventional missions are illustrated by Figure 1-5.

~~(S)~~ Mission radius comparisons with the same internal fuel for the two conventional missions in the second and third columns of Figure 1-4 and the quiet mission in the first column show substantial increases in radius on conventional missions in spite of increased weight and drag. This is due primarily to much better specific fuel consumption at optimum speed/altitude. Overseas ferry flight capability without external fuel tanks is also indicated by the last two columns. Since external fuel tanks are not required, the entire wing is made available for armament or other stores on conventional combat missions.

~~(C)~~ The other performance data in Figure 1-4 shows the aircraft is comparable to many existing conventional attack aircraft, while having the additional unique capability of performing a covert mission when low signatures are essential. It should also be noted that the catapult, arrestment, landing, and takeoff performance, which is enhanced by the low wing loading and high C_L, could be made even more attractive by the addition of flaps.

~~(C)~~ FIGURE 1-4
MODEL 226-458 WEIGHT AND PERFORMANCE
No Flaps

		Internal Bombs (1)	External Bombs (2)		Ferry Flight	
		2-500 lb	8-1000 lb	6-2000 lb	Internal Fuel Only	150 Gal. in Bomb Bay
Weights						
TOGW	lb	16,530	23,435	27,275	15,310	16,635
Fuel	lb	← 4,615 →				5,655
Weight Empty	lb	10,270	10,515	10,390	10,270	10,270
Performance						
Mission Radius	nm	400	725	650	2,520	3,010
Max Speed at 2500 ft	kts	445	385	365	–	–
Initial Climb	ft/min	4,950	2,885	2,250	–	–
Catapult WOD						
Standard Day	kts	–48	–13	+4	–	–
Tropical Day	kts	–44	–8	+9	–	–
Arrestment WOD						
Standard Day	kts	–56	–56	–56	–	–
Tropical Day	kts	–53	–53	–53	–	–
Takeoff Ground Run						
Standard Day	ft	1,525	3,330	4,795	1,300	1,550
Tropical Day	ft	2,330	5,175	7,450	1,990	2,370
Landing Ground Roll						
Standard Day	ft	720	730	725	720	725
Tropical Day	ft	770	780	775	770	775
Sustained Turn Radius						
At 300 Knots	ft	1,445	2,560	3,340	–	–
Minimum	ft	825	1,280	1,565	–	–

(1) Quiet mission at 116 knots, 2500 ft altitude.
(2) Conventional missions at optimum speed/altitude.

DP74 0009 154

~~(C)~~ The weapon delivery studies reported in Section 4 are all based on a quiet mission, where penetration and target approach is at a quiet speed of 112 knots at 2500 ft above ground level to minimize both noise and IR signatures. It is shown that target acquisition by the aircraft's FLIR sensor and bomb release can be made on the same pass. After target identification at a ground range of 25,000 ft the aircraft has the acceleration to reach a speed of over 300 knots at bomb release, and the on-board laser designator eliminates any need for another FAC aircraft to illuminate the target for laser guided bombs. At the higher bomb release speeds the aircraft's low wing loading and good thrust-to-weight ratio give it a tight turn radius, for jinking or bomb fragment avoidance, which is less than half the turn radius of conventional attack aircraft such as the F-4 or A-7.

~~(C)~~ The use of VRS lights on the aircraft is considered feasible for forward viewing aspects to reduce visual detection to a range of 7500 ft for daylight conditions and even less for moonlight. VRS lights could also be used to minimize visual detection for all aspect viewing angles in starlight, but are not considered necessary. Since an aircraft almost always appears to a ground observer as a dark object against a brighter sky background, the lights are used to minimize contrast by replacing the sky brightness blocked out by the aircraft silhouette.

~~(S)~~ FIGURE 1-5
ATTACK MISSIONS

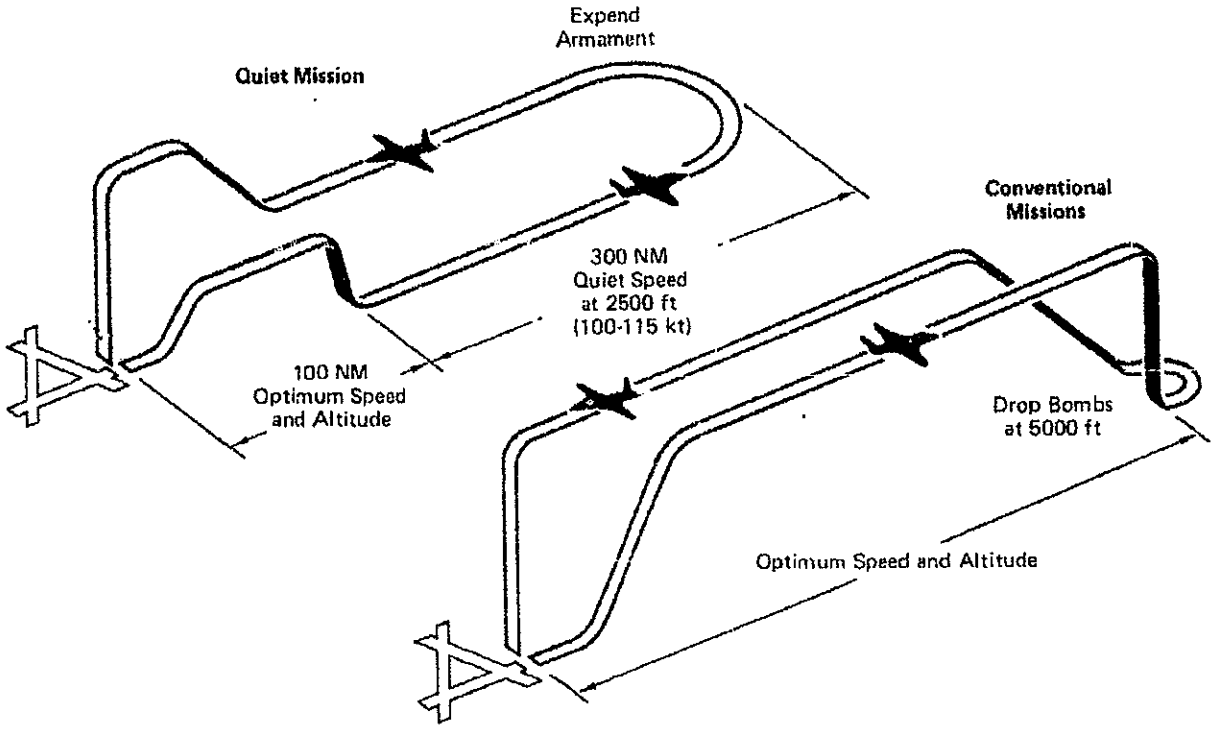

~~(C)~~ Detection of the aircraft in the 8-14 micron bandwidth used by a ground-based FLIR sensor can be reduced to less than a mile by use of an exterior surface coating having an emissivity of 0.6. This is for clear night conditions when the aircraft is approaching at its quiet speed of 115 knots at 2500 ft. Because of the scarcity of data on an aircraft's 8-14 micron IR signature, the work described in Section 8 is considered to be a significant advancement of the analysis for this spectral region.

~~(C)~~ In the 1.7-5 micron IR spectral band, which is used by heat-seeking missiles, substantial reduction has been made in aircraft IR signature by the use of a high bypass propulsion system and a plug nozzle to hide hot metal from direct view. IR signature and detectability increase with speed, due to aerodynamic heating of exterior surfaces and higher thrust producing higher exhaust gas temperature. The effects of speed on the tracking capabilities of the Soviet SA-7 STRELLA missile or the U.S. REDEYE missile are illustrated by Figure 1-6. The STRELLA contours are for the same aircraft speeds as noted for the REDEYE, and each contour represents a signal-to-noise (S/N) ratio of 3. This is considered the minimum S/N ratio acceptable by the detector in the missile to permit it to track the aircraft. The distance below the aircraft for a given contour thus represents the minimum height above ground level (AGL) that the aircraft could be to avoid being tracked and fired upon by the particular missile. At a low speed of 150 knots the quiet attack aircraft could be as low as 200 ft AGL without being tracked by the STRELLA, but at maximum speed of 445 knots it would have to stay at least 1300 ft AGL. For the same speeds the minimum AGL heights are greater, at 1300 and

4300 ft. respectively, for the REDEYE, and the aircraft at 2500 ft AGL would have to keep its speed below 350 knots. In any event, these minimum heights AGL are substantially less than they would be with turbojet or low bypass turbofan propulsion.

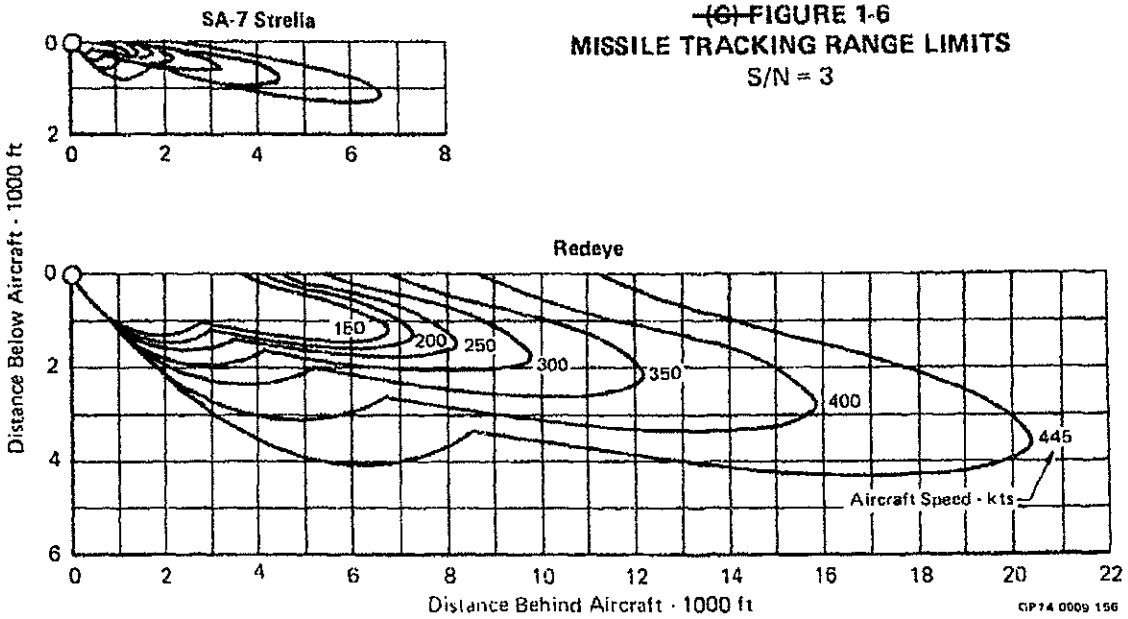

~~(C)~~ FIGURE 1-6
MISSILE TRACKING RANGE LIMITS
S/N = 3

~~(S)~~ Due to nearly identical size, shape, and other radar cross section (RCS) reduction features, the RCS values as a function of radar frequency and viewing aspect are considered the same for Model 226-458 as they were previously for Model 226-454A. At X-band frequency of 9.2 GHz and for a head-on viewing aspect the RCS of the quiet attack aircraft is only 0.3 square meters, which is only about 1% of that for the F-4, and similar major RCS reductions have been made for other viewing aspects and frequencies. However, although it is virtually impossible to reduce RCS to the point where the aircraft cannot be detected, the real payoff of low RCS comes when ECM is used. In Section 6 it is shown that when the quiet attack aircraft carries an existing ALQ-119 ECM pod it can approach a Soviet FANSONG E radar head-on and jam it until the radar burnthrough range of 1.6 nm is reached. Since this is less than the minimum launch range of the SA-2 missile, the SA-2 kill probability would be significantly reduced.

~~(S)~~ Because of the different maximum lift coefficient, weight, and propulsion system used on Model 226-458, the noise and acoustic detection ranges have been recalculated for a clean aircraft without external stores. A method was developed to estimate the overall noise from external stores and pylons, but no measured data was found to determine the noise spectrum needed to evaluate acoustic detection distance. Aerodynamic noise is still more dominant than propulsion noise at any speed. Compared to model 226-454A, the heavier weight of model 226-458 tends to increase noise but this is overcome by the higher lift coefficient, resulting in a lower quiet speed and less noise.

~~(C)~~ In summary, the additional studies performed in this contract extension period reconfirm the initial conclusion that an attack aircraft with good mission capabilities and significantly reduced signatures is feasible. The speed and maneuverability of the quiet attack aircraft make it attractive for another attack mission, where it could act as a fast Forward Air Control (FAC) aircraft. In addition, the techniques for signature reduction could be applied to the design of other new aircraft.

2. DESIGN

(C) During the original contractual period an initial quiet attack aircraft, Model 226-454A illustrated by Figure 2-1, was developed after a series of parametric studies. This aircraft featured a considerable amount of exterior shaping to reduce radar cross section, low wing loading and an internal bomb bay to reduce aerodynamic noise, and an internally mounted high bypass (6.45) propulsion system with one gas generator and two tip-driven fans to reduce both propulsion noise and IR signatures. A turret-mounted 7.62 mm minigun was also provided but the turret was made retractable to avoid the increased aerodynamic noise and radar cross section of a protruding one. Because of the low wing loading no high lift devices were used.

(C) In this follow-on contractual period the quiet attack aircraft, Model 226-458 shown by Figure 2-2, was developed by retaining the same features, design payload, and design mission profile as for Model 226-454A, but the scaled GE1/10 gas generator was replaced by the core gas generator from the TF-34 engine. With the same wing area of 400 ft^2 at an aspect ratio of 8, this propulsion system change resulted in a bypass ratio of 5.0 and a somewhat heavier aircraft which still has attractive performance and low signatures. A comparison of Figures 2-1 and 2-2 shows virtually no difference in external dimensions and appearance.

(C) The significant size and weight figures for the two aircraft are tabulated in Figure 2-3. The higher wing loading and lower thrust loading for Model 226-458 would seem to indicate poorer performance than Model 226-454A, but there are two compensating factors which favor Model 226-458. One of these is a higher wing maximum lift coefficient, discussed in Section 3. The other is higher thrust at higher speeds for the TF-34 gas generator, as shown in the next section.

2.1 PROPULSION SYSTEM COMPARISON

(C) The tip driven fans are practically identical in size and weight for either the original scaled GE1/10 or the TF-34 gas generator. The differences between the two propulsion systems are thus almost completely due to the different gas generators. The GE1/10 uses more advanced technology which gives it a lower weight of 270 lb compared to 875 lb for the TF-34 core gas generator. Other characteristics are tabulated below:

	Scaled GE1/10	TF-34
FANS		
Pressure Ratio	1.5	1.5
Max. SLS Airflow - lb/sec	200.0	175.7
Fan Tip Diameter - in.	25.0	23.0
Turbine Tip Diameter - in.	27.5	28.2
GAS GENERATOR		
Compressor Pressure Ratio	15.8	15.5
Turbine Inlet Temperature - °F	2450	2166
Max. SLS Airflow - lb/sec	31.1	35.4
Length - in.	43.3	54.2
Diameter - in.	16.4	28.9

~~(C)~~ FIGURE 2-1
INITIAL QUIET ATTACK AIRCRAFT
Model 226-454A

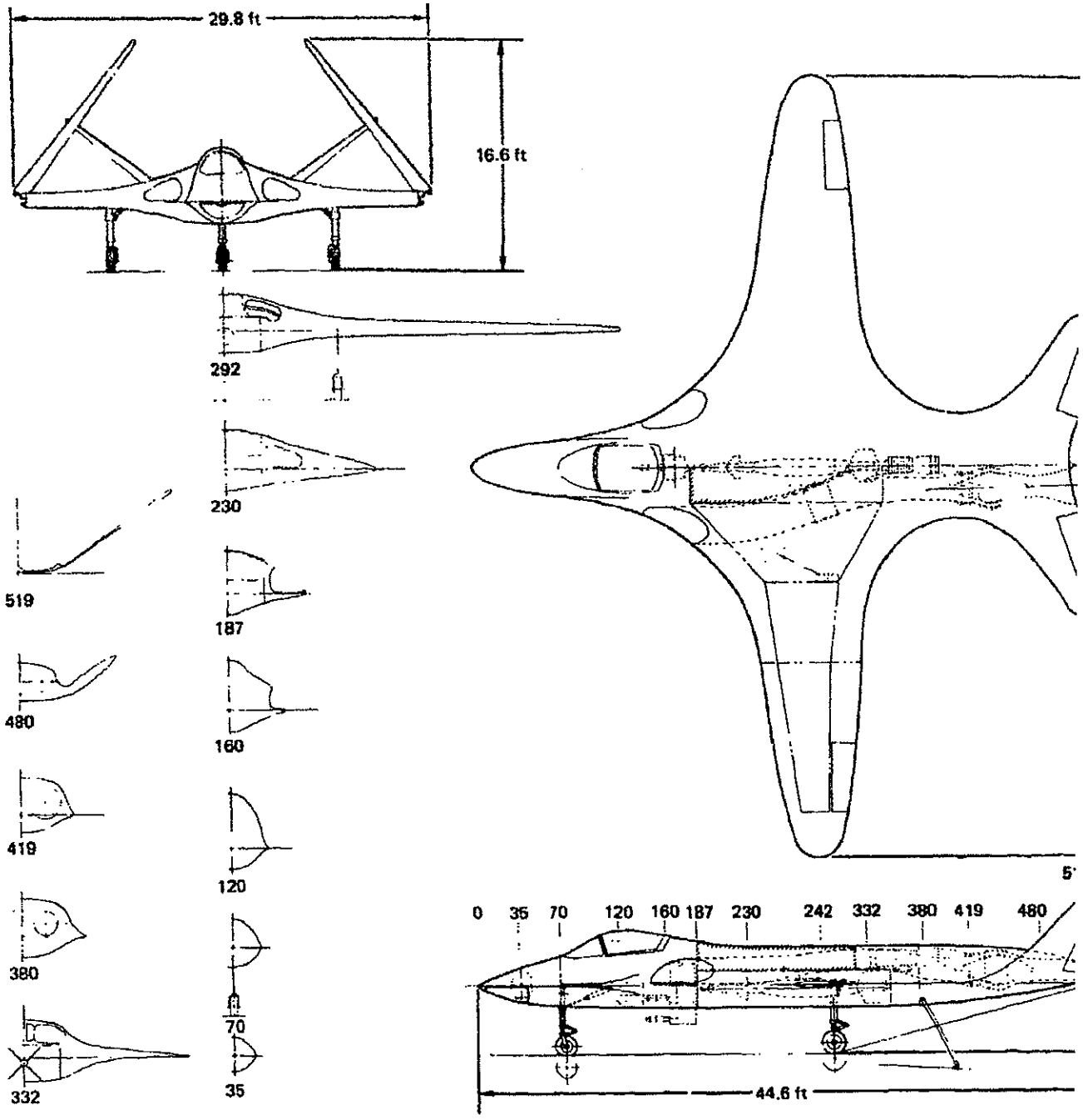

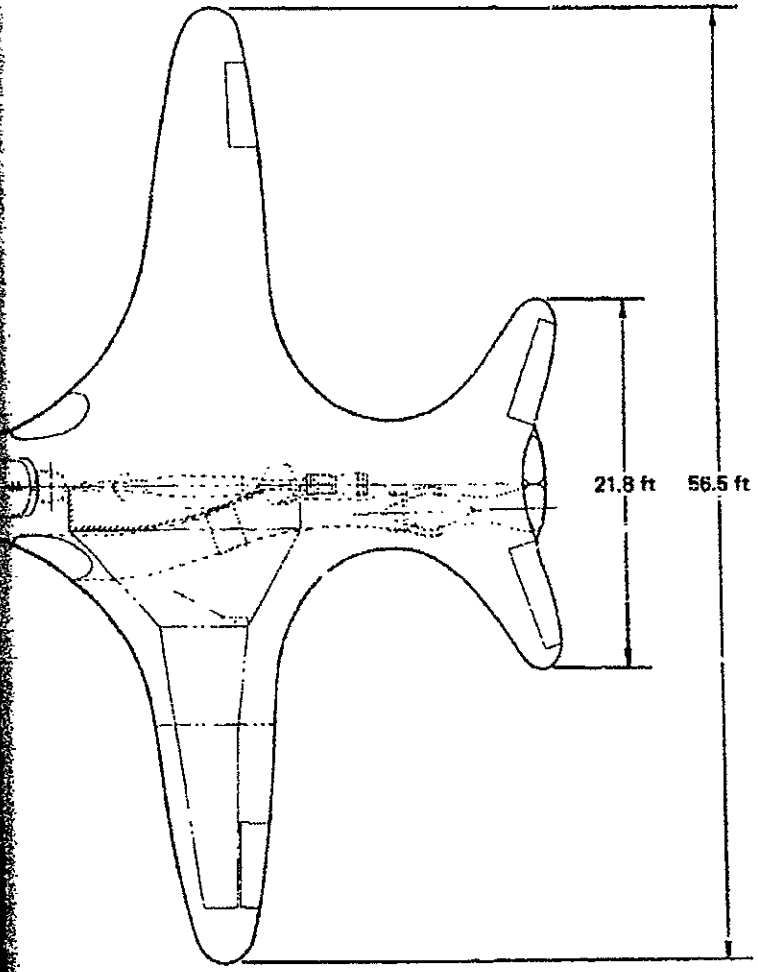

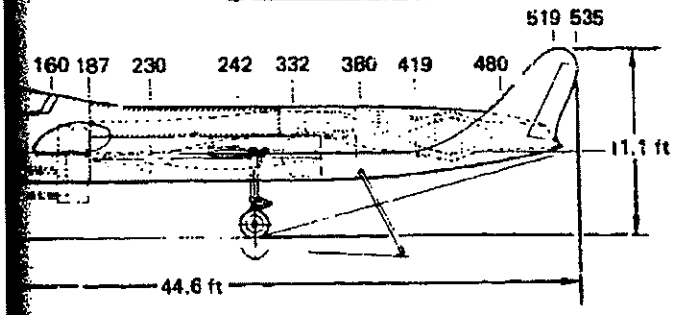

Physical Characteristics

		Wing	Tail (Exposed True)
S_w	ft^2	400	70
AR		8	5.2
λ		0.35	0.3
b/2	in.	339.4	114.5
C_R	in.	125.7	67.4
C_T	in.	44	20.4
MAC	in.	91.45	48.3
$\Lambda_{C/4}$	deg	2	21
Airfoil		$NACA63_2$-415	NACA-014
Dihedral	deg	0	35

Propulsion
GE1/10J1(46%) Gas Generator (2) Tip Driven Fan (23%) 1.5 R_F

Landing Gear
Nose: 18 x 5.5 Type VII Tire Main: 20 x 5.5 Type VII Tire

Armament
(1) GAU-281A 7.62 mm Minigun (1000 Round) (2) MK-8[illegible] Laser Bomb (611.0 lb Each) or (1) MK-83 Laser Bomb (1159 lb)

~~CONFIDENTIAL~~

~~CONFIDENTIAL~~

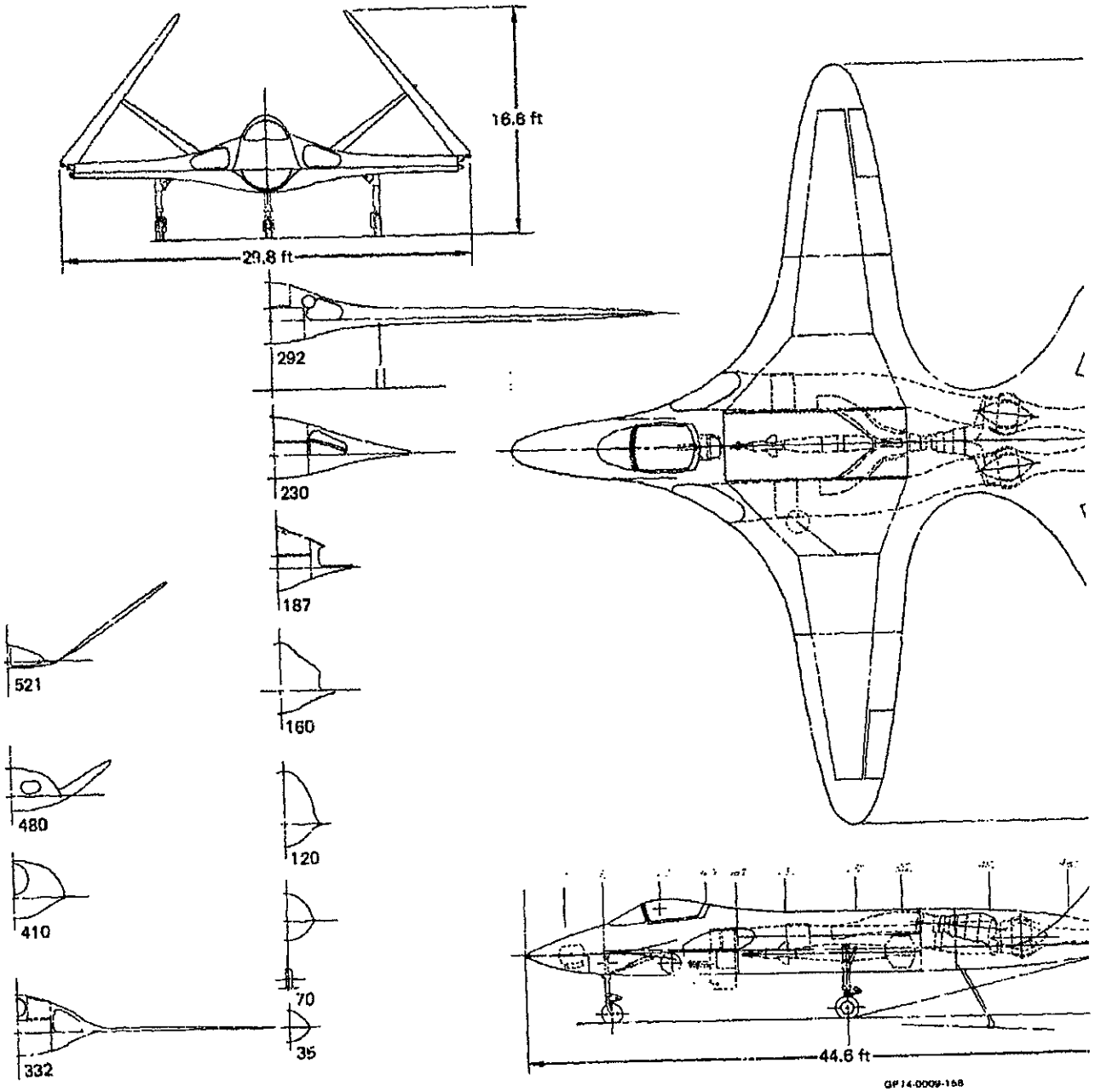

~~(C)~~ FIGURE 2-2
QUIET ATTACK AIRCRAFT
Model 226-458

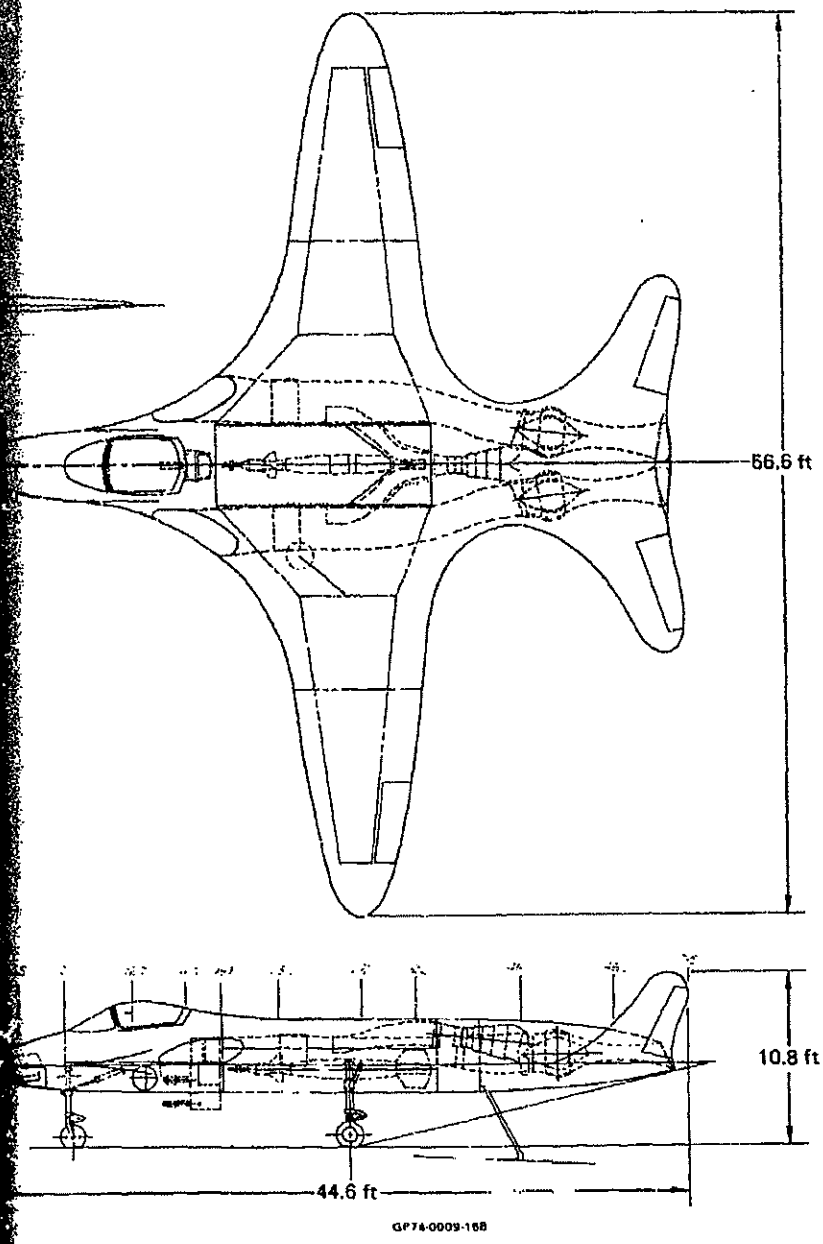

		Wing	Tail(Exposed True)
S_W	ft^2	400	70
AR		[illegible]	5.2
λ		0.568 (Theo)	0.3
b	ft	56.56	19.1
b/2	in.	339.41	114.6
C_R	in.	108.23	67.4
C_T	in.	61.5 (Theo)	20.4
MAC	in.	91.8	48.3
Λ c/2		0^o	21^o
Airfoil		$NACA63_2$-415	NACA-014
Dihedral		0^o	35^o

Propulsion
GE TF34 (Core) Gas Generator (2) Tip Driven Fans 1.5 R_F
Landing Gear
Nose: 18 x 5.5 Type VII Tire Main: 22 x 6.6 Type VII Tire
Armament
(1) GAU-2B1A 7.62 mm Minigun 1000 Round (2) 500 lb Laser Bomb or (1) 1000 lb Laser Bomb

~~(C)~~ FIGURE 2-3
SIZE AND WEIGHT COMPARISON
Design Mission/Payload

		Model 226-454A	Model 226-458
Wing Area	ft^2	400	400
Aspect Ratio		8	8
Span	ft	56.6	56.6
Length	ft	44.6	44.6
Height	ft	11.1	10.8
Takeoff Gross Weight	lb	14,410	16,530
Weight Empty	lb	9,360	10,270
Fuel	lb	3,415	4,615
Gas Generator Weight	lb	270	875
Internal Bomb Load	lb	1,222	1,222
Wing Loading at TOGW		36.0	41.3
Takeoff Thrust Loading		0.440	0.368

(C) The more advanced technology of the GE1/10 also gives it better specific fuel consumption at the same quiet speed, which accounts for most of the fuel required. Figure 2-4 compares fuel flow of the two propulsion systems over the ranges of thrust required as shown by the solid lines, for each aircraft from the start to the end of quiet cruise. Maximum thrust and fuel flow at quiet speed occur at the start of the quiet cruise when each aircraft's weight and drag are highest for the 300 nm outbound and 300 nm inbound quiet cruise. Even at the same thrust the TF-34 fuel flow is about 25% higher than the scaled GE1/10. This and the higher thrusts required for the TF-34 aircraft account for most of the difference in mission fuel shown in Figure 2-3.

(C) Maximum thrust of the two propulsion systems is shown for both sea level and 2500 ft standard day conditions by Figure 2-5. At low speed the higher thrust of the scaled GE1/10 system, along with the aircraft lower weight, is responsible for the better takeoff run and initial climb of Model 226-454A. On the other hand, the higher thrust above 200 knots at 2500 ft for the TF-34 accounts for the higher maximum speed of Model 226-458.

2.2 WEIGHTS

(C) Figure 2-6 compares the weights of Models 226-454A and 226-458, when both aircraft are carrying two 500 lb laser guided bombs in the internal bomb bay, and fuel is determined by the basic covert mission illustrated later by Figure 2-8. Both aircraft employ conventional aluminum alloy structure except for the use of graphite epoxy skins for weight saving on the wing torque box, ailerons, tail surfaces, and fuselage bomb bay doors. Both aircraft also include 219 lb of radar absorbing material and 90 lb of acoustic treatment in the inlet and exhaust ducts to reduce radar cross section and propulsion noise. Model 226-458 includes an additional 150 lb in the electrical system for the lighting system used to reduce visual signature.

~~(C)~~ FIGURE 2-4
FUEL FLOW AT QUIET SPEED
112 Knots at 2600 Ft, S_W = 400 Ft^2

	Aircraft Weight
With TF-34	
Start Outbound Quiet Cruise	16,145
End Inbound Quiet Cruise	11,260
With Scaled GE1/10	
Start Outbound Quiet Cruise	13,960
End Inbound Quiet Cruise	10,210

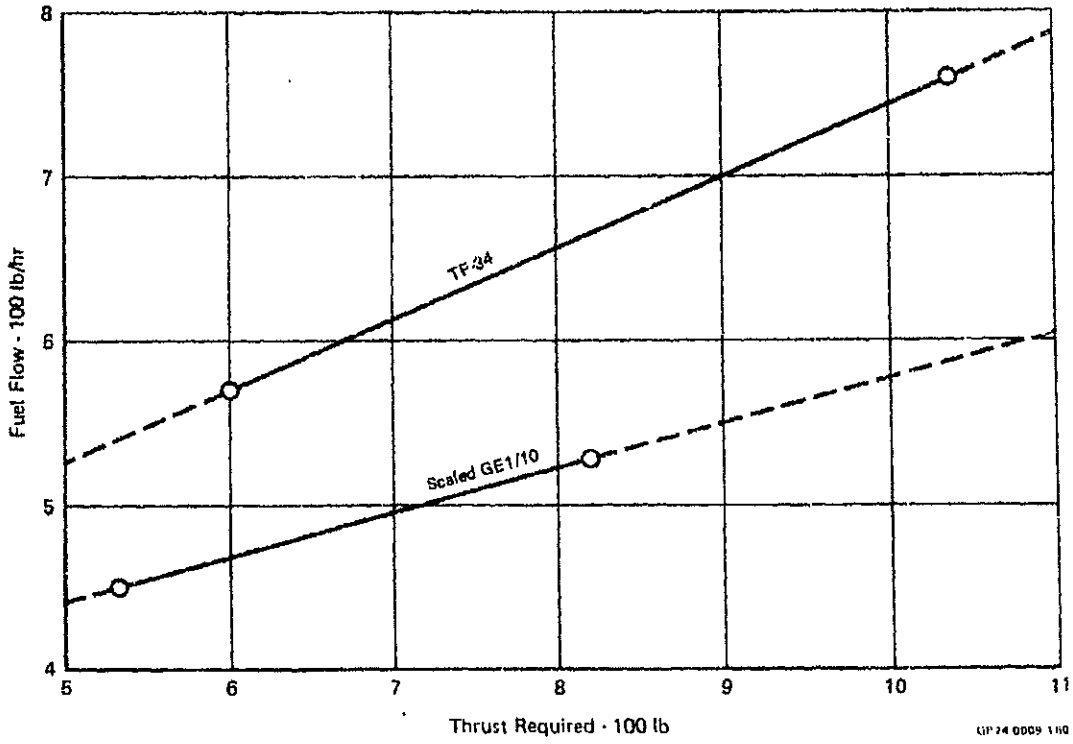

~~(C)~~ FIGURE 2-5
MAXIMUM THRUST

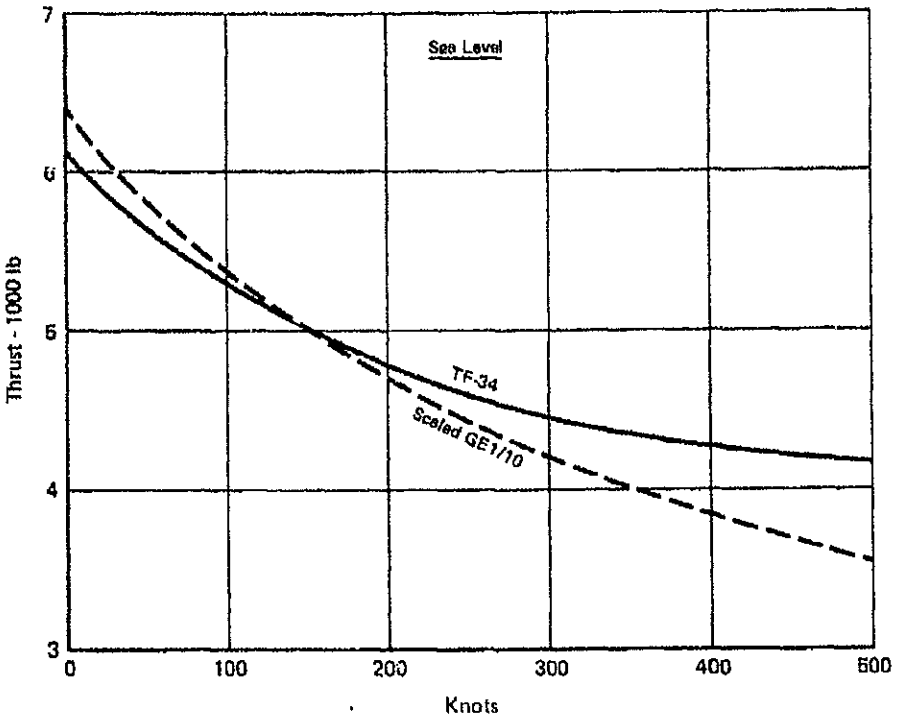

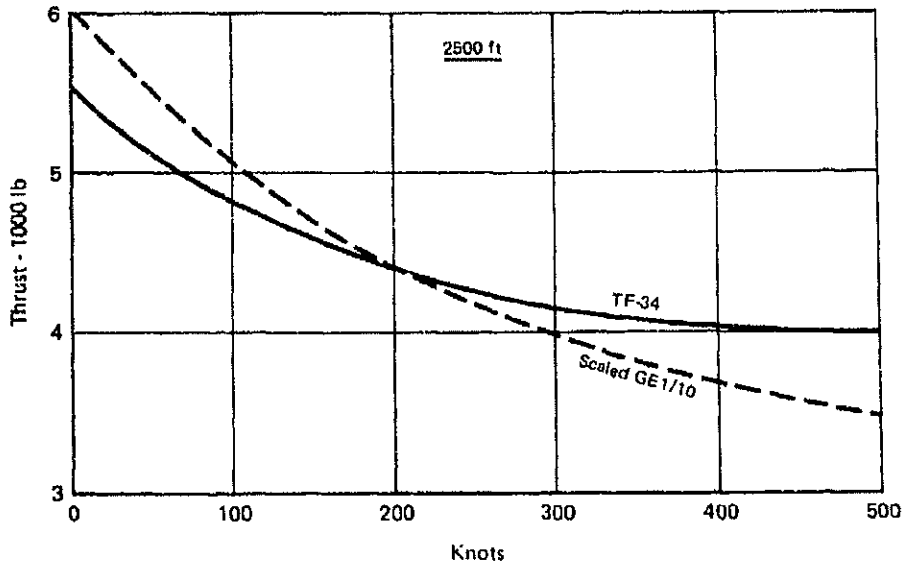

~~(C)~~ FIGURE 2-6
DETAIL WEIGHT COMPARISON
Internal Bombs

	Model 226-454A	Model 226-458
Wing	1,770	1,865
Tail	243	243
Fuselage	2,655	2,655
Landing Gear - Nose	128	128
- Main	467	475
Surface Controls	149	149
Engine Section	39	39
Propulsion		
Gas Generator	270	875
Fans (2)	302	302
Air Induction and Fan Exhaust	523	523
Lube and Cooling	10	10
Fuel System	252	280
Engine Controls	30	30
Auxiliary Drives and Starting	120	120
Instruments	125	125
Hydraulics	141	141
Electrical	270	420
Electronics	1,060	1,060
Armament	260	260
Furnishings	190	190
ECS	120	120
Auxiliary Gear	62	62
Contingency	184	198
Weight Empty	9,360	10,270
Crew	200	200
Crew Equipment	40	40
Oil	18	18
Trapped Fuel	35	46
Gun and Ammunition	120	120
Bombs	1,222	1,222
Operating Weight Empty	10,995	11,916
Fuel	3,415	4,615
Takeoff Gross Weight	14,410	16,531

GP74 0089 162

~~(C)~~ While Model 226-454A was designed to carry only internal bombs, subsequent investigations of Model 226-458, as discussed in Section 3, showed that the low wing loading and reasonably good thrust-to-weight ratio made it possible to carry much larger bomb loads externally with attractive performance. Consequently the landing gear and wing of Model 226-458 include additional weight increments for carrying up to six 2000 lb MK84 bombs on individual pylons under the wing. Figure 2-7 tabulates the weights for Model 226-458 for the basic covert mission with internal bombs and for two alternate missions with either eight 1000 lb MK83 or six 2000 lb MK84 bombs on individual pylons. Note that the same amount of internal fuel is used for all three missions.

~~(C)~~ FIGURE 2-7
MODEL 226-458 WEIGHT STATEMENT

	Bomb Load		
	2-500 lb Internal	8-1000 lb External	6-2000 lb External
Wing	1,865	1,865	1,865
Tail	243	243	243
Fuselage	2,655	2,655	2,655
Landing Gear - Nose	128	128	128
- Main	475	475	475
Surface Controls	149	149	149
Engine Section	39	39	39
Propulsion			
TF-34 Gas Generator	875	875	875
Fans (2)	302	302	302
Air Induction and Fan Exhaust	523	523	523
Lube and Cooling	10	10	10
Fuel System	280	280	280
Engine Controls	30	30	30
Auxiliary Drives and Starting	120	120	120
Instruments	125	125	125
Hydraulics	141	141	141
Electrical	420	420	420
Electronics	1,060	1,060	1,060
Armament	260	505	380
Furnishings	190	190	190
ECS	120	120	120
Auxiliary Gear	62	62	62
Contingency	198	198	198
Weight Empty	10,270	10,515	10,390
Crew	200	200	200
Crew Equipment	40	40	40
Oil	18	18	18
Trapped Fuel	46	46	46
Gun and Ammunition	120	120	120
Bombs	1,222	7,880	11,844
Operating Weight Empty	11,916	18,819	22,658
Fuel	4,615	4,615	4,615
Takeoff Gross Weight	16,531	23,434	27,273

GP74 0009 183

2.3 DESIGN CRITERIA

(U) A key objective throughout this study has been that the quiet attack aircraft be practical in design and have attractive operational capabilities for either carrier or land basing. In many cases signature reduction, especially aerodynamic noise reduction, can unduly penalize aircraft size, weight, and performance if carried to extremes without regard to the overall objective. Consequently, significant and realistically adequate signature reductions have been attained with minimum compromise to other desirable qualities.

~~(S)~~ DESIGN MISSION PROFILE - The covert mission profile used to size all the aircraft in the study on a common basis is illustrated by Figure 2-8. It is assumed that the carrier is standing 100 nm offshore from enemy held territory, so that the first and last 100 nm of the mission can be flown at optimum speed and altitude without regard to how much noise or IR signature is produced. The remaining 600 nm is flown at quiet speed, using the FLIR sensor to search for targets or to avoid alerting enemy ground defenses enroute to and from a pre-planned target. The quiet speed altitude of 2500 ft about ground level was selected as a reasonable compromise between conflicting objectives. Flight at a lower altitude, close to treetop level, would have the advantages of minimizing enemy ground radar or visual detection and minimum exposure time to enemy ground fire. The disadvantages would be more noise propagated to a ground observer, within range of small arms and possibly ground based IR missiles, target masking by foliage or terrain, terrain avoidance at night, and weapon delivery problems. The advantages of higher altitude flight, say at 5000 ft, would be less chance of a ground observer hearing the aircraft, less masking of targets, less terrain avoidance problems, and more standoff range for weapon launch. The aircraft would be immune to small arms fire and ground IR missiles, but this is also the case at 2500 ft. Disadvantages would be easier enemy radar and visual detection, higher CEP for unguided weapons, less chance of finding small targets in background clutter, and more exposure time to radar or optically tracked AAA.

~~(C)~~ FIGURE 2-8
DESIGN MISSION PROFILE

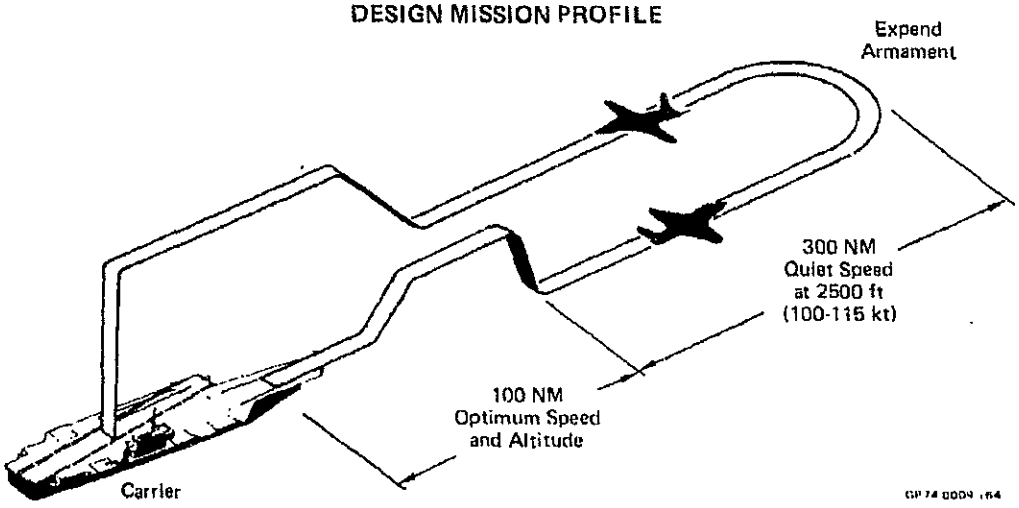

MCDONNELL AIRCRAFT COMPANY

~~CONFIDENTIAL~~

~~(C)~~ DESIGN PAYLOAD - All aircraft in the study have been sized to carry the same payload on the design mission. The avionics, including sensors, and the armament have been selected to make the aircraft capable of autonomous operation in day or night clear weather, and with some self-defense capability. The aircraft is able to search for, identify, and destroy targets without assistance from other aircraft or ground forces. The internal bomb bay is designed to accept a variety of weapons. Sin- external stores and protuberances increase noise, all payload is carried internally on the covert design mission.

~~(C)~~ AVIONICS - The list of avionics equipment, including uninstalled component weights and volume requirements, is shown in Figure 2-9. The navigation system, which does not require any electro-magnetic radiation from the aircraft, provides for undetectable quiet penetration. Radar altimeter radiation is not considered a problem in quiet penetration because it is confined to a narrow beam directly below the aircraft, and also during clear daylight or moonlight with the aircraft at 2500 ft altitude the pilot should be able to see the ground. ACLS (automatic carrier landing system) provides the flight aid needed for operation from an aircraft carrier.

~~(C)~~ The Communication and Identification equipment is more or less standard for this type of application. VHF or HF radio is not included because when the aircraft is beyond the line-of-sight UHF range from the carrier, it is assumed to be over enemy territory where any ·dio transmission could betray its location. Aircraft location betrayal is also the reason for not including radar.

~~(C)~~ HUD and helmet sight are included to aid the single crew member during flight and target search at the relatively low altitude of 2500 ft. Laser designator eliminates the need for a FAC support aircraft when using Laser guided bombs. The FLIR is the Texas Instruments Model AN/AAS-28A which has been successfully flight demonstrated. Both the FLIR and Laser designator are mounted on gimbals in the fuselage nose to provide variable sensor aiming in both azimuth and elevation.

~~(C)~~ WEAPONS - The bomb bay is sized to accommodate a variety of weapons for maximum mission flexibility. The combination of weapons in the bomb bay is limited to a total weight of approximately 1250 lbs.

~~(C)~~ A Model GAU-2B1A 7.62 mm minigun with 1000 rounds of ammunition is mounted in a retractable belly turret just forward of the bomb bay. The turret is retracted flush with the underside of the aircraft during quiet penetration to minimize acoustic noise and radar cross section, and is extended only when the gun is to be fired. This type of gun installation is produced by the Emerson Electric Company in St. Louis and, except for the retractable feature, has been widely used on the helicopter gunships in SEA. Our quiet attack installation has been reviewed with Emerson Electric, and no development problems are expected.

~~(C)~~ FIGURE 2-9
NAVY QUIET ATTACK AVIONICS

	Weight (lb)	Volume (ft^3)
Navigation and Flight Aids		
Inertial Navigation System (Platform)	52	1.00
Backup Attitude and Heading Ref. System	24	0.42
Backup Flux Gate Compass	2	0.10
Air Data System	20	0.34
LORAN (Receiver, Antenna, Coupler)	10	0.20
TACAN (with Antenna)	30	0.50
UHF-ADF	13	0.30
ACLS and Beacon	20	0.40
Radar Altimeter (with 2 Antennas)	10	0.10
Communication and Identification		
UHF Transmitter, Receiver (2), Antenna (2)	60	0.90
KY-28 Secure Communication System	16	0.30
IFF Transponder	16	0.20
Kit-1A/tsec Secure IFF	11	0.20
Central Digital Computer	50	1.00
Displays and Controls		
HUD, HSI, Helmet Sight	120	2.50
CNI and Miscellaneous Control Panels		
Stores Monitor and Management Set	20	0.60
Flight Control System (Autopilot, APC, Stabilator Augmentation)	40	0.87
Sensors		
Laser Designator	25	0.50
FLIR	200	9.00
FLIR/Laser Turret Mount		
Counter Measures		
Radar Warning System	80	2.00
	809	21.43

GP24 0009 165

~~(C)~~ GROUND RULES - Listed below are key ground rules, used in the study:

- Carrier suitability based on unrestricted operation from CVA-59
- Extended wing span less than that of the A-3D (72.5 ft)
- Maximum speed capability at least as good as the AD Skyraider (317 knots at 15000 ft)
- One man crew
- Near term technology
- Structural limit load factor of 8 g with internal bomb load
- Fuel allowance of 2 minutes at SLS intermediate power for start, warmup, takeoff, and a reserve of 5% total fuel.

3. AERODYNAMIC CHARACTERISTICS AND PERFORMANCE

(U) Flaps have not been used on the quiet attack aircraft because the low wing loading for the design mission/payload made them unnecessary. With more emphasis on W.O.D. or takeoff distance reduction, especially with large external bomb loads, flaps could be added but a wind tunnel test program would be desirable to determine the lift coefficients available, which are difficult to predict analytically because of the unconventional wing planform. Nevertheless, investigations were made for the purpose of increasing the lift coefficient without flaps. Initially, an airfoil specifically designed for high lift, as well as the use of an inflatable boot to change airfoil contour for either high lift at low speed or low drag at high speed were investigated but subsequently discarded as being impractical. However, later analytical studies indicated that the fillets or strakes on the sides of the forward fuselage, due to the blending of the wing into the fuselage for radar cross section reduction, would also substantially increase the maximum lift coefficient. This increased lift coefficient has been accounted for in the performance analysis of Model 226-458.

(U) Because of the differences in weight, thrust, and lift coefficient of the aircraft with TF-34 instead of the initial scaled GE1/10 propulsion system, a comparison was made of the effects of two different wing areas of 400 and 350 ft^2 at the same aspect ratio of 8, and using preliminary weight estimates. After considering the effects on weight, performance, and signatures it was decided to stay with the 400 ft^2 wing area for Model 226-458. Section 3.4 shows the resulting performance for the basic covert or quiet mission, as well as performance for alternate missions including ferry flight.

3.1 MAXIMUM LIFT AIRFOIL

(U) The maximum lift airfoil section developed by Dr. Liebeck at Douglas Aircraft was examined for use in the low speed portion of the design mission. For high speed operation, the airfoil section might also be recontoured by means of an inflatable boot to produce a section shape having more acceptable high speed characteristics.

(U) Figures 3-1 and 3-2, based on References (2) and (3), contain comparisons of the section lift and drag characteristics of the currently employed 63_2-415 section and the Liebeck section optimized for maximum lift. The Liebeck section has a $C_{L_{MAX}}$ approximately 0.47 higher than the conventional NACA section. In the section drag comparison of Figure 3-2, the Liebeck section has the lower drag above a lift coefficient of approximately 0.88; below a C_L of 0.58, the shape of the drag polar indicated lower surface separation with its attendant drag increase.

(U) In Figure 3-3, the complete airplane drag polars are compared for both airfoil sections at the 400 ft^2 wing area and aspect ratio of 8. Above 0.9 C_L the Liebeck section produced a small drag reduction. At lift coefficients below 0.58 the Liebeck configuration had considerably more drag than the conventional configuration. Due to this large drag increase, the maximum speed of Model 226-454A would be reduced from 430 knots to 275 knots at 2500 ft altitude for a 400 ft^2 Liebeck wing without a boot. Although the increased value of $C_{L_{MAX}}$ permitted a reduction in wing area from 400 to 291 ft^2, for the same quiet speed, the maximum speed attainable with this smaller Liebeck wing without a boot would still only be 321 knots.

(This Page is UNCLASSIFIED)

(U) FIGURE 3-1
SECTION LIFT COMPARISON

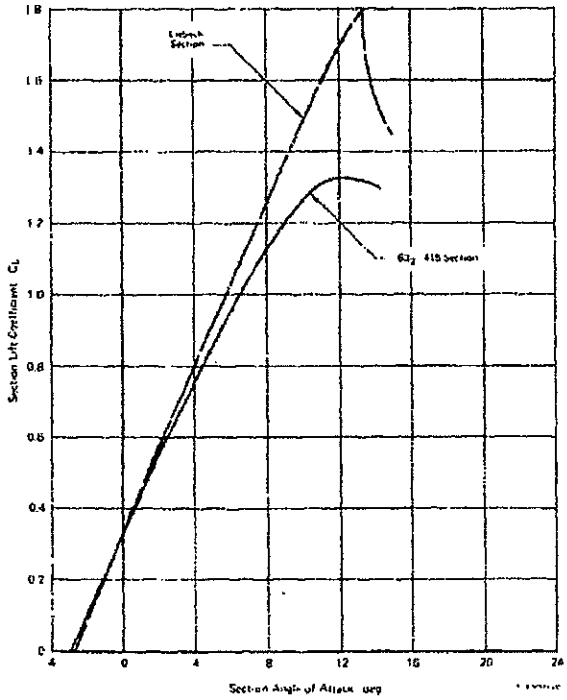

(U) FIGURE 3-2
SECTION DRAG COMPARISON

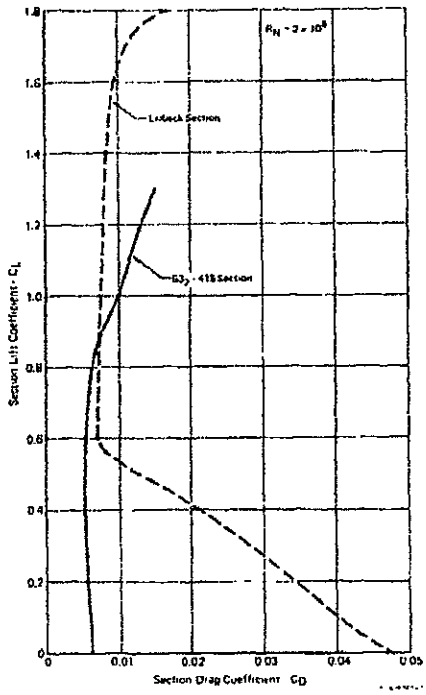

(U) FIGURE 3-3
AIRCRAFT DRAG POLAR COMPARISON
Sw = 400 Ft^2 AR = 8

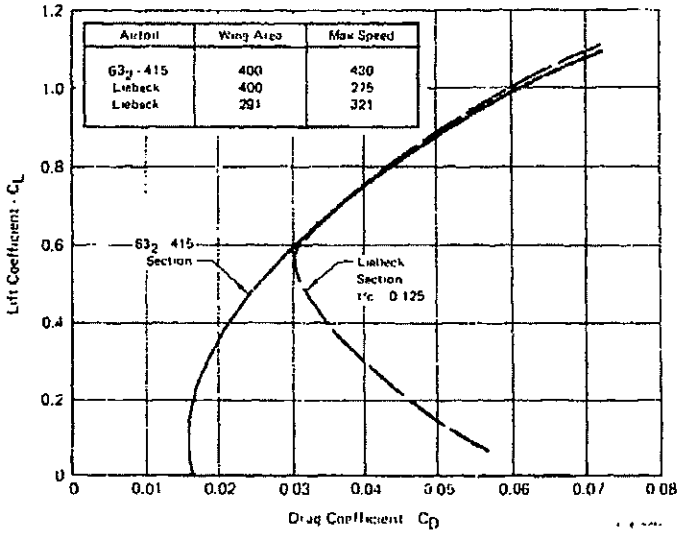

(U) Since the Liebeck airfoil is not acceptable for high speed, an investigation was also made to see if an inflated boot could be used to change from the current 63_2-415 conventional airfoil for high speed to the Liebeck airfoil for low quiet speed. Figure 3-4 compares the shapes of these airfoils, and illustrates what a radical departure the Liebeck airfoil is from a conventional one. Because of these large contour differences the concept of an inflatable boot with the Liebeck airfoil does not appear practical. Since there would be little gain in maximum lift coefficient by using an inflated boot with a conventional airfoil to increase its thickness ratio, both the Liebeck airfoil and the inflated boot concept were dropped from further consideration.

(U) FIGURE 3-4
AIRFOIL GEOMETRY COMPARISON

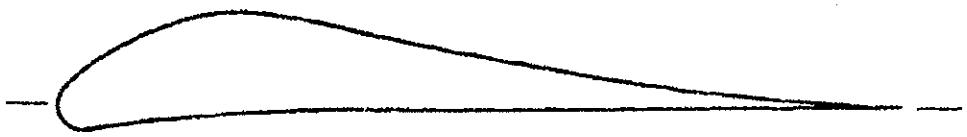

Liebeck Section - t/c = 0.125

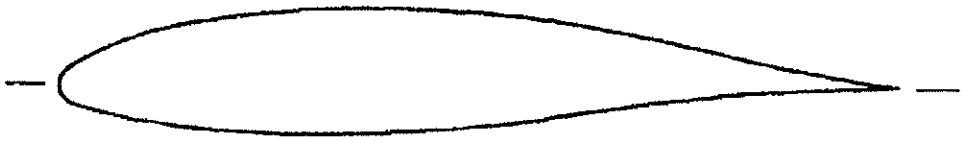

63_2 - 415 Section

GP74 0009 22

(U) The possibility of using a mechanically actuated variable camber system, such as that being developed by Boeing under ONR sponsorship, was also considered. However, this type of system requires single curvature (wrapped) wing skin which is temporarily deformed to a different curvature to provide the increased lift. Because of the curved leading and trailing edges, the wing skin on the quiet attack aircraft is double curvature, and this makes such a variable camber scheme impractical. Another possibility considered was mechanically actuated leading edge slats or Kreuger flaps. These high lift devices require a straight hinge line, and because of the curved wing leading edge they would have to be broken up into a number of individually actuated segments. This could probably be done but the major objections would be the detrimental effects on signatures. From an aerodynamic noise standpoint the air flowing through the gaps between adjacent segments in the extended position would create whistles to increase the acoustic detection distance. Radar cross section would also be increased because of the multitude of surface discontinuities and the additional reflecting surface area from extended Kreuger flaps.

3.2 WING-BODY FILLET CONTRIBUTIONS

(U) The initial estimate of maximum lift coefficient for the quiet airplane configuration was based on the theoretical wing planform excluding the wing-fuselage fillets added to reduce radar cross section. Wind tunnel tests conducted by NASA Langley, Reference (4), indicate that the addition of these fillets substantially increases the maximum lift coefficient of the theoretical wing planform. Figure 3-5 presents the increase in $C_{L_{MAX}}$ as a function of the ratio of fillet area shown by the cross hatched area on the planform sketch, to theoretical wing reference area, which is an ellipse as indicated by the planform dotted lines. For the quiet attack aircraft, with its theoretical wing reference area of 400 ft^2, the increase in maximum lift coefficient is 0.38, which is nearly as much as the basic Liebeck airfoil would have provided. The lift characteristics for the configuration, including the addition of the lift due to the fillets, is shown in Figure 3-6.

(U) FIGURE 3-5
LEADING EDGE FILLET EFFECT ON $C_{L_{MAX}}$

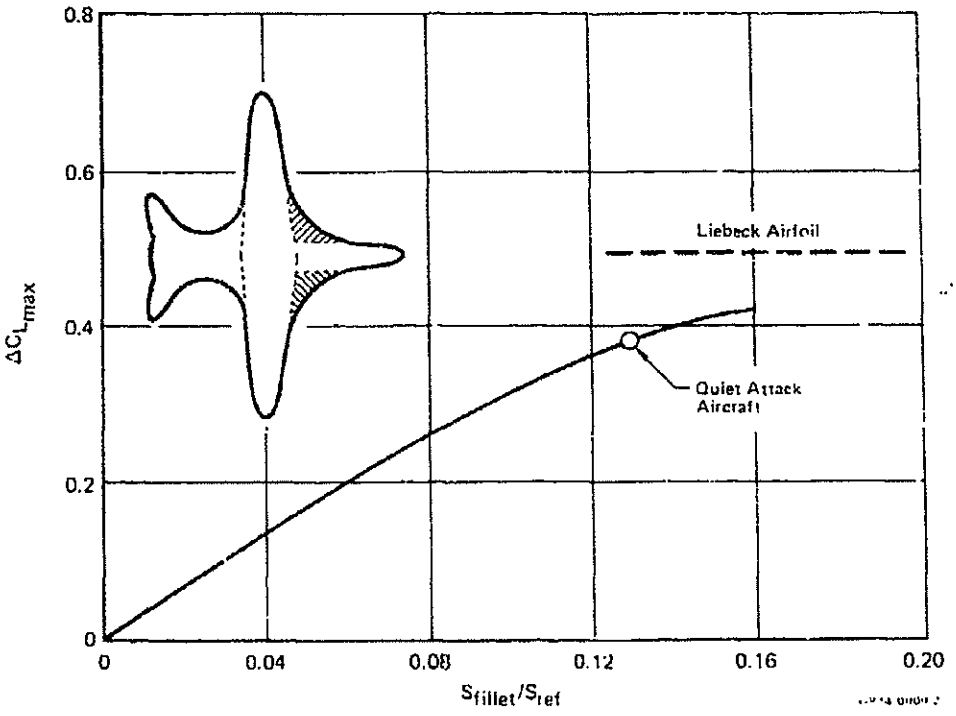

(U) FIGURE 3-6
LIFT CHARACTERISTICS

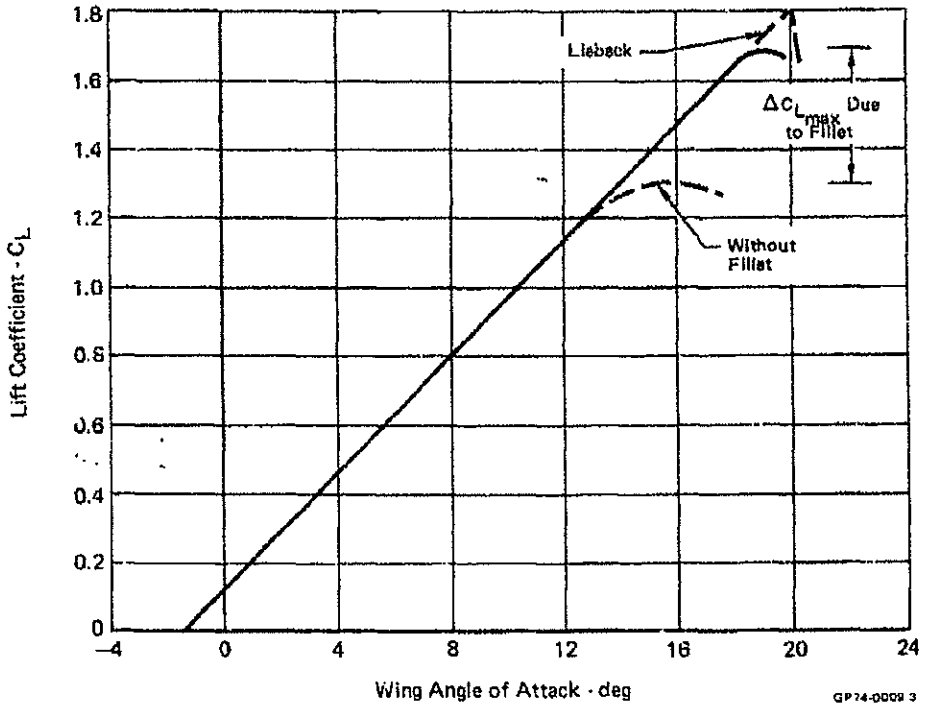

3.3 WING AREA SELECTION

~~(C)~~ Preliminary studies were made to redefine the aircraft configuration and performance with the TF-34 core gas generator instead of the original scaled GE1/10, and with the higher predicted maximum lift coefficient of 1.68 instead of 1.30. The original wing area of 400 ft^2 as well as a smaller wing of 350 ft^2, both without flaps and at the same aspect ratio of 8, were studied. The aircraft with either wing area was sized for the basic covert mission with internal bomb load, but consideration was also given to the effects of carrying larger bomb loads externally under the wings.

~~(U)~~ Compared to the scaled GE1/10, the TF-34 gas generator is larger and heavier and specific fuel consumption is higher, but it does have the advantage of higher thrust at speeds above about 200 knots. Thus, for the same wing area and mission the TF-34 aircraft is heavier, but this weight increase is at least partially offset for takeoff, landing, and quiet speed by the increase in lift coefficient.

~~(C)~~ The smaller 350 ft^2 wing would give a lighter weight aircraft having better climb, acceleration, and high speed. The lower wing loading with the 400 ft^2 wing would be better for takeoff, landing, quiet speed, and maneuverability, especially when carrying large external payloads. The lower quiet speed with the 400 ft^2 wing would result in less aerodynamic noise, but radar cross-section and visual signature might be slightly less with the 350 ft^2 wing. With the same

propulsion system, there would be little if any difference in propulsion noise or IR signature for either wing.

~~(C)~~ Figure 3-7 summarizes the preliminary weight, performance, and aerodynamic noise characteristics of the aircraft with the TF-34 gas generator as functions of wing area and bomb load. For comparison the first column also shows the original Quiet Attack Aircraft Model 226-454A with scaled GE1/10 gas generator and 400 ft^2 wing. The weights shown with the TF-34 gas generator are approximate in that no weight has been added yet for visual camouflage, but the wing and landing gear weights have been increased to provide the added strength needed when carrying external bombs. No additional fuel is used with external bombs. This is because separate studies made of the original aircraft show substantial increases in mission radius for the same amount of fuel when the external bomb missions are flown in a conventional manner at optimum speed/altitude except for bomb release at 5000 ft., as illustrated by Figure 3-8. Compared to the basic mission radius of 400 nm with internal bombs and mostly at quiet speed, the radius increased to 650 nm with 8-1000 lb. bombs and to 575 nm with 6-2000 lb. bombs. These radii increases, in spite of the increased weight and drag of external bombs, are primarily due to much better specific fuel consumption at optimum speed/altitude, and similar increases could be expected with the TF-34 gas generator for the same reason.

~~(C)~~ FIGURE 3-7
WEIGHT/PERFORMANCE/NOISE COMPARISON

		Internal Bombs			External Bombs/TF-34 Gas Generator			
		GE1/10 Gas Gen	TF-34 Gas Gen		8-1000 lb Bombs		6-2000 lb Bombs	
		S_W = 400	S_W = 400	S_W = 350	S_W = 400	S_W = 350	S_W = 400	S_W = 350
Weights								
TOGW	lb	14,410	16,500	16,230	23,405	23,135	27,240	26,970
Fuel	lb	3,415	4,615	4,570	4,615	4,570	4,615	4,570
Combat Weight	lb	12,700	14,195	13,945	21,095	20,845	24,930	24,680
Combat W/S	lb/ft^2	31.7	35.5	39.8	52.7	59.5	62.3	70.5
Weight Empty	lb	9,360	10,240	10,015	10,485	10,260	10,380	10,155
Performance								
Maximum Speed	kt	430	445	455	385	390	365	370
Quiet Speed	kt	112	98	105	120	127	130	139
Bomb Release Speed	kt	317	309	312	264	267	248	252
Takeoff Ground Run	ft	1,400	1,525	1,685	3,330	3,765	4,795	5,360
Initial Climb	ft/min	5,400	4,950	5,075	2,885	2,910	2,250	2,255
Sustained Turn Radius								
At 300 knots	ft	1,350	1,445	1,525	2,560	2,700	3,340	3,530
Minimum	ft	925	825	930	1,280	1,450	1,565	1,760
Quiet Speed Aero Noise								
OASPL 5000 ft Away	dB	47.4	43.9	45.1	49.1+	50.1+	51.3+	52.4+

~~(C)~~ FIGURE 3-8
ATTACK MISSIONS

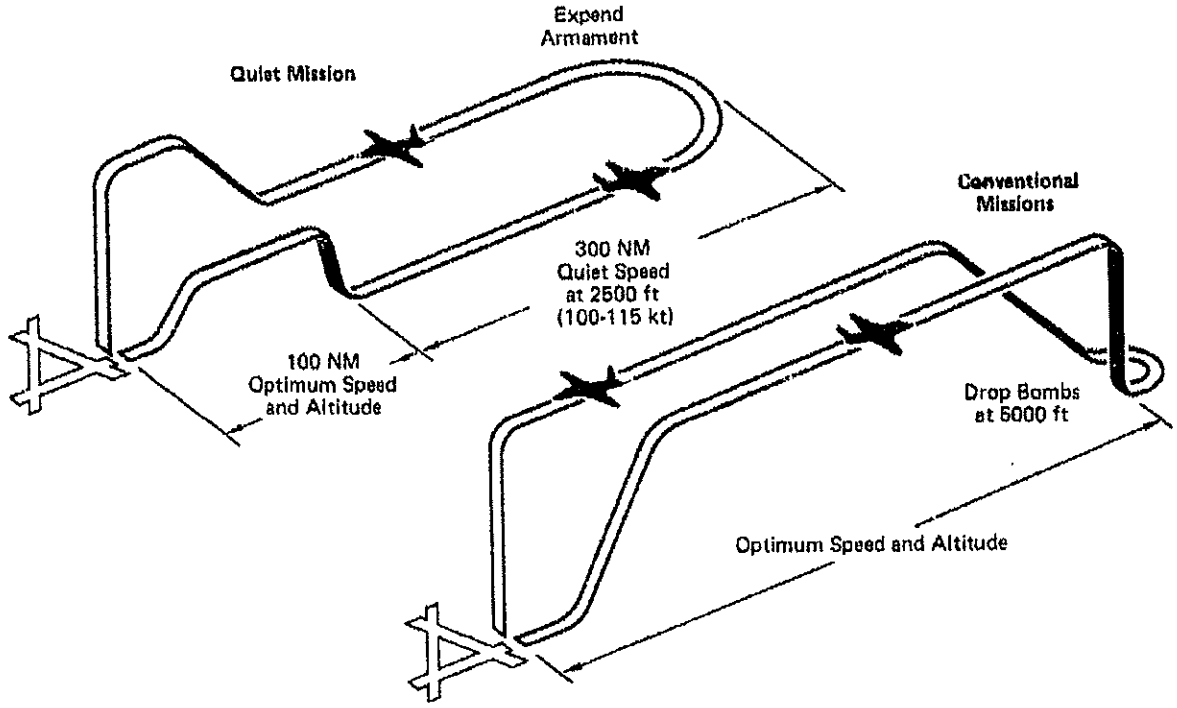

~~(C)~~ In all cases combat weight is defined as TOGW less 50% fuel, and this is the weight used for the maximum, quiet, and bomb release speeds at 2500 ft. altitude. Previously, a nominal C_L value of 0.8 was used to determine the quiet speed with adequate stall margin of 112 knots shown in the first column. This was before it was realized that the exterior shaping of the aircraft to reduce radar cross-section would also increase the maximum lift coefficient beyond the value of 1.30 for a conventional wing planform. Quiet speed shown in Figure 3-7 for the aircraft with TF-34 propulsion is 1.2 stall speed, the same criteria acceptable for landing approach speed in commercial transport operation. With the higher predicted maximum lift coefficient of 1.68 this gives a quiet speed C_L value of 1.16, which permits a significant reduction of quiet speed and aerodynamic noise. Some additional increment of aerodynamic noise is indicated by the + signs for the dB with external bombs. This is due to turbulent airflow around the bombs and pylons, but no technique has been found yet to predict the amount of this incremental noise increase.

~~(C)~~ Maximum speed with the TF-34 propulsion system and 400 ft^2 wing is better with internal bombs than the original 430 knots shown in the first column. This is due to the higher TF-34 thrust with no change in drag, while the lower drag with the 350 ft^2 wing gives an additional speed increase. The reductions in maximum speed when carrying the large external bomb loads shown are not as much as might be

expected. This is because, as shown later by Figure 3-9, the sizable weight increases have practically no effect on drag at high speed, so that the speed reduction is due only to the added drag of the bombs and pylons.

~~(C)~~ The bomb release speed is the speed attained at bomb release 2500 ft. above ground level when the aircraft starts to accelerate from quiet speed at a target identification range of 25,000 ft. This is primarily a function of combat weight and the quiet speed from which the acceleration at maximum thrust started, with lesser effects due to drag. In the weapon delivery studies discussed in Section 4, the critical minimum bomb release speed was found to be about 250 knots for laser guided bombs. Figure 3-7 shows this criteria could be met with any of the bomb loads shown for either wing area.

~~(C)~~ The weights used for takeoff ground run and initial climb are of course higher than combat weight and are equal to TOGW less 90 lb. of warmup fuel. The takeoff ground runs are all based on liftoff speed being 1.2 times stall speed, but the first column is based on the original maximum lift coefficient of 1.3 while the other columns for the aircraft with TF-34 propulsion are based on the new value of 1.68. While the TF-34 aircraft may have an unfair advantage in lift coefficient, they have the disadvantage of less low speed thrust as well as heavier weight which combine to reduce acceleration. The heavier weight also increases the wing loading and liftoff speed for a given lift coefficient. Thus, the takeoff ground runs with TF-34 propulsion are longer than the original aircraft, but still appear reasonable and could be reduced with flaps. In view of the large negative W.O.D. value of -49 knots for the original configuration, the heavier aircraft with TF-34 propulsion were not expected to present any W.O.D. problems for catapult. The difference in maximum lift coefficient does not affect initial climb, which is primarily dependent on weight and thrust. Here again, as was the case with takeoff acceleration, the TF-34 aircraft are at a disadvantage but the absolute values of initial climb shown are still attractive.

~~(C)~~ The sustained turn radii shown are all for a turn at combat weight (bombs on board) at constant speed at 2500 ft. altitude with maximum thrust. Since the lift coefficient for the turns at 300 knots is in the range of only 0.57-0.75, these turns are thrust-limited. The minimum radius sustained turns are both thrust-limited and lift-limited, for the highest usable lift coefficient of 1.26 (75% MaxC_L) for the TF-34 aircraft. The speeds at minimum turn radius for these aircraft range from 194 to 186 knots with the 400 ft^2 wing and from 219 to 208 knots with the 350 ft^2 wing. The lift coefficient for minimum sustained turn radius of the original GE1/10 aircraft in the first column is 1.0, which is the main reason for its larger turn radius at a higher speed of 233 knots. Lift-limited decelerating turns could also be made at higher speeds, providing the structural limit load factor is not exceeded, to give a tighter turn radius than that for a sustained turn.

~~(C)~~ While the data in Figure 3-7 is based on approximate weights, it turned out to be quite accurate and was therefore adequate for selecting the wing area of the aircraft with TF-34 propulsion. From these comparisons, the advantages of the 400 ft^2 wing for noise and certain performance items appeared to be more significant than the 350 ft^2 wing advantages in the other performance items and in weight. Another consideration was the possibility of a subsequent weight increase, which would have less effect with the 400 ft^2 wing. For these reasons the 400 ft^2 wing was retained.

(This Page is UNCLASSIFIED)

LIFT AND DRAG - (U) Figure 3-9 illustrates the drag polars of the clean TF-34 aircraft for the two wing areas of 400 and 350 ft^2 at the aspect ratio of 8. Also noted are the additional drag increments for externally carried bombs and for extended landing gear. These drag polars are without flaps and reflect the new predicted maximum lift coefficient of 1.68. The quiet speed lift coefficient at 1.2 VSTALL ($1.68/1.2^2 = 1.165$) is also indicated. The three short lines drawn across the polars near a C_L of 0.1 indicate the C_L required for each wing area at the three arbitrary aircraft weights shown for a level flight speed of 400 knots at 2500 ft. It can be seen that weight has practically no effect on the high speed clean drag coefficient, which is also at its minimum value for either wing area. The same would be true for the higher maximum speeds shown in the second and third columns of Figure 3-7. Thus, the reduced maximum speeds with external bomb loads noted in Figure 3-7 are due solely to the incremental ΔC_D increases shown here.

(U) FIGURE 3-9
CLEAN AIRCRAFT DRAG POLARS

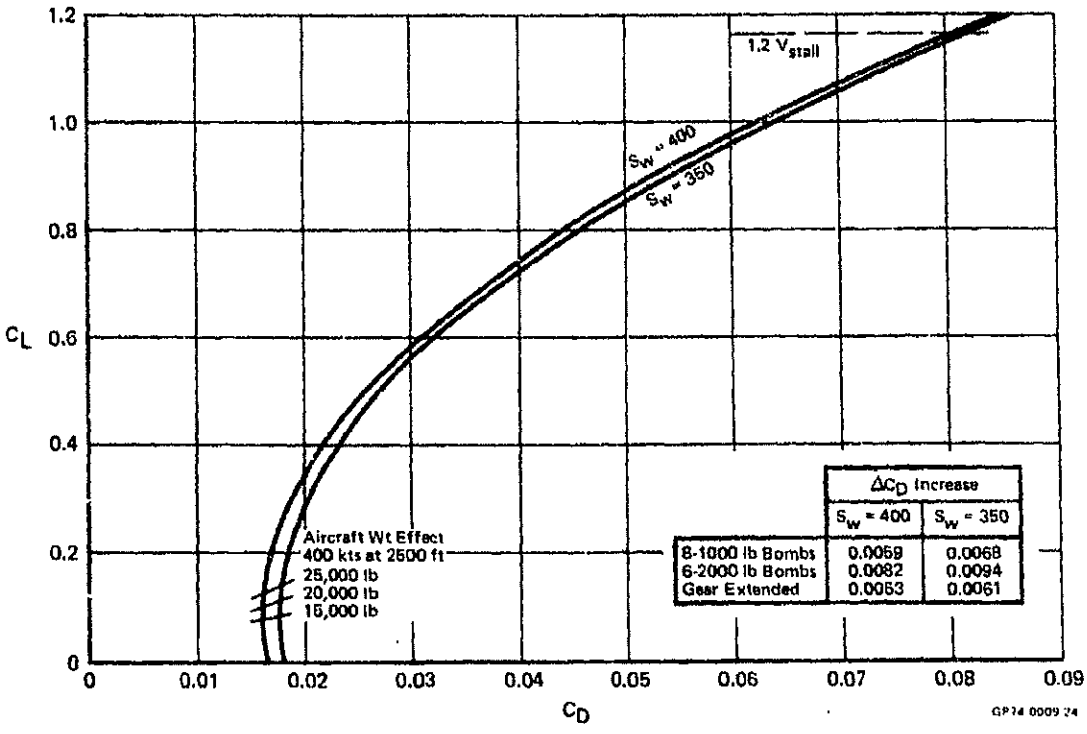

	ΔC_D Increase	
	S_W = 400	S_W = 350
8-1000 lb Bombs	0.0059	0.0068
6-2000 lb Bombs	0.0082	0.0094
Gear Extended	0.0053	0.0061

(C) The drag data from Figure 3-9 are used to determine the aircraft drag curves in Figure 3-10. It can be seen that for the same speed and bomb load the 350 ft^2 wing gives slightly lower drag than the 400 ft^2 wing, but the speed at 1.2 V_{STALL} is slightly higher with the 350 ft^2 wing. The drag shown here is at 2500 ft. at the combat weights noted in Figure 3-7. The maximum thrust is the TF-34 thrust previously illustrated by Figure 2-5 at 2500 ft., and the intersection of the thrust and drag curves establishes the maximum speeds noted in Figure 3-7. Fairly sizable percentage-wise drag increases, especially at low speed, are evident when carrying external bombs. Contrary to the situation at high speed, most of this low speed drag increase with external bombs is due to added weight rather than the ΔC_D of the bombs and pylons. This is illustrated by the following example for the TF-34 aircraft with 400 ft^2 wing at a speed of 150 knots, where the dynamic pressure, q, is only 70.6 lb/ft^2. C_L is found by dividing combat W/S by q, and then Figure 3-9 is used to find C_D.

	Bomb Load		
	Internal	8-1000 LB	6-2000 LB
Combat W/S	35.5	52.7	62.3
C_L	.503	.746	.882
C_D			
- Clean	.0257	.0403	.0515
- ΔC_D	-	.0059	.0082
- Total	.0257	.0462	.0597
Drag - lb	725	1305	1685

(C) ACCELERATION FROM QUIET SPEED - Acceleration at 2500 ft. with maximum thrust, Figure 3-11, is a function of thrust, weight, and drag. For the three aircraft shown, the drag is nearly the same but at low speed the original GE1/10 aircraft has the advantage of both lower weight and higher thrust. As speed increases, however, the thrust advantage reverses above 200 knots, and this accounts for acceleration being nearly the same for all aircraft at 300 knots. The trend of the curves also shows that for conventional weapon delivery at higher speeds the TF-34 aircraft, in spite of being heavier, would have better acceleration which could also be translated into better climbout recovery after dive bombing.

(C) Figures 3-12, 3-13, and 3-14 for the TF-34 aircraft with wing areas of 400 and 350 ft^2 and with three different bomb loads are the source of the bomb release speeds previously shown in Figure 3-7. Acceleration starts at maximum thrust from quiet speed. The target is 25,000 ft. away at the start of acceleration. The distance between the dotted lines labeled "target" and "bomb release" represents the distance the bomb travels for level release at 2500 ft., and this bomb travel increases with bomb release speed as shown later by Figure 4-3. The distance between the dotted lines labeled "bomb release" and "end acceleration" represents stabilized flight for 3 seconds at release speed prior to bomb release. The figures show wing area has only a small effect on bomb release speed and, since the same propulsion system is used, the differences are primarily due to the added weight of the external bomb loads.

~~(C)~~ FIGURE 3-10
DRAG AND SPEED AT 2500 FT

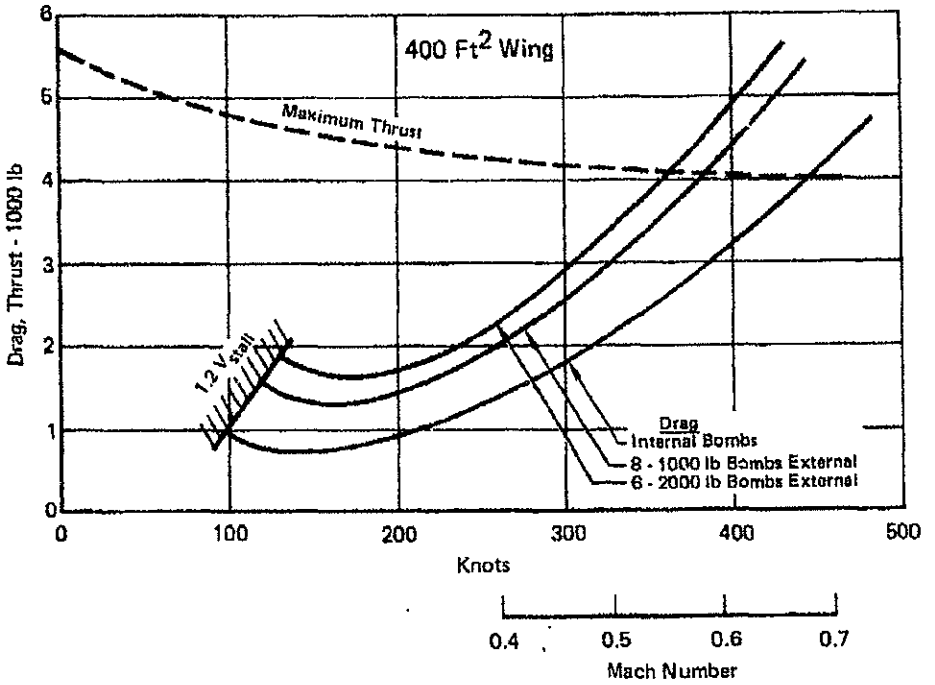

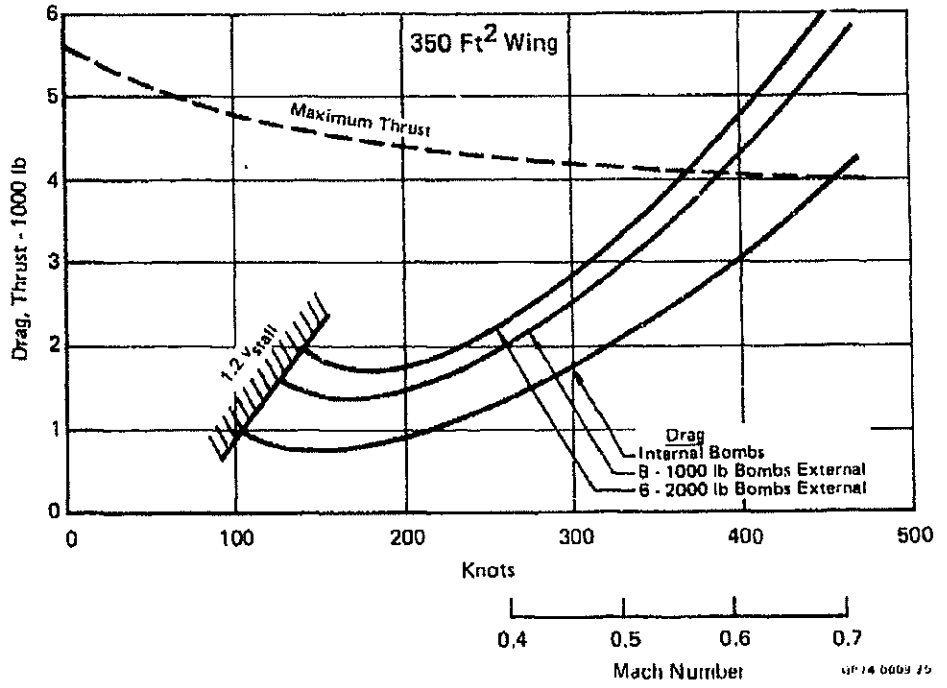

~~(C)~~ FIGURE 3-11
CLEAN AIRCRAFT ACCELERATION AT 2500 FT
Two 500 Lb Laser Bombs Internal

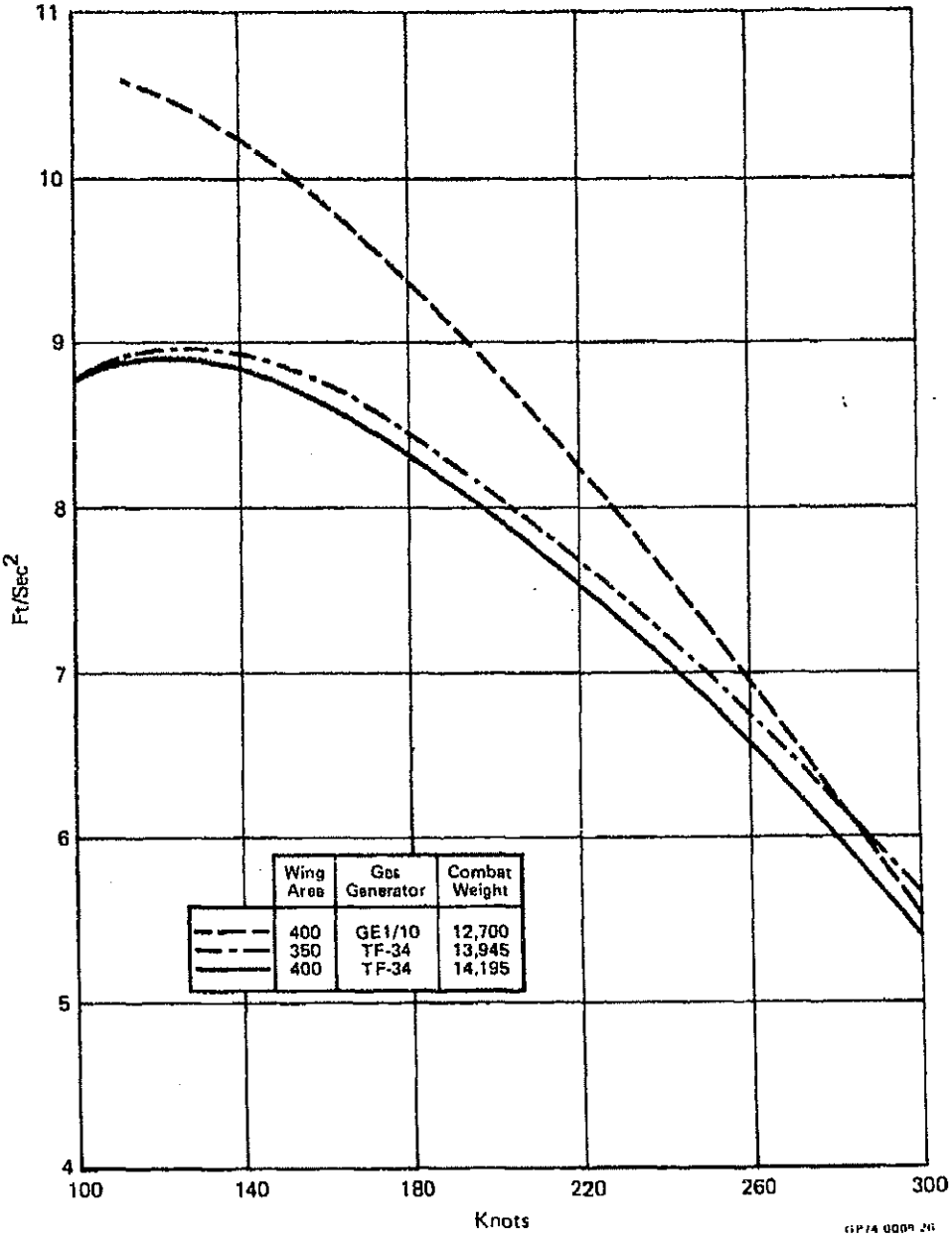

~~(C)~~ FIGURE 3-12
ACCELERATION FROM QUIET SPEED AT 2500 FT
Clean Aircraft - Internal Bombs

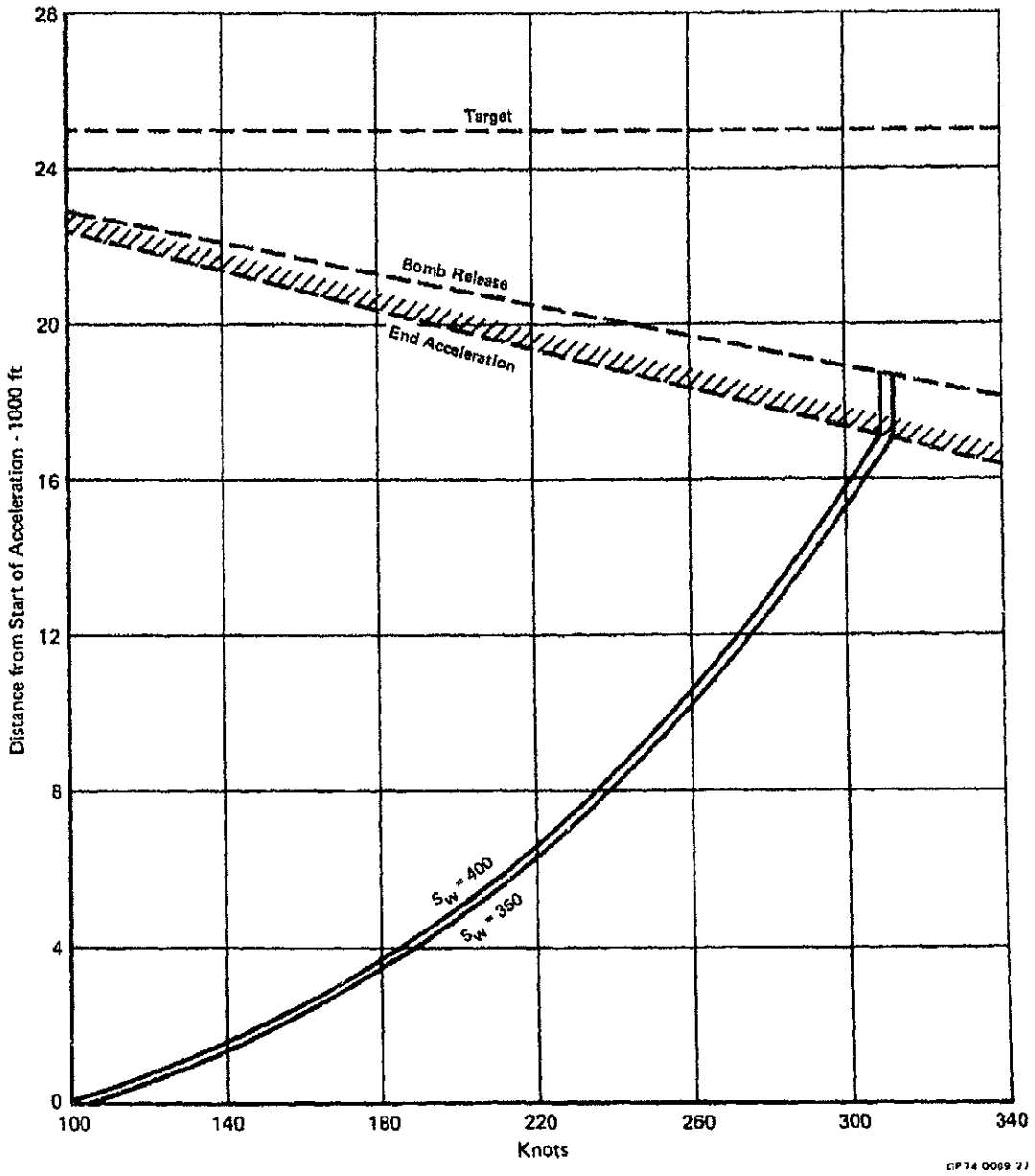

~~(C)~~ FIGURE 3-13
ACCELERATION FROM QUIET SPEED AT 2500 FT
Eight 1000 Lb Bombs External

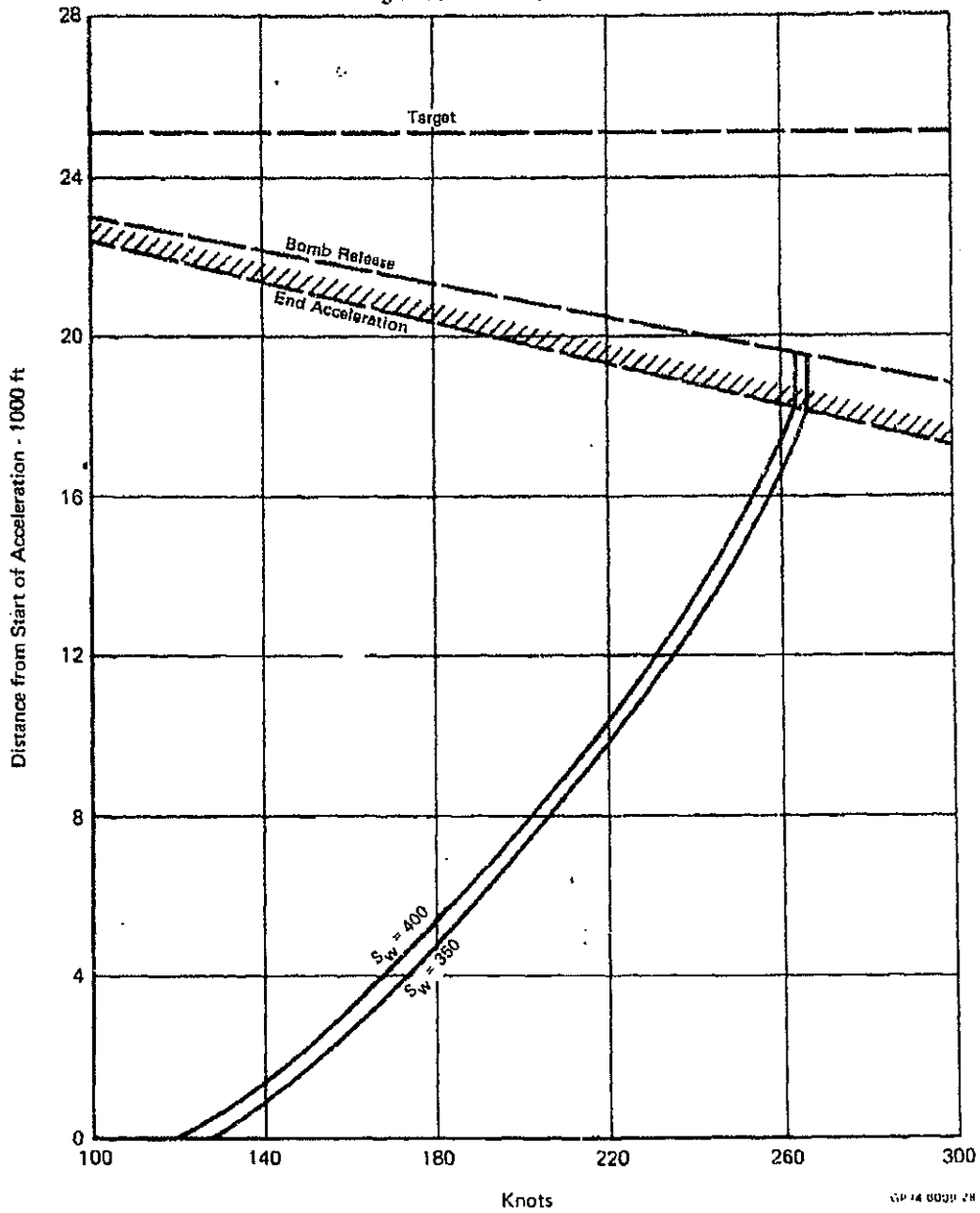

~~(S)~~ FIGURE 3-14
ACCELERATION FROM QUIET SPEED AT 2500 FT
Six 2000 Lb Bombs External

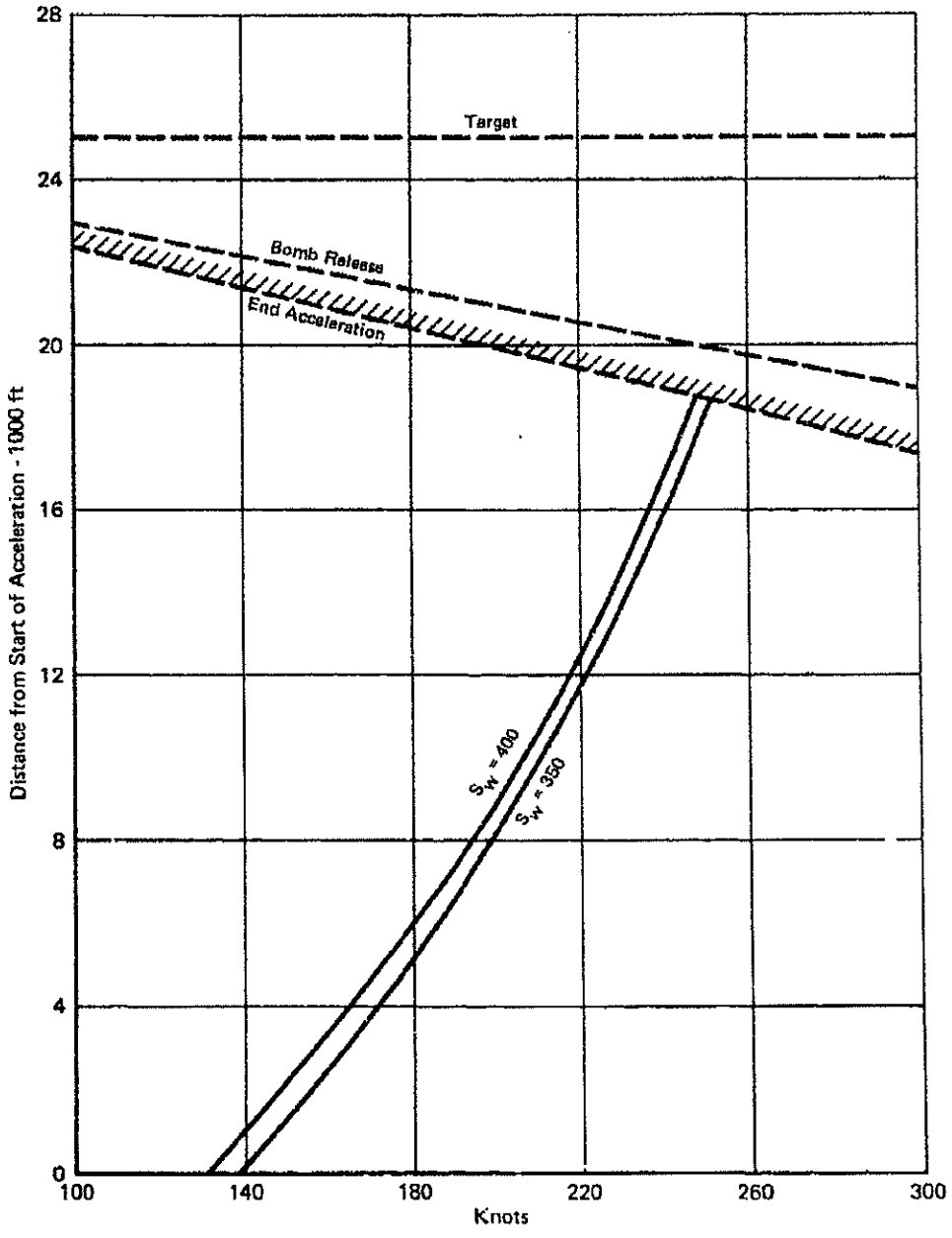

3.4 MODEL 226-458 PERFORMANCE

(C) Figure 3-15 summarizes the weight and corresponding performance for the Model 226-458 quiet attack aircraft with TF-34 tip-driven fans and a 400 ft^2 wing without flaps. The design mission in the first column is with two 500 lb. laser guided bombs carried in the internal bomb bay, and the quiet mission profile was previously illustrated by Figure 3-8. The 300 nm outbound and inbound at 2500 ft. is at a quiet speed of 115 knots. Compared to the minimum quiet speed of 98.3 knots (1.2 V_{STALL}), the 115 knot speed produces only about 1/2 dB more noise but gives the advantages of less IR signature, more stall margin for better maneuverability and more comfortable ride, and requires less fuel.

(C) FIGURE 3-15
MODEL 226-458 WEIGHT AND PERFORMANCE
No Flaps

		Internal Bombs (1)	External Bombs (2)		Ferry Flight	
		2-500 lb	8-1000 lb	6-2000 lb	Internal Fuel Only	150 Gal. in Bomb Bay
Weights						
TOGW	lb	16,530	23,435	27,275	15,310	16,635
Fuel	lb	←	4,615	→		5,655
Weight Empty	lb	10,270	10,515	10,390	10,270	10,270
Performance						
Mission Radius	nm	400	725	650	2,520	3,010
Max Speed at 2500 ft	kts	445	385	365	–	–
Initial Climb	ft/min	4,950	2,885	2,250	–	–
Catapult WOD						
Standard Day	kts	–48	–13	+4	–	–
Tropical Day	kts	–44	–8	+9	–	–
Arrestment WOD						
Standard Day	kts	–56	–56	–56	–	–
Tropical Day	kts	–53	–53	–53	–	–
Takeoff Ground Run						
Standard Day	ft	1,525	3,330	4,795	1,300	1,550
Tropical Day	ft	2,330	5,175	7,450	1,990	2,370
Landing Ground Roll						
Standard Day	ft	720	730	725	720	725
Tropical Day	ft	770	780	775	770	775
Sustained Turn Radius						
At 300 Knots	ft	1,445	2,560	3,340	–	–
Minimum	ft	825	1,280	1,565	–	–

(1) Quiet mission at 115 knots, 2500 ft altitude.
(2) Conventional missions at optimum speed/altitude.

~~(C)~~ The alternate missions with external bomb loads in the second and third columns are with the eight MK83 or six MK84 bombs each mounted on its individual pylon under the wing, and no bombs in the internal bomb bay. The mission profile with external bombs is the one labeled "conventional missions" in Figure 3-8. Optimum speed and altitude for the second column of Figure 3-15 is Mach 0.45 at 24000-27000 ft., and for the third column is Mach 0.44 at 19000-22000 ft. Note that fuel for either of these alternate missions is the same, 4615 lb., as for the first column design mission.

~~(C)~~ The one-way ferry flight in the fourth column is also with the same 4615 lb. of internal fuel, without any bombs, but the 7.62 mm minigun with 1000 rounds of ammunition is still on board. The speed is Mach 0.49 at 36000 ft. In the last column the one-way ferry flight is made with additional fuel in a standard 150 gallon drop tank carried for the entire flight on the centerline bomb rack in the bomb bay. This longer range ferry flight, or ferry flight against headwinds, is also without bombs but with minigun and ammo, and the speed is Mach 0.50 at 36,000 ft.

~~(C)~~ The considerable improvement in combat mission radius in the second and third columns and ferry mission range in the last two columns is due to most of the flight being at higher optimum speed and altitude where specific fuel consumption (SFC) is good. In contrast, 300 of the 400 nm radius in column one is flown at near idle throttle setting where SFC is relatively poor, but this is one of the penalties that must be accepted to minimize noise and IR signature in an aircraft which also has good performance and payload capabilities for attack missions. Since external fuel tanks are not required on any combat missions, this leaves the entire wing available for a wide variety of external payloads such as ordnance, gun pods, rockets, or ECM and sensor pods.

~~(C)~~ The maximum speeds at 2500 ft. altitude shown in the first three columns correspond to Mach 0.68, 0.59, and 0.56 respectively. These speeds are at combat weight, defined as TOGW less 50% fuel, bombs on board. Maximum speed at any altitude occurs at about 10,000 ft. where the speeds shown would be increased about 5 knots. These maximum speeds at 2500 ft. are about 15 knots higher than they were for the initial quiet attack aircraft, Model 226-454A with scaled GE1/10 propulsion system and lighter weight.

~~(C)~~ The initial rates of climb are at sea level on a standard day, and are for a weight of TOGW less 90 lb. of warmup and takeoff fuel. Corresponding airspeeds in the climb are about 400, 390, and 370 knots respectively for the first, second, and third columns.

~~(C)~~ For the catapult and arrestment W.O.D. (wind over deck) analysis for carrier basing, the standard day is a temperature of 59°F and the tropical day is 89.6°F. The aircraft is based on a CVA-59 Forrestal class carrier with C-7 catapult and MK-7 Mod 2 arresting gear. The catapult endspeeds required at launch are based on limiting the amount of aircraft sink below the carrier deck to a maximum of 5 ft. The endspeed capability of the C-7 catapult includes an additional 3 knot effect due to aircraft thrust, and the aircraft nose gear strut is extended to provide a 3° angle of attack on the deck. The approach speed for arrestment is at 1.1 V_{PA} MLN

(1.1 times the minimum speed for power approach) and is based on the aircraft's capability to achieve a 50 ft. incremental increase in altitude in 5 seconds with a fixed throttle setting. The catapult W.O.D. is based on the full takeoff gross weight shown in each column, and represents the difference in endspeed between C-7 catapult capability and required endspeed for the specified aircraft weight. Arrestment W.O.D. is based on aircraft weight with bombs gone and 5% fuel reserve remaining, and is the difference between the arresting gear capability, in terms of maximum allowable approach speed in still air, and actual approach speed. Positive W.O.D. values indicate a headwind from carrier bow to stern is required, while negative W.O.D. values indicate the amount of tailwind from stern to bow that can be tolerated. Although the arrestment W.O.D. does not present any problems and the catapult W.O.D. values appear to be acceptable, the use of flaps could appreciably reduce catapult W.O.D. requirements for heavy loads on hot days. The sensitivity of catapult and arrestment W.O.D. to aircraft weight is illustrated later by Figure 3-18.

(C) The takeoff ground runs shown are based on takeoff gross weight less 90 lb. of warmup and takeoff fuel, at sea level, with maximum thrust. Liftoff occurs at 1.2 V_{STALL}, where the lift coefficient without flaps is $1.68/1.2^2$ or 1.165. Ground run drag includes rolling resistance equal to 2.5% of the difference between aircraft weight and lift at 0° angle of attack, clean aircraft C_D of .0163, extended landing gear ΔC_D of .0053, and bombs and pylons ΔC_D of either .0059 or .0082 for columns two or three respectively. The ground run distances shown are the result of step integrations which account for increasing drag and decreasing thrust as speed increases, and also account for the reductions in dynamic pressure q and thrust for a given speed on a tropical day. Although not shown, the additional distance from liftoff to over a 50 ft. obstacle is 190, 330, and 440 ft. respectively for columns one, two, and three.

(C) The landing ground rolls are without bombs and with 10% fuel remaining, at sea level. Touchdown speed is at 1.2 V_{STALL}. Thrust reversing is not used, and the only decelerating forces are due to drag at 0° angle of attack and braking friction coefficient of 0.4. Again, the ground roll distance is a step integration which accounts for the variation of drag with speed. At a 4° glide slope, the additional distance over a 50 ft. obstacle to touchdown is 715 ft. in all cases.

(C) The sustained turn radii in Figure 3-15 are for standard day conditions at 2500 ft. altitude, and at maximum thrust. The radii at 300 knots are thrust limited, while the minimum sustained turn radii are both thrust and lift limited. All radii are at combat weight (TOGW less 50% fuel).

(C) SUSTAINED TURN RADIUS - The above sustained turn radii in Figure 3-15 are at a specific speed. Figure 3-16 illustrates how the sustained turn radius varies with speed at 2500 ft. altitude. The three solid lines represent the Model 226-458 quiet attack aircraft at combat weight, with the same bomb loads as previously noted in the first three columns of Figure 3-15. The bubble on each solid line corresponds to the minimum sustained turn radius noted in Figure 3-15, and it can be seen that this occurs at a speed around 190 knots. Below this speed the turn radius is lift limited by a lift coefficient of 1.26 which, in the absence of any wind tunnel test data on buffet onset, has been chosen as a reasonable value representing 75% of the maximum lift coefficient of 1.68 without flaps. At these lower speeds the maximum thrust available exceeds the drag, and the aircraft would accelerate in the turn if

the thrust were not reduced to equal the drag. At higher speeds the drag equals the thrust, and the lift coefficient becomes progressively less than 1.26 as speed increases and available thrust decreases (see Figure 2-5).

~~(C)~~ FIGURE 3-16
SUSTAINED TURN RADIUS AT 2500 FT
Military Thrust, 50% Fuel

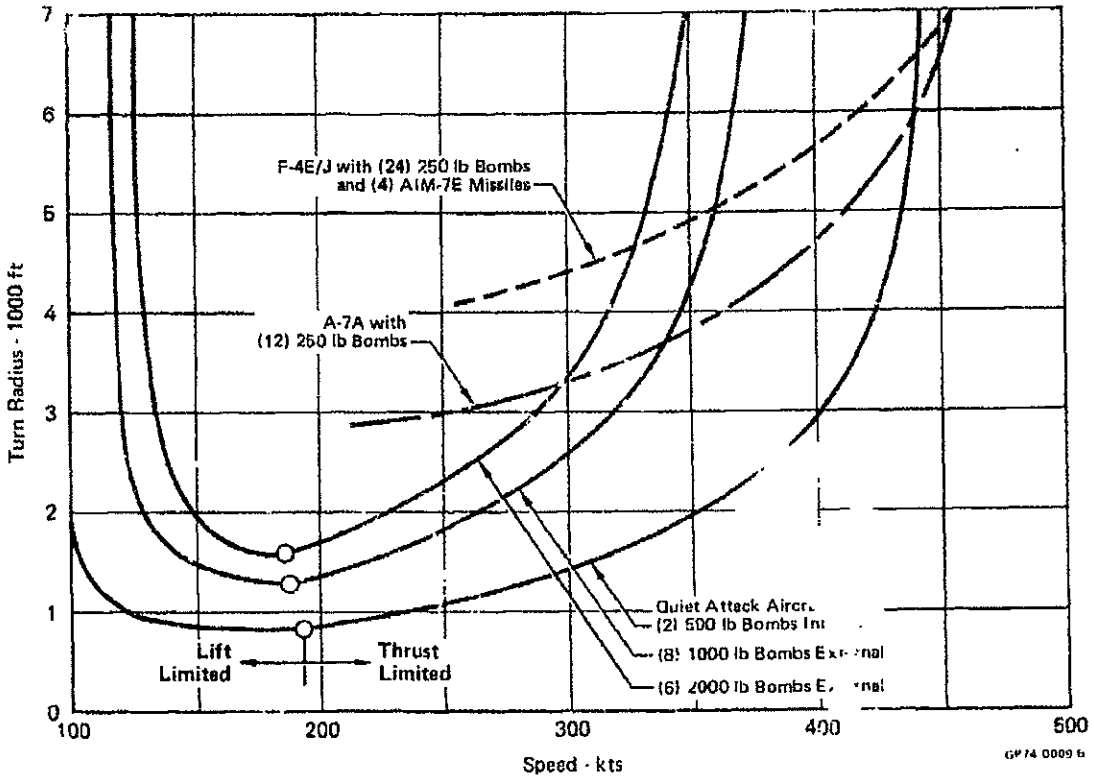

(C) Figure 3-16 also shows for comparison the sustained turn radius capabilities of the A-7A and F-4E/J with typical ordnance payloads for the same ground rules of no flaps, 2500 ft. altitude, military power (non-afterburning), and 50% fuel gone. The A-7 and F-4 sustained turn radii shown are thrust limited and at any lower speeds they would also become lift limited. The quiet attack aircraft with eight 1000 lb. bombs is carrying over twice the 3000 lb. load on the A-7 and about the same load as the F-4, and still has a clear cut turn radius advantage over either of them at speeds below about 350 knots. With six 2000 lb. bombs the quiet attack aircraft bomb load is four times the A-7 load and one and one half times the F-4 load yet it still has better turn radius below 330 or 300 knots. Maximum sustained g load for the quiet attack aircraft is 5.7g at 330 knots with internal bombs, 3.3g at 290 knots with eight 1000 lb. bombs, and 2.7g at 270 knots with six 2000 lb. bombs.

~~(C)~~ TRANSIENT TURN RADIUS - Figure 3-17 illustrates how transient turn radius achievable at the start of the turn varies with speed. This is for the Model 226-458 quiet attack aircraft at the same altitude of 2500 ft. with the same three bomb loads previously shown by Figures 3-15 and 3-16 and for the same corresponding combat weights. At higher speeds the turns are limited by the noted allowable limit load factor, N_Z. After starting the turn the aircraft will decelerate at a rate depending on the amount of thrust used, and turn radius will decrease from the value shown for the start of the turn. At lower speeds than those shown by bubbles the turns are lift limited for the same C_L of 1.26 used for Figure 3-16. With maximum thrust, the aircraft will still decelerate in the turn until thrust equals drag at the speed noted by the corresponding bubble previously noted on Figure 3-16. Thus, the aircraft with internal bombs will decelerate in lift limited turns at speeds between 193 and 267 knots. At speeds below 193 knots the turns with internal bombs are the same as they are in Figure 3-16. Comparison of Figures 3-16 and 3-17 shows the decided advantage in tightness of turn at higher speeds by using a transient instead of a sustained turn. Although some speed is lost in a transient turn, it is not a large loss. As an example, if the aircraft with eight 1000 lb. bombs starts a load factor limited turn at 350 knots with maximum thrust and turns through a heading change of 90°, the time to turn is less than 5 seconds and the speed loss is only 15 knots.

~~(C)~~ FIGURE 3-17
TRANSIENT TURN RADIUS AT 2500 FT

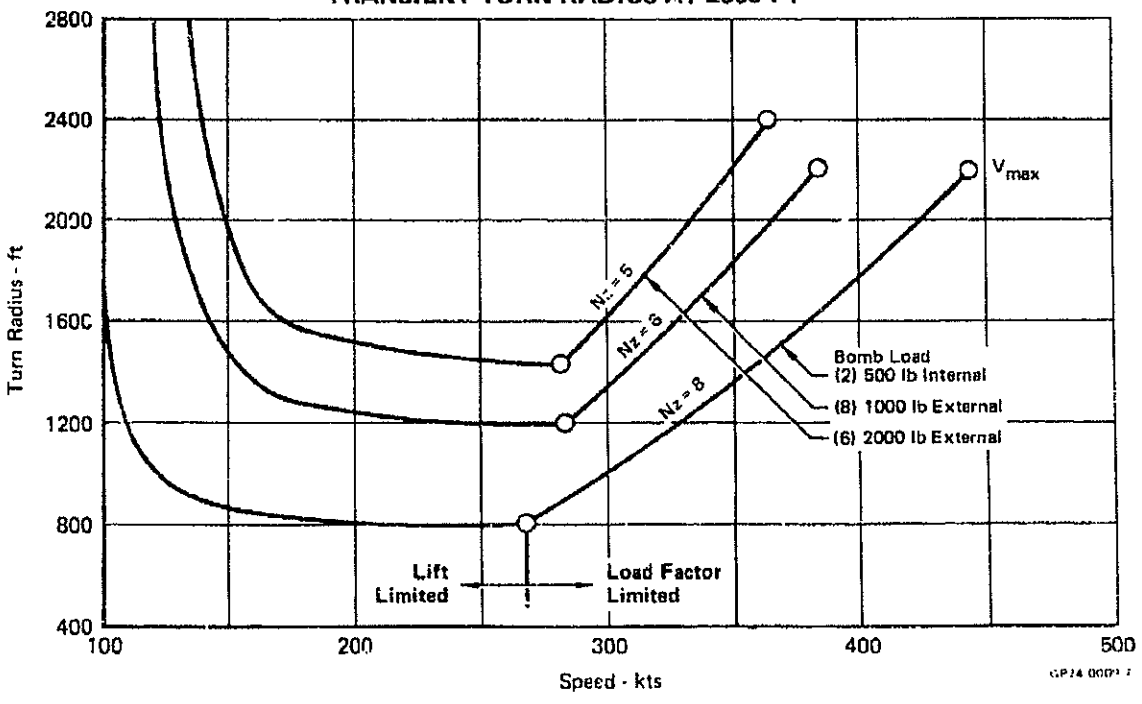

~~(C)~~ W.O.D. REQUIREMENTS - Figure 3-18 illustrates the effects of aircraft weight on speed requirements for catapult and arrestment, and the corresponding capabilities of the C7 catapult and the MK7 MOD 2 arresting gear as a function of weight when there is no wind over the deck from either bow or stern. The only case where the requirement exceeds the capability would be for catapult when the aircraft is carrying six MK84 (2000 lb.) bombs. Here a headwind of 4 knots on a standard day or 9 knots on a tropical day is required. This could be supplied by carrier forward speed in still air, or a breeze coming over the bow with the carrier not under way, or by the sum of carrier speed and breeze when the carrier is heading into the wind. In the other cases the carrier could be stopped and a tailwind equal to the difference between catapult or arresting gear capability and requirement could be coming over the stern.

~~(C)~~ FIGURE 3-18
CATAPULT AND ARRESTMENT
No WOD

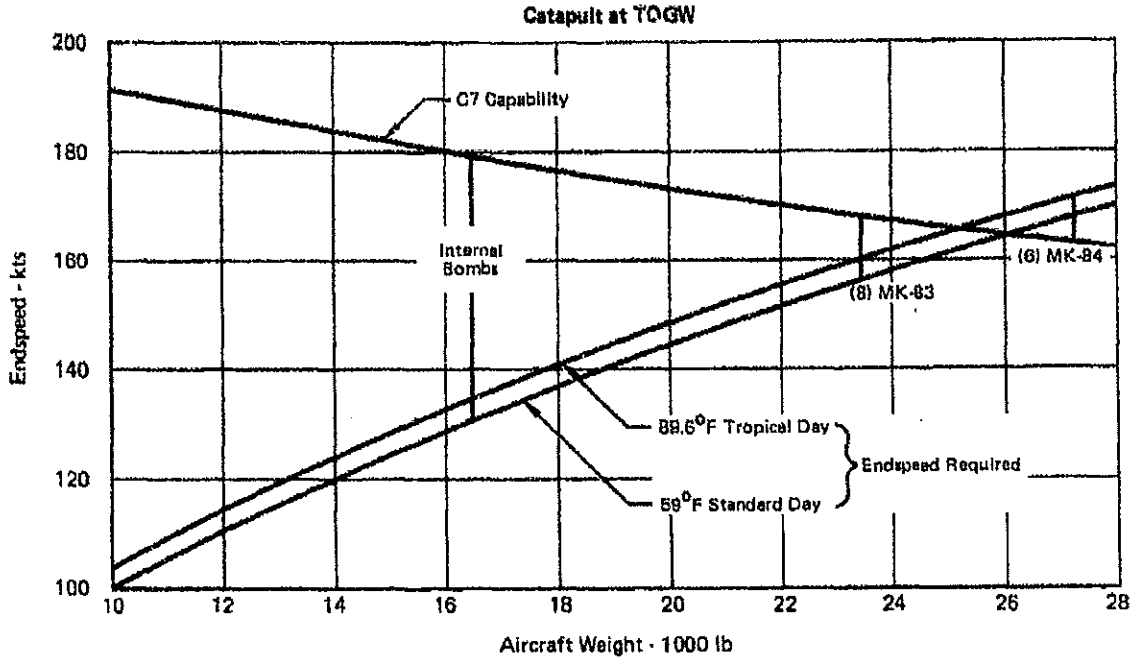

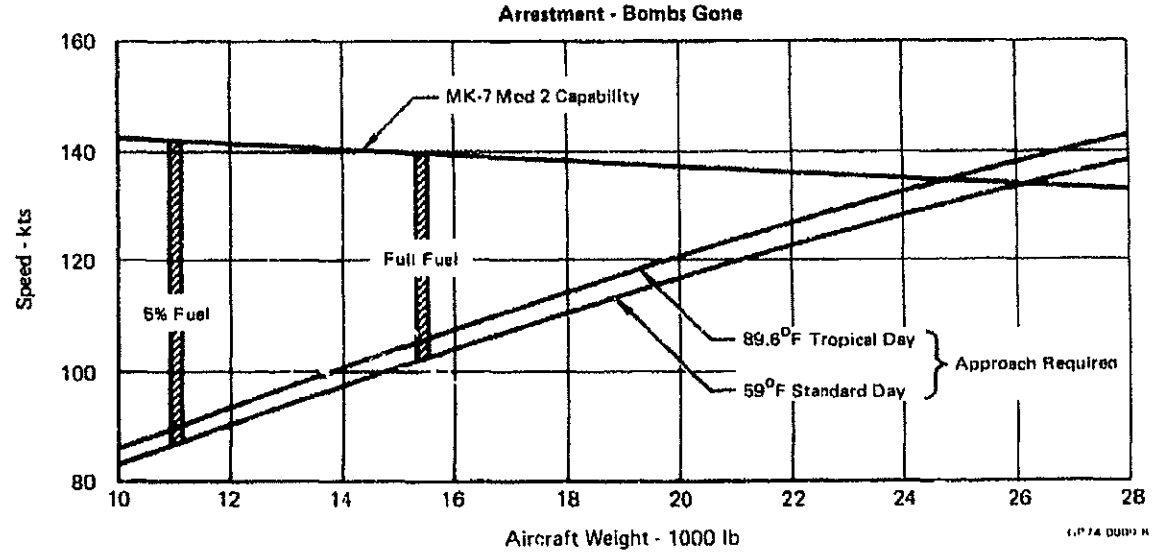

4. WEAPON DELIVERY

(S) This section addresses weapon delivery by the Initial Quiet Attack Aircraft, Model 226-454A, when the approach to the target is made at the quiet penetration speed of 112 knots at 2500 ft above ground level for covert operations. In this mode the bomb load is restricted to internal carriage only in the fuselage bomb bay to eliminate any increases in noise and radar cross section from external stores. Fuel is also carried internally for the same reasons, and the specific range in nautical miles per lb of fuel is fairly low due to the higher SFC from operating the propulsion system at minimum throttle setting for 300 of the 400 nm mission radius. Since the Model 226-458 aircraft with TF-34 propulsion system has comparable performance and the same FLIR/laser designator system as Model 226-454A, the weapon delivery discussion herein can also be considered applicable. The performance capabilities of Model 226-458 on more conventional missions with externally carried bombs were discussed in Section 3. Thus the aircraft's capabilities appear comparable to other conventional attack aircraft, but with the additional unique capabilities of covert operation and better survivability due to low signatures.

(S) Unguided and unpowered bomb release from a quiet speed of 112 knots at 2500 ft above ground level (AGL) is technically possible, but is not considered practical against a defended target. However, after target identification by FLIR the aircraft can accelerate to over 300 knots at bomb release. The higher speed in level flight provides excellent aircraft maneuverability for jinking and also increases standoff range at release. Target acquisition and weapon delivery can be accomplished on the same pass. The use of laser guided bombs (LGB), also looks feasible. Release from level flight is more attractive than dive bombing or toss bombing at this lower speed and altitude.

4.1 CONSTRAINTS AND CONSIDERATIONS

(U) Major constraints and considerations for weapon delivery, most of which are interrelated, are:

- o Bomb release speed
- o Bomb release altitude
- o Bomb release attitude
- o Fuse arming delay time
- o FLIR and laser designator viewing angles
- o Time from target acquisition to bomb release
- o Aircraft maneuvers after release.

(S) Mechanical bomb fuses, where a vane mounted on the bomb nose spins to arm the bomb, require a release speed high enough to reliably spin the vane. This minimum speed for mechanical fuse arming, Reference (5), is 175 knots for iron bomb fuses and 225 knots for airburst dispenser (ROCKEYE) fuses. On some bombs this constraint is not applicable when electrical fuses can be used. Bomblet dispensers such as ROCKEYE II also require a minimum speed of 200 knots to separate the two halves of the dispenser in flight. Laser guided bombs require a release speed greater than 250 knots to provide enough dynamic pressure on the control surfaces

for guidance maneuvers. Increased release speed gives the advantage of more standoff range for unpowered bombs. On the other hand, decreased release speed steepens the bomb trajectory at impact for improved accuracy and impact on a target surrounded by a revetment, but the speed must not be so low that the trajectory becomes erratic due to insufficient dynamic pressure on the stabilizing fins. Weapon release at the quiet speed of 112 knots and 2500 ft AGL appears feasible for unguided bombs, using an electrical fuse against an undefended or lightly defended target. Against a more heavily defended target the aircraft would be exposed for too long a time to enemy ground fire and its maneuverability for escape would be marginal.

(C) Release altitude from a level flight attitude must be high enough to avoid damage to the aircraft from bomb fragments or target debris. In addition to a target hit the bomb fragments could also result from an early burst due to a faulty fuse detonating the bomb the instant it becomes armed before impact. For level release the time of fall of the bomb increases with release altitude, which permits a longer fuse arming delay time for fragment avoidance. Another constraint is that release altitude must be high enough to give at least 8.5 seconds fall time for laser guided bombs to stabilize on the target. The disadvantages of higher than necessary release altitude are decreased accuracy for unguided bombs and easier acquisition of the aircraft by enemy ground defenses, but the advantage would be increased standoff range for a given release speed. The nominal release altitude has been chosen as 2500 ft AGL, the same as for quiet penetration.

(U) The principal options for release attitude are level flight, dive bombing, or toss bombing where the aircraft is in a climb at the time of release. In each case with unguided bombs the aircraft must be lined up with the target. Compared to level bombing from a moderately high cruise altitude, dive bombing reduces the range at release and gives a flatter bomb trajectory, both of which tend to increase accuracy while making it harder for ground defenses to track the aircraft. The disadvantage of dive bombing is that at release both the bomb and aircraft are heading for the target. Therefore the release must be far enough from the target to maneuver for safe escape from the bomb fragments. SNAKEYE bombs with high drag tail fins to increase the bomb fall time can also be used to permit release at closer range, while still allowing enough time for escape maneuvers before impact. When the aircraft is only 2500 ft AGL there may not be much advantage in dive bombing, but it would be an attractive option for more conventional penetration at higher speed and altitude when the target is visually acquired and an optical sight is used. Toss bombing, by imparting an upward component to the bomb trajectory at release, will increase the standoff range for the same speed and altitude, and thus make fragment escape easier. However, it is not needed for the quiet bombing mode. For the above reasons, level attitude at release appears to be the most attractive.

(U) Besides arming the bomb, the purpose of the fuse is to delay that arming for a predetermined number of seconds after release until a safe separation distance is reached between bomb and aircraft. This safe separation distance is based on the possibility, however remote, that a fuse malfunction could detonate the bomb at the instant of arming, or that a midair collision between bombs dropped in salvo or from different aircraft could also detonate the bomb before it reaches the ground. The safe separation distance, or fuse arming delay, depends on the fragment trajectory time history for the type of bomb being used and the tolerance on the arming delay time. Thus the fuse arming delay time and the release altitude which controls the bomb time of fall are directly related, and must be chosen so that the aircraft will not be hit by any bomb fragments from an inadvertent early burst but the bomb must positively be armed when it hits the ground. In line with the recommendations in Reference (5), an arming delay time of 10 seconds has been selected. Since the bomb time of fall from level release 2500 ft AGL is 12.4 seconds, this delay time meets both requirements for safe separation and positive arming at impact.

(U) The FLIR and laser designator have not been mounted in a protruding chin turret in the usual fashion because it was felt that the acoustic noise and the radar cross section produced by such a turret would be unacceptable. Instead both sensors look out through a window having the normal fuselage contour on the lower surface of the fuselage nose. This window has a very thin metallic coating to deflect enemy radar beams away from the interior components while still permitting transmission of infrared and laser energy. Because the sensor elevation and azimuth viewing angles are limited by the window size and shape and the sensor mounting with respect to the window, it has been necessary to check the required sensor viewing geometry to ensure that the window is adequate. This has been done for the condition of straight and level flight from the time a prospective target first comes into view on the FLIR display until the bomb is released, and also during target illumination by the laser designator from LGB launch to impact while the aircraft is maneuvering. In both cases the window is large enough.

~~(C)~~ The time available from target acquisition by FLIR to bomb release is important for a number of reasons. In order to find a target and release a weapon against it on the same pass the time must be adequate to identify the target, accelerate to the desired release speed, stabilize speed, heading, and altitude, and then release at the required range. Previous studies reported in Section 6.2.5 of Reference (1) have shown that a target, such as a truck or bridge against which a bomb instead of the minigun would be used, will first appear on the FLIR display at a ground range of 30,000 ft and will be positively identified at 25,000 ft. Delaying the start of acceleration from quiet speed until after the target is identified still leaves sufficient time and distance to reach a release speed of over 300 knots on the same pass. The reasons for maintaining the quiet speed of 112 knots until after the target is positively identified and a decision is made to attack it are two-fold. One is that if the FLIR image turns out to be a false alarm or not a desirable target, the aircraft can continue to remain covert while penetrating further. Another is that when a decision to attack is made the increase in noise due to higher speed and power for acceleration has been delayed as long as possible.

(U) It is desirable to maneuver the aircraft after the bomb has been released. This greatly reduces the probability of the aircraft being hit by ground fire and also, in some cases, the aircraft could be hit by bomb fragments if it did not turn away from the target. For unguided bombs a "launch and leave" technique can be used since the aircraft has excellent maneuverability when accelerated up to a release speed of 250 knots or higher. The greatest constraints on post release aircraft maneuvers are for laser guided bombs. Here the FLIR and laser designator must illuminate the target through the fuselage window continuously from release to impact, but the aircraft must still turn away from the target to avoid any bomb fragments from an early burst and to reduce the chances of being hit by ground fire. For laser bomb delivery the most attractive maneuver appears to be to maintain release speed in level flight but in a constant bank angle turn. A diving turn would increase the chances of being hit by fragments, while a climbing turn would make it harder to evade ground defenses.

4.2 BOMB FRAGMENT ENVELOPES

~~(S)~~ The bomb fragment trajectories were obtained from Reference (5). Figure 4-1 shows the fragment trajectories for the 750 lb M117A1 GP (general purpose) bomb and the 1000 lb MK83 LDGP (low drag general purpose) bomb. Trajectories for the smaller 500 lb MK82 LDGP and the 250 lb MK81 LDGP bombs are shown by Figure 4-2. These are all unguided and unpowered bombs having conical stabilizing fins. The dotted lines on each figure represent the fragment envelope at the time after burst in seconds noted. Note that for all bombs the maximum fragment trajectory height is reached 9 seconds after burst. The trajectory heights shown represent heights above ground for a burst at impact, or height above the point where an inadvertent early burst might occur before impact. By taking a horizontal cut through the dotted line envelopes the time history can be obtained for fragments at the same height above the ground as the aircraft. Comparison of the four bomb trajectories shows that for unguided and unpowered bombs the M117A1 has the largest envelope and is most critical for aircraft avoidance of fragments.

~~(S)~~ The MK81, 82, and 83 SNAKEYE bombs are the same, except for the extendable high drag tail fins, as the corresponding LDGP bombs and therefore have the same fragment trajectory envelopes. The Quiet Attack Aircraft can carry either the 500 or 1000 lb laser guided bombs internally. These have the same bomb body as the MK82 or MK83 LDGP bombs and the same fragment trajectories. The MK83 trajectories in Figure 4-1 are therefore most critical for laser guided bombs. The 500 lb MK36 and the 1000 lb MK40 destructor bombs also have the same body and same fragment trajectories as the corresponding MK82 and MK83 LDGP bombs. These destructor bombs do not detonate on impact but are fitted with a nose arming device and a tail firing mechanism that allows the weapon to function as a magnetic influence weapon, or mine, for use against shallow water and land targets. Therefore the only danger from destructor bomb fragments would be from an early burst.

(U) Fragment avoidance is no problem with the 500 lb MK77 MOD 4 fire bomb, the 835 lb CBU-24, -29, -49 bomblet dispenser, the 475 lb ROCKEYE II bomblet dispenser, or the 500 lb CTU-1/A delivery container. Powered bombs, such as the SHRIKE anti-radiation missile, are not considered to pose any fragment avoidance problem from either early burst or impact.

(U) FIGURE 4-1
BOMB FRAGMENT TRAJECTORIES
M117A1 and MK83

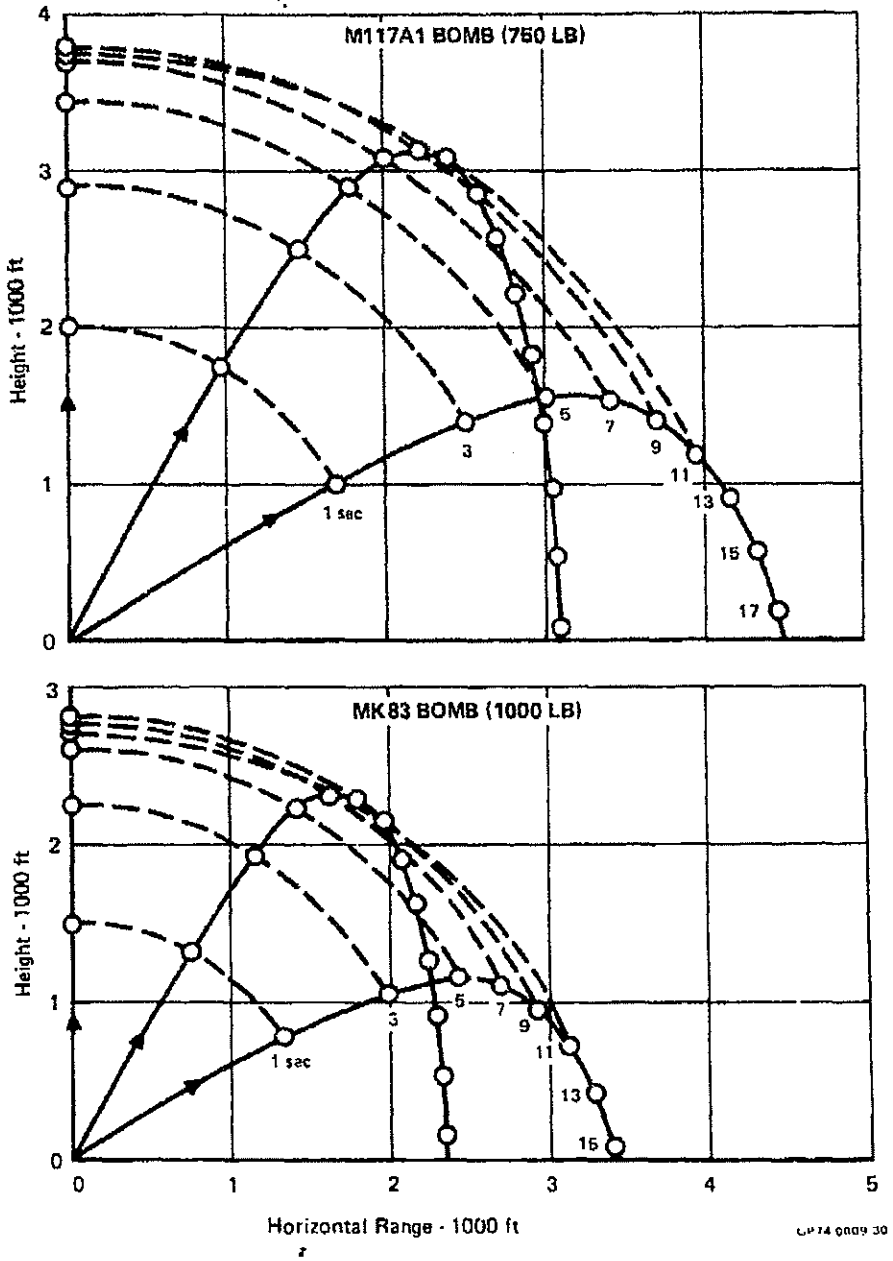

(U) FIGURE 4-2
BOMB FRAGMENT TRAJECTORIES
MK82 and MK81

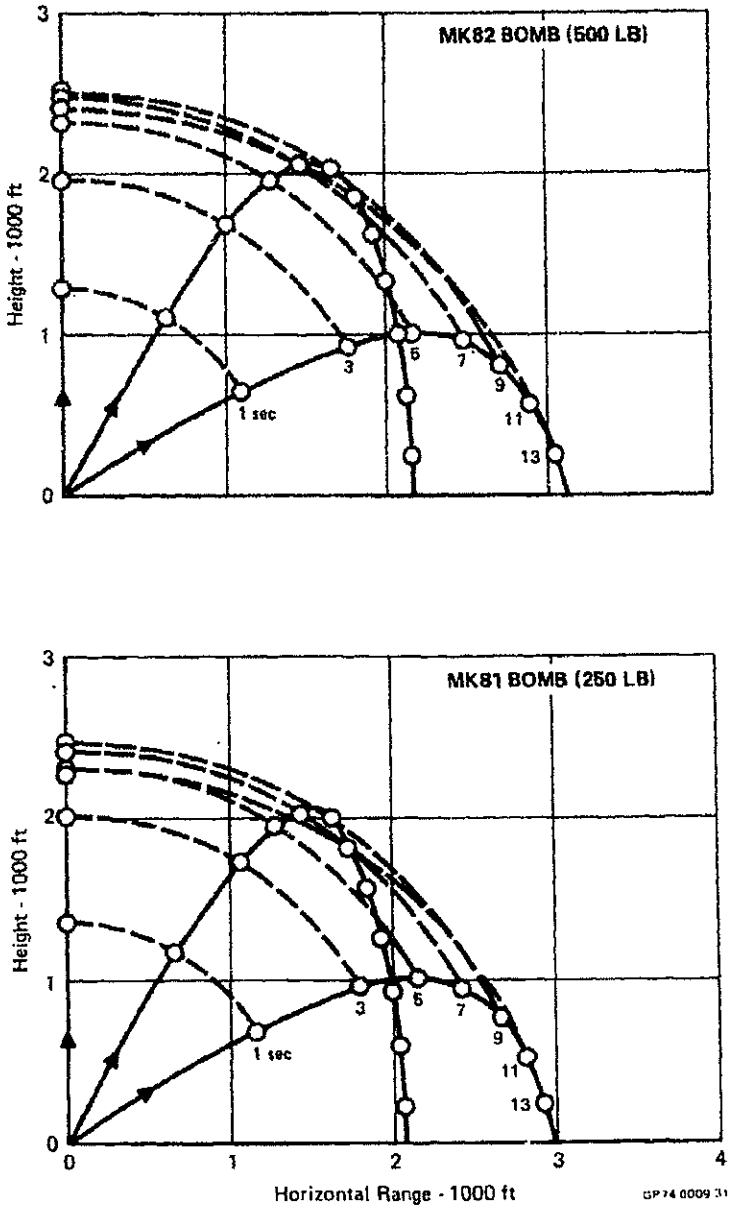

(U) In summary, the two most critical cases for fragment avoidance are for an early burst of a M117A1 bomb with "launch and leave" tactics, or an early burst of the MK83 laser guided bomb where the aircraft must remain in the vicinity to illuminate the target until impact.

4.3 BOMB FALL TRAJECTORIES

(U) The trajectories for level release of unpowered bombs as a function of release speed are illustrated by Figure 4-3. In all cases the bomb is forcibly ejected from the rack with an initial downward velocity of 6 ft per second. Although all releases are shown for a height above ground level of 2500 ft, the figure can also be used to illustrate how standoff range would decrease if release height were reduced. The horizontal dotted lines show that for a given time after release the bomb has fallen essentially the same vertical distance regardless of release speed, and that in all cases ground impact for release 2500 ft AGL would be at 12.4 seconds after release.

(U) FIGURE 4-3
UNPOWERED BOMB TRAJECTORIES
Level Release 2500 Ft AGL, 6 FPS Ejection Velocity

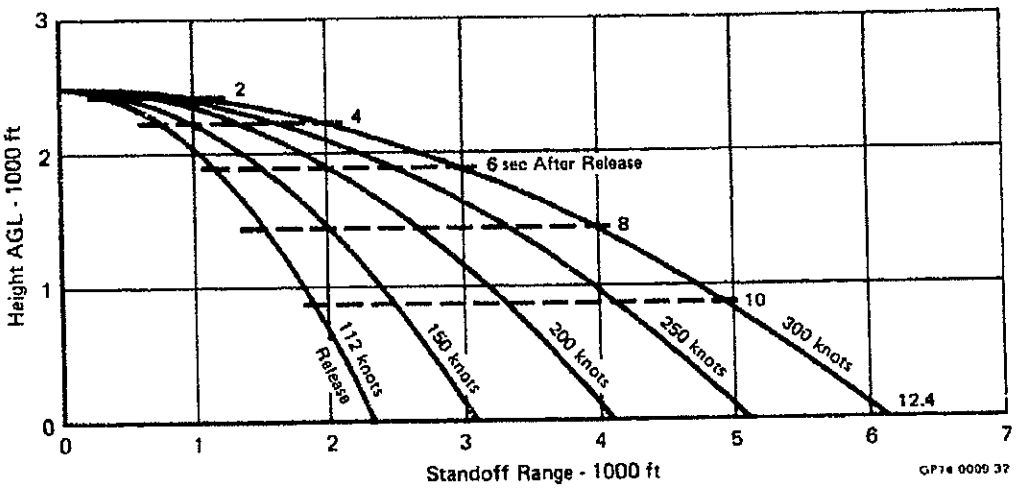

(U) As previously noted, an arming delay time of 10 seconds has been selected, and if an early burst were to occur at arming the bomb would be 850 ft above the ground. This figure of 850 ft must then be added to the fragment heights previously shown in Figures 4-1 and 4-2 to find the fragment envelope with respect to the ground for an early burst.

(U) Assuming the aircraft remains 2500 ft AGL after release, a horizontal cut at 2500-850, or a height of 1650 ft, can be made through the fragment envelopes of Figures 4-1 and 4-2 to see if the aircraft could continue to fly straight over the target without the fragments from an early burst catching up to it. For an aircraft speed of 300 knots, Figure 4-3 shows the range from release to a 10 second early burst is 4956 ft. In the same 10 seconds after release the aircraft travels 5070 ft, or 114 ft beyond the early burst. Figure 4-4 shows that for a M117A1

(U) FIGURE 4-4
AIRCRAFT/FRAGMENTS FOR EARLY BURST
300 Knots, 2500 Ft AGL, 10 Sec Burst

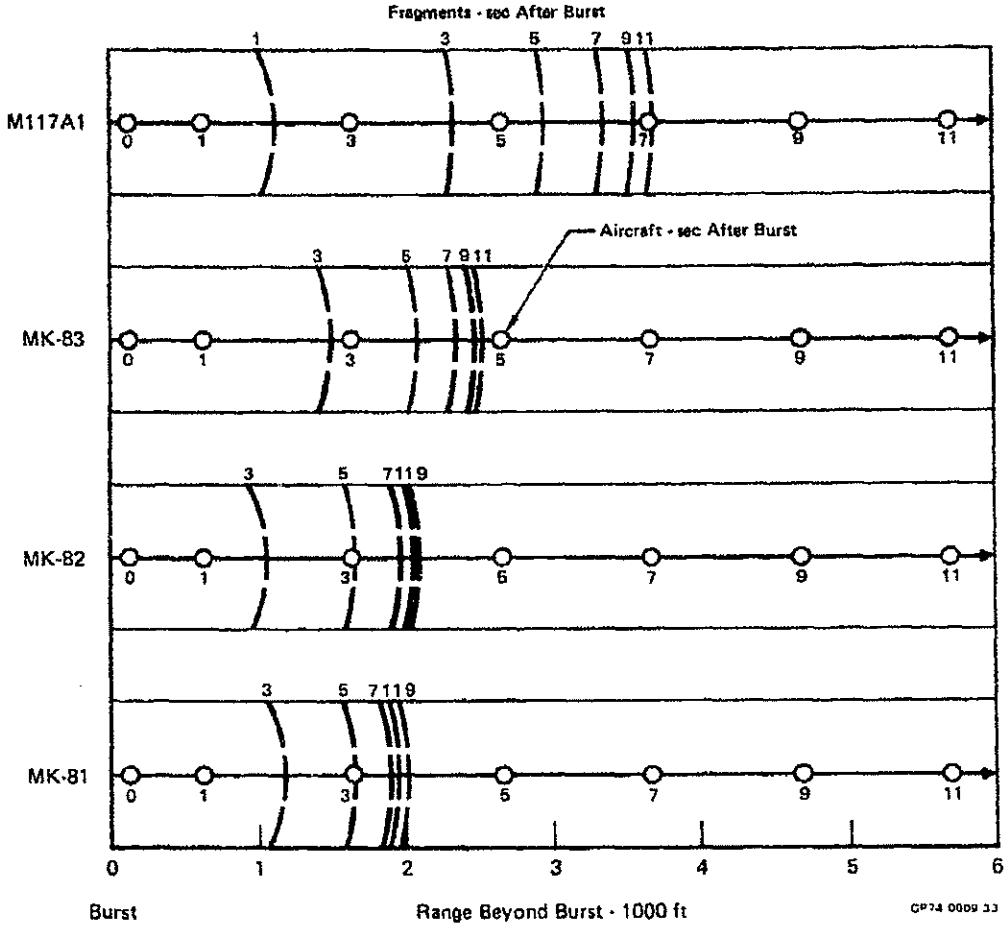

bomb the aircraft would be hit by fragments less than 1 second after burst, and would continue to be hit until about 6 seconds after burst. For the 1000 lb MK83 bomb, the aircraft would probably be hit about 2 seconds after burst. The aircraft would avoid any fragments from the MK82 or MK81 bombs. If speed were lower the chances of being hit would increase.

(U) If there were no early burst and the bomb hit the target, for the same 300 knot speed Figure 4-3 shows the standoff range from release to target is 6111 ft in a time of 12.4 seconds. In this same time the aircraft would travel 6285 ft, or 174 ft beyond the target. If a lower speed of 250 knots were used, the standoff range would be reduced to 4106 ft in the same time of 12.4 seconds. In this case the aircraft would travel 5230 ft and would be only 124 ft beyond the

target at impact. For this burst at impact the fragment envelope is determined at a height of 2500 ft instead of at 1650 ft, as was done for an early burst. Figure 4-5 shows the aircraft/fragment relationships for the M117A1 and MK83 bombs for the above two release speeds of 300 and 250 knots, with the aircraft still flying straight and level 2500 ft AGL. At 300 knots the aircraft stays ahead of the fragments from either bomb, because of the longer time required for the fragments to ascend the additional 850 ft. Fragment velocity is independent of release speed, so at 250 knots the aircraft is not as far beyond impact at the same time

(U) FIGURE 4-5
AIRCRAFT/FRAGMENTS FOR TARGET IMPACT
2500 Ft AGL

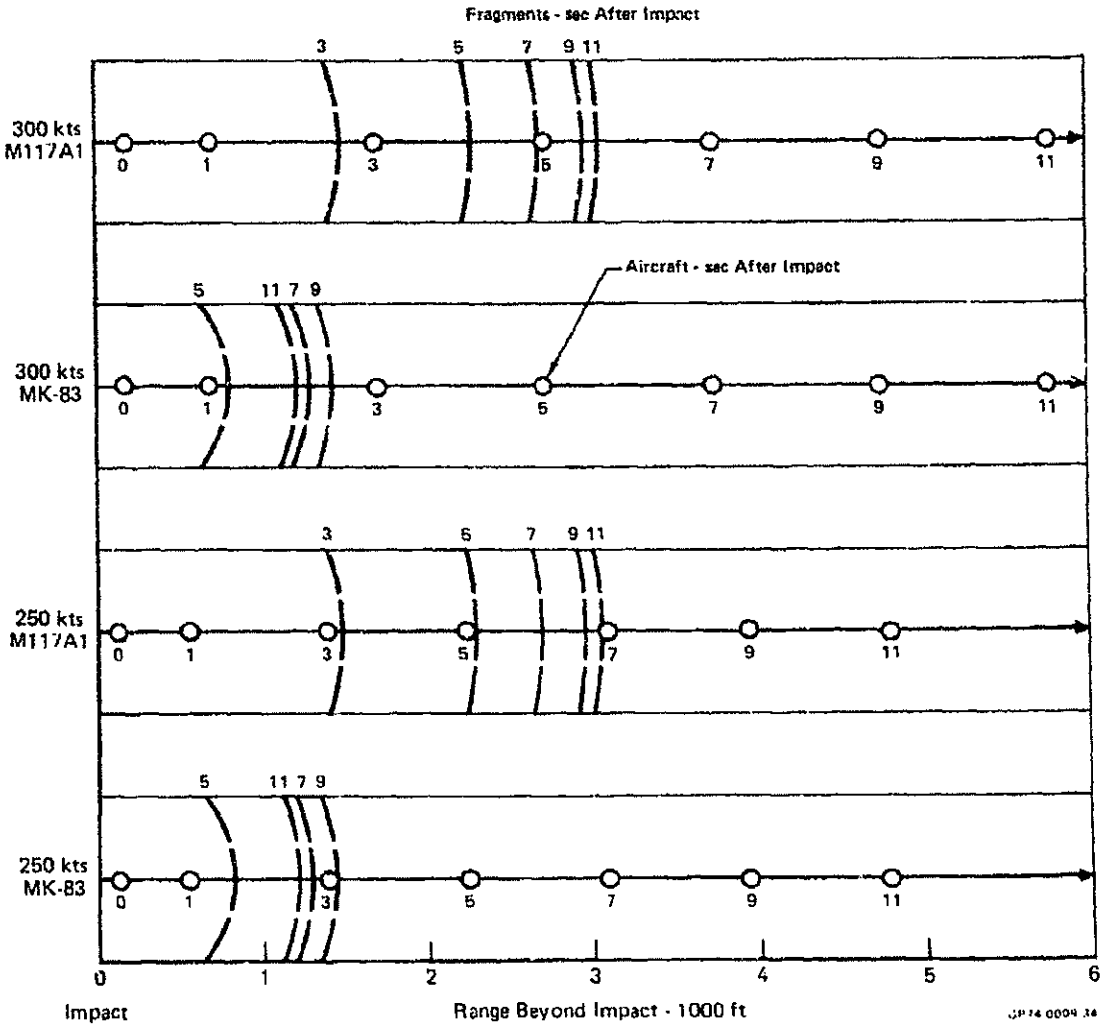

as it was at 300 knots. As a result, it is struck by the M117A1 fragments about 3-5 seconds after impact, but it still stays ahead of the MK83 fragments. Of course, it would also stay ahead of fragments from the MK82 or MK81 bombs at either speed.

4.4 AIRCRAFT CAPABILITIES

[redacted] The bomb release minimum speed constraints discussed in Section 4.1 and the need for higher speed to avoid bomb fragments impose a requirement on the Quiet Attack Aircraft for good acceleration from the quiet penetration speed of 112 knots at 2500 ft AGL. Since the propulsion system was sized to provide the required quiet penetration thrust at minimum power setting, advancing the throttle to intermediate power setting produces over seven times as much thrust at the same quiet speed. As the aircraft accelerates the intermediate thrust falls off and drag increases but there is still a large amount of excess thrust available. The resulting level flight acceleration 2500 ft AGL and starting from the 112 knot quiet speed is shown in terms of speed and distance as a function of time by Figure 4-6. The initial acceleration rate is over 10 ft per sec^2, and is still over 5 ft per sec^2 when the speed reaches 300 knots.

[redacted] Good turn capability is another requirement during weapon delivery to avoid being hit by enemy ground fire as well as bomb fragments. At quiet speed the aircraft can turn at a reasonably short turn radius with adequate stall margin. This is sufficient for target search and surveillance but the aircraft would be too vulnerable in a defended target area. The above requirement for higher speed at weapon delivery produces substantial increases in dynamic pressure, q. This, combined with the aircraft's low wing loading and excess thrust available, gives it excellent turn capability in the target area, as illustrated by Figure 4-7. If a lift coefficient of 1.0 is used in the turn with intermediate thrust, the aircraft will accelerate in a turn started at a speed below 233 knots and will decelerate when starting a turn at a higher speed. Since the aircraft has a maximum speed of 430 knots at 2500 ft, turns can be started at higher speeds than 233 knots even though thrust is less than drag in a turn at a C_L of 1.0. As speed at the start of the turn with a C_L of 1.0 is increased to 283 knots the structural limit load factor of 8 g is reached. The aircraft could enter a decelerating turn at still higher speeds but the starting lift coefficient would have to be less than 1.0 to avoid exceeding the structural limit. At speeds above 233 knots the turn lift coefficient can be reduced until turn drag equals thrust to give a sustained turn at constant speed and turn radius. This sustained turn capability is illustrated by the curved line starting at 233 knots and ending at the maximum speed of 430 knots in 1 g straight flight. The turn radii are noted at 40 knot intervals starting at 120 knots. The noted radii are constant during a sustained turn, but are applicable only at the start of the turn for a C_L of 1.0 or at the structural limit.

[redacted] For perspective the sustained turn radius of the Quiet Attack Aircraft is compared to that for the F-4J and A7A aircraft in Figure 4-8. The comparison is made at the same altitude of 2500 ft, at military power, and at combat weight as determined by the weapons shown in parenthesis for the other two aircraft. The appreciably tighter turn radius for the Quiet Attack Aircraft is one of the fallout benefits of low wing loading and propulsion sizing at minimum power setting at quiet speed to reduce noise.

~~(C)~~ FIGURE 4-6
MODEL 226-454A STRAIGHT AND LEVEL ACCELERATION
Intermediate Thrust at 2500 Ft

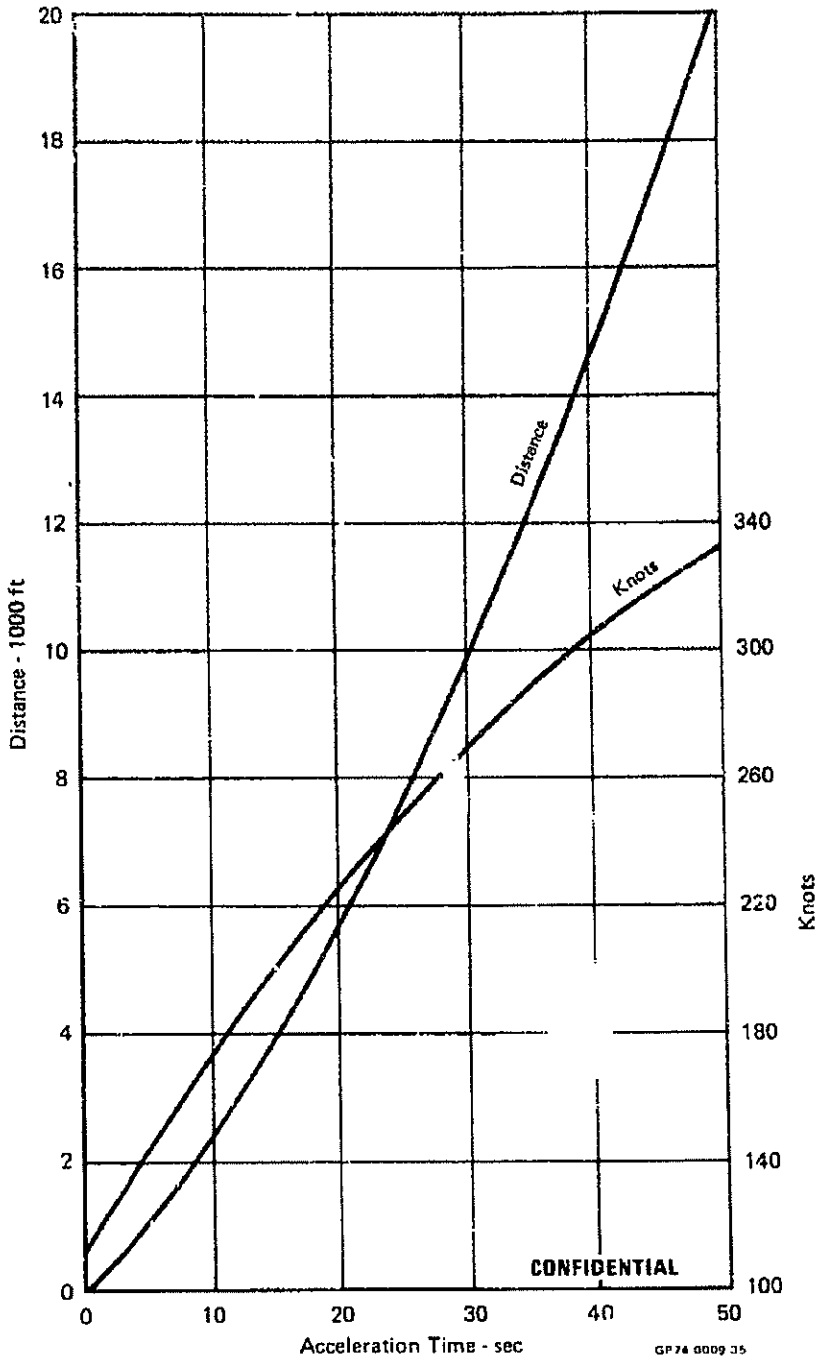

~~(C)~~ FIGURE 4-7
MODEL 226-454A LEVEL TURN CAPABILITY
Intermediate Thrust at 2500 Ft

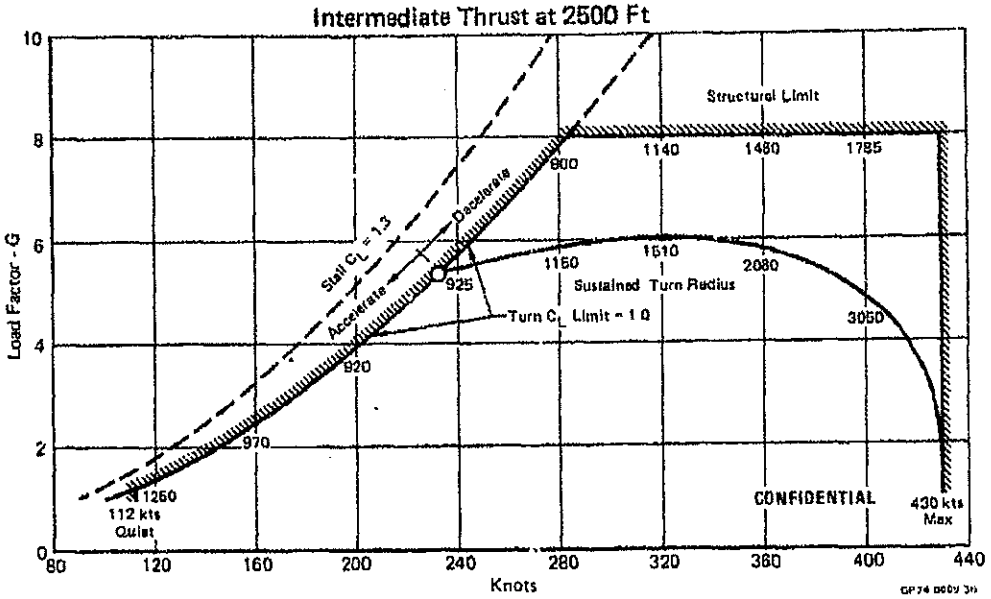

~~(C)~~ FIGURE 4-8
SUSTAINED TURN RADIUS AT 2500 FT
Military Thrust - Combat Weight

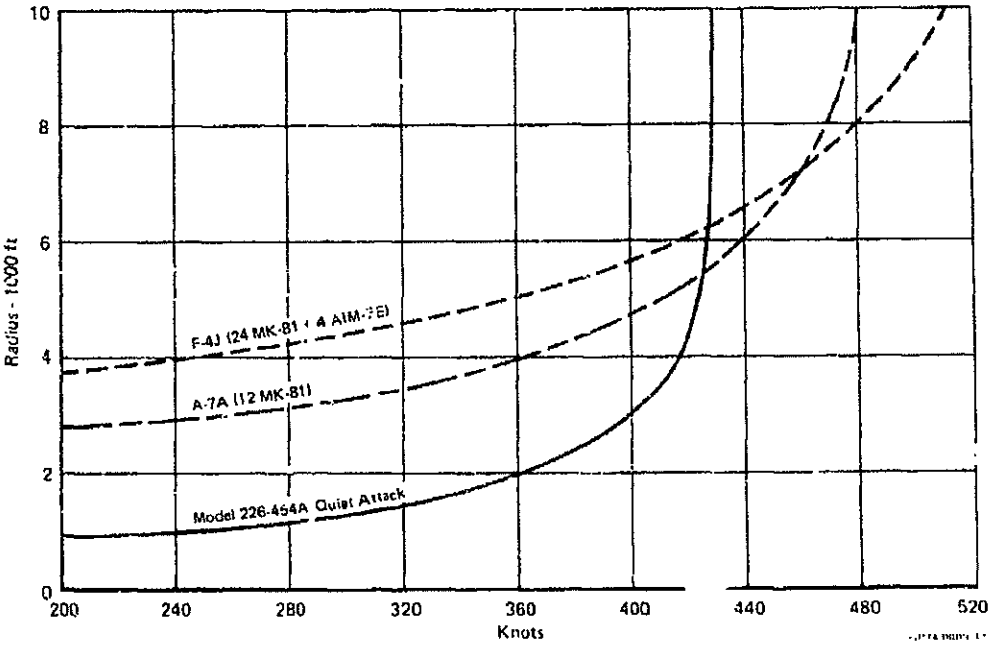

4.5 TACTICS

~~(C)~~ Based on the acceleration capability from Figure 4-6 and starting acceleration when the target is identified at a range of 25,000 ft, Figure 4-9 further illustrates the advantage of higher bomb release speeds in cutting down exposure time for the aircraft after target acquisition. A minimum time of three seconds to stabilize the aircraft prior to bomb release has been selected as recommended in Reference (5). A maximum release speed of 317 knots can be attained for this minimum stabilization time. The release range to target varies with speed as previously shown by Figure 4 3. At release speeds lower than 317 knots the additional time available for stabilization could be used for a combination of jinking followed by the minimum stabilization time of three seconds. For example, if a 250 knot release speed were chosen, 28-3 or 25 seconds of jinking time would be available after a 54-28 or 26 second acceleration to 250 knots.

~~(C)~~ FIGURE 4-9
UNPOWERED BOMB LEVEL DELIVERY RANGE
Model 226-454A 2500 Ft AGL

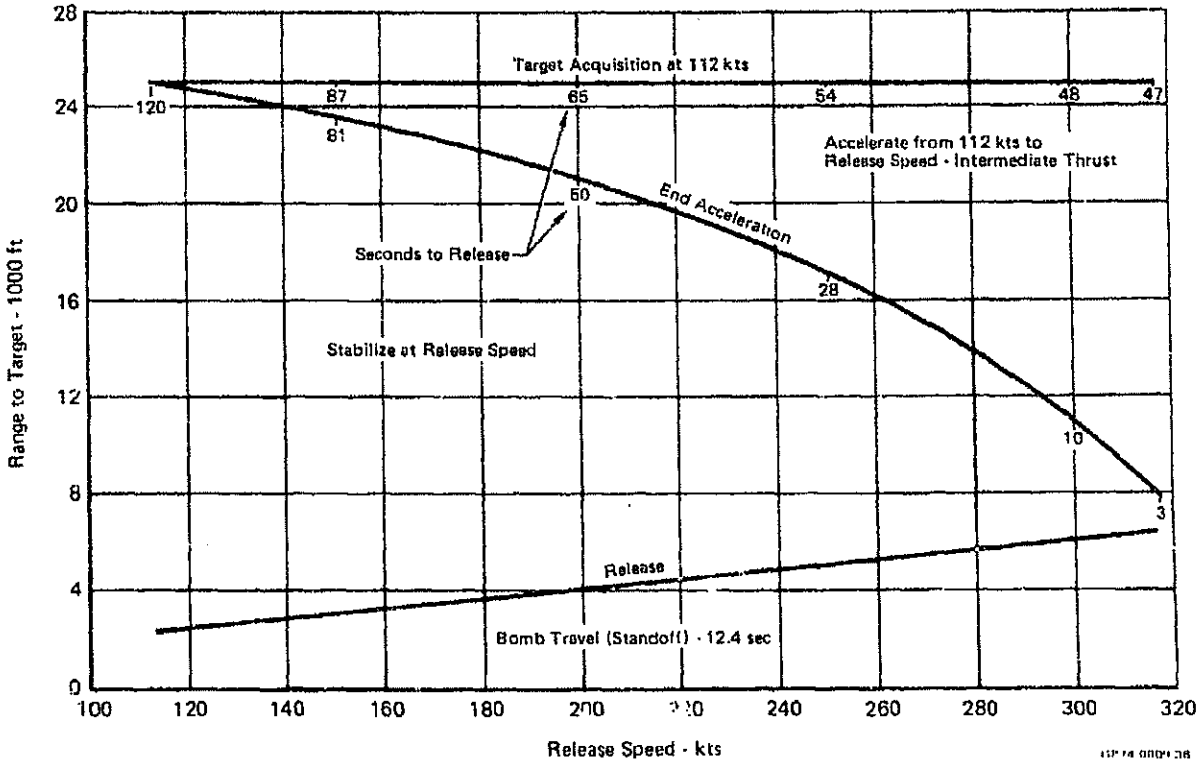

(U) After bomb release, and as further recommended by Reference (5), the aircraft continues straight and level for two additional seconds to make certain it is stabilized at release.

~~(C)~~ For minimum noise, and thus maximum covertness, the bomb should be released at the 112 knot quiet speed. However, if the aircraft were to continue straight ahead after release, it would be hit by fragments from an early burst of either the M117A1 or MK83 bombs. It was, therefore, decided to see if the aircraft could avoid fragments from the more critical M117A1 bomb by doing an accelerating level turn at 45° bank angle and intermediate thrust starting two seconds after release at 112 knots. If an early burst occurred 10 seconds after release, Figure 4-10 shows that the aircraft would be hit by fragments at less than 13 seconds after release. In this maneuver the aircraft turns 90° in 11.78 seconds and its speed at the end of the turn has increased to 178 knots. However, if there were no early burst, Figure 4-11 shows that the aircraft would not be hit by fragments. At this minimum delivery speed an electrical rather than a mechanical fuse would have to be used. According to Reference (5) the probability of an early burst due to fuse malfunction is considerably higher for electrical fuses but the expected rate is still no greater than one in one thousand. In the case of the smaller MK81 or MK82 LDGP bombs or for fire bombs there would be no danger from fragments. For surprise attack against a target defended by nothing more than small arms, this weapon release at quiet speed could be an attractive tactic.

~~(C)~~ FIGURE 4-10
EARLY BURST OF M117A1 (750 LB) BOMB AT 112 KNOTS

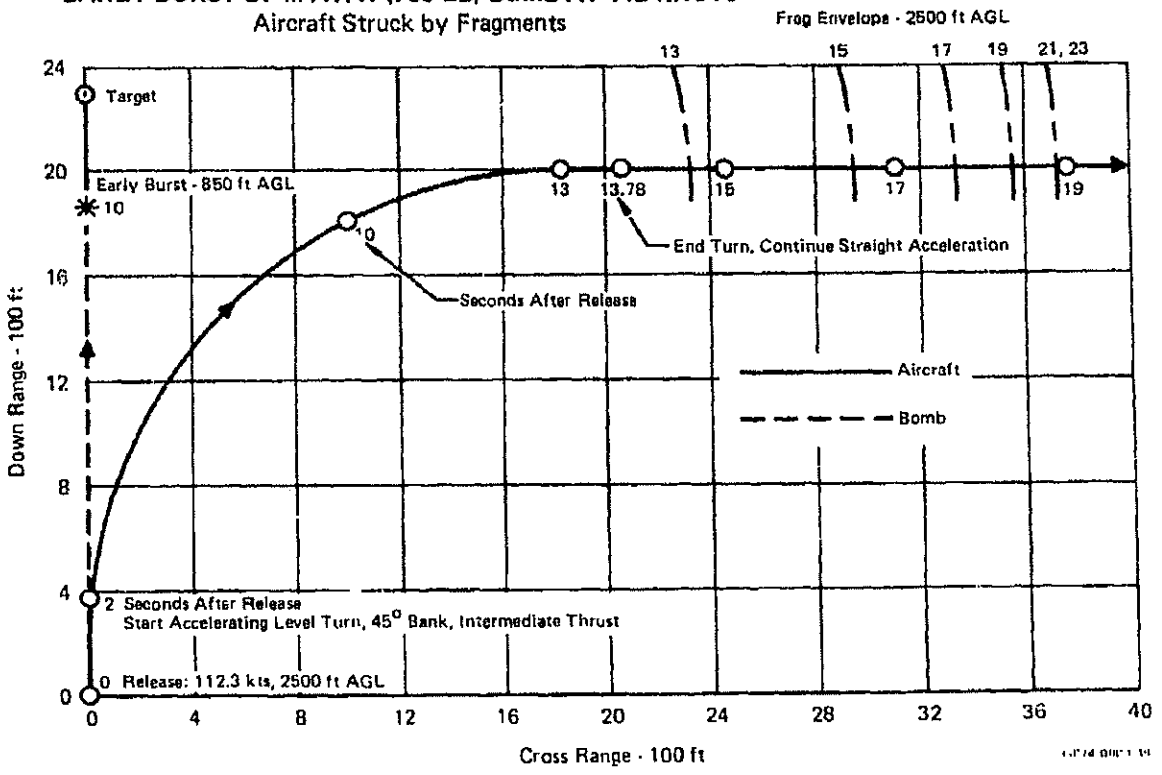

(C) FIGURE 4-11
M117A1 (750 LB) BOMB DELIVERY AT 112 KNOTS
No Fragment Hits on Aircraft

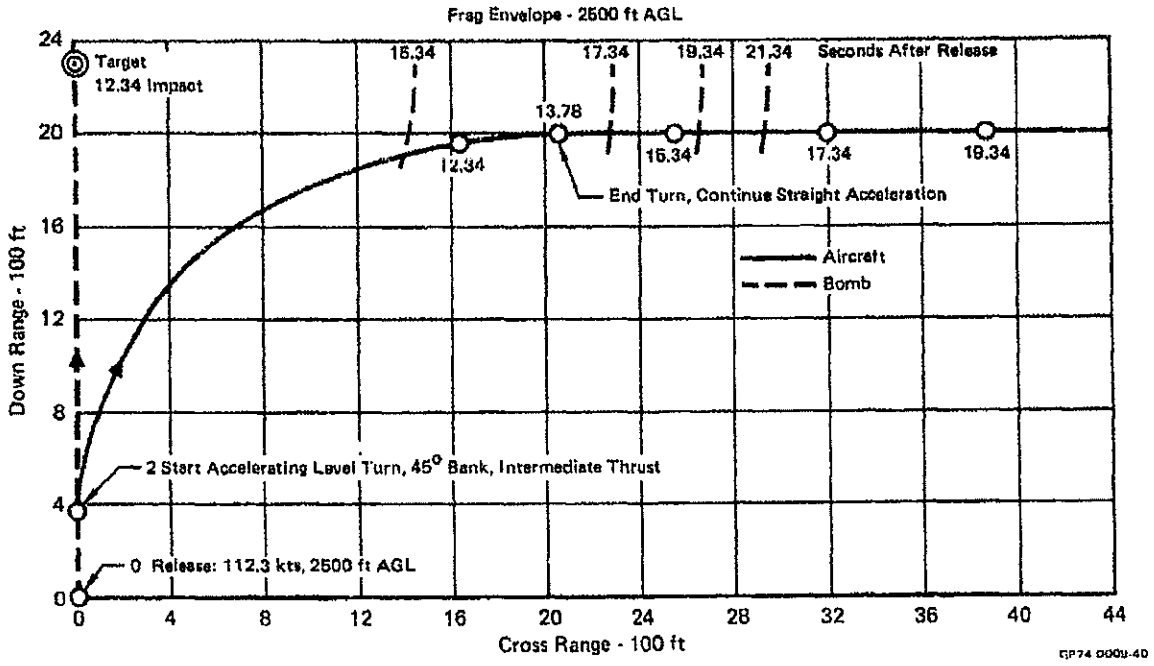

(C) Against more heavily defended targets where minimum exposure time is the objective, the bomb should be released at a higher speed for more standoff range, and maximum advantage should be taken of the aircraft's turn capability previously illustrated by Figure 4-7. To avoid fragments from an early burst of the M117A1 bomb, the aircraft could enter a sustained turn two seconds after release and turn through 135°, so that it ends the turn going directly away from the early burst. This tactic is illustrated for different speeds by Figure 4-12, using the sustained turn radii from Figure 4-7. It can be seen that the minimum speed for fragment avoidance is about 150 knots, and both fragment avoidance and exposure are improved by higher release speeds.

(S) The severe turns in Figure 4-12 would probably not be usable with laser guided bombs and the internally mounted laser designator because of the large elevation and azimuth sight angles required to illuminate the target up to the time of impact. More gentle constant speed turns at 250 and 300 knots with a constant bank angle of 30° or 45° have been investigated to ensure that the aircraft could avoid fragments from an early burst of the 1000 lb MK83 laser guided bomb while keeping the FLIR and laser designator sight angles within practical limits. These tactics are illustrated by Figure 4-13 for a speed of 250 knots and by Figure 4-14 for 300 knots. Although the aircraft stays ahead of the early burst fragments in all cases, it can be seen that for both speeds the aircraft is closer to the fragments in the 30° bank. On the other hand, the location of the cross mark on each

~~(C)~~ FIGURE 4-12
M117A1 EARLY BURST FRAGMENT AVOIDANCE
135° Max Sustained Turn - 2500 Ft AGL - Intermediate Thrust

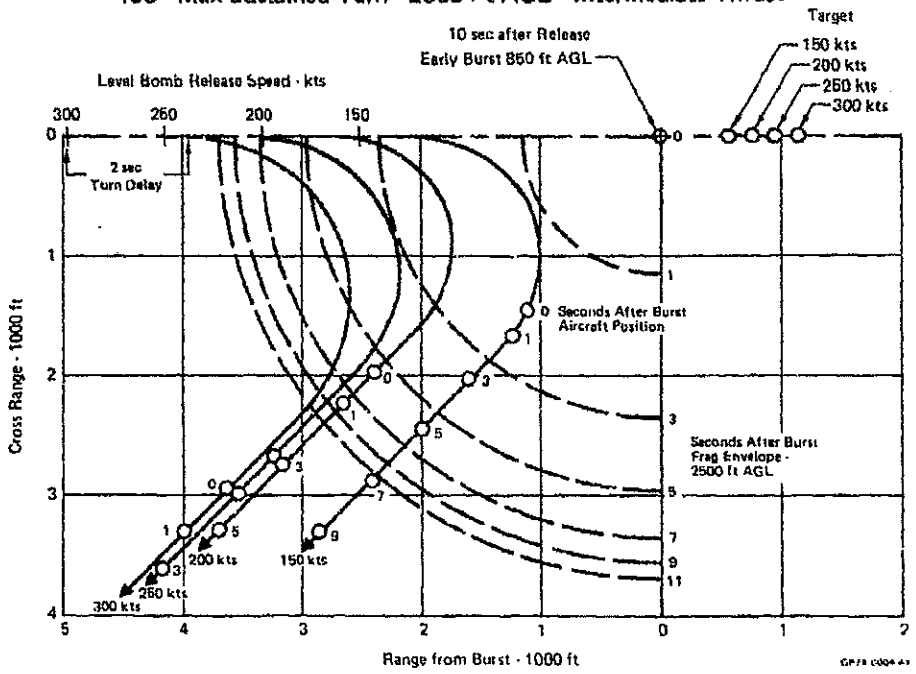

~~(C)~~ FIGURE 4-13
MK83 LASER BOMB DELIVERY AT 250 KNOTS
Level Release, 2500 Ft AGL

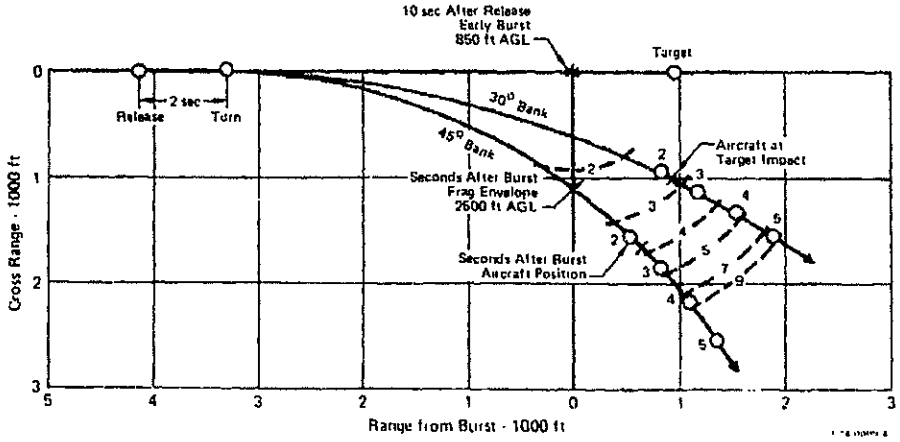

(S) FIGURE 4-14
MK83 LASER BOMB DELIVERY AT 300 KNOTS
Level Release, 2500 Ft AGL

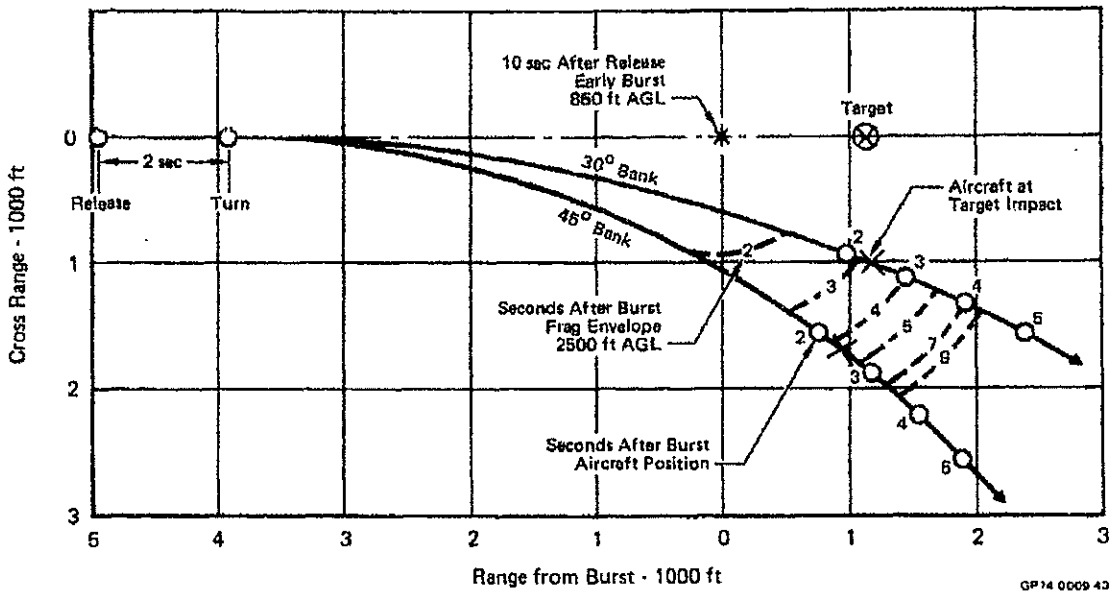

curved flight path indicates where the aircraft is at the time of impact and this shows that the target is further astern at impact for a 45° bank. Thus the bank angle selected is a compromise between fragment avoidance and sensor viewing angles, but any bank angle in the 30°-45° range, and to some extent on either side of this range, should be satisfactory. Even in straight flight directly over the target, the target would still be astern of the aircraft at the time of impact. In an attempt to avoid or at least reduce this rearward looking requirement, another investigation was made where the throttle was moved back to idle at the start of the turn to decelerate the aircraft. Although not illustrated here, this showed that because of the short time of 12.4 seconds from release to impact the reduction in speed and look angle was negligible.

4.6 SENSOR VIEWING REQUIREMENTS

(U) The above four cases of two speeds and two bank angles for LGB delivery were analyzed to determine the FLIR/laser designator viewing angles involved. The case of 250 knots speed and 45° bank angle will be used as an example to show what was done for each of the four cases. The first step is to determine for a given aircraft position the distance the target is offset to the side of the flight path, and also the distance the target is forward or aft of the aircraft. This is done at a number of aircraft positions on its flight path from start of the turn to target hit, as illustrated by Figure 4-15. The sensor viewing geometry relationships shown by Figure 4-16 illustrate the process used to arrive at the azimuth and elevation viewing angles at each aircraft position. The process starts with a head-on view which takes into account the aircraft height of 2500 ft AGL, the bank angle, and the offset. Because of the bank angle, the PROJECTED LOS (line of sight from aircraft to target) is out the bottom of the aircraft toward the inside instead of the outside of the turn. The second step is a view looking toward the side of the aircraft in the bank, and this view accounts for the angle of attack and whether the target is forward or aft of the aircraft. The third step is a top view of the aircraft and target projected normal to the fuselage reference plane to determine the azimuth angle, and shows azimuth angle for one case where the target is forward and another case where the target is aft of the aircraft. The fourth and final step is a true view in the plane of the azimuth angle to determine the true LOS from aircraft to target and the elevation angle in the azimuth plane. The true view shown is for the case when the target is aft, and a similar technique is used when the target is forward.

(U) FIGURE 4-15
LASER GUIDED BOMB DELIVERY
250 Knots, 45° Bank Turn, 2500 Ft AGL

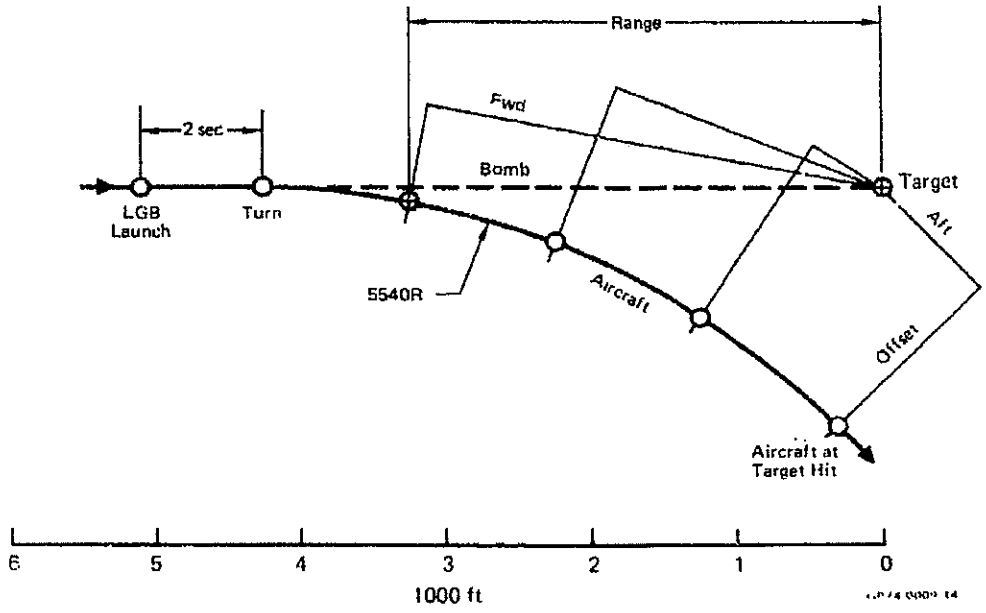

(U) FIGURE 4-16
SENSOR VIEWING GEOMETRY

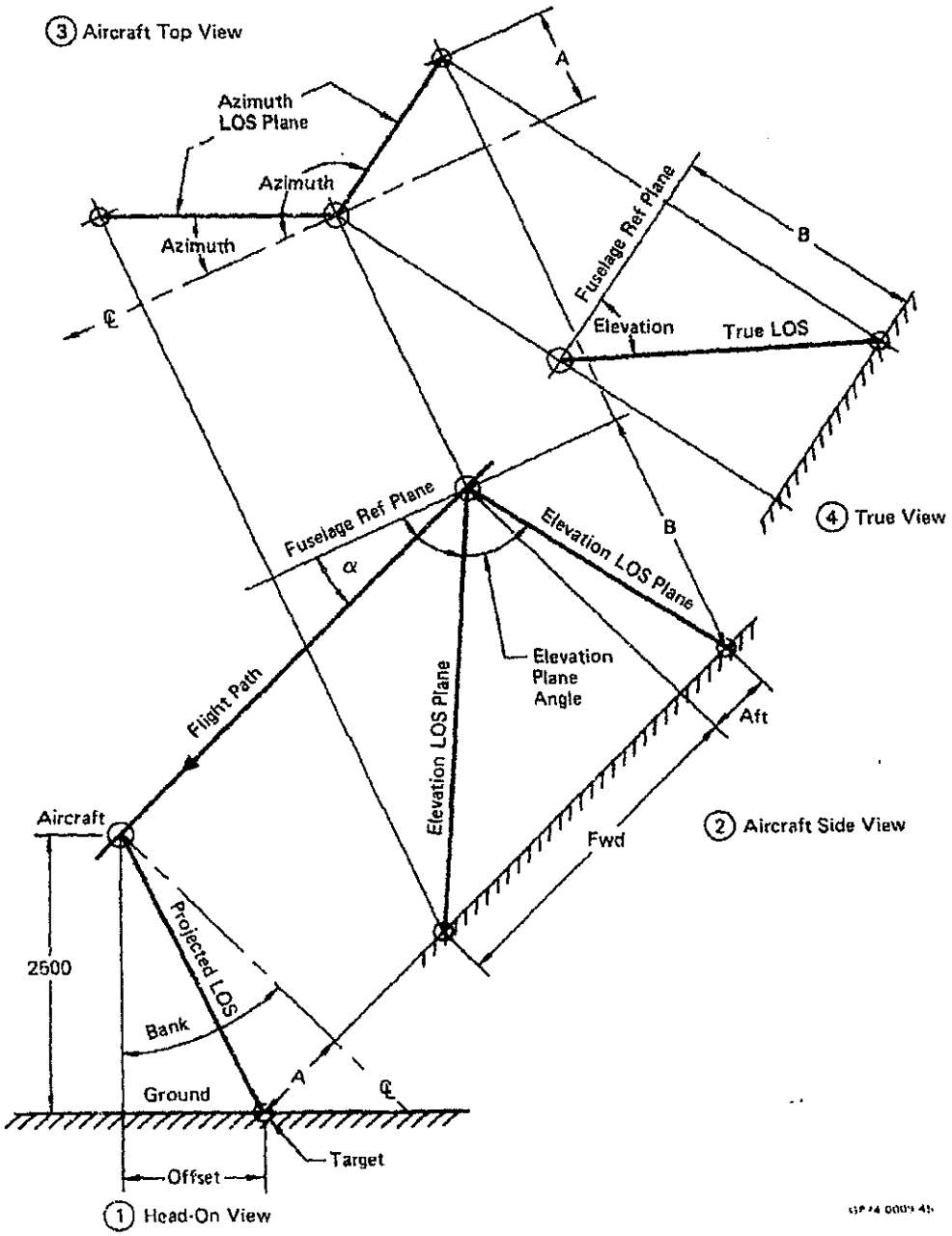

(U) The forward/aft and the offset distances from Figure 4-15 and the azimuth and elevation plane (not elevation angles) determined from Figure 4-16 are plotted as a function of range in Figure 4-17 to show how they typically vary from the start of the turn to target hit. Figure 4-15 also defined the range.

(U) The elevation and azimuth angles for the four cases of speed and bank angle are shown by Figure 4-18. Since the elevation angle is in the azimuth plane and is measured in degrees below the fuselage horizontal reference plane, the case where the elevation angle is the least will be the most critical for the sensor window. In other words for an azimuth angle of say 90°, if the elevation angle were 0° the line of sight would be straight out the side of the aircraft but with a 90° elevation angle the LOS would be straight out the bottom in the middle of the window.

(U) The FLIR line of sight angles prior to the turn must also be considered to be sure the window is adequate. In addition to the FLIR depression angle between the horizontal flight path and the line of sight from aircraft to target, the angle of attack must be accounted for. Since the FLIR is assumed to be looking ahead at 0° azimuth, the elevation angle is then the sum of the depression angle and the angle of attack. The depression angle decreases as range is increased, while the angle of attack decreases as speed is increased. The angle of attack is 8° at the quiet speed of 112 knots, but because of the low wing loading it is only 0.45° at 250 knots and a negative 0.2° at 300 knots. At the maximum FLIR range of 30,000 ft the depression angle is only 4.76° for level flight 2500 ft AGL. This is another reason for not accelerating the aircraft before target identification, and for not approaching the target in a dive when using FLIR. Assuming no acceleration until the target is identified at a range of 25,000 ft, the worst case would presumably be when the release speed is 300 knots. This is illustrated by Figure 4-19 for 250 knots as well as 300 knots, and is based on the data previously shown on Figure 4-9. Although the depression angle is continually increasing, the angle of attack, α, decreases rapidly after acceleration starts at 25,000 ft range. As a result of these opposing trends the minimum FLIR elevation angle of 8.2° occurs at a range around 20,000 ft when the aircraft has accelerated to only slightly more than 200 knots.

(U) The sight angles from Figures 4-18 and 4-19 are used with the FLIR/laser designator and window relationship to see where the FLIR and laser beams pierce the window. The area pierced is illustrated by the cross hatched areas in the upper plan view of the fuselage nose in Figure 4-20. The figure also shows the azimuth and elevation gimbal mount axes at station 40 for the FLIR/laser designator combination. In the side view at the bottom of the figure the FLIR beam is conical starting with a diameter of seven inches and is more critical than the two inch cylindrical laser beam. The window area pierced by the laser beam, due to mounting the laser designator below the FLIR, is always smaller than the FLIR area. Station plane cuts through the fuselage nose contours are shown in the middle of Figure 4-20, and illustrate the edge along the side of the fuselage in the fuselage reference plane to reduce radar cross section. Although the fuselage nose is pointed in side view, it is rounded in plan view to provide as much window width as possible forward for rotating the FLIR in azimuth to pick up targets to the side of the flight path during search.

(U) FIGURE 4-17
AIRCRAFT POSITION AND DESIGNATOR ANGLES
LGB Delivery, 45° Bank at 250 Knots

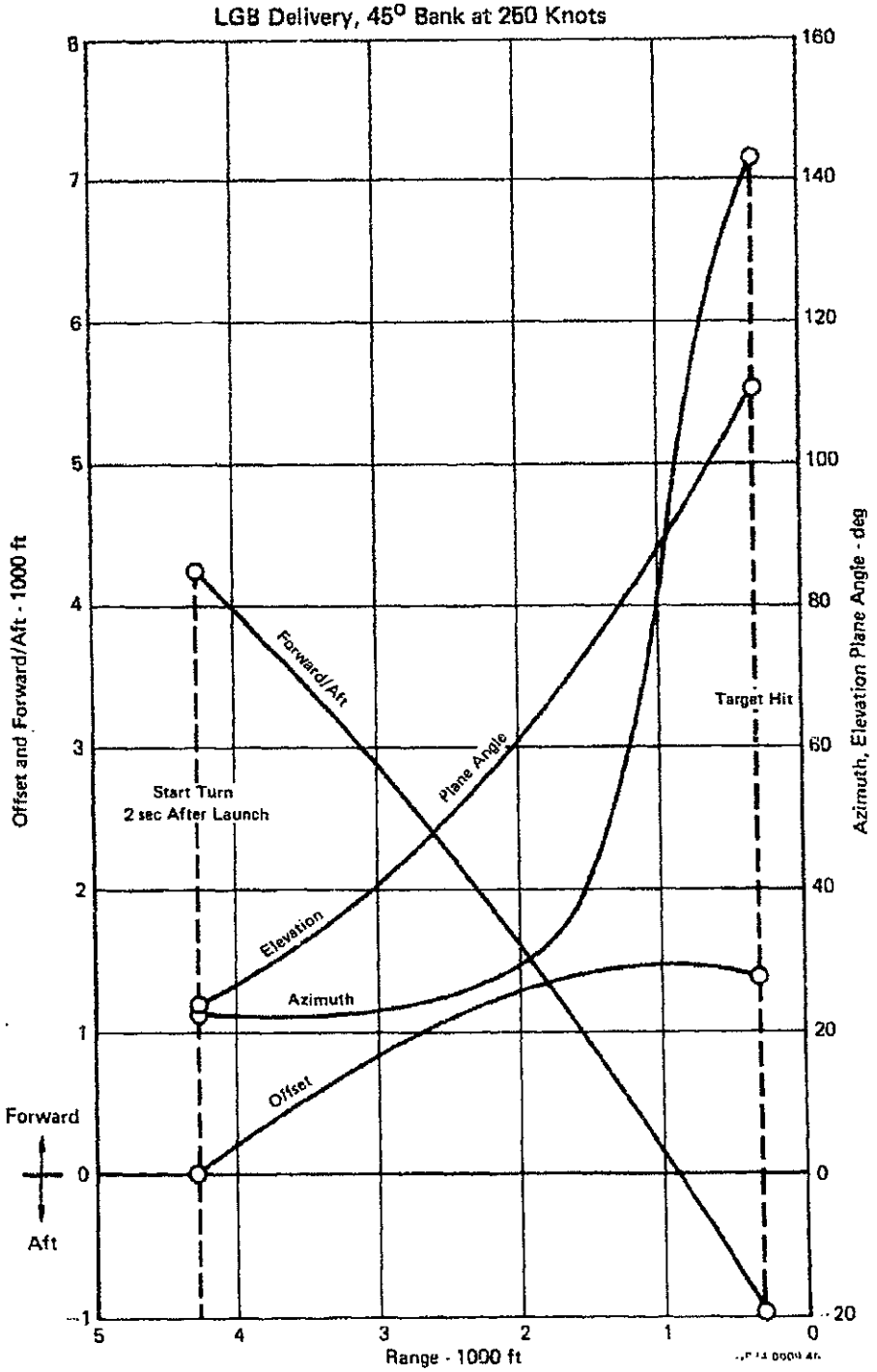

(U) FIGURE 4-18
LASER DESIGNATOR SIGHT ANGLES
Constant Speed and Bank Turn Started 2 Sec After LGB Release

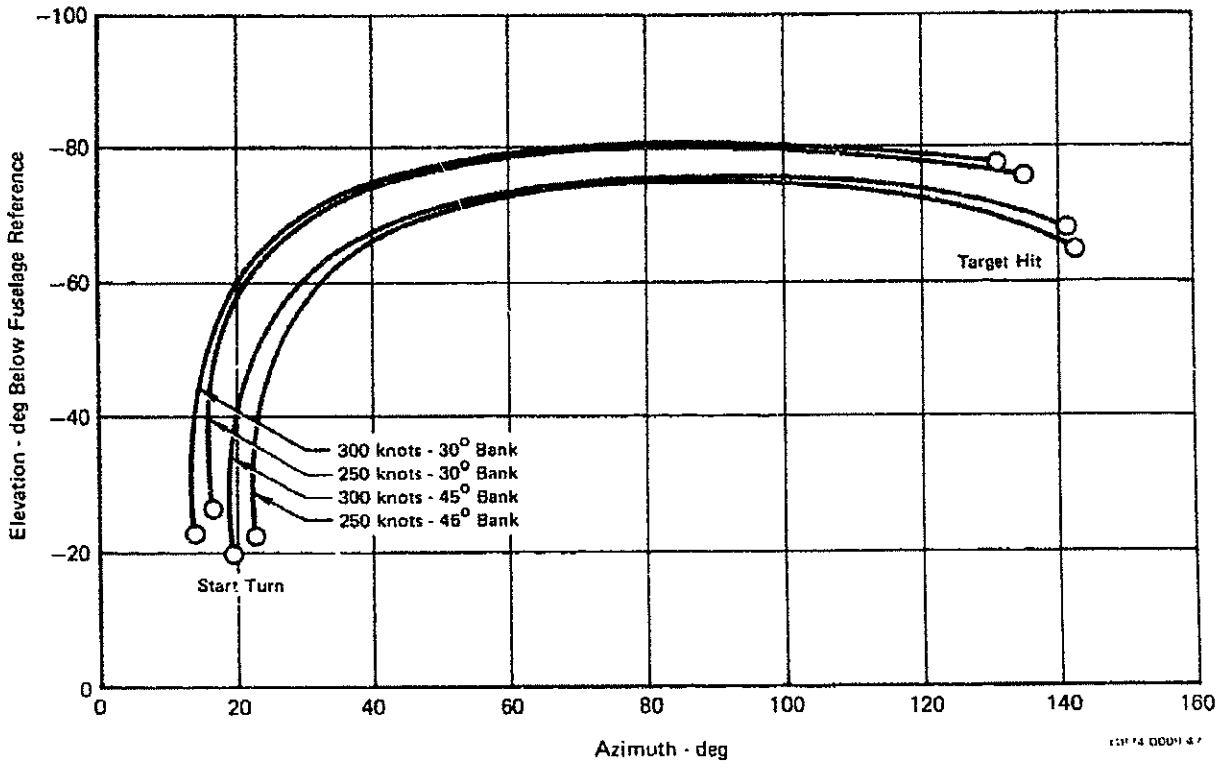

~~(C)~~ FIGURE 4-19
FLIR ELEVATION ANGLE PRIOR TO TURN
Model 226-454A 2500 Ft AGL, Intermediate Thrust Acceleration

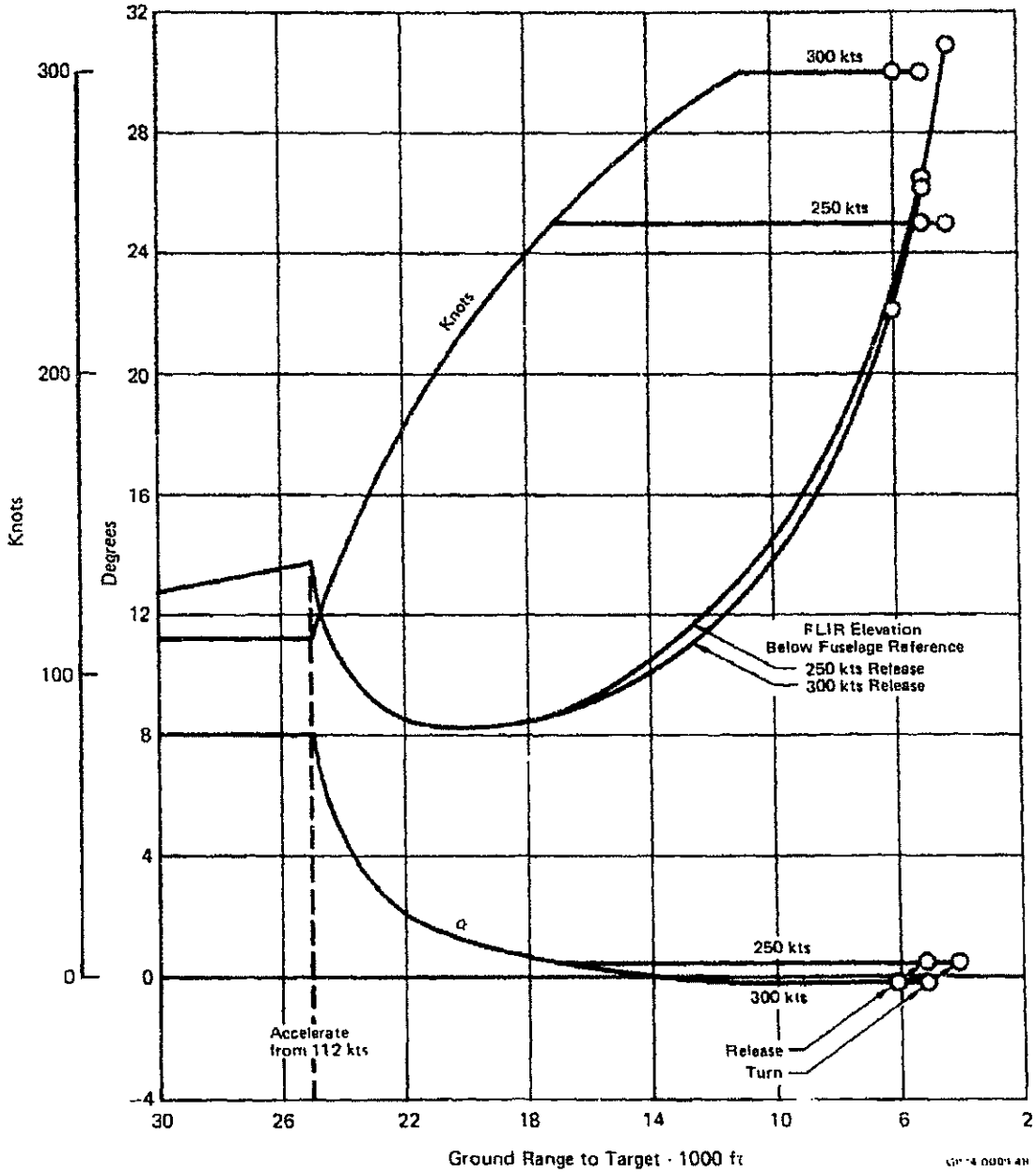

~~(C)~~ FIGURE 4-20
FLIR/LASER WINDOW

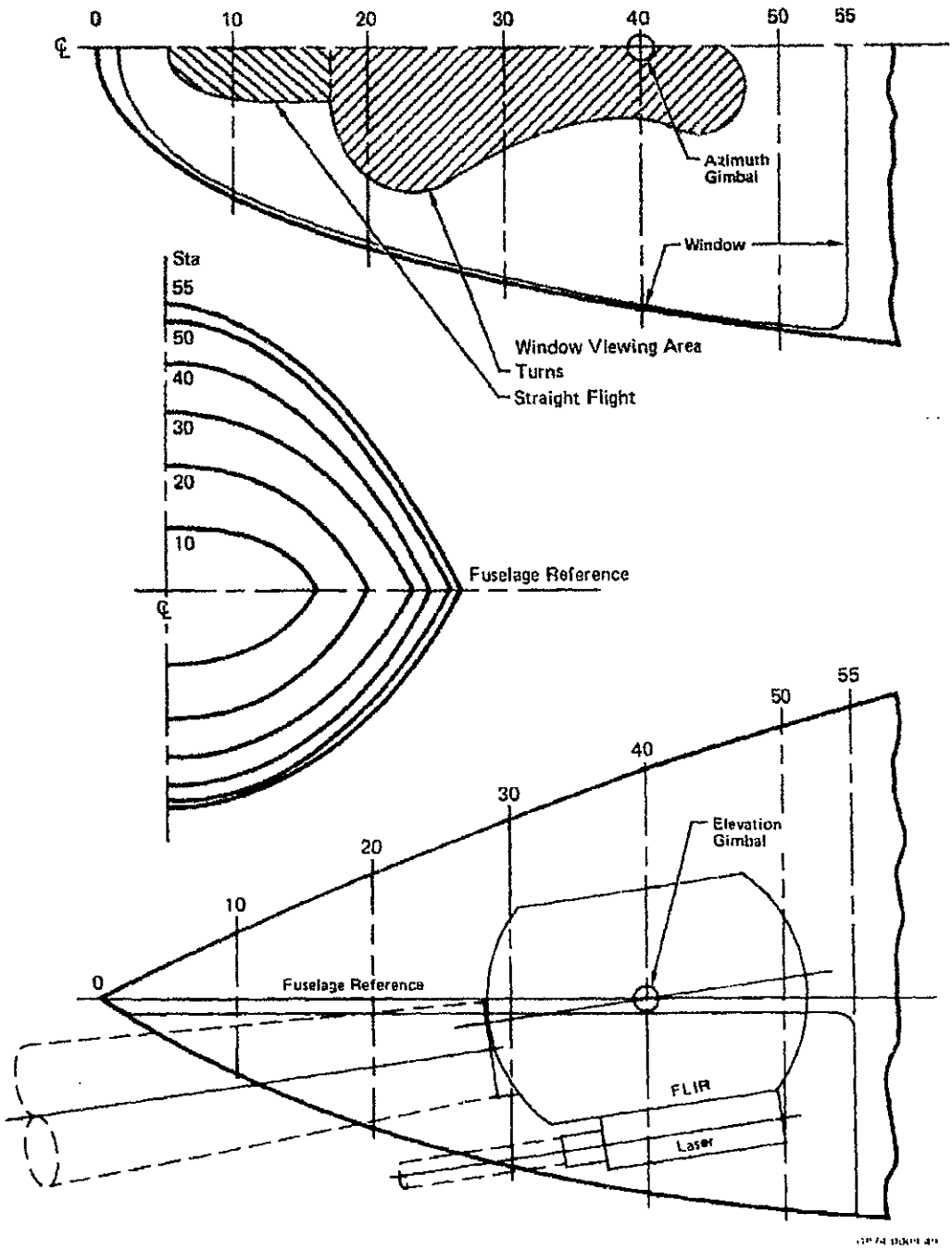

(U) A single piece window of this size may be difficult to manufacture due to the grinding and polishing processes required. The window thickness would have to be about 0.2 inch to withstand the airloads. For this thickness, in order to minimize distortion, the radii of curvature should be no less than 80 inches. Typical roll plane radii of curvature in the nose area are about 20 inches, which may result in unacceptable distortion. A window comprised of eight or ten flat glass panels would alleviate both the manufacturing and distortion problems while not affecting radar cross section or acoustic noise.

(U) The desirability of internal FLIR and laser designator installation on this aircraft is clear. However, if the above flat glass panel alternative is still unacceptable from either a technical or cost standpoint a chin-mounted turret would be considered.

(Page 4-26 is blank)

5. 1.7-5 MICRON IR SIGNATURE

(U) This section addresses infrared signature of the aircraft in the 1.7-5 micron bandwidth. This is the spectral region where peak IR radiation occurs for jet engine exhaust temperatures, and consequently is the region in which heat seeking missiles operate. As temperature decreases the wavelength for peak radiation moves toward the longer wavelengths, such as the 8-14 micron bandwidth used by forward looking infrared (FLIR) systems. The aircraft IR signature in that band is discussed later in Section 8.

(U) The techniques used to predict these IR signatures were previously discussed in Section 4 of Reference (1). The IR signature of the aircraft at a given flight condition and viewing aspect is the sum of the radiation from each hot metal component exposed to view. Component radiation depends on temperature, projected area and emissivity. At that time the IR signatures were for the scaled GE1/10 gas generator operating at minimum throttle setting, and it was shown that exhaust plume radiation was negligible so that essentially all the aircraft's IR radiation was due to visible hot metal in the exhaust system.

(U) The IR signatures and missile tracking ranges discussed herein are for the Model 226-458 quiet attack aircraft, which uses the TF-34 core gas generator with different exhaust gas characteristics than the scaled GE1/10. However, the hot metal radiation is still predominant, with radiation from either the exhaust plume or from aerodynamic heating of aircraft exterior surfaces being negligible. This is true for all operating conditions from quiet speed to maximum speed and minimum to maximum thrust. At minimum throttle setting the exhaust gas temperature of the TF-34 core gas generator is lower than the scaled GE1/10, but the aircraft's IR signature for either gas generator is so low that any difference is not noticeable.

~~(C)~~ As was the case previously, at quiet speed the aircraft cannot be tracked by the Soviet SA-7 STRELLA missile as long as it stays more than about 200 ft. above the ground. Even at maximum speed and thrust the STRELLA cannot track the aircraft when it is more than about 1300 ft. above ground level (AGL). The U.S. REDEYE missile has a more sensitive detector than the STRELLA, but the aircraft could also deny REDEYE tracking if it stays more than about 1300 ft. AGL at quiet speed or about 4300 ft. AGL at maximum speed. All these heights AGL are based on 50% probability of detection and no atmospheric attenuation of the aircraft's IR radiation, and are therefore conservative. For an 80°F day with 70% relative humidity, the water vapor in the atmosphere would reduce the above minimum height AGL to roughly 75% of the values noted.

5.1 IR SIGNATURE

(U) A body at a given temperature radiates IR energy over a broad range of wavelength in microns (μ), but as temperature increases the peak radiation occurs at a shorter wavelength and the intensity increases at all wavelengths. This is illustrated by Figure 5-1, using as examples the freezing and boiling points of water and a third temperature midway between them. Since the bandwidth of an IR system is limited by the characteristics of the detector material used, it follows that the further away the IR system bandwidth is from the wavelength for peak emittance of an object the less chance there is of detecting the object. At the low throttle setting used for quiet speed the aircraft's nozzle exit temperature is only 154°F, which gives a peak radiation in the neighborhood of 8 microns, while at maximum power the nozzle exit temperature is 336°F with peak radiation at 6.5 microns.

(U) FIGURE 5-1
RADIANT EMITTANCE vs WAVELENGTH FOR SEVERAL BLACK BODY TEMPERATURES

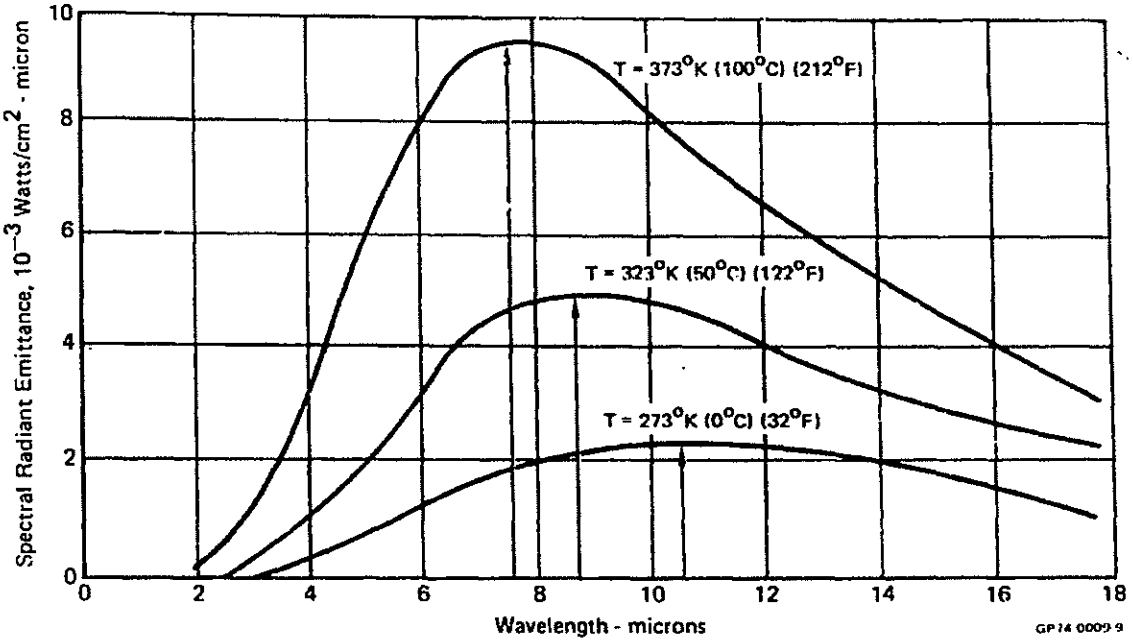

(U) In a given bandwidth and for a given aspect or viewing angle, the total hot metal radiation in watts/steradian is the sum of the radiation from each of the hot metal elements exposed to view. The radiation from each hot metal element depends on its projected area at the given aspect angle, its surface temperature, and its surface emissivity. In this report all IR signature analysis is based on the maximum black body emissivity of unity, so that the results are somewhat conservative. For the 3-5 micron bandwidth, Figure 5-2 shows the aircraft's IR signature at quiet speed as functions of elevation and azimuth aspect angles. The highest intensity is determined by the shape of the nozzle exit, and is seen to be 13.02 watts/steradian directly behind the aircraft in azimuth and looking down at the aircraft at an elevation aspect of +10°. The nozzle does not end in a vertical fuselage station plane, but is designed to reduce detection by a ground based IR missile by extending the lower portion further aft than the upper portion so that the nozzle ends in a canted plane 50° off vertical. At zero azimuth angle this accounts for some IR signature existing when looking straight down at +90° elevation aspect, but no signature when looking up at elevation aspects greater than -50°.

(S) Intensity isograms can also be developed for the specific bandwidth used by a specific IR missile. This has been done for the Soviet SA-7 STRELLA missile for its bandwidth of 1.7-2.8 microns, Figure 5-3, and for the U.S. REDEYE missile for its bandwidth of 3.0-4.2 microns, Figure 5-4. Since the STRELLA bandwidth is furthest away from the aircraft's wavelength for peak radiation, the IR signatures in Figure 5-3 are also the lowest. Compared to the maximum of 13.02 watts/steradian for the 3-5 micron bandwidth of Figure 5-2, the maximum at the STRELLA bandwidth is only 0.34 but it occurs at the same aspect of 0° azimuth and +10° elevation. The 3.0-4.2 micron bandwidth for the REDEYE is closer to peak radiation wavelength than the STRELLA, but is not as close or as wide a bandwidth as 3-5 microns. Consequently, the IR signatures for the REDEYE bandwidth are higher than for the STRELLA but less than at 3-5 microns.

~~(C)~~ FIGURE 5-2
3 - 5 MICRON INTENSITY ISOGRAM
Quiet Speed

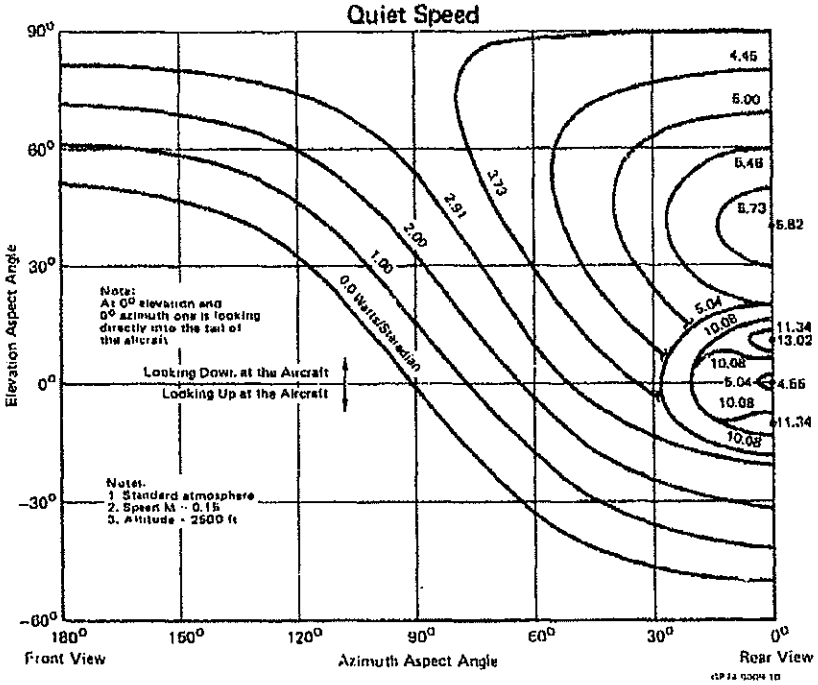

~~(C)~~ FIGURE 5-3
1.7 - 2.8 MICRON INTENSITY ISOGRAM
Quiet Speed

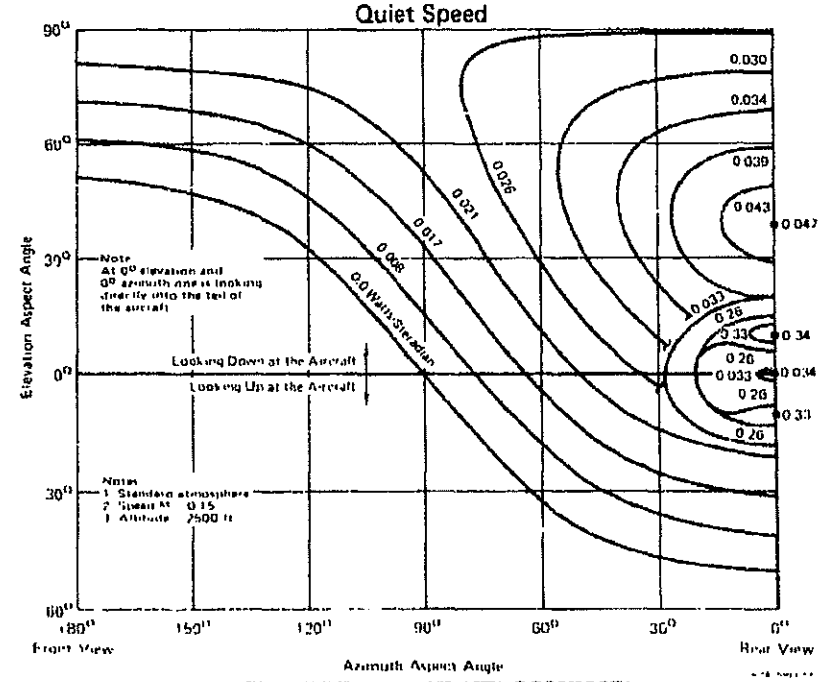

~~(C)~~ FIGURE 5-4
3.0 - 4.2 MICRON INTENSITY ISOGRAM
Quiet Speed

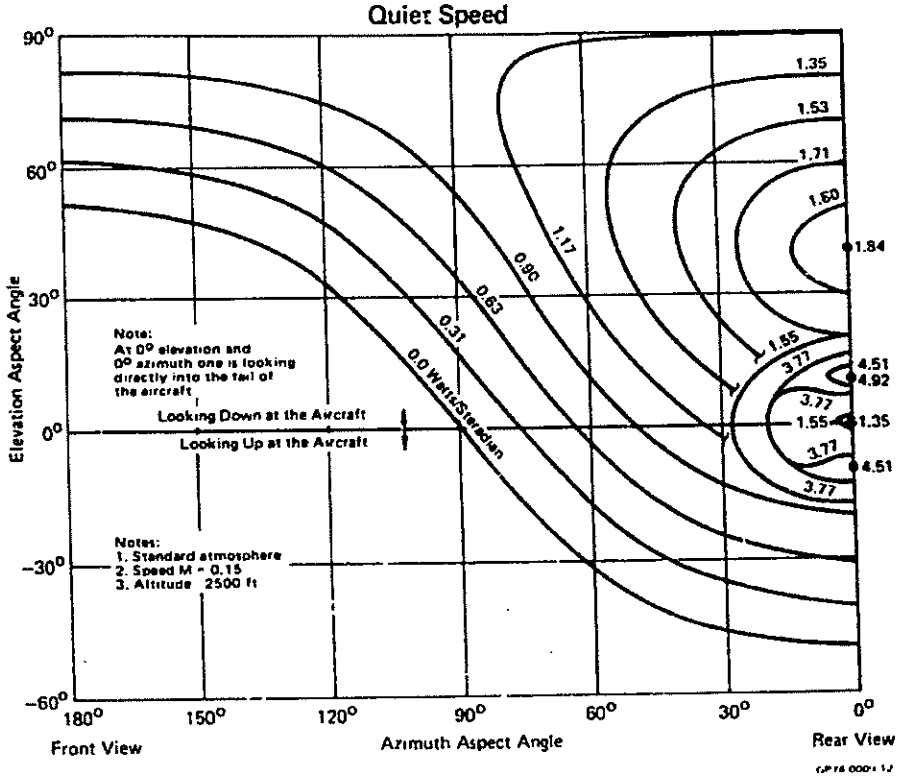

5.2 IR MISSILE TRACKING

~~(C)~~ The isograms in Figures 5-3 or 5-4 for the operating bandwidth of the STRELLA or REDEYE missiles can be used to predict the maximum (critical) tracking range of each missile as a function of aspect angle. This critical tracking slant range, R_C, is:

$$R_C = K \sqrt{\frac{J_\theta \ \tau}{(S/N)_T \ (NEI)}}$$

Where

J_θ = aircraft IR radiance in the missile spectral band in watt/steradian at an aspect angle of θ.

τ = effective atmospheric transmission

NEI = noise equivalent input at the missile aperture in watt/cm^2.

$(S/N)_T$ = minimum signal to noise ratio required for tracking

K = .0328 $\frac{ft}{cm}$

J_θ is obtained from either Figure 5-3 or 5-4 for each aspect angle. Since maximum radiation occurs at 0^o azimuth aspect angle, θ represents different negative elevation aspect angles at 0^o azimuth.

(U) The effective atmospheric transmission, τ, depends on weather conditions and can vary from a value of near zero for high humidity or rain to near unity for dry air. In other words, a value of zero means all the IR radiation is absorbed by the atmosphere and none of it reaches the missile detector, while a value of unity represents ideal weather conditions for the missile with no atmospheric absorption. In this analysis the most conservative value of unity has been used.

~~(C)~~ The NEI, or sensitivity of the missile detector, depends on detector characteristics such as the detector material and whether or not the detector is cryogenically cooled to reduce noise. Different detector materials respond to different bandwidths in the IR spectrum. The STRELLA uses a lead sulfide detector which is uncooled while the REDEYE uses a cooled lead selenide detector. The NEI is 1×10^{-10} watts/cm^2 for the STRELLA and 0.5×10^{-10} for the REDEYE. Thus the REDEYE detector is twice as sensitive as the STRELLA detector, while the cooling of the REDEYE detector reduces noise to make the increased sensitivity usable in detecting weak IR radiation signals.

(U) As is the case with any electromagnetic radiation, such as radio or TV, as the distance between the radiation source and the receiver or detector increases, the received signal becomes progressively weaker while the internal noise generated within the receiver remains constant, and it becomes increasingly difficult to separate the signal from the noise. The minimum acceptable signal-to-noise ratio depends on what false alarm rate and what probability of detection/tracking are acceptable. Generally a S/N ratio of about 10 is considered necessary for positive identification of a signal. In this analysis a S/N ratio of 3 is used to extend the missile tracking range to the maximum acceptable limit where the false alarm rate is .0013 and the probability of detection/tracking is 50%.

~~(C)~~ For a given IR missile detection system with τ=1, the only variable in the expression for critical tracking slant range R_C is the aircraft IR radiance J_θ. Since J_θ increases with aircraft speed and thrust, a complete analysis of the capabilities of either the STRELLA or REDEYE to track the aircraft throughout its speed range from quiet to maximum speeds requires additional isograms similar to Figure 5-3 or 5-4, but at higher increments of speed and corresponding thrust. Some of the data needed to generate these additional isograms is illustrated by Figure 5-5. Although not shown here, isograms for each missile have also been calculated for each speed noted in Figure 5-5, and tracking ranges for a $(S/N)_T$ of 3 have also been calculated for each missile and speed.

~~(C)~~ FIGURE 5-5
AIRCRAFT FLIGHT CONDITIONS AT 2500 FT ALTITUDE

Velocity kts	Mach No.	Fuel/Air Ratio	Nozzle Exit Pressure Ratio	Nozzle Exit Temperature ^{o}R
150	0.2285	0.001917	1.1184	632
200	0.305	0.001833	1.1810	644
250	0.381	0.001838	1.2414	658
300	0.4575	0.002023	1.3554	681
350	0.533	0.002312	1.4932	712
400	0.610	0.002738	1.6594	752
445	0.678	0.003184	1.8472	796

GP74 0009 13

~~(S)~~ Figure 5-6 illustrates the critical tracking range contours for each missile and each aircraft speed at 0^{o} azimuth aspect angle, but instead of a polar plot of elevation aspect angle and slant range a more convenient set of coordinates has been used to show distance below and behind the aircraft. The contours for the STRELLA are for the same speeds as noted for the REDEYE. These contours can be used to determine the minimum height above ground level at which the aircraft can fly at a given speed to deny tracking to each missile. Thus at 150 knots the corresponding height AGL against the STRELLA is 200 ft. or 1300 ft. against the REDEYE, while at maximum speed the corresponding heights AGL are 1300 ft. against the STRELLA or 4300 ft. against the REDEYE. Again it should be remembered that there is only a 50% probability of tracking at these heights AGL and they would also be reduced by weather conditions.

~~(C)~~ At a quiet speed (1.2 V_{STALL} with internal bombs) of 98 knots the thrust required, and consequently the nozzle exit temperature, is slightly higher than at 150 knots but still less than at 200 knots. This is illustrated by Figure 5-7. The nozzle exit temperature, which directly affects IR signature, is seen to have the same value at about 129 knots as it does at quiet speed, and lower values in between these speeds. This indicates there is a fairly wide speed range for loiter or ground search where IR signature is at its minimum value.

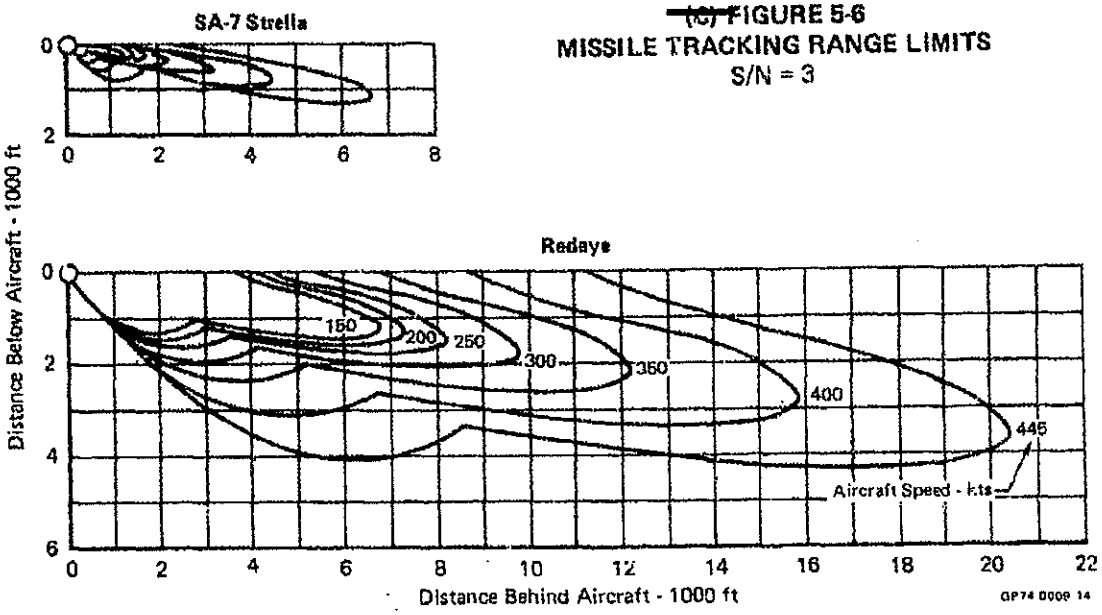

~~(C)~~ FIGURE 5-6
MISSILE TRACKING RANGE LIMITS
S/N = 3

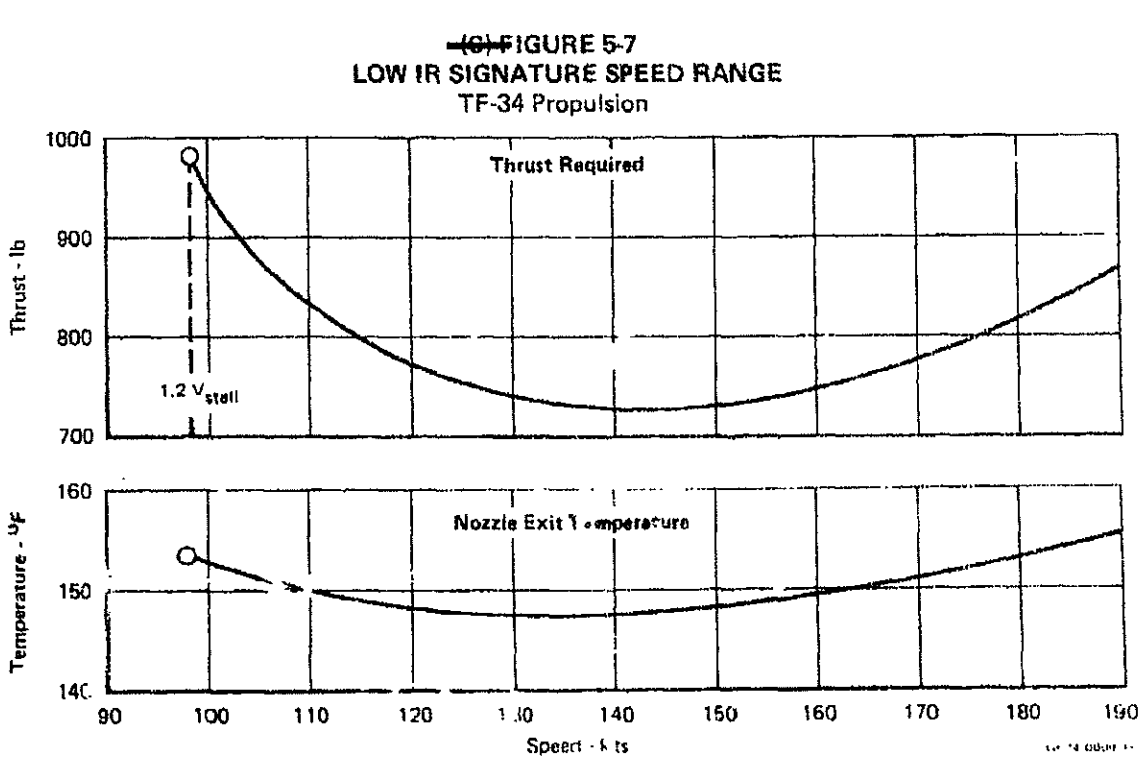

~~(C)~~ FIGURE 5-7
LOW IR SIGNATURE SPEED RANGE
TF-34 Propulsion

6. RADAR CROSS SECTION

(U) The methods for estimating radar cross section (RCS) and the techniques available for reducing RCS were discussed in Section 5 of Reference (1). At that time the RCS of the original quiet attack aircraft, Model 226-454A, was reduced by the use of such techniques as exterior shaping to eliminate straight edges and flat reflecting surfaces, and by the use of radar absorbing material (RAM) in the inlet and exhaust ducts. The RCS of that aircraft was then calculated for 0° elevation viewing angle and all azimuth angles for two Soviet early warning and two SAM fire control radar frequencies. These RCS calculations were made for both horizontal and vertical polarization of the radar.

~~(S)~~ A comparison of Model 226-454A previously shown by Figure 2-1 and the current quiet attack aircraft, Model 226-458 in Figure 2-2, shows practically no difference between them in shape, size, or any of the other factors which affect RCS. Model 226-458 also includes the same interior features that were used on Model 226-454A to reduce RCS, such as RAM in the inlet and exhaust ducts and plug nozzles. Consequently, the RCS values previously established for Model 226-454A are also considered applicable to Model 226-458, and are repeated here as Figures 6-1 through 6-4.

6.1 RADAR CROSS SECTION VALUES

~~(S)~~ Polar plots of the quiet attack aircraft RCS at two early warning radar frequencies are shown by Figures 6-1 and 6-2, and for two SAM fire control frequencies by Figures 6-3 and 6-4. These four figures are extracted from Reference (1). Another plot has been added by Figure 6-5 for RCS at 15.56 GHz, which is the frequency used by the radar fire control for the Soviet ZSU-23 23mm quad AAA guns. All the RCS values in these figures are expressed in dBSM (decibels relative to one square meter of RCS). dBSM is a logarithmic scale where dBSM is equal to 10 times the log to base 10 of the RCS in square meters. Thus for example, dBSM values of -10, 0, 10, 20, 30 correspond to 0.1, 1, 10, 100, 1000 square meters respectively. Figure 6-6 summarizes the aircraft's RCS in square meters for each of the five radar frequencies at the important viewing aspects of head-on, broadside, and tail-on. All of these RCS values are for a clean aircraft without external stores. The effects of stores, such as bombs carried on pylons under the wing, have not been included in this analysis because the unpredictable interactions between the stores and the underside of the wing should be determined by a RCS test program.

6.2 RADAR DETECTION RANGE

~~(S)~~ Although the RCS values shown for the quiet attack aircraft are in most cases orders of magnitude less than those for existing conventional aircraft, it is virtually impossible to reduce RCS to the point where the aircraft cannot be detected. This is illustrated by Figure 6-7, also extracted from Appendix B of Reference (1), where the radar detection range for 85% cumulative probability of detection of the quiet attack aircraft is shown as a function of RCS for the two early warning and the two SAM fire control radars. The aircraft is assumed to be flying at a quiet speed of 112 knots at 2500 ft altitude. Assuming scope detection by radar operators, the KNIFE REST C and the FLAT FACE early warning radars are horizon limited, while the FANSONG E and LOW BLOW fire control radars are limited by the range scale on their scope.

~~SECRET~~
(This Page is CONFIDENTIAL)

~~(C)~~ FIGURE 6-1
RCS AT 0.080 GHz

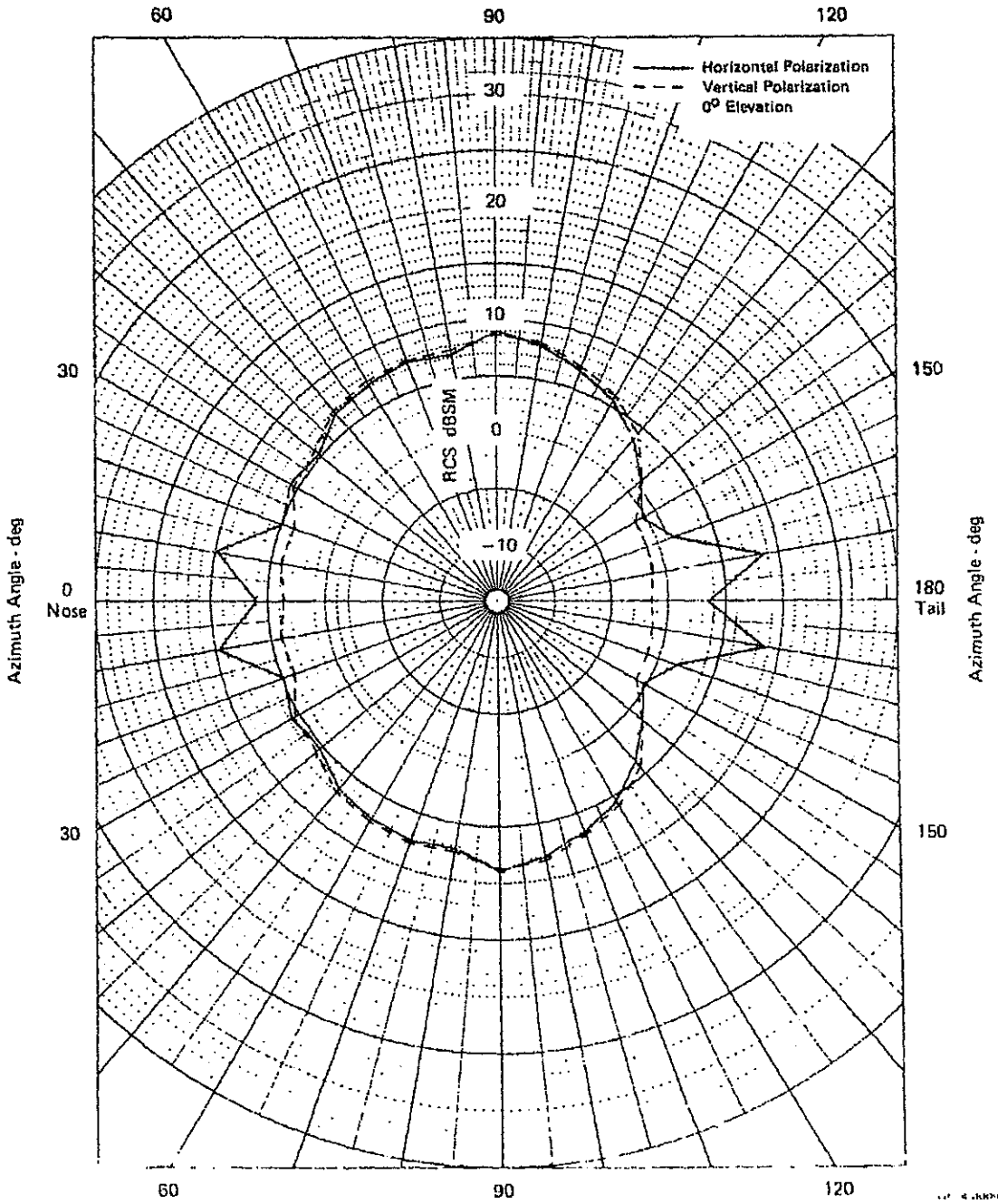

~~(C)~~ FIGURE 6-2
RCS AT 0.815 GHz

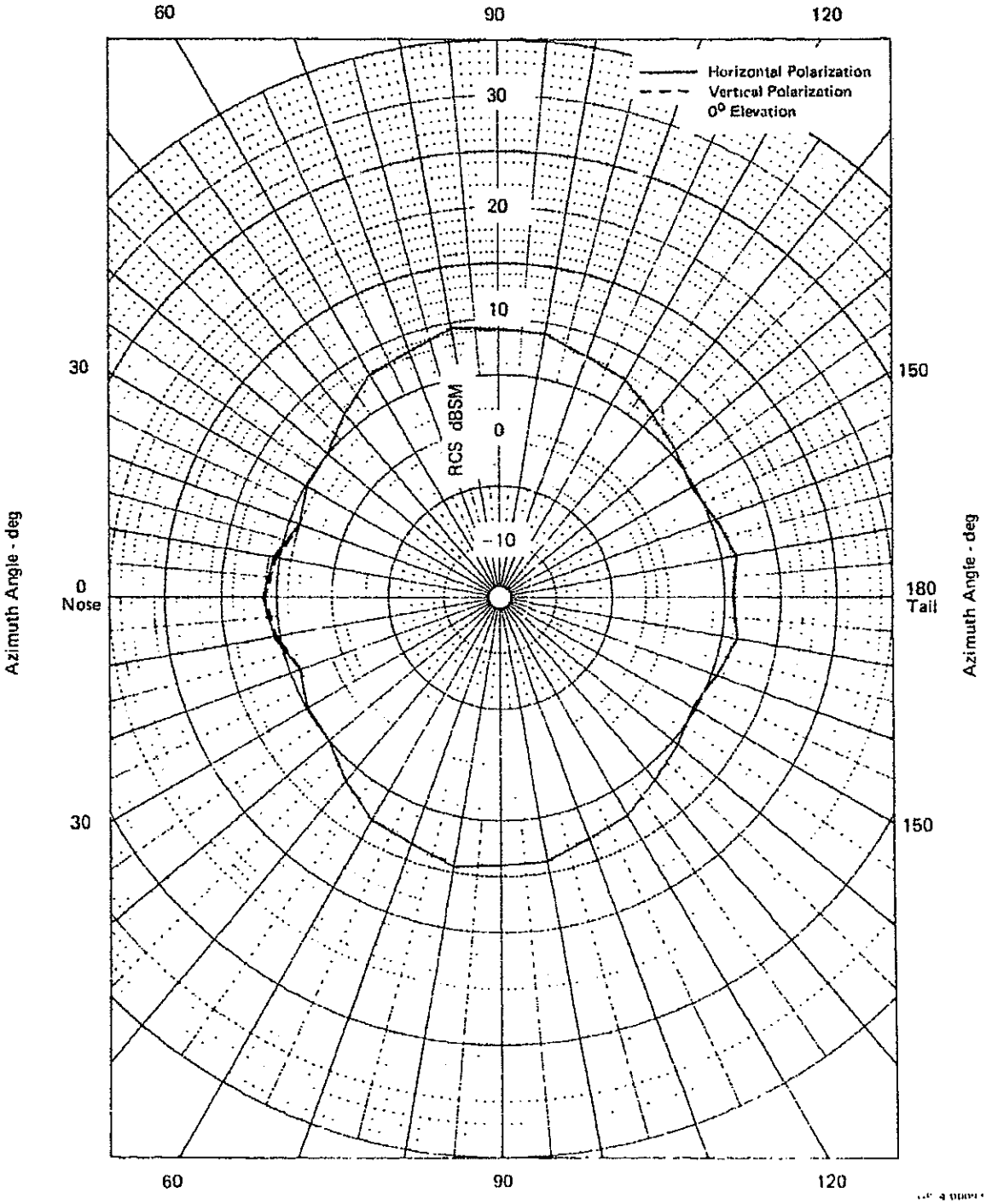

~~(C)~~ FIGURE 6-3
RCS AT 5.0 GHz

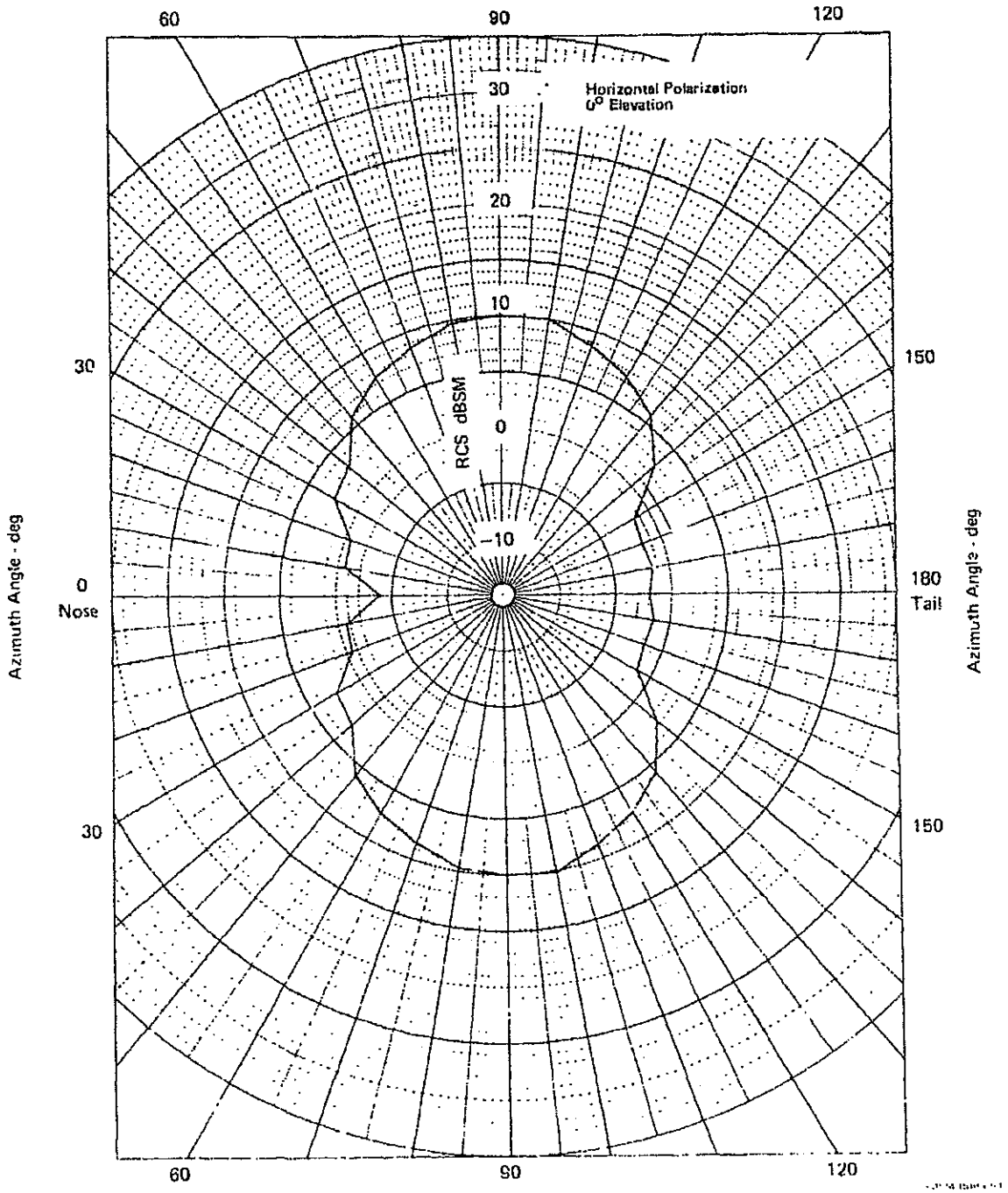

~~(C)~~ FIGURE 6-4
RCS AT 9.2 GHz

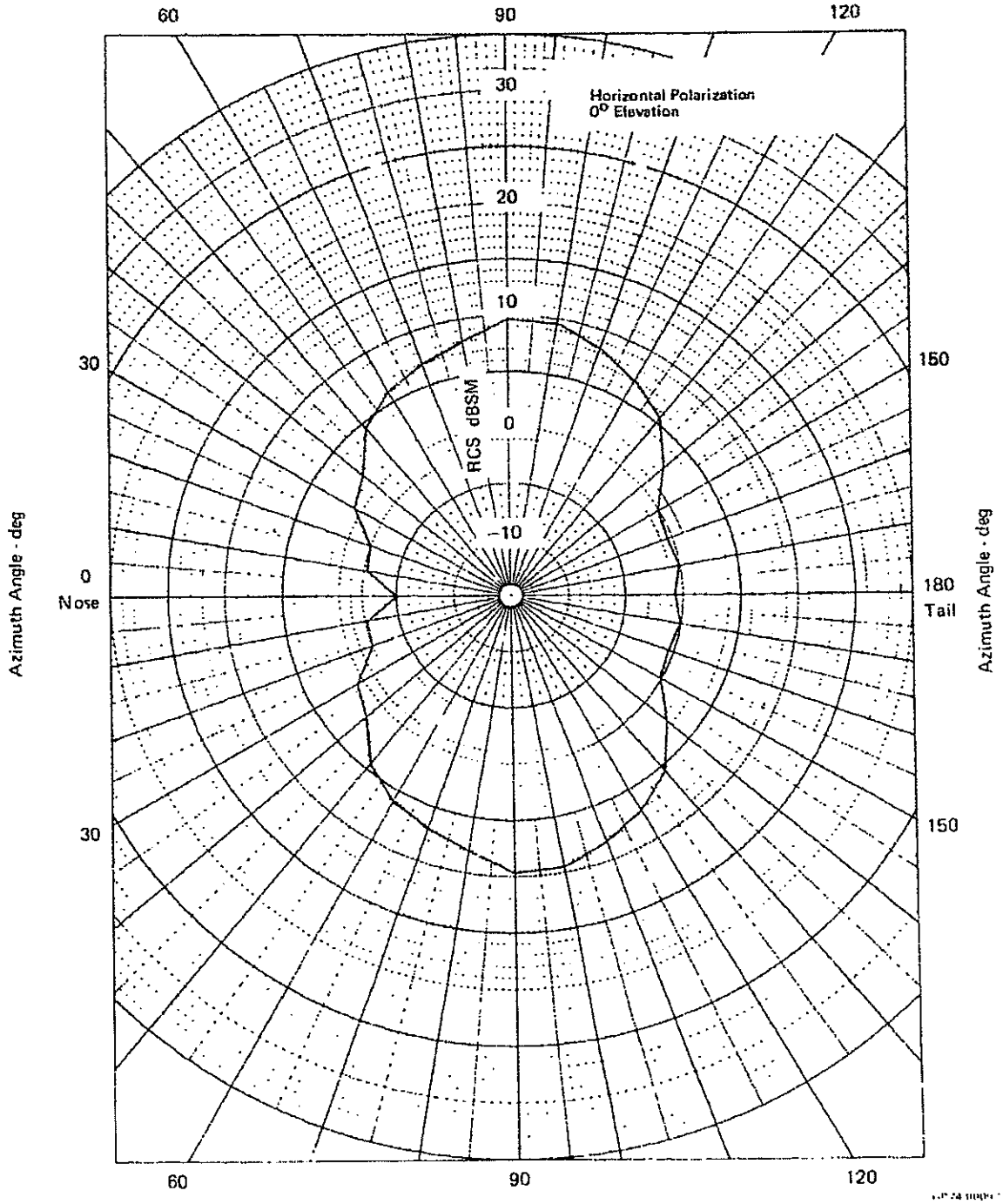

~~(C)~~ FIGURE 6-5
RCS AT 15.56 GHz

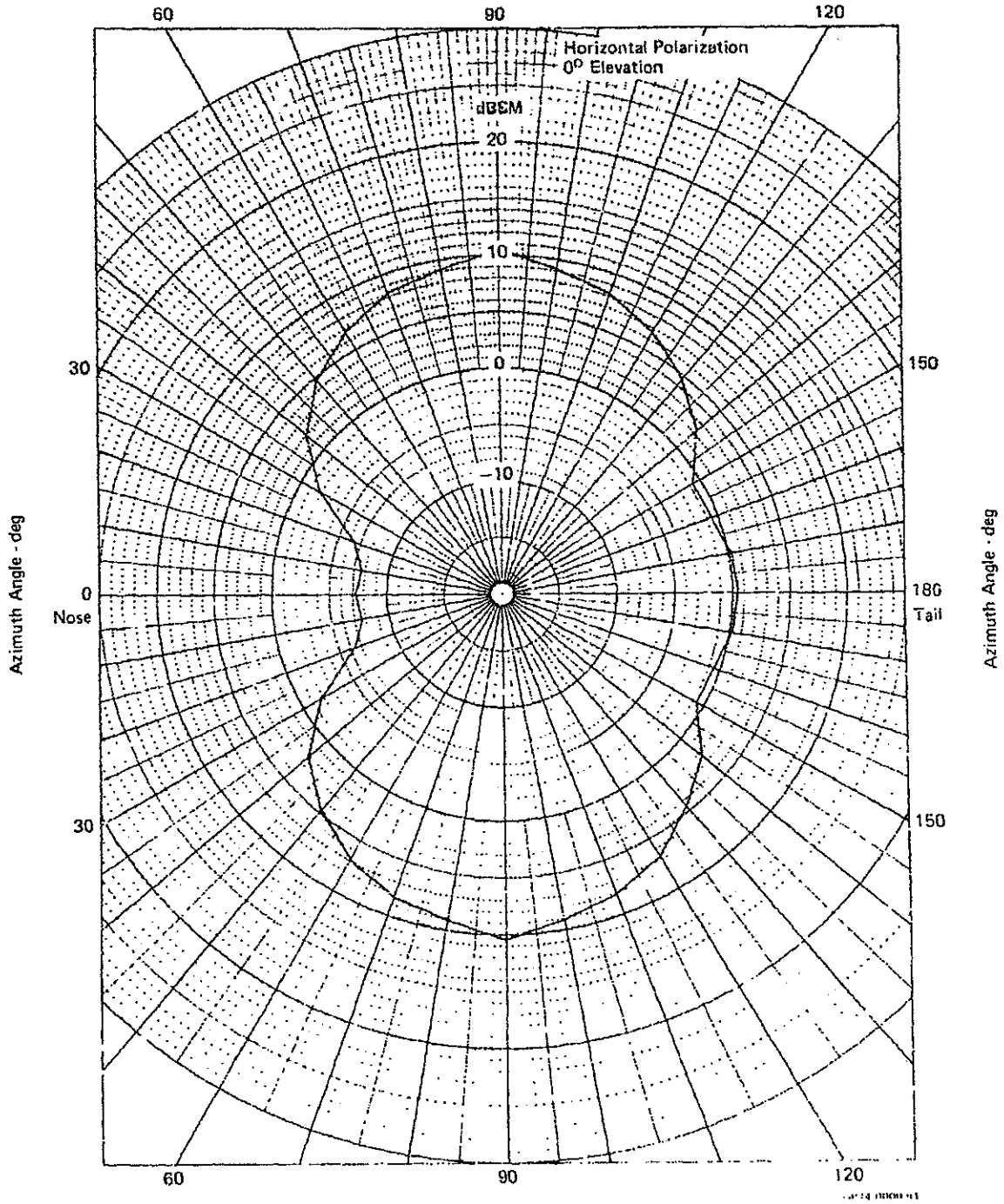

~~(S)~~ FIGURE 6-6
RCS vs FREQUENCY
Square Meters at 0^{o} Elevation, Horizontal Polarization

Threat Radar	Head-On	Broadside	Tail-On
Early Warning			
Knife Rest C (0.08 GHz)	4.0	7.8	2.3
Flat Face (0.815 GHz)	4.1	8.1	3.8
SAM Fire Control			
Fan Song E (5.0 GHz)	0.4	10.3	0.6
Low Blow (9.2 GHz)	0.3	9.3	0.9
AAA Fire Control			
Gun Dish (15.56 GHz)	0.2	10.9	1.1

GP74 0009 58

~~(S)~~ FIGURE 6-7
SOVIET RADAR RANGE vs RADAR CROSS SECTION

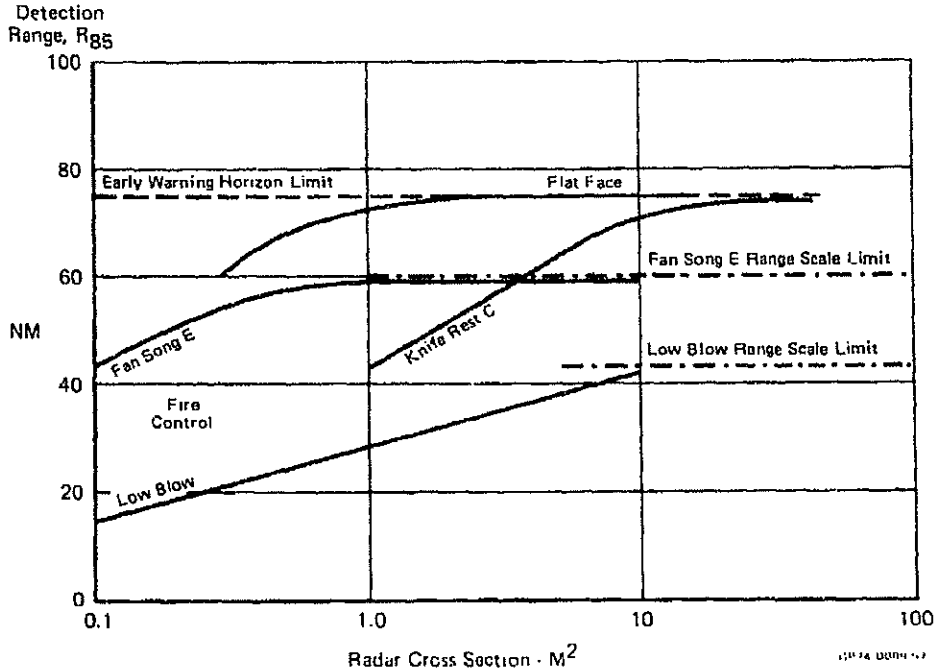

~~(S)~~ As an example, the head-on RCS of the quiet attack aircraft at the X-band radar frequency of 9.2 GHz used for the LOW BLOW is only 0.3 M^2, which is only 1% of the F-4B RCS under the same conditions. However, Figure 6-7 shows that even with this low RCS the aircraft can be detected about 20 nautical miles away. The reason for this discouraging situation is that radar detection varies as the fourth root of RCS. This relationship is illustrated by Figure 6-8 which shows the % reduction in detection range as a function of % reduction of RCS. The small plot on the right side of the figure is a blown-up view of RCS reduction from 95 to 100% to more clearly illustrate the large RCS reductions needed to appreciably reduce detection range. Also illustrated is an example to show the % detection range reduction if RCS is reduced from 81 down to 1 square meter (81 is used for the example because its fourth root is an even number of 3). Even though the RCS reduction is 80 out of 81 square meters, or 98.7%, the range reduction is only 2 out of 3, or 67%. Thus, if the original detection range for an RCS of 81 M^2 were 100 miles, reducing the RCS to 1 M^2 would still leave a detection range of 33 miles.

(U) FIGURE 6-8
DETECTION RANGE vs RADAR CROSS SECTION REDUCTION

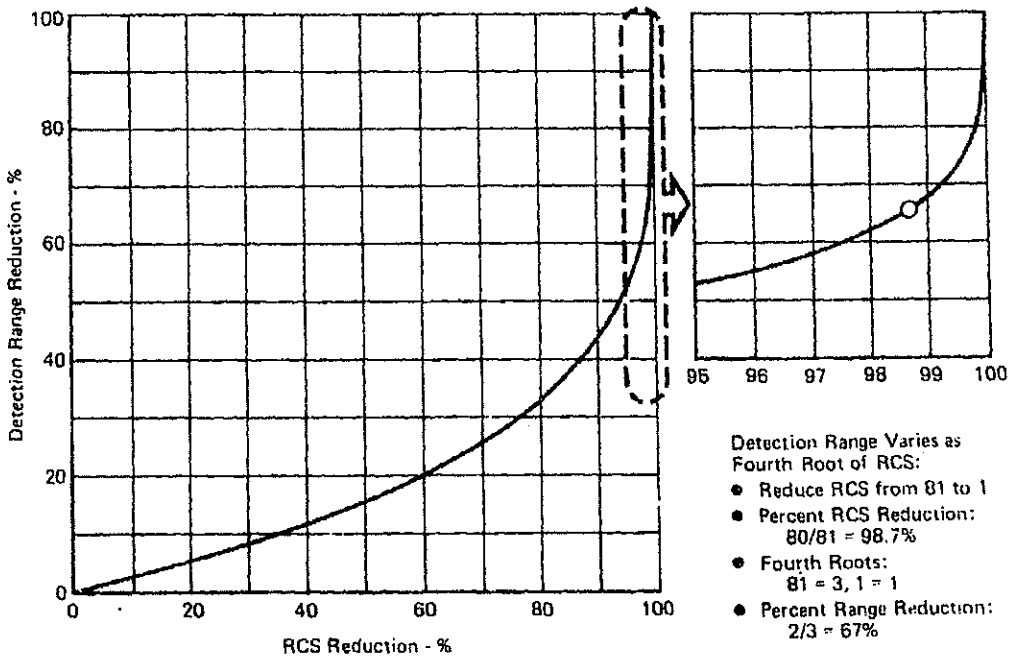

6.3 RCS AND ECM

(U) The real benefit of low RCS comes when electronic countermeasures (ECM) is used by the aircraft to jam the enemy radar. With ECM operating, the erratic or unusual behavior of his radar scope alerts the enemy radar operator that he is being jammed by an unfriendly aircraft in the general direction his radar antenna is pointing. Noise jamming is intended to overwhelm the ground radar operator by filling his radar scope with "snow." Deception jamming is more subtle and is intended to confuse or deceive the radar operator into thinking the aircraft is at a different range or bearing angle from the ground radar than it really is. Obviously, the aircraft is not covert or "quiet" when it is using ECM, so it should only be used after the radar homing and warning system (RHAW) alerts the pilot that he is being painted by radar.

(U) With ECM operating, the aircraft transmits a jamming signal which is received by the enemy radar. At the same time the enemy radar is also receiving the return echo resulting from its own transmitter painting the aircraft. The received jamming signal strength, J, varies as $1/R^2$, where R is the slant range between the radar and the aircraft. The received echo signal strength, S, varies as $1/R^4$ and it also becomes weaker at a given range if RCS is reduced. Effective jamming requires the J/S ratio be greater than some critical value, usually about 10. At long range J/S is greater than 10, but as range decreases S increases at a faster rate than J, and the range at which the critical ratio is reached is called the aircraft self-screening range or the radar burnthrough range. This relationship is illustrated by Figure 6-9 for a given enemy radar operating against a given aircraft having a fixed RCS value and using a given set of ECM equipment. For a J/S ratio of 10, the relative range for self-screening is at $\sqrt{10}$, or 3.16.

(U) From inspection of Figure 6-9, it is evident that increased power of the jamming equipment or reduced RCS would decrease the relative range for self-screening at the same J/S ratio against the same enemy radar. Conversely, the relative range for the same J/S ratio would increase with a higher power enemy radar, or with a larger RCS of the aircraft, or with lower power ECM equipment.

~~(S)~~ The effects of both the aircraft's radar cross-section and ECM jamming power on relative self-screening range against a given enemy radar is illustrated by Figure 6-10. The minimum effective screening range, RS, is proportional to the square root of the radar cross-section, σ, divided by the ECM jamming power, P_j. Thus in general, a decrease in radar cross-section by a factor of 10 will have the same effect on reducing RS as an increase in jamming power by the same factor of 10. As an example, assume we start with a radar cross-section of 1.0 square meters and an average jamming power of 1.0 kilowatts, which would give a relative minimum screening range of 1.0. If we reduce RCS to 0.1 square meters and keep the same jamming power then RS is reduced from 1.0 to $\sqrt{1/10}$, or 0.316. On the other hand if RCS remains at 1.0 square meters, an increase in jamming power from 1.0 to 10 kilowatts would be required to reduce RS to the same value of 0.316. The importance of RCS reduction as a weight saving tool can be appreciated on the basis that the total installed weight of an ECM system is roughly 1000 lb per kilowatt, plus the additional weight of a pod to house the system. For the above example the RCS reduction would mean a weight saving of over 9000 lb in ECM equipment alone, without even considering the additional benefits of not penalizing the aircraft's performance or payload with higher power ECM equipment.

(U) FIGURE 6-9
ECM SELF-SCREENING RANGE

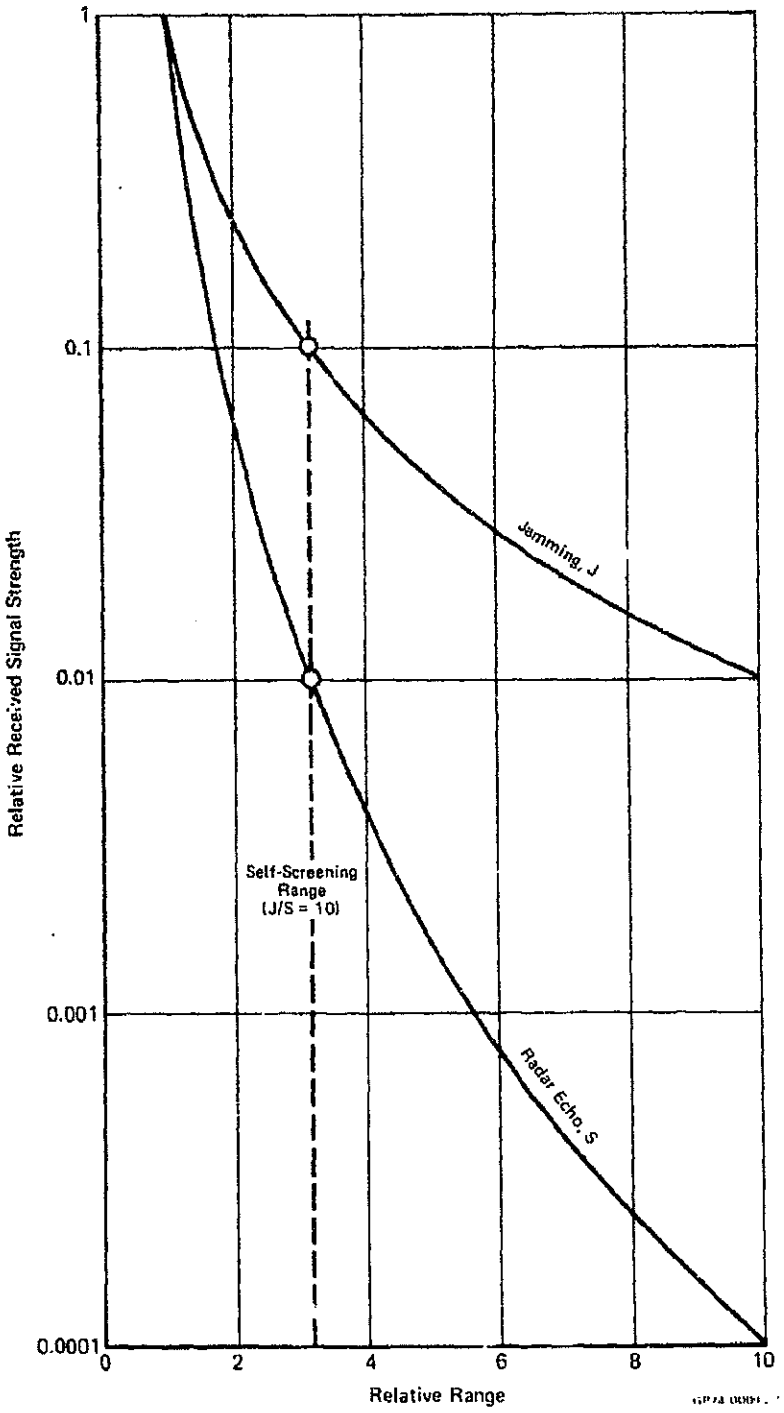

(S) FIGURE 6-10
ECM SCREENING RANGE vs RCS AND JAMMING POWER

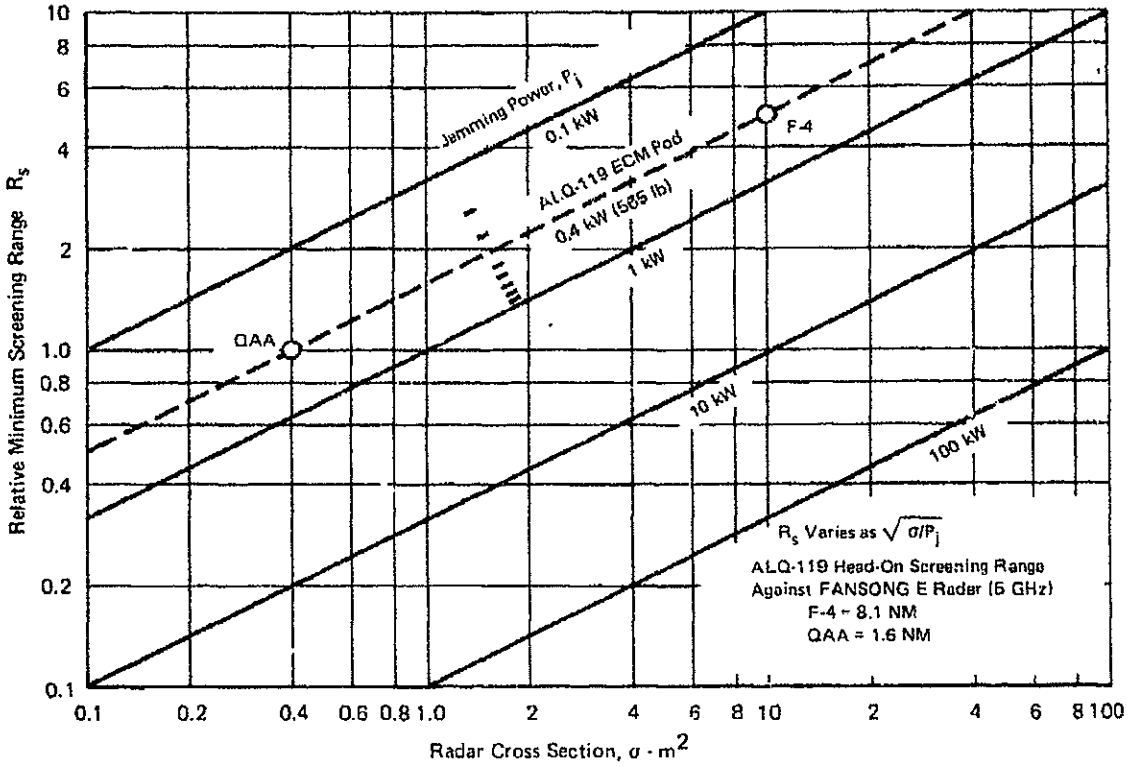

(S) Figure 6-10 also gives a concrete example of the benefits of RCS reduction when a specific ECM pod, the ALQ-119, is used against a specific enemy radar, the FANSONG E. The FANSONG E is the fire control radar for the Soviet SA-2 SAM missile. The ALQ-119 ECM pod, represented by the dashed line in Figure 6-10, is currently used on F-4 aircraft and produces 0.4 kilowatts of jamming power against the FANSONG E radar. The ECM pod weighs 565 lb and is completely self-contained, including an electrical power generating system driven by a ram air turbine. At the FANSONG E frequency of 5 GHz the F-4 RCS for a head-on viewing aspect is 10 square meters, and its self-screening range with ALQ-119 pod is 8.1 nautical miles. At the same frequency and head-on viewing aspect the quiet attack aircraft (QAA) RCS is only 0.4 square meters. Thus at this frequency and with any given jamming power the relative head-on screening range of the F-4 compared to the QAA is a ratio of five to one. Using the ALQ-119 ECM pod against the FANSONG E radar, the actual screening range of the QAA is only one fifth of 8.1, or 1.6 nautical miles. The real significance of this close screening range of 1.6 nautical miles is that it is less than the minimum launch range of about 2 nautical miles for the SA-2 missile. Since the SA-2 can not home on jam and accurate tracking at any usable head-on launch range is denied, the chances of the SA-2 hitting the quiet attack aircraft are low.

(S) The foregoing discussion was concerned only with screening range at a head-on viewing aspect when the aircraft flight path is directly over the enemy radar. However, when there is a group of dispersed SAM sites, each having its own fire control radar, most of them will be viewing the aircraft at other azimuth angles than head-on. Since the aircraft's RCS varies with the azimuth (as well as elevation) viewing angle and the jamming of the ALQ-119 ECM pod is not omni-directional, it becomes important to take a broader look at ECM effectiveness.

(S) The quiet attack aircraft's RCS at 5 GHz frequency was previously shown by Figure 6-3 in dBSM as a function of azimuth viewing angle, for a constant elevation angle of 0° corresponding to flight at low altitude. Each dBSM value can first be converted to RCS in square meters, and then converted again to nautical miles of self-screening range for the quiet attack aircraft with ALQ-119 pod against the FANSONG E radar by using the relationships between RCS and screening range discussed in connection with Figure 6-10. Since the ALQ-119 antennas transmit jamming signals only within a 60° included angle cone forward and aft of the aircraft, the azimuth viewing angles of interest are those within $\pm 30°$ of head-on and tail-on.

(S) Figure 6-11 shows the shaded sectors on the ground forward and aft of the aircraft, in the center of the figure and flying towards the left, within which a FANSONG E radar would be jammed. The cross hatched circle of two mile radius centered about the aircraft represents the ground area in which a SAM site could not attack the aircraft because launch range is less than the minimum required. The clear areas without shading or cross hatching on Figure 6-11 therefore represent possible SAM site locations which could attack the aircraft. However, if we assume the SAM sites are in a group no larger than about a mile wide and the aircraft heads for the center of the group, only those sites near the outer edges of the group would have an opportunity to fire without being jammed or minimum launch range limited. Even so, a SAM site offset 1/2 mile from the oncoming flight path would have this opportunity for only about 0.35 miles of flight path distance, which can be translated into less than 4 seconds firing time available if the aircraft were flying at 350 knots. The opportunity after the aircraft has flown past the site would be even less.

~~(S)~~ FIGURE 6-11
ECM EFFECTIVENESS
ALQ-119 ECM Pod Against Fansong E Radar

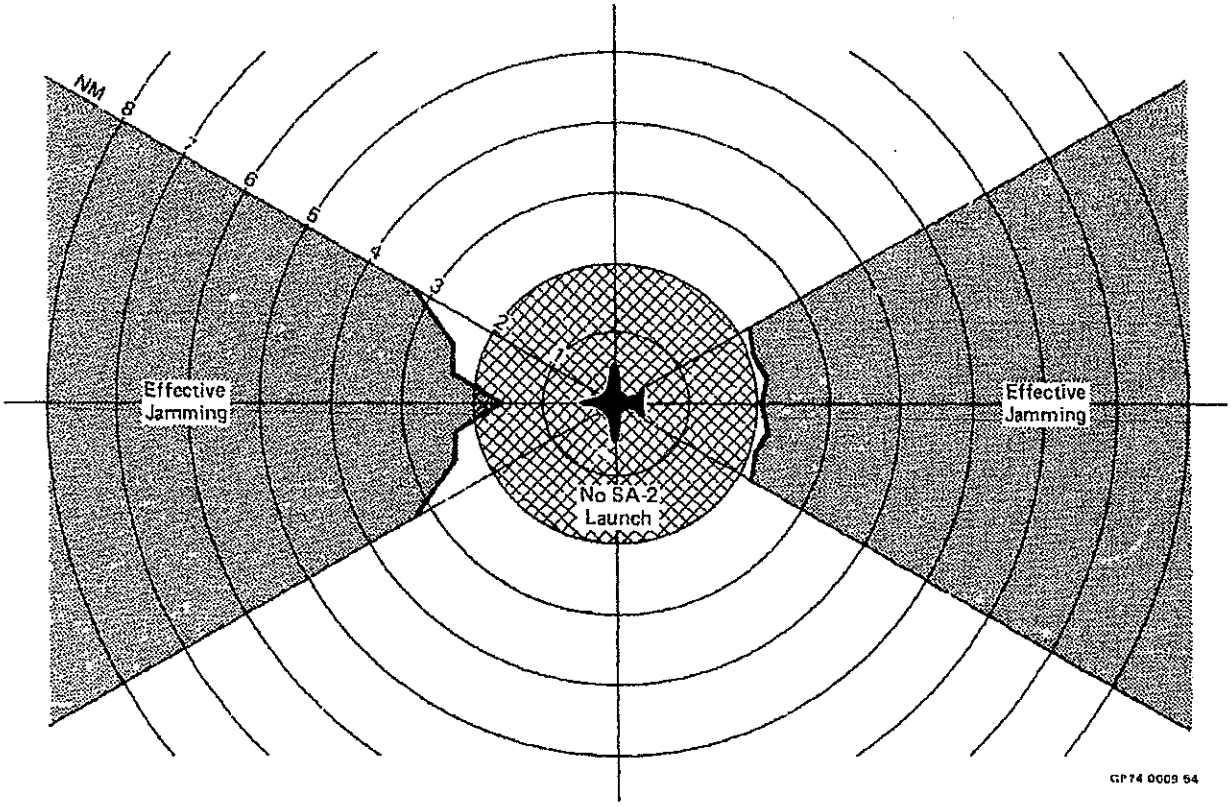

7. VISUAL SIGNATURE

(C) An aircraft almost always appears as a dark object against the background sky. This is true even at night. The aircraft becomes detectable when its contrast against the background sky as seen by an observer exceeds the contrast threshold level of the human eye. The contrast threshold level is a function of the background luminance (sky brightness) and of the angle subtended by the aircraft. The application of light colored paint to the aircraft results in only a small reduction in visual detection range. Further reduction in the detection range can be accomplished by replacing the background luminance blocked by the aircraft with light sources on the aircraft, thus reducing the aircraft/background contrast and the associated range of visual detectability. The resulting system comprises Visual Radiation Source (VRS) camouflage.

(S) The use of VRS camouflage is examined for daylight, moonlight, and starlight conditions. A separate VRS system for starlight could be provided but is not considered necessary. A VRS system has been incorporated for forward viewing aspects for a range of conditions from daylight through twilight to moonlight.

7.1 HISTORY

(C) The problem of reducing daytime visibility of military aircraft has been periodically investigated for at least the past 55 years. For instance, immediately after WW I Mr. Luckiesh, Reference (6), reported that uncamouflaged aircraft appear very dark when viewed against a sky background. He stated that ideally an aircraft would have to be rendered equal in color and brightness to the sky background to prevent visual detection. To achieve this goal Luckiesh investigated possible use of transparent covering materials such as bleached linen, white silk and celluloid for aircraft structure which would allow the sky to be seen through the aircraft, but he concluded that use of such materials was not feasible. He also investigated the use of various colored paints to minimize aircraft detectability and he suggested that white or light blue paints should be used on the opaque under sides of the aircraft. Mr. Luckiesh also theoretically investigated the possibility of illuminating the undersides of the aircraft to match the brightness of the sky to prevent detection. These same general concepts are still being considered.

(S) The VRS camouflage technique was first used during WW II and found to be feasible for daylight operations. The need arose because B-24 bombers with depth charges were unable to attack a surfaced German submarine before it could visually detect the bomber and crash dive to escape. A requirement was then established to equip a B-24 with "YEHUDI lights" to prevent its visual detection until it could approach to within 30 seconds flying time, or about 2 miles, of an observer. Since the aircraft would be headed directly towards the submarine, the minimum amount of electrical power (500 watts) would be required when the lights are designed to focus their beam to the smallest angle consistent with the pitching and yawing of the B-24. Specially made sealed beam automobile headlights were installed in the fuselage nose, in the wing leading edges inboard of the nacelles, and on brackets below the wing outboard of the nacelles. This installation is illustrated by Figures 7-1 and 7-2. The effectiveness of the camouflage is demonstrated by Figure 7-3 showing how the B-24 would appear when viewed head-on at a distance of two miles against a daylight sky background. The left side of the figure shows the aircraft silhouette when the lights are turned off. On the right side of Figure 7-3 the lights are

~~(S)~~ FIGURE 7-1
B-24 BOMBER EQUIPPED WITH YEHUDI LIGHTS

GP74-0009-83

~~(S)~~ FIGURE 7-2
YEHUDI LIGHTS MOUNTED IN B-24 WING LEADING EDGE

FIGURE 7-3
B-24 WITH YEHUDI LIGHTS OFF AND ON
Head-On View at 2 Miles

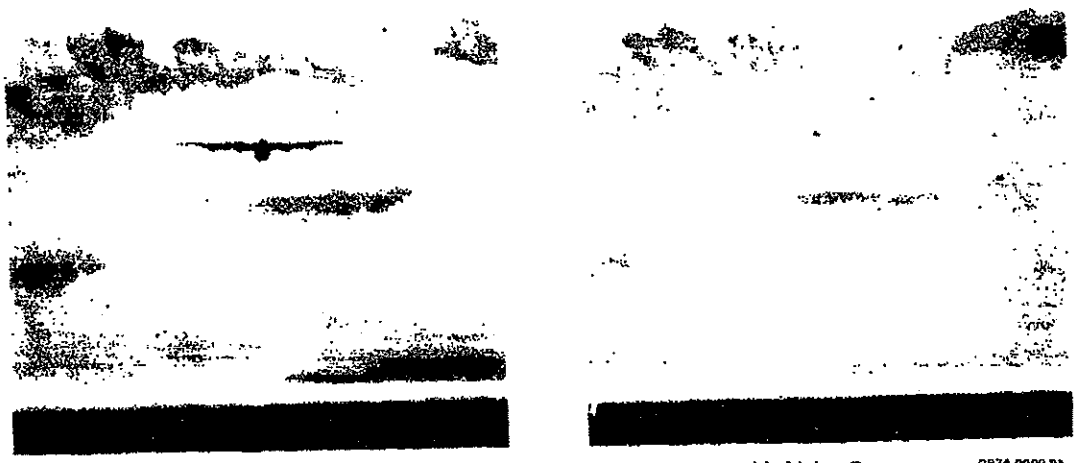

a) Lights Off b) Lights On GP74-0609-28

turned on and the aircraft has virtually disappeared into the sky background. Although prototype systems were flight tested, the VRS systems did not go into production because of the war's ending.

(S) Towards the end of WW II a Grumman TBF torpedo bomber was similarly equipped with lights for daytime visual camouflage. These were placed along the wing leading edges and on brackets attached to the forward part of the engine cowl, Figure 7-4. With the lights on the head-on visual detection range was reduced to less than two miles.

(S) Recent interest in this visual camouflage technique has been rekindled by the high aircraft loss in SEA attributed to visually directed antiaircraft artillery fire. An F-4 with a VRS camouflage suit for daytime protection is currently undergoing tests at Eglin AFB. This daytime system is designed to camouflage the aircraft only in the forward sector at ranges beyond approximately two miles, but even so the input electrical power required for the lights is 14.2 KVA. This illustrates the large amount of electrical power needed to simulate the bright daytime sky. In contrast, only small flashlight bulbs are needed for night camouflage.

7.2 UNCAMOUFLAGED AIRCRAFT DAYLIGHT DETECTION TESTS

(U) A significant consideration that bears on the reduction of aircraft visibility is the range (slant distance) at which a non-camouflaged aircraft can be visually detected. Such data provide important "baseline" information for the evaluation of visibility reduction techniques.

~~(S)~~ FIGURE 7-4
TBF TORPEDO BOMBER EQUIPPED WITH YEHUDI CAMOUFLAGE

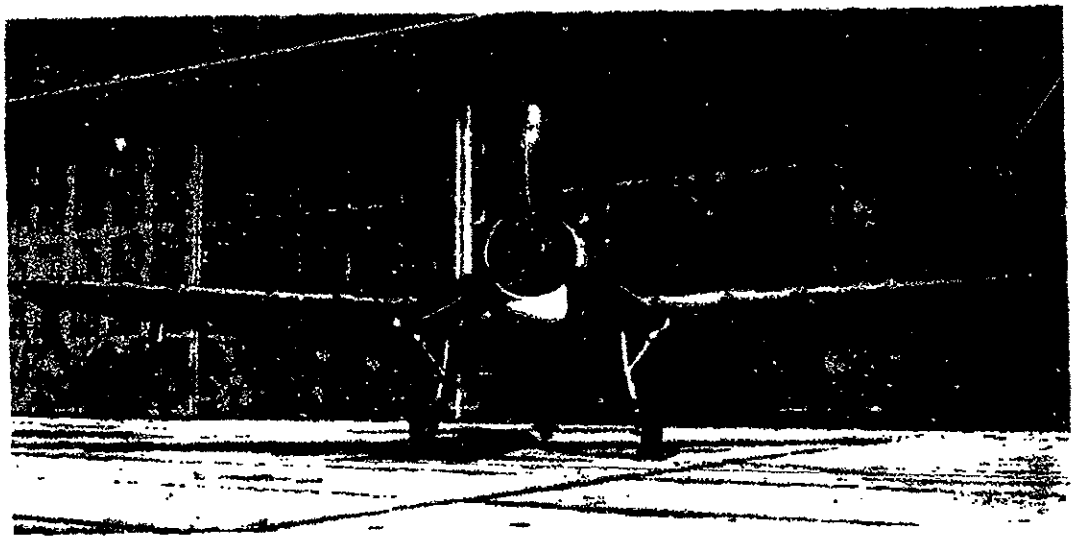

GP74-0009-86

(U) Two experimental studies, References (7) and (8), were performed by the Human Resources Research Office (HumRRO) to determine the perceptual skill of observers in detecting and tracking aircraft by the unaided eye. These studies were conducted under optimum meteorological conditions and involved the acquisition and tracking of non-camouflaged jet and propeller aircraft flying at tactical speeds (400 and 100 knots, respectively) at altitudes between 100 to 300 feet. The observers participating in the study were given approximately five minutes of early warning of the aircraft's approach, and knew the approach direction within a sector of ±15 degrees. The results obtained indicated that if visibility is good, the terrain unobstructed, and observers have early warning they have a 50 percent chance of detecting the aircraft before it reaches a slant range of about 33,000 feet. Visual detection usually preceded auditory detection except when terrain masking was such as to deny unobstructed sight. The aircraft (F-4C, F-100, T-33 and others) employed in these studies have smaller wing spans than the Quiet Attack Aircraft (QAA), which suggests that a QAA might have been detected at greater slant ranges under the same ideal conditions.

(U) Recognition of jet aircraft (as compared to detection) required a larger apparent target for perception of distinctive features. Tentative recognition occurred at approximately 21,000 feet and positive recognition at 10,500 feet. In several of the detection and recognition tests, propeller aircraft were included. In general, acquisition ranges for these aircraft were shorter than those for jets. The detection range associated with the F-4C was somewhat greater than the ranges associated with the other aircraft and was probably attributed to the very noticeable F-4C smoke trail.

(U) Another experimental study, Reference (9), was performed in which the observers were not given early warning and where larger search sectors were involved; i.e., the observers had less accurate knowledge of the aircraft's direction of approach. The same types of jet aircraft were involved as were used in the previously mentioned studies and they were flown at speeds of 400 knots and at altitudes of either 500 or 1,500 feet. The average slant range by which 50 percent of the aircraft were detected was approximately 6,500 feet.

(U) Figure 7-5 summarizes the conditions and approximate slant range results for the studies discussed above. It will be noted that the combination of early warning and small search sector appear to have a highly significant influence on aircraft acquisition range. The limited data available indicates that the detection range of non-camouflaged aircraft may vary by as much as 25,000 feet, depending upon such factors as whether the ground observer knows approximately when and where to expect the aircraft.

(U) FIGURE 7-5
AVERAGE RANGES OF AIRCRAFT DETECTION

Aircraft Type	Speed (kts)	Altitude (ft)	Search Sector Size (deg)	Early Warning	Average Detection Range (ft)*
Propeller and Jet Aircraft	100 and 400	100 to 300	±15	Up to 5 min	33,000
Jet Fighters	400	500 and 1,500	45 and 90 180 and 360	None	7,000 5,500

*Approximate slant ranges for a detection probability of 0.5 in daylight.

OP74 0009 87

~~(C)~~ For operational conditions in which the detection ranges are 25,000 to 35,000 feet, an aircraft will generally appear as a dark unresolved spot. Mottled camouflage paints (consisting of different shaded blotches) or illusory patterns that depend upon visual resolution will not be effective under such conditions. Instead, techniques that focus on reducing the target-background contrast must be employed. Two such techniques would be the use of paint which minimizes aircraft/sky background contrast and use of VRS camouflage.

7.3 PAINT CAMOUFLAGE

(U) Aircraft color has not been generally recognized as being a significant feature in determining the ranges at which ground based personnel can visually detect incoming aircraft. Only recently have tests suggested that color may actually have some significance after all in daylight detection.

~~(C)~~ According to Reference (10), a fleet evaluation of green paint was conducted by the Navy in 1966 and indicated that aircraft camouflaged by green paint were more easily detected than standard gray-white airplanes under most conditions. Reference (10) also describes experiments in which F-4 aircraft were painted with either a combination of low gloss gray and white paints or with low gloss or high

gloss gray paint, and the corresponding aircraft detection ranges were experimentally determined in runs against Soviet Bloc FIRECAN, an optical director and a 57 millimeter anti-aircraft gun system, on the EWTES range at the Naval Weapons Center at China Lake. The aircraft made both level passes at 1,500 feet altitude and 20 degree dives from an initial altitude of 22,500 feet. The high gloss gray aircraft produced somewhat lower detection ranges to the observers using optical aids but was reported not to affect the range at which unaided visual detection occurred.

~~(C)~~ Reference (11) states that the Navy Operational Test and Evaluation Force conducted a test where A-4C and A-4E aircraft were painted with either standard gull gray, light sky blue or green paint, or they were painted with a combination of tan and black paint. They reported that the dark colors made the aircraft easiest to detect against daytime sky backgrounds and that the light blue aircraft were most difficult to see.

~~(C)~~ The latest reported study, Reference (11), employed F-4s which were either painted with a light blue Desthal gloss enamel or with conventional Navy gray paint. The aircraft made dives from 10,000 feet at the observer locations, with 4,500 foot altitude pull-outs employing minimum afterburner so as to eliminate the smoke trail. The dives were initiated at a ground range of 12 nm from the observers, who were told when and where to look for the aircraft. The pull-out speed was 450 knots. The average slant range for unaided visual detection was 11,900 feet for the blue F-4s and 16,300 feet for the gray aircraft. The visible cross-section of the aircraft is minimized during this diving approach and it is less than it would be on high level aircraft passes.

~~(C)~~ It also is reported in Reference (11) that E.G.&G. Corporation at Santa Barbara, California has compared blue, gray and white aircraft and has concluded that white is the most difficult to detect.

~~(C)~~ In summary there seems to be no conclusive evidence to date that the color of paint used on an aircraft will substantially affect the range where unaided daylight visual detection occurs although there are indications that light colored, glossy paints may produce somewhat shorter detection ranges than darker paints. Based on the information presently available, it appears that an appropriate choice for the QAA would be a light blue gloss paint. Assuming unobstructed vision and advance warning, the QAA, if so painted, will normally be detected at ranges equal to or greater than 11,900 feet, since smaller wing span F-4 aircraft moving at high speeds have been detected at this range when diving at the observer to minimize their visible cross-section. The QAA should present a somewhat larger visual stimulus because of its longer wing span and it probably will be flying at slower speeds than the F-4s, thereby increasing the probability of earlier detection.

~~(C)~~ At night, color appears to have little if any effect on detection, except for the case where the aircraft is caught in the glare of a searchlight. In that event a dull black paint, as used by WW II night fighters, is still probably the best choice.

7.4 VRS CAMOUFLAGE FACTORS

(C) This section is devoted to a discussion of the various factors involved in VRS camouflage, which includes the luminance or brightness of the sky, visual contrast threshold levels, atmospheric contrast transmittance, visual point sources, and visual acuity. The level of sky luminance determines the total amount of VRS light required for camouflage and is needed to define visual contrast threshold. The visual contrast threshold and atmospheric contrast transmittance are used to determine how closely the aircraft luminance has to match sky background luminance at various ranges such that the aircraft will not be visually detected. The discussion on point sources determines the minimum apparent brightness of a point source of light which could be seen by a distant observer. The brightness of an individual VRS light must be less than the calculated minimum apparent brightness or the aircraft's position will be revealed by the observers detection of the point source. Visual acuity must be considered in defining required VRS light spacing.

7.4.1 SKY LUMINANCE - (U) The discussion of sky luminance can best be divided into moonless and moonlit/daylight categories since daylight sky luminance data can also be scaled to provide moonlit data. The sky luminance for each of these conditions is likewise influenced by the degree of existing cloud cover.

Moonless Night - (U) On moonless nights when the sun is at least 18 degrees below the celestial horizon, the faint diffused radiation which reaches the earth's surface is airglow caused primarily by the radiation of atoms and molecules in the upper atmosphere (80 to 120 kilometers in altitude). These atoms and molecules are excited by direct solar radiation. No direct radiation from the sun or moon reaches the earth's surface on a moonless night. Secondary and weaker sources of night sky illumination include stellar (star) radiation, nebular (cloud-like patches of light) radiation, zodiacal (planet) radiation and in some cases, at higher latitude, auroral (e.g., northern lights) radiation.

(U) A literature search was conducted to locate measured nighttime sky luminance data. The few reports found, References (12), (13), and (14), which were published prior to 1968 contained data which were sketchy but generally indicated that the luminance of the starlit night sky near the horizon usually has values lying somewhere between 2×10^{-5} candles/ft^2 and 6×10^{-4} candles/ft^2. The luminance usually peaks at elevation angles approximately 15 degrees above the horizon and decreases from that value as the angle of sight approaches the horizon.

(U) A comprehensive report, Reference (15), written in 1968 by the Scripps Institute of Oceanography of the University of San Diego, contains information on a detailed measurement program of night sky luminance. These measurements were made under contract to the Air Force Avionics Laboratory. Portions of the measurements, which are of concern here, were made from a specially equipped C-130 aircraft during two field trips to Thailand. The first trip was made during September and October of 1968, the wet monsoon season, and the second trip was made during February, March and April 1969, the dry season. During both trips data were recorded over the Khorat Plateau forested area, over cultivated areas of the Chao Phraya River delta, over the gulf of Siam, and over land areas adjacent to the Gulf in the vicinity of Rayong.

(U) Scripps Institute's flights numbered 82I, 87, 88I, 88II, 89, 101 and 102 were essentially made during moonless conditions and are the ones of interest to this discussion. The following illustrations are developed based on the data from these flights.

(U) Figure 7-6 presents the average sky radiance measured at 1000 ft. altitude on each of the above flights as a function of zenith angle (0^o directly overhead). Radiance is the flux density of radiant energy per unit solid angle per unit surface area, and has the units of watts per solid angle per square meter per micron of wavelength. (While radiance is the measure of total energy, luminance is the measure of visual energy). The phototube used in these tests approximates the spectral response characteristics of the human eye. The data in Figure 7-6, therefore, can be used as relative sky luminance characteristics. The curves in Figure 7-6 are reported to be typical for each flight and varied very little for altitudes between 0 and 5000 ft. With the exception of Flight 82I, which shows the effect of the moon behind overcast at a zenith angle of 75^o, the data shows that the variation of sky radiance, and hence sky luminance, varies over a very small range as the zenith angle is varied. The data in Figure 7-6, including that for Flight 82I, was averaged over all azimuthal angles.

(U) The curves for Flights 88I and 89 were taken under thick overcast conditions and show increasing values of radiance as the zenith angle approaches 90^o. This is largely due to the reflection of ground sources which collectively tend to create a peak luminance at a 90^o zenith. The general shape of the remaining curves show a rise in sky radiance as the zenith angle increased from 0^o to 70^o followed by a drop as the zenith angle increases further. The most significant observation is that radiance or luminance levels for the moonless night sky vary only slightly with zenith angle and can usually be represented by the measured radiance value at an 80^o zenith angle with less than 25% error for other angles. This accuracy will be adequate for later VRS calculations.

(U) Figure 7-7 is a plot of the measured vertical transmission coefficients; i.e., the relative amount of light which when transmitted directly downward reaches the ground without being scattered or absorbed, as a function of altitude for five of the flights. The transmission coefficient, T, of a given path through the atmosphere for a given wavelength is

$$T = e^{-\tau}$$

where

$$\tau = \int \sigma(L)\, dL$$

where $\sigma(L)$ is the atmospheric extinction coefficient σ at some distance, L, along the path and dL is differential path length. Figure 7-8 gives the average atmospheric extinction coefficient corresponding to the data in Figure 7-7 for the 5000 foot altitude range. Figure 7-9 indicates typical values of atmospheric extinction coefficients for various atmospheric conditions. It can be seen that all five flights were made during very clear or exceptionally clear atmospheric conditions.

(U) The ratio between the radiation flux moving through the atmosphere in the upward direction and that moving downward, the albedo, was also measured on five of the flights and is plotted as a function of altitude in Figure 7-10. These are used

(U) FIGURE 7-6
STARLIGHT AND OVERCAST NIGHT SKY RADIANCE

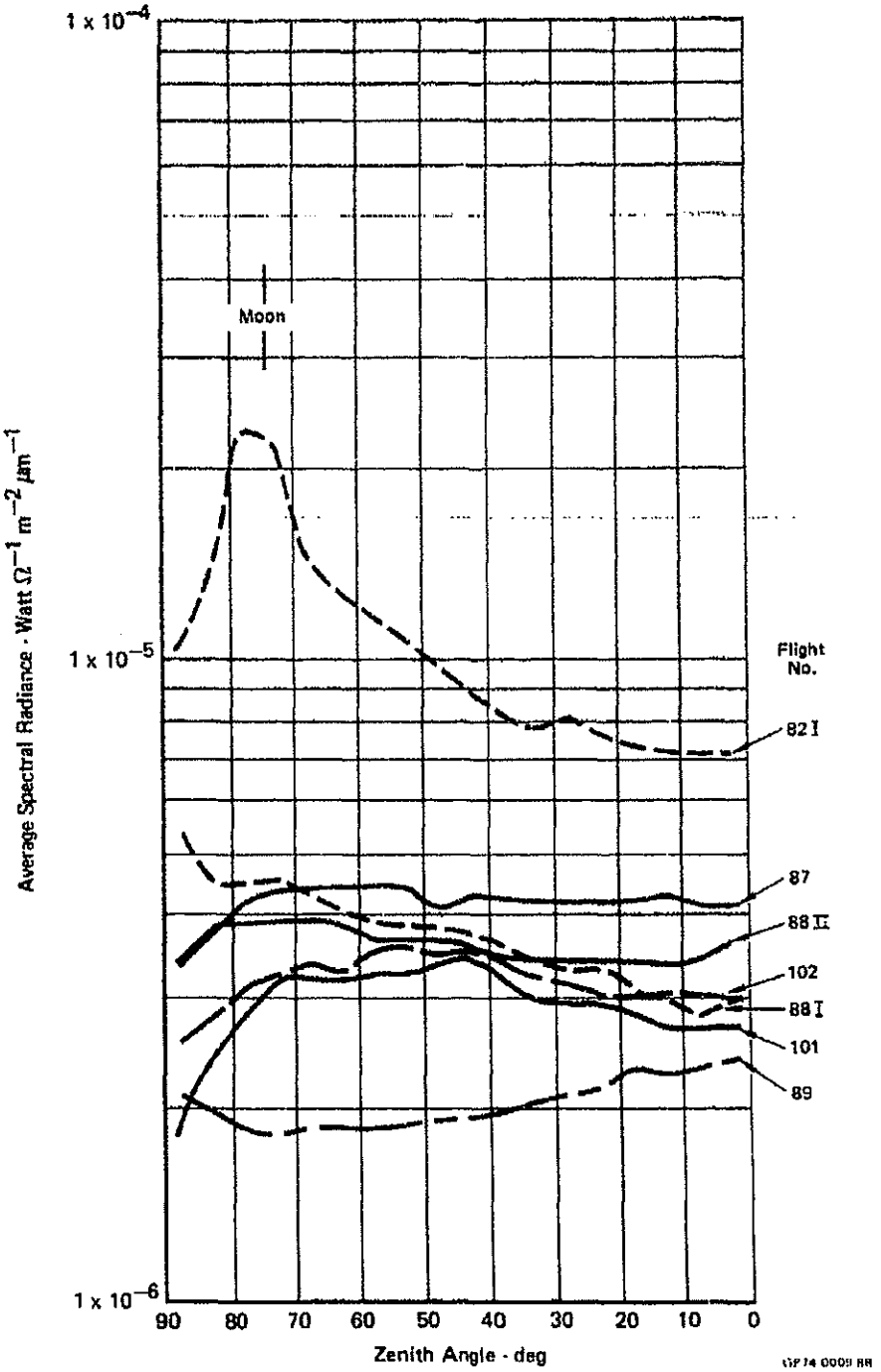

(U) FIGURE 7-7
MEASURED VERTICAL TRANSMISSION COEFFICIENT

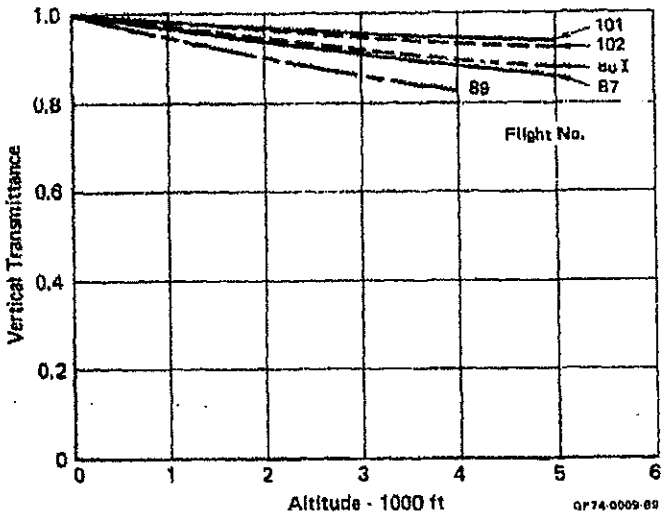

(U) FIGURE 7-8
AVERAGE ATMOSPHERIC EXTINCTION COEFFICIENTS

Flight No.	Transmittance (Ground Level to 5000 ft)	Extinction Coefficient (ft^{-1})
1	0.937	1.30×10^{-5}
2 Wet Season	0.928	1.49×10^{-5}
88 I	0.877	2.62×10^{-5}
87 Dry Season	0.859	3.04×10^{-5}
89	0.800	4.46×10^{-5}

$T = \exp(-\sigma L)$

GP74-0009-90

(U) FIGURE 7-9
TYPICAL VALUES OF ATMOSPHERIC EXTINCTION COEFFICIENT

Atmospheric Conditions	Visibility Range (NM)	σ (1/ft)
Exceptionally Clear	50	1.31×10^{-5}
	20	3.12×10^{-5}
Very Clear	12	5.25×10^{-5}
	10	6.40×10^{-5}
Clear	6.2	1.03×10^{-4}
	5.0	1.28×10^{-4}
Light Haze	2.5	2.62×10^{-4}
	2.0	3.20×10^{-4}
Haze	1.2	5.25×10^{-4}
	1.0	6.40×10^{-4}
Thin Fog	0.62	1.03×10^{-3}
Light Fog	0.3	2.13×10^{-3}
Moderate Fog	0.12	5.24×10^{-3}
Very Light Rain (0.06 in./hr)		$*5.07 \times 10^{-5}$
Light Rain (0.12 in./hr)		$*1.03 \times 10^{-4}$
Moderate Rain (0.27 in./hr)		$*1.56 \times 10^{-4}$

*Addition to 0 above.

GP74 0009-91

(U) FIGURE 7-10
RATIO BETWEEN RADIATION FLUX MOVING UPWARD AND DOWNWARD

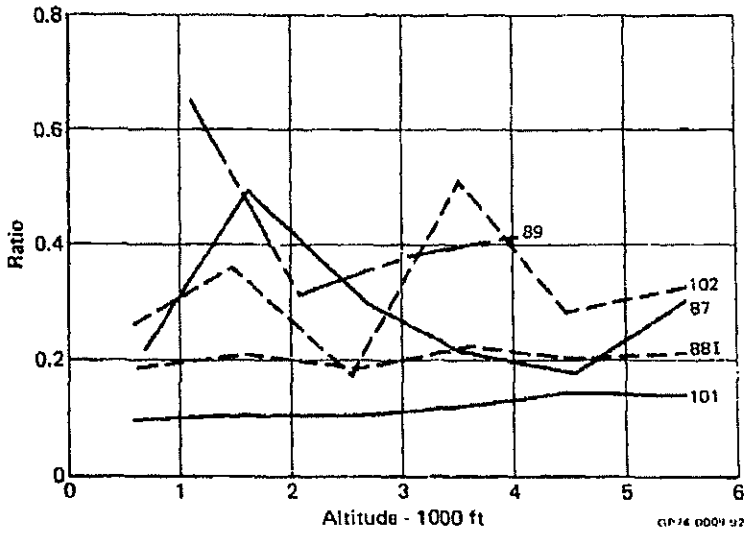

GP74 0009-92

later to determine the maximum range at which an uncamouflaged aircraft can be visually detected. The erratic nature of the curves for Flights 87, 89 and 102 was caused by ground light. The curves for Flights 101 and 881 are probably representative of the data if such extraneous sources had not been present.

Moonlit and Daylight Skies - (U) When the moon is nearly full and high in the sky, it is the dominate source of night sky luminance, thus paralleling the role of the sun during daytime. Therefore, when moonlit sky luminance data is unavailable it is assumed that daytime sky luminance data can be scaled and used. An example, Reference (16), of such daytime data was measured over Florida in 1956. Daytime sky luminance contours (in candles per square foot) for a 2000 ft. altitude are plotted in Figure 7-11 using this data. The center point of the figure represents the 0^{o} zenith angle while the outer circle represents the 90^{o} horizon. The sky luminance is seen to increase as the horizon is approached, i.e., as the zenith angle approaches 90^{o}, except at azimuth angles close to the sun. In this region the sky luminance increases as the zenith angle approaches that of the sun. The scaling factor of this data for nighttime use corresponds to the ratio between the daytime and nighttime ground level illumination. Figure 7-12, based on Brown's data in Reference (17) can be used to determine the required scaling factor. Observe that the nighttime/daytime illumination ratio corresponding to a full moon and an unobscured sun is approximately 3×10^{-6}. Figure 7-11 scaled by 3×10^{-6} is plotted as Figure 7-13 and thus represents the sky luminance data which would be measured on a clear night with a full moon at a zenith angle of 41.5^{o}. Although sky luminance for moonlit skies is a function of azimuth angle, it is nearly constant over 270^{o}. Moonlit sky luminance appears to continuously increase with increasing zenith angle, and the magnitude of luminance, except in the direction of the moon, is approximately 100 times greater than the corresponding luminance of moonless night skies.

7.4.2 HUMAN EYE RESPONSE - (U) Since the human eye is the detector which can sense the presence of the QAA, it is in order to briefly describe some of its characteristics. In the human eye, the retina is the actual organ within which the stimulation by physical light takes place and where the sensation of vision is initiated. Near the surface of the retina is a layer of rod-like and cone-like cells within which the first steps of the physiological process of light reception takes place. It is believed that the rods function principally in weak light, such as exists during twilight; they mediate to so-called scotopic vision that responds to weak stimuli but is not capable of distinguishing colors. The cones in turn function in bright light and respond specifically to certain wavelengths of the spectrum (i.e., to colors) and besides, serve the perception of much finer details (acuity).

(U) The cones are most dense in the foveal (the center part of the retina) and the density decreases rapidly with distance outward from the retina center. Vision attributed to the cones is called foveal vision. The excitation of the foveal corresponds to vision of objects positioned within approximately 2^{o} of the eye's optical axis. In contrast, the density of the rods at first increase with distance outward from the center of the retina, peaks at positions corresponding to vision of objects positioned at approximately 20^{o} from the optical axis, and decreases thereafter with distance. There are essentially no rods located at the center of the retina. Vision attributed to rods is called parafoveal vision.

(U) FIGURE 7-11
DAYTIME SKY BRIGHTNESS

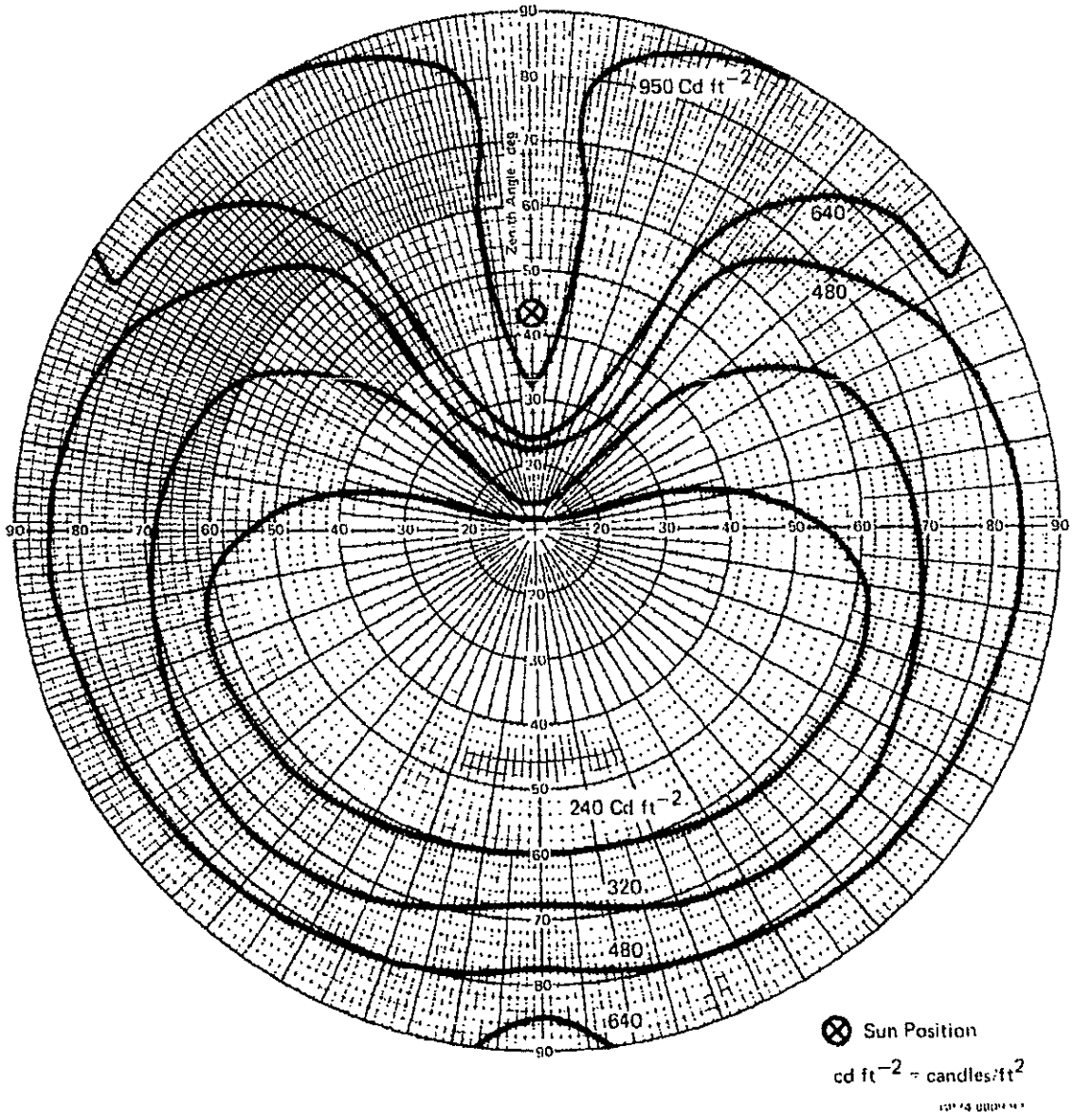

(U) FIGURE 7-12
GROUND LEVEL ILLUMINATION

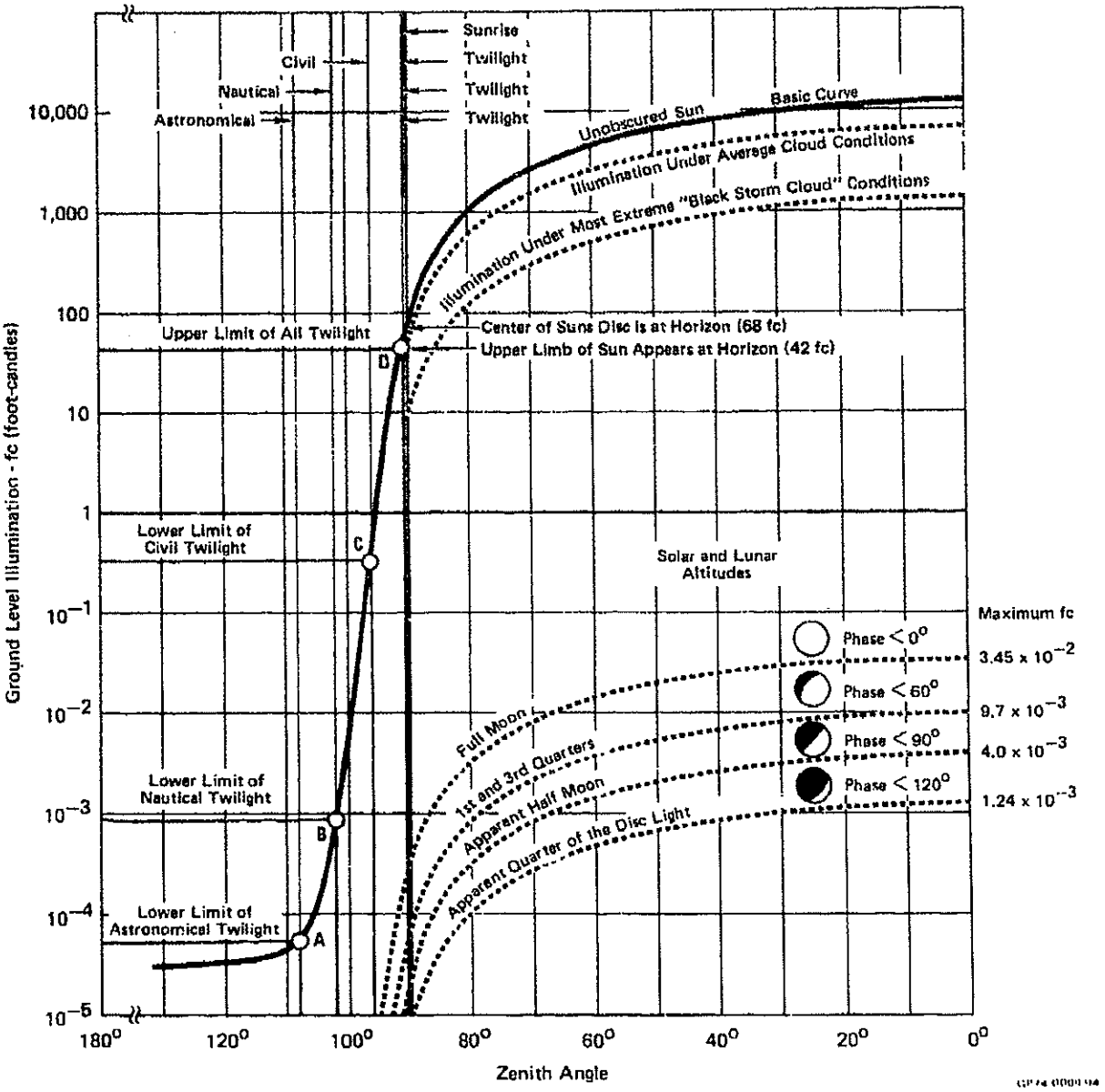

(U) FIGURE 7-13
MOONLIT SKY BRIGHTNESS

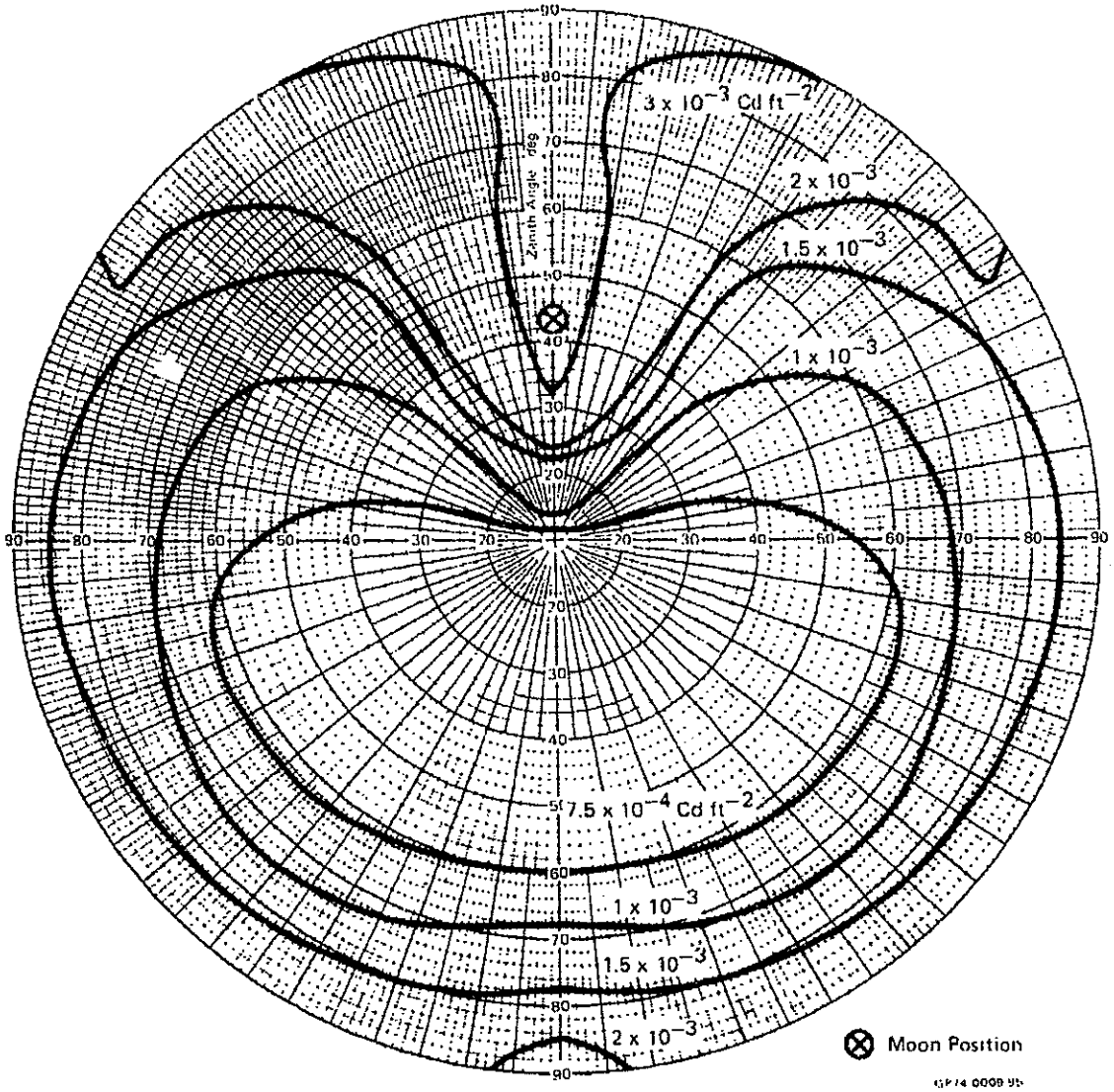

(U) Maximum object detectability occurs within the rod-free central fovea under conditions of high-level (photopic) daytime adaptation conditions, but at scotopic levels in darkness the detectability is virtually uniform throughout the region within 20° of the fovea, with resolution diminishing toward the periphery. For the scotopic adaptation the sensitivity of the rod-free central fovea effectively vanishes and the greatest sensitivity occurs in the ring-shaped parafovea where the population of rod receptors is dense.

(U) The transition between the photopic and scotopic regions occurs at a background illumination in the vicinity of 10^{-3} to 10^{-4} footcandles. Therefore, for daylight and moonlit conditions with quarter-moon or greater brightness the photopic adaptation is applicable and for moonless conditions the scotopic adaptation is applicable.

7.4.3 VISUAL CONTRAST THRESHOLD LEVELS - (U) Visual contrast threshold levels were experimentally determined during WW II by H. R. Blackwell's group at the L. C. Tiffany Institute, Reference (18). Experiments were conducted which employed the projection of a spot of light on a white screen for a short period of time. Observers scanned the screen and indicated if and where they believed the stimulus had occurred.

(U) The resulting data, presented in Figure 7-14, is accepted as representing the 50% probability of detecting a visual stimulus given an unlimited observation time and similar experimental conditions. The discontinuities in the curves at about 2×10^{-4} candles/ft^2 marks the transition from photopic to scotopic vision. Observe that the visual contrast threshold associated with night sky luminance levels of 5×10^{-4} candles/ft^2 may be up to 1000 times (depending on stimulus size) the threshold contrast levels associated with typical daytime skies luminance levels of 1000 candles/ft^2.

(U) FIGURE 7-14
THRESHOLD CONTRAST FOR DIFFERENT OBJECT SIZES AND BACKGROUND LUMINANCE LEVELS

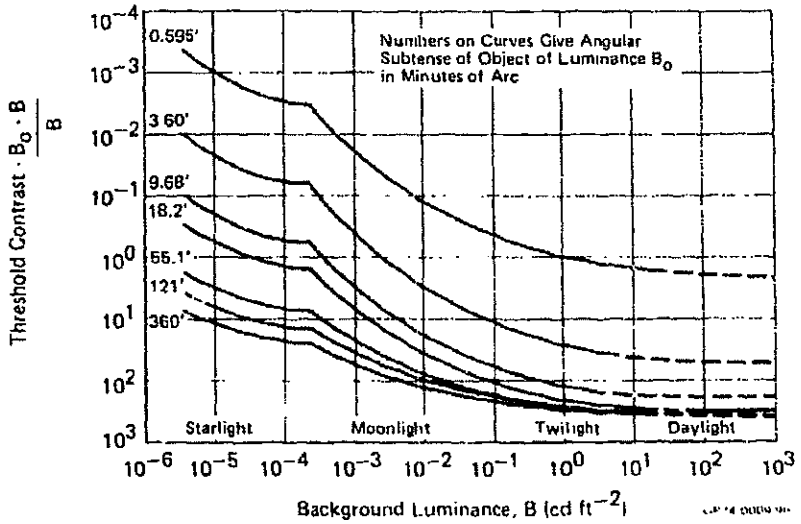

MCDONNELL AIRCRAFT COMPANY UNCLASSIFIED

(U) Figure 7-15 gives a contrast threshold adjustment factor used to correct the data in Figure 7-14 to other values of probability of detection. Observe that a four-to-one variation in contrast corresponds very nearly to a variation in probability of detection from 10% to 95%.

(U) FIGURE 7-15
CONTRAST THRESHOLD ADJUSTMENT FACTOR

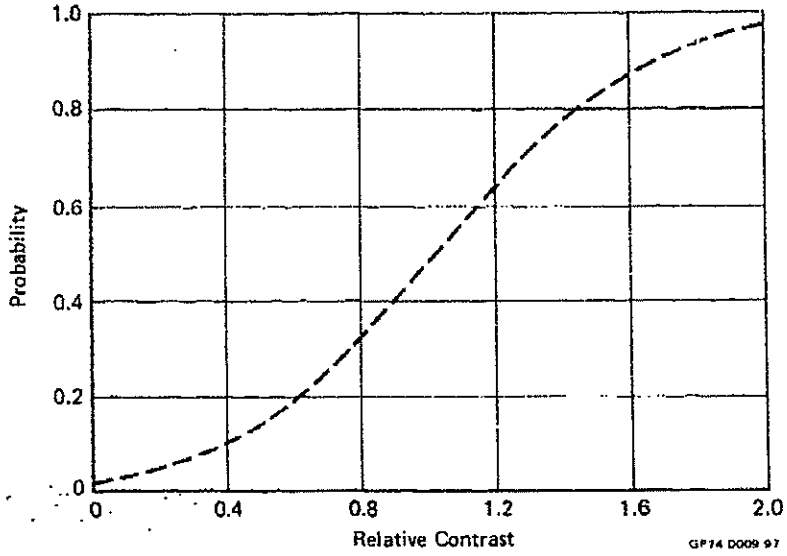

(U) It is obvious that Blackwell's data corresponds to ideal experimental conditions. During a period of several weeks, the observers were allowed to become thoroughly experienced before experimental data was taken. They were well rested, and their concentration was required for periods of only a few seconds per observation after which they were allowed to relax. Fatigue and distraction were essentially absent.

(U) Many multiplicative correction factors have been proposed to allow use of Blackwell's data under less than ideal experimental conditions, Reference (19). For instance, a correction factor of 1.19 has been suggested for correcting for vigilance and is probably satisfactory when a stimulus occurs randomly at approximately 10 minute intervals. A correction factor of 1.90 has been suggested for use when untrained observers are involved. Other correction factors are required for fatigue, distraction, anxiety and a host of other circumstances.

7.4.4 ATMOSPHERIC CONTRAST TRANSMITTANCE - (U) Per References (20, (21), and (22), the apparent luminance of a distant object is the sum of two independent components:

(1) The residual image forming light from the object that has traversed the atmospheric path to the observer without having been scattered or absorbed.

(2) The additional light arriving at the observer that is attributed to the scattering of ambient light throughout the path of sight, including sunlight, moonlight, skylight, earth-shine, etc.

The first component of light contains information concerning the object whereas the second component, depending on scattering and absorbing processes throughout the path of sight, is independent of the nature of the object. As a result of the above processes, the apparent contrast between an object and its background is attenuated as the position from which the object is viewed is located further from the object itself. It is shown in Appendix A that when the attenuation length, L(z), which is the reciprocal of the extinction coefficient, and background luminance are constant over the path of sight, such as for horizontal paths of view, the apparent contrast C_r (z, θ, Φ) is related to the actual contrast C_o (z_t, θ, Φ), by:

$$C_r(z,\theta,\Phi) = C_o(z_t, \theta,\Phi) \quad \exp\left[\frac{-(z-z_t)\sec\theta}{L(z)}\right] \qquad (1)$$

where

z is the altitude from which the object is being viewed

z_t is the altitude of the object

θ and Φ define the direction of view

In this special case, atmospheric contrast transmittance is the same as the direct atmospheric transmission of a light beam. This equation will be used later when determining the feasibility of using VRS camouflage.

7.4.5 POINT SOURCES - (U) If the data in Figure 7-14 on visual contrast thresholds is crossplotted for constant values of background luminance, B, it is observed that the product of contrast, between the object and the background, and subtended solid angle remains constant for objects sufficiently small in terms of subtended solid angle. The largest angular width of the object for which this product remains constant is called the "critical visual angle". This is shown in Figure 7-16 as a function of background luminance, and it affords a practical definition of "point sources" as far as the eye is concerned.

~~(S)~~ The total power radiated by an object of uniform luminance which just subtends the critical angle with a contrast that gives a 50% probability of detection defines the total power radiated by a point source which has the same 50% probability of being detected. To illustrate this concept and its use in VRS calculations, assume that a 1.45 foot diameter circular object is located 5000 ft. from an observer and that the background brightness is 10^{-1} candle/ft^2. For simplicity, assume that there is no atmospheric contrast attenuation. The object just subtends the critical angle of 1 minute (Figure 7-16) for the stated background brightness and if it has a luminance of approximately 0.2 candles/ft^2, i.e., if its contrast $\frac{(0.2 - 10^{-1})}{10^{-1}}$ is approximately unity, it will have a 50% probability of being visually detected (Figure 7-14). The object's total radiant intensity for

(U) FIGURE 7-16
CRITICAL VISUAL ANGLE FOR VARIOUS BACKGROUND LUMINANCE LEVELS

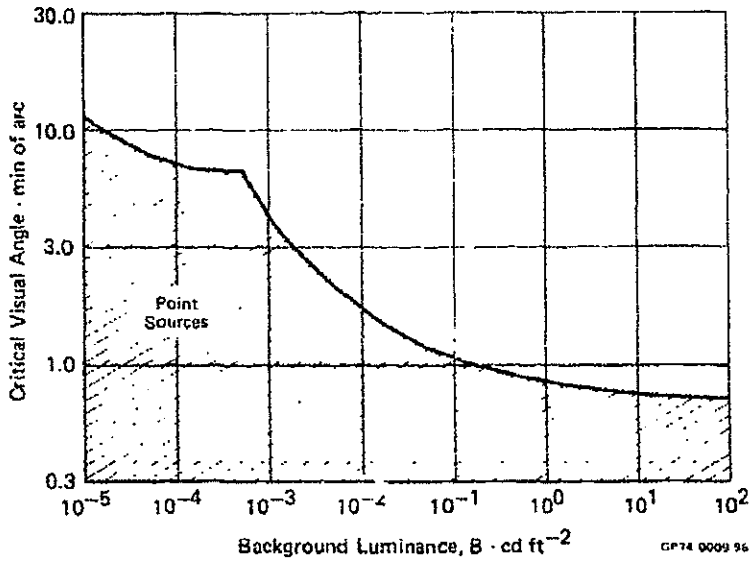

this example would be 0.33 candles (1.65 ft^2 area x 0.2 candles/ft^2 luminance). If the "point source concept" is employed, the above object can be replaced by a perfectly absorbing (black) screen of the same size with a small 0.33 candle source centered on this black screen and have the same probability of being detected. If a higher intensity is radiated, the average contrast between the source and absorbing screen and the background increases, and the source has a higher probability of being detected. On the other hand, if the intensity of the source is decreased slightly, the average contrast drops below threshold and the screen and source becomes invisible.

7.4.6 VISUAL ACUITY - (U) From the discussion in the preceding sections it is apparent that objects which are brighter than the background can always be seen regardless of size if they are bright enough. The same thing is not true of objects which are darker than the background. There is always a minimum object size (defined by the subtended angle) which has a 50% or higher probability of being detected. Objects much smaller cannot be seen regardless of their degree of darkness; even if the object is perfectly black, it cannot be seen. Visual acuity is defined as the reciprocal of the above minimum subtended angle in minutes. Visual acuity is thus directly related to the ability to resolve an object. In fact, an alternate definition of acuity, the "minimum separable" is sometimes used. The "minimum separable" is the minimum angular distance required between two large dark objects for discrimination of separateness. Experimental measurements have shown that both definitions give essentially the same results. Figure 7-17, adapted from Reference (23), presents visual acuity as a function of background luminance. Under starlight

conditions visual acuity is about 0.05 for parafoveal vision and lower for foveal vision. This means that perfectly dark objects which subtend less than 20 minutes arc will probably not be seen. Under conditions of full moon light the foveal visual acuity exceeds the parafocal visual acuity and it is about 0.16. Dark objects which subtend much less than 6 minutes of arc will probably not be seen.

(U) FIGURE 7-17
VISUAL ACUITY vs BACKGROUND LUMINANCE

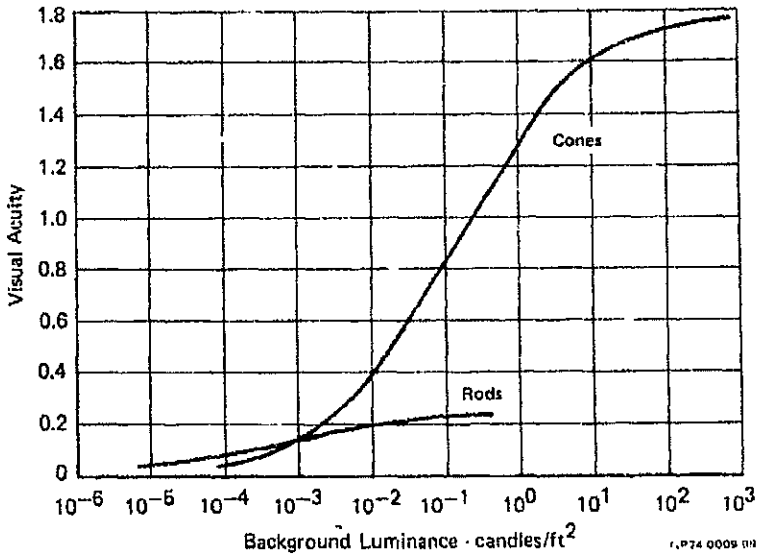

7.5 VRS CAMOUFLAGE APPLICATION

7.5.1 UNCAMOUFLAGED DETECTION RANGE - ~~(S)~~ In order to establish a basis for comparative purposes, the maximum range at which an uncamouflaged QAA flying at 2500 ft. altitude might be visually detected under starlight conditions is first calculated. Calculations were made for both a white and a black aircraft. The white aircraft was assumed to have a reflectivity of 0.9 and the black aircraft reflectivity or zero. The results are shown in Figures 7-18 and 7-19. The following comments pertain:

1. The luminance of the starlit sky is assumed to be 3.0×10^{-5} candles/ft^2 based on the earlier discussion of nighttime sky luminance.

2. The wing span of the QAA is 56.5 ft. which defines the angles subtended by the aircraft at various ranges for head-on viewing. These angles are used to define the object angular sizes when employing Figure 7-14, since Lamar et al in Reference (24) have shown that the threshold contrasts of rectangular type objects are defined by the objects largest angular dimension and are independent of the shorter dimension providing that the shorter dimension exceeds 2 or 3 minutes of arc, as in this case.

(U) FIGURE 7-18
THRESHOLD CONTRAST AND APPARENT AIRCRAFT CONTRAST

Ground Range (ft)	Slant Range (ft)	Angle Subtended by Aircraft (minutes)	Threshold Contrast (starlight)	Albedo	Reflectivity of Paint	Intrinsic Contrast	Contrast Transmittance	Apparent Contrast
2,500	3,536	54.1	0.25	0.22	0.9	0.8	0.90	0.72
5,000	5,590	34.2	0.40	0.22	0.9	0.8	0.86	0.68
7,500	7,906	24.2	0.65	0.22	0.9	0.8	0.79	0.63
10,000	10,308	18.6	1.00	0.22	0.9	0.8	0.74	0.59

GP74-0009 100

(U) FIGURE 7-19
MAXIMUM VISUAL DETECTION RANGE
OF UNCAMOUFLAGED AIRCRAFT
Starlight

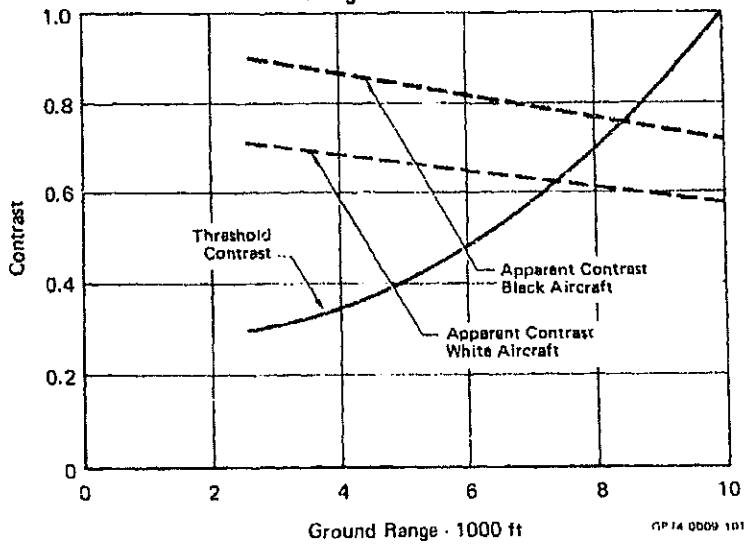

3. Threshold contrast is found by using Figure 7-14, the above value for sky luminance, and the angle subtended by the aircraft. The resulting values of threshold contrast are plotted in Figure 7-19.

4. The ratio between the luminance of the bottom of the aircraft and the sky background was assumed to be the albedo multiplied by the reflectivity of the paint. An albedo of 0.22 was assumed as representative of the data measured by Scripps Institute (Figure 7-10). The luminance of the bottom of the aircraft is then $.22 \times .9 \times (3.0 \times 10^{-5})$ or 6.0×10^{-6} candles/ft^2. The intrinsic contrast at the aircraft is $\frac{(3.0 \times 10^{-5}) - (6.0 \times 10^{-6})}{3.0 \times 10^{-5}}$ or 0.8.

5. The vertical beam transmittance between ground and 2500 ft. was assumed to be 0.93 and is representative of the results obtained by Scripps Institute for the Thailand night sky (Figure 7-7). This value of 0.93 is then corrected for the actual slant range.

6. The background sky luminance and the attenuation length, as defined in Section 7.4.4, are assumed constant over the path of sight.

7. The resulting apparent contrast of the white aircraft (from Equation 1) is shown in Figure 7-19. The intersection of this curve and the threshold contrast curve gives the maximum detectable range of the aircraft, about 7500 ft., based on a 50% or better probability of detection.

8. A similar calculation for the black aircraft was made and the results also shown in Figure 7-19. The maximum detectable range for this case is about 8400 ft.

Similar calculations could be made for full moon or daylight conditions.

7.5.2 VRS ELEMENT INTENSITY - ~~(S)~~ A VRS camouflage system requires individual illumination elements (lights) located discretely on the aircraft. If an individual element becomes too bright, it can aid the enemies visual acquisition capability. It is necessary to determine the maximum intensity that a VRS element might reach before becoming visible to an observer. This calculation is indicated in Figure 7-20 for starlight, full moon, and daylight conditions. The results are plotted on the right side of Figure 7-21. The following additional comments pertain to this calculation:

1. The critical visual angle was found using Figure 7-16.

2. The critical circle is the circular area at the QAA's position that just subtends the critical visual angle.

3. The correction factor of 0.5 was arbitrarily chosen to reduce the probability-of-detection from 50% to about 15% and thereby adopt a more conservative design approach (Figure 7-15).

4. The results of this calculation are conservative because no adjustment has been made to the threshold contrast to compensate for less-than-laboratory viewing conditions, and because an observer may not be sure that he has actually seen an object when the probability-of-detection is less than 90%, as discussed in the section on visual contrast threshold levels.

~~(S)~~ FIGURE 7-20
MAXIMUM INTENSITY OF A VRS ELEMENT

Sky Luminance (cd ft^{-2})	Critical Visual Angle (min)	Contrast Threshold for the Critical Angle	Ground Range (ft)	Slant Range (ft)	Elevation Angle (deg)	Critical Circle Diameter (ft)	Contrast Transmittance	Intrinsic Contrast	Correction Factor	Maximum Point Source Intensity (Candle)
Starlight (3×10^{-5})	9.0	3.0	2,500	3,536	35.2	9.26	0.90	3.33	0.5	0.005
	9.0	3.0	5,000	5,590	24.1	14.63	0.85	3.53	0.5	0.014
	9.0	3.0	7,500	7,906	17.5	20.70	0.79	3.80	0.5	0.029
	9.0	3.0	10,000	10,308	13.6	26.99	0.74	4.05	0.5	0.052
Full Moon (1.5×10^{-3})	3.0	1.0	2,500	3,536	35.2	3.09	0.90	1.11	0.5	0.017
	3.0	1.0	5,000	5,590	24.1	4.88	0.85	1.18	0.5	0.046
	3.0	1.0	7,500	7,906	17.5	6.90	0.79	1.27	0.5	0.092
	3.0	1.0	10,000	10,308	13.6	9.00	0.74	1.35	0.5	0.160
Daylight (480)	0.75	0.5	2,500	3,536	35.2	0.77	0.90	0.56	0.5	285.0
	0.75	0.5	5,000	5,590	24.1	1.22	0.85	0.59	0.5	726.0
	0.75	0.5	7,500	7,906	17.5	1.73	0.79	0.63	0.5	1484.0
	0.75	0.5	10,000	10,308	13.6	2.25	0.74	0.68	0.5	2557.0

GP74 0000 102

~~(S)~~ FIGURE 7-21
INDIVIDUAL LIGHT SPACING AND INTENSITY

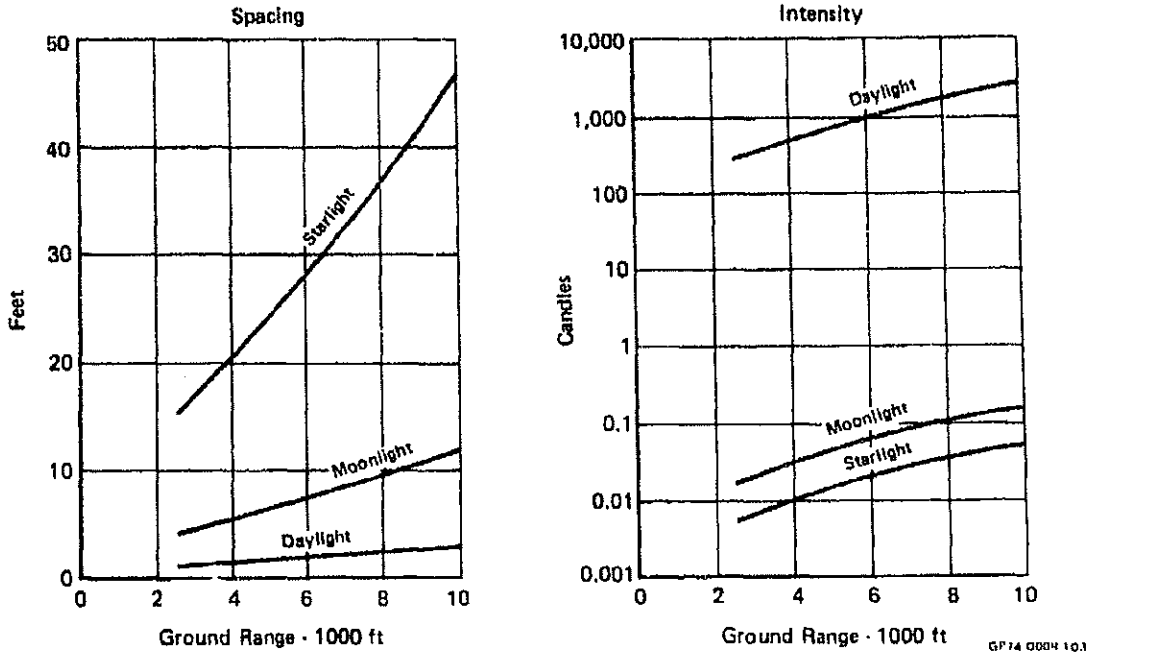

GP74 0000 103

7.5.3 NIGHT VRS CAMOUFLAGE - ~~(S)~~ The density of elements (spacing of individual lights) required for VRS camouflage is inversely related to the Maximum Aircraft Cross Section that can be Camouflaged (MACSC) by one element. The MACSC is simply the maximum intensity that can be radiated by one VRS element divided by the background sky luminance. The MACSC for various aircraft ground ranges is indicated in Figure 7-22 for both starlit and moonlit sky backgrounds. The angle subtended by the camouflaged cross section assumes that a circular aircraft cross section is being camouflaged by each VRS element. The subtended angles are considerably less than the resolution of the human eye at these background luminance levels, as discussed in the section on visual acuity. This means that the maximum allowable intensity of the VRS elements, and not human visual resolution, is the limiting factor when minimizing the number of VRS elements on an aircraft. The data in Figure 7-22 indicates that a VRS element spacing of 3.8 ft. is required to camouflage an airplane as it approaches to 2500 ft. ground range during full moonlight, whereas the individual elements can be spaced up to 15 feet apart for starlight operation. The required spacing vs. camouflage range, for daylight as well as starlight and moonlight conditions, is shown on the left side of Figure 7-21.

~~(S)~~ FIGURE 7-22
MAXIMUM AIRCRAFT CROSS SECTION CAMOUFLAGED BY EACH VRS ELEMENT

			Starlight (3×10^{-5} cd ft^{-2})			Moonlight (1.5×10^{-3} cd ft^{-2})		
Angle Subtended by Aircraft (min)	Ground Range (ft)	Slant Range (ft)	Maximum Cross Section (ft^2)	Diameter (ft)	Angle Subtended by Cross Section (min)	Maximum Cross Section (ft^2)	Diameter (ft)	Angle Subtended by Cross Section (min)
54.1	2,500	3,536	179	15.0	14.6	11.5	3.8	3.7
34.2	5,000	5,590	469	24.2	14.9	29.6	6.1	3.75
24.2	7,500	7,906	975	35.2	15.3	61.0	8.8	3.8
18.6	10,000	10,308	1731	47.0	15.7	106.5	11.6	3.85

~~(S)~~ As a visual target becomes larger, its visual threshold decreases. This suggests that the tolerance on individual VRS element intensity is less critical than the tolerance on average aircraft luminance. The latter is evaluated in Figure 7-23. It is obvious that accurate measurements of sky background luminance and close control of total radiated light will be required for a VRS system to provide moonlight camouflage at short ground ranges. This coupled with the high density of VRS elements required does not make VRS camouflage attractive for all aspect viewing at short range during moonlight conditions.

(S) FIGURE 7-23
REQUIRED REGULATION ON AVERAGE AIRCRAFT LUMINANCE

			Starlight (3×10^{-5} cd ft^{-2})		Moonlight (1.5×10^{-3} cd ft^{-2})	
Angle Subtended by Aircraft (min)	Ground Range (ft)	Slant Range (ft)	Contrast Threshold	Regulation on Average Aircraft Luminance (%)	Contrast Threshold	Regulation on Average Aircraft Luminance (%)
54.1	2,500	3,636	0.20	± 20	0.010	± 0.10
34.2	5,000	5,590	0.34	± 34	0.012	± 0.12
24.2	7,500	7,906	0.58	± 42	0.015	± 0.15
18.6	10,000	10,308	1.00	±100	0.018	± 0.18

GP74 0009 105

(S) One additional expected difficulty caused by the low visual thresholds associated with moonlight conditions concerns the variation of sky luminance with elevation. (It was stated earlier that this variation should not be a limiting factor during moonless conditions.) As the QAA flies toward an observer, its elevation angle changes. For instance, the aircraft elevation angle increases from 13.6° to 35.2° as the QAA flies in at 2500 ft. AGL from a 10,000 ft. ground range to 2500 ft. Figure 7-13 indicates that a 2:1 or greater variation in sky luminance is associated with this angular variation. Thus it would be extremely difficult if not impossible to tailor the aircraft luminance to elevation variations unless the aircraft flew closer to ground level in level flight, or unless it were in a shallow dive straight at the observer and target.

7.5.4 DAYLIGHT VRS CAMOUFLAGE - (U) The application of the VRS concept to daytime condition is somewhat similar to moonlight conditions. In moonlight conditions the VRS element radiation intesity would have to be adjusted to compensate for changes in background sky brightness associated with aircraft position with respect to the ground observer and the moon. This becomes very complex when all aspect capability is required. Limiting the VRS camouflage to only the nose viewing aspect would probably be practical for moonlight. It follows that since all aspect capability during daytime is most likely impractical, a limited aspect daylight VRS system would be the best to study.

(S) The case studied was where the QAA is flown at an altitude of about 200 feet directly toward enemy personnel on the ground or aboard ship. The objective of the investigation is to specify the general characteristics of a VRS system which will prevent nose-on QAA visual acquisition until the aircraft is within 7500 feet range of the observers. The VRS system has to provide camouflage only within a very small angular sector forward of the aircraft; e.g., within a 10 degree half angle cone about the nose of the aircraft. For this analysis, the frontal aspect of the QAA is assumed to be painted black, which presents the worst case and also simplifies the analysis since no allowance is necessary for variations in aircraft reflected sunlight. If the front of the aircraft were painted light blue,

as suggested earlier, lower levels of VRS radiation would be required but the difference would be small.

(S) The frontal cross section of the QAA is approximately 90 square feet. The brightness of the sky background is assumed to be 500 candles per square foot, which is typical for near the horizon on a clear day. One half of the VRS system radiant energy is assumed to fall outside the desired sector. The solid angle for a 10 degree half-angle cone is $\pi/4 \times (20/57.3)^2$, or .0955 steradians. The radiant energy which must be emitted by the VRS system to provide camouflage in the 10 degree half-angle cone is

$$1/2(I) = (90\ ft^2)\ \ (500\ \frac{candles}{ft^2})\ \ (0.0955\ steradians)$$

$$I = 8600\ lumens$$

Assuming each VRS element produces 20 lumens for each inputted watt of electrical power and there is a 75 percent efficiency associated with converting aircraft prime power to input power for the VRS system, approximately 575 watts of aircraft prime power will be needed. Required aircraft prime power requirements are, thus, modest compared to that which would be necessary if camouflage would have to be provided for large angular sectors.

(S) Figure 7-17 indicates that human visual acuity, the reciprocal of the eye's ability to resolve objects at high background luminance levels such as provided by the daytime sky, is approximately 1.7. This data indicates that two dark objects, such as the darker aircraft surfaces lying midway between VRS elements, may be resolved when their separation exceeds 0.7 minutes of arc. In practice, it has been found that VRS element spacing can be increased to approximately 1.4 minutes of arc before the effect of the camouflage is lost. The apparent above discrepancy is probably due to partial illumination of the surfaces midway between VRS elements. Based on the 1.4 minute of arc criteria, the spacing between VRS elements should be no greater than approximately 3.25 feet for a 7500 foot ground range. If a VRS element compensates for a 3.25 ft x 3.25 ft rectangular element of sky (with a sky intensity of 500 candles per square foot) it should radiate an intensity equal to

$$3.25^2\ ft^2 \times 500\ \frac{candles}{ft^2} = 5300\ candles$$

(S) Figure 7-24 depicts the QAA with a possible arrangement of 23 VRS elements which have a maximum spacing of approximately 3.25 feet. Exact element location would be determined experimentally during the system's design phase. One or two additional VRS elements may be needed along the sides of the QAA since the side may be partially visible to observers located nearly 10 degrees off the aircraft's flight path.

~~(S)~~ FIGURE 7-24
POSSIBLE VRS ELEMENT LOCATIONS

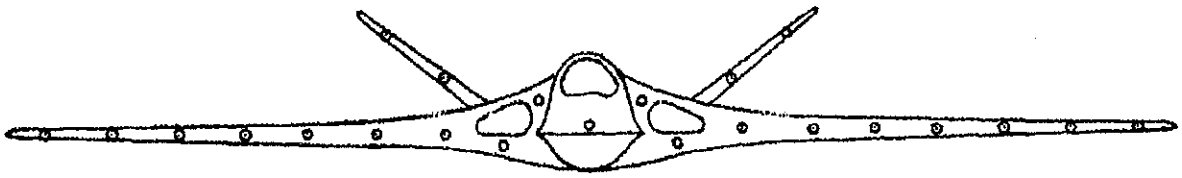

GP74-0009-106

~~(S)~~ General Electric was contacted concerning seal beam lamps which might be used as VRS elements. Their 4589 seal beam, whose characteristics are given in Figure 7-25, approximately fulfills the above requirements. The lamps could be operated approximately 4% in excess of rated voltage to obtain 5300 beam candle power, which would lower expected life to 80% of the rated value. The total weight of a system based around use of these bulbs is estimated at approximately 100 lbs.

(U) FIGURE 7-25
CHARACTERISTICS OF GE4589
SEALED BEAM LAMP

Voltage	28 Volts
Electrical Power Required	50 Watts
Beam Candle Power	5000
Beam Coverage	25^{o} x 30^{o}
Diameter	4.5 in.
Depth	2.75 in.
Rated Life	400 hrs

GP74 0009 107

~~(S)~~ The power required and the diameter of the above lamps are somewhat greater than desired. Discussions with lamp manufacturers indicate that other smaller lamps could be used, including the development of a 2 inch lamp with a beam coverage of 20 degrees to meet the requirements of this example. The total weight of the required VRS system would be in the area of 150 lb., which was included in the electrical system weight in Figure 2-6.

7.5.5 VRS CAMOUFLAGE CONCLUSIONS - ~~(S)~~ All viewing aspect camouflage could be provided for starlight conditions by using very small (grain-of-wheat size) light bulbs. However, under realistic conditions it is probable that a ground observer may not know when and where to look for the aircraft, and therefore the probability of detection would be so low that the added complexity of a separate VRS system for starlight would not be warranted.

(S) VRS camouflage for forward aspect viewing under conditions ranging from moonlight to daylight is considered desirable and practical. This is done by a single VRS camouflage installation, but each light should probably have a small filament for moonlight and another larger filament for daylight.

(S) A sensor similar to a photographic light meter would be used to measure the background sky brightness aft of the aircraft. This would provide the input to regulate the VRS light intensity to match the sky brightness.

(S) In order to maintain low radar cross section, each light should be mounted in a cavity which is covered by a glass having a transparent metallic coating to maintain exterior surface contour and electrical conductivity.

(S) When using VRS camouflage the aircraft should be flown at as low an altitude as possible in level flight, or else it should be flown in a shallow dive straight at the target. The objective with either approach is to minimize the variation in elevation angle between the ground observer and the aircraft, and consequently the variation in background sky brightness, as a function of range.

(S) The total amount of light emitted by the aircraft is governed by the background sky brightness and is essentially independent of the minimum range at which the aircraft is to be camouflaged. Individual light spacing, illustrated by Figure 7-21, determines the number of lights required and is governed by daylight conditions for the specified camouflage range. For the 7500 ft. daylight range specified herein the camouflage range in dimmer light, such as overcast or twilight or moonlight, would be considerably less than 7500 ft. with the same VRS system. Ideally, the largest practical number of smaller individual lights at closer spacing should be used to minimize visual detection range. This would enhance survivability and would not require any additional electrical power for the same viewing aspect angle coverage.

8. 8-14 MICRON INFRARED SIGNATURE

~~(C)~~ Continuing advances in infrared (IR) technology and recent demonstrations have made it probable that forward looking infrared (FLIR) systems, which operate in the 8-14 micron spectral band, will find increasing use by ground forces for the detection and identification of airborne aircraft, especially at night. These FLIR systems have been used for many years on aircraft in an air-to-ground mode for ground mapping and to locate potential targets, but their use in the ground-to-air mode discussed herein has just started to receive attention by the U.S. Army, and presumably by the Soviets. The Army's demonstrated superiority of FLIR over the human eye highlights the need for an analytical technique to predict the capabilities of a FLIR system to detect an aircraft under the variety of conditions which affect detection range and probability, and then to evaluate what can be accomplished in reducing the aircraft's IR signature. Such a prediction technique has been developed under separate funding and used here for analyses of the quiet attack aircraft.

(U) The ground observer's probability of detecting an aircraft on his FLIR display, and the detection range, depends on the contrast between the aircraft image and the sky background, and the amount of time the aircraft is in view. The contrast depends on the aircraft image seen on the FLIR display being large enough and with enough resolution to be recognizable (spatial signature), and on the aircraft image being sufficiently lighter or darker than the sky background to make it stand out (spectral signature difference, or differential radiance, between the aircraft and background sky in the FLIR spectral bandwidth). Atmospheric conditions, such as time of day, cloud cover, humidity, and temperature can cause wide variations in sky background radiance. The aircraft spectral signature is a function of its temperature, its projected area as seen by the FLIR, and the emissivity of its exterior surfaces.

~~(C)~~ In the development of the ground-to-air prediction technique the first step was to collect and consolidate the available 8-14 micron measured data on IR signature characteristics of other aircraft and sky backgrounds, and the distances at which the aircraft were detected and identified by the specific FLIR system used. This measured data was then compared with theory from which the mathematical model for the prediction technique was developed. The data used was provided by the Army's Frankford Arsenal, the Army Night Vision Laboratories at Fort Belvoir, and the Army Missile Command at Redstone Arsenal. All this data is based on the aircraft flying towards the ground based FLIR, which means the FLIR was detecting IR radiation of the aircraft's exterior surfaces at temperatures resulting from aerodynamic heating.

~~(C)~~ The prediction technique has been used in this study to determine an emissivity value for exterior surfaces which will minimize FLIR detection of the quiet attack aircraft by minimizing its contrast with the background for a fixed set of conditions. However, as conditions such as speed or atmospheric conditions change, some other value for emissivity would be expected to be optimum. Since emissivity is fixed by the type of paint or surface coating used on the aircraft, it is obviously impractical to change emissivity in flight. The most practical solution appears to be the use of different emissivities on different exterior portions of the aircraft to make the FLIR image unrecognizable as an aircraft. Further work needs to be done in this direction, and to compare predictions with measured detection probability and range and to further refine the prediction technique.

8.1 IR SIGNATURE MEASUREMENT DATA

(U) A search for measured 8-14 micron IR signature characteristics of tactical aircraft has yielded data on the F-105 and F-8 aircraft. This data (References 25 and 26) was measured by the Army's Night Vision Laboratory (NVL) within two minutes after each aircraft landed. The F-105 was tethered at 90% military power, and the F-8 was at idle power.

(U) The instrument used in these measurements was a Texas Instrument Thermoscope with the following characteristics:

- o single scanning detector
- o 0.75 to 1.0 milliradian instantaneous field of view
- o 525 lines scanned in 4.5 seconds
- o 0.1°C sensitivity
- o film type - TXP523
- o output image - 4x5 inches

~~(C)~~ The signatures were constructed into a pictorial format showing the equivalent black body temperature of the various aircraft surface segments. A very significant point was made regarding the F-105 IR signature. At the 90% military power condition, the exhaust plume was a significant radiation source. The F-8 signature at the idle power condition showed negligible radiation attributable to the exhaust plume. The measured data is summarized in Figure 8-1, where J is the IR signature in watts/steradian.

~~(C)~~ Specific IR signature data head-on at 300 knots for the F-4 and A-4 aircraft, using the HAC (Hughes Aircraft Company) FLIR, were reported in Reference (27). These data have been reproduced in Figure 8-2. Differential radiance is the arithmetical difference in watts/steradian between the radiation from the aircraft and the radiation from the atmosphere. The data have been converted into equivalent black body temperatures to be consistent with the previous signature measurements, Figure 8-1. The increasing equivalent black body temperature with decreasing slant range is due to the aircraft filling the FLIR instantaneous field of view at 3 km, and to the atmospheric transmittance which increases with decreasing range.

8.2 MEASURED FLIR DETECTION CAPABILITY

(C) The Night Vision Laboratories have conducted tests in which FLIR systems were used to detect airborne aircraft (Reference 27). The primary goal was to obtain detection and identification ranges for various aircraft such as the A-3, A-4, A-6, A-7, F-4, F-5 and T-2. Three FLIR systems were used in these tests: a Hughes advanced FLIR design operating in the 8-11.5 micron band, a Hughes PINE FLIR operating in the 8-11.5 micron band, and a Night Observation Device-Long Range Thermal system (NODLRT) operating in the 3-5 micron band. In these tests each aircraft approached the sensors at an altitude of 2500 ft. At a slant range of 60,000 ft., the aircraft began a descending trajectory toward the test site at a nominal speed of 300 kts, and leveled off at an altitude of 1500 ft.

(U) A summary of the resulting head-on mean detection and identification ranges are provided in Figure 8-3. It should be pointed out that this data is dependent on the prevailing atmospheric conditions and the particular FLIR system, and care must be used in extrapolating these results to other systems.

(C) FIGURE 8-1
8-14 MICRON SPECTRAL BAND SIGNATURES
Side View of Aircraft

a) F-8 Aircraft Immediately After Landing - Engines at Idle Thrust

- o ambient air 7.2°C
- o relative humidity 48%
- o date 12-11-71
- o time 2120

Areas ($ft.^2$)	**Temp °C	J (w/sr)	% Total
8.6	36.	49.72	3.13
10.8	33.	59.80	3.76
3.6	30.	19.08	1.20
11.5	24.	55.67	3.50
5.8	21.	26.80	1.69
3.0	18.	13.22	0.83
320.0	16.	1365.57	85.88
* -----	---	None	-----
Totals 363.3		1589.86	99.99

*Plume
**Equivalent Black Body Temperature

b) Tethered F-105 Aircraft - Engines at 90% Military Thrust (Within Two Minutes After Landing)

- o ambient air 21.1°C
- o relative humidity 60%
- o date 12-15-71
- o time 1910

Areas ($ft.^2$)	**Temp °C	J (w/sr)	% Total
4.5	102.	57.22	3.40
* 42.3	57.	324.31	19.29
1.4	44.	9.05	0.54
7.7	43.	49.10	2.92
2.7	41.	16.75	1.00
19.8	30.	104.92	6.24
221.1	27.	1120.24	66.60
Totals 399.5		1681.60	99.99

*Plume
**Equivalent Black Body Temperature

~~(C)~~ FIGURE 8-2
AIRCRAFT DIFFERENTIAL RADIANCE LEVELS - HAC FLIR

a) F-4, Ambient Air @ 21°C, 300 kts

Range (km)	Differential Radiance (w/cm^2)	Elevation Angle	Equivalent Black Body Temperature °C
6.4	0.338×10^{-2}	4.1°	34
4.0	0.406×10^{-2}	6.6°	35
2.9	0.673×10^{-2}	9.1°	45

b) A-4, Ambient Air @ 21°C, 300 Kts

Range (km)	Differential Radiance (w/cm^2)	Elevation Angle	Equivalent Black Body Temperature °C
4.8	0.306×10^{-2}	5.5°	30
3.0	0.446×10^{-2}	8.8°	33

~~CONFIDENTIAL~~

(C) FIGURE 8-3
DETECTION AND IDENTIFICATION RANGES

AIRCRAFT	Mean Range ± Standard Deviation (Meters)					
	HAC FLIR (8-11.. microns)		PINE FLIR (8-11.5 microns)		NODLRT (3-5 microns)	
	Day	Night	Day	Night	Day	Night
A-4 Detection	6421 ± 1711	12075 ± 4980	----------	----------	5473 ± 540	----------
A-4 Identification	1966 ± 872	2670 ± 889	1544 ± 535	1300 ± 279	2146 ± 347	2064 ± 138
F-5 Detection	6133 ± 2395	5875 ± 740	4467 ± 565	----------	----------	----------
F-5 Identification	1700 ± 957	1557 ± 177	1178 ± 243	1437 ± 437	2144 ± 290	----------
F-4 Detection	----------	----------	----------	----------	6883 ± 739	----------
F-4 Identification	----------	2017 ± 300	----------	----------	3046 ± 442	----------
A-7 Detection	----------	----------	7900 ± 1500	----------	6978 ± 985	----------
A-7 Identification	----------	----------	1508 ± 228	1733 ± 335	2466 ± 200	2352 ± 560

~~CONFIDENTIAL~~

~~(C)~~ The Army's Missile Command conducted field tests, Reference (28), to measure the capability of the unaided eye and a FLIR in searching, acquiring, and tracking airborne aircraft. The sensor used in these tests was the Hughes PINE FLIR.

~~(C)~~ A total of sixty-five valid passes were flown at about 400 knots at 3000 and 6000 ft altitudes, at 0-3 Km cross track ranges and at various meteorological conditions. Figure 8-4 illustrates the probability of detecting an F-100 aircraft by FLIR, under nighttime conditions, for the 65 passes. These test data illustrate the following:

- Using a PINE FLIR system, the ground observer has a 50% probability of detecting the airborne F-100 aircraft at 9° above the horizon (yielding an average 7.9 Km slant range) and a maximum probability of detection of 83% (in other words, only 11 of the 65 valid flights were undetected).

In comparison, the unaided ground observer did not detect 57 of the 65 valid flights, yielding a 12% probability of detection and showing the improvement afforded by the PINE FLIR system. These probability of detection values are conditioned upon the fact that the ground observer knows where to look for the aircraft.

~~(C)~~ The data used to formulate Figure 8-4 were further segmented to construct the curves shown in Figures 8-5 and 8-6 for a 3000 ft and 6000 ft aircraft altitude, respectively. Comparison of the probability of detection vs elevation angle for Figures 8-5 and 8-6 shows that at low elevation angles of less than 10° there is a higher probability of detection for the lower altitude of 3000 ft in Figure 8-5. This might imply that it is easier to detect an airborne F-100 aircraft near the horizon at a 3000 ft altitude than at a 6000 ft altitude. This is misleading, because the real reason for this higher probability is that for the same elevation angle the aircraft at lower altitude is closer to the FLIR. The important thing is how far away the aircraft can be detected, and comparison shows the aircraft at higher altitude is more vulnerable to detection by FLIR. For the same 50% probability of detection, the slant range of 10.2 kilometers is longer at 6000 ft altitude than the 7.1 kilometers at 3000 ft. Similarly, at the same slant range of say 10 kilometers, the probability of detection is higher at 54% for the 6000 ft altitude than the 8% probability at 3000 ft altitude. Therefore, one way to minimize detection by a ground-based FLIR is to fly as close to the ground as possible.

~~(C)~~ Hughes Aircraft Company has reported on their tests at Fort Bliss and San Clemente Island, Reference (29), in the detection of low flying aircraft with the PINE FLIR system. The Fort Bliss data is a duplication of the MICOM reported data in Reference (28), while the San Clemente Island tests employed A-4 and F-4 aircraft in the PINE FLIR shakedown tests prior to the Fort Bliss tests. These San Clemente Island data (Figure 8-7) are consistent with the Fort Bliss tests in that the lower altitude aircraft is detected neare the horizon, and the longer detection ranges are achieved for the higher altitudes.

FIGURE 8-4
PINE FLIR PROBABILITY OF DETECTING AN F-100 AIRCRAFT
3000 and 6000 Ft Altitude

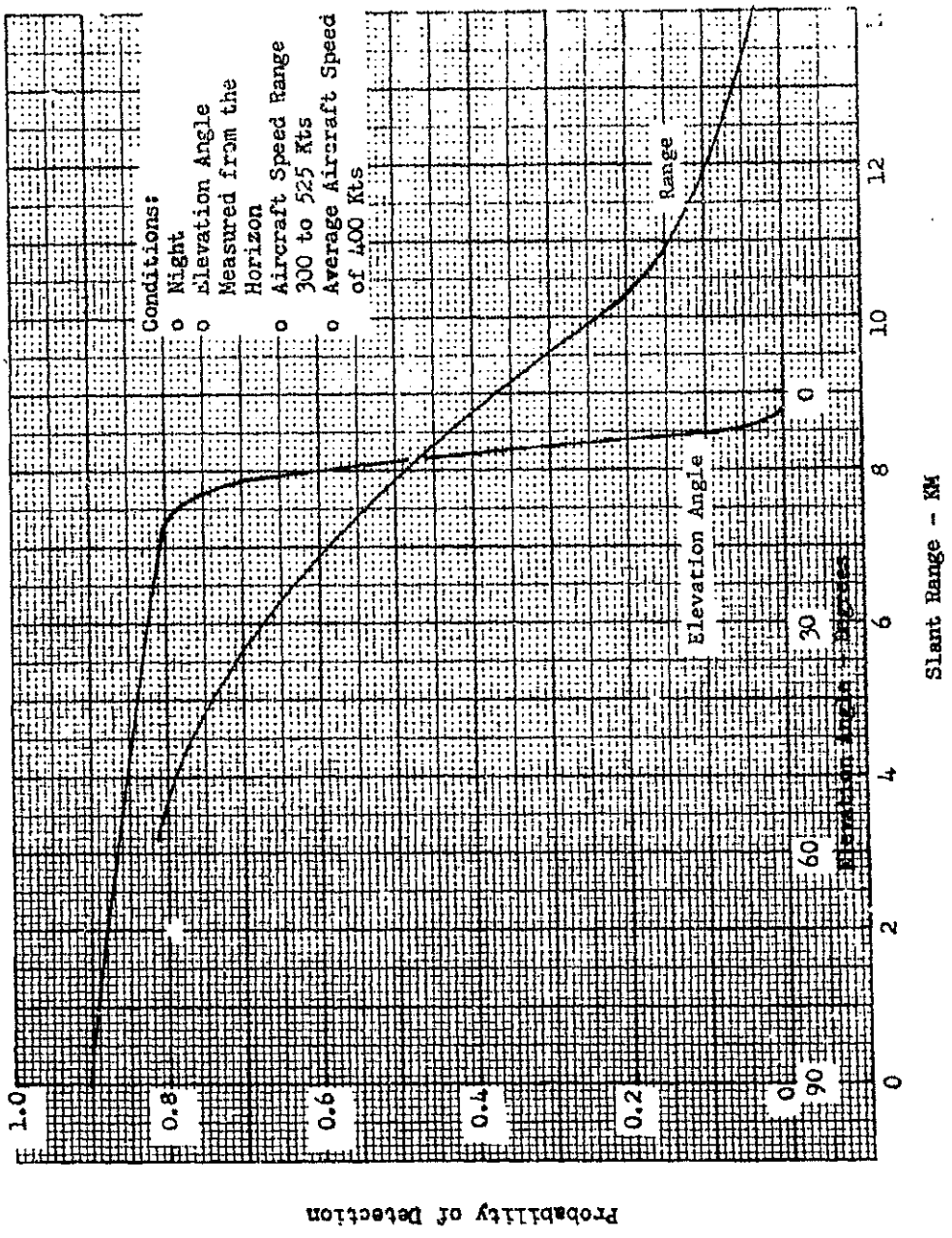

~~CONFIDENTIAL~~

~~(C)~~ FIGURE 8-5
PINE FLIR PROBABILITY OF DETECTING AN F-100 AIRCRAFT
3000 Ft Altitude

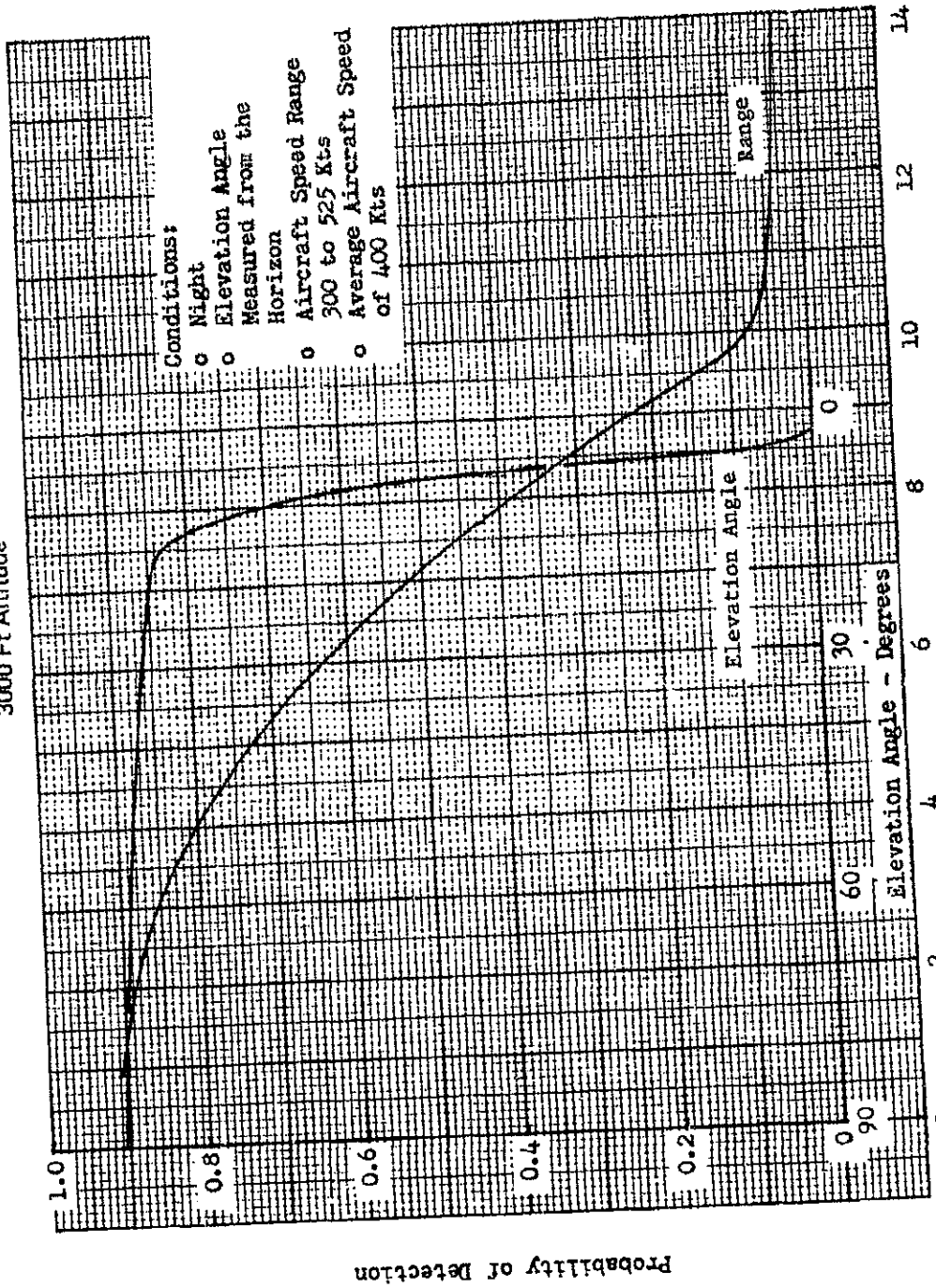

~~CONFIDENTIAL~~

(C) FIGURE 8-6
PINE FLIR PROBABILITY OF DETECTING AN F-100 AIRCRAFT
6000 Ft Altitude

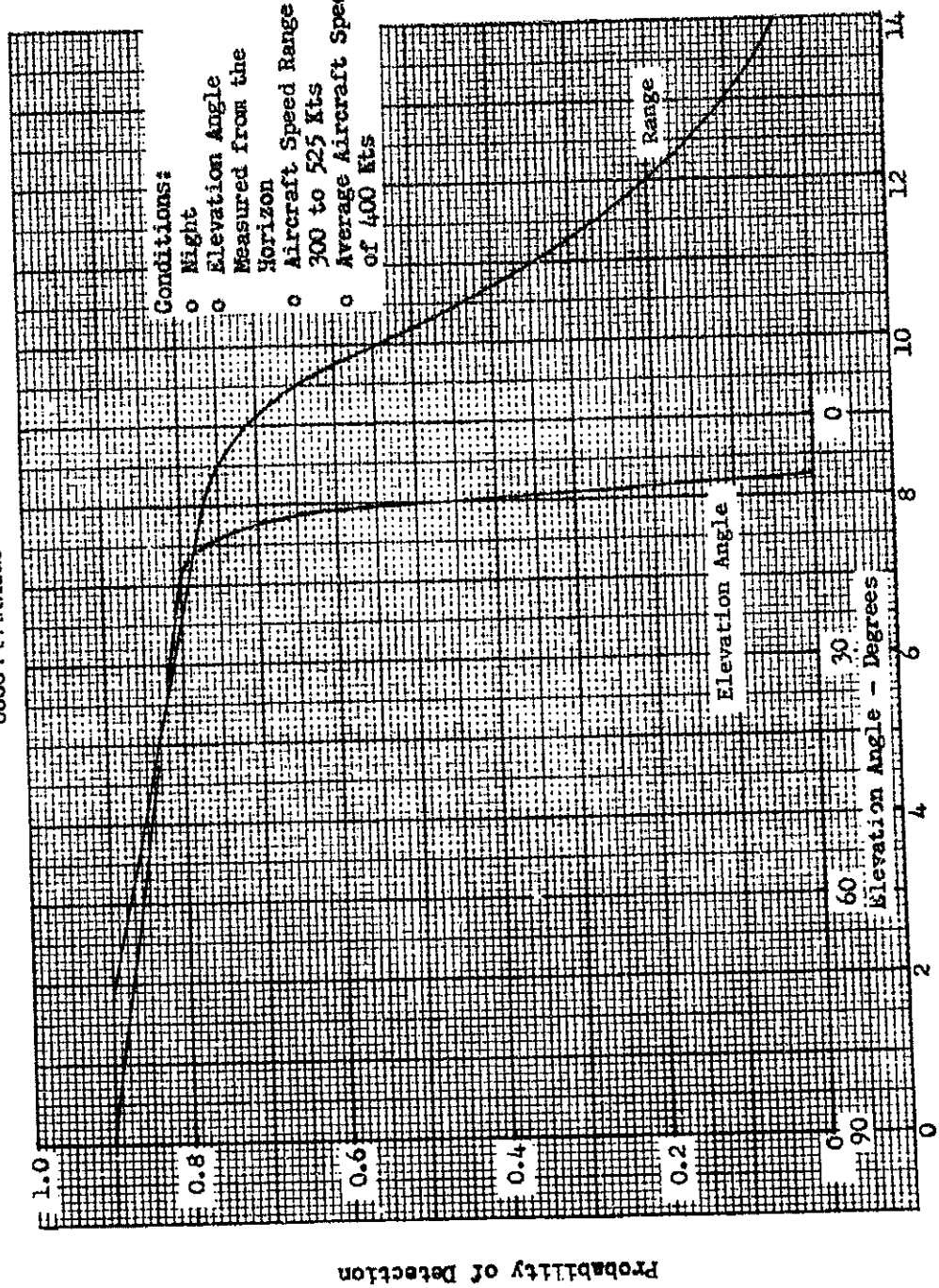

~~(U)~~ FIGURE 8-7
PROBABILITY OF DETECTING F-4 AND A-4 AIRCRAFT WITH A PINE FLIR, UP TO A 2000 FT ALTITUDE

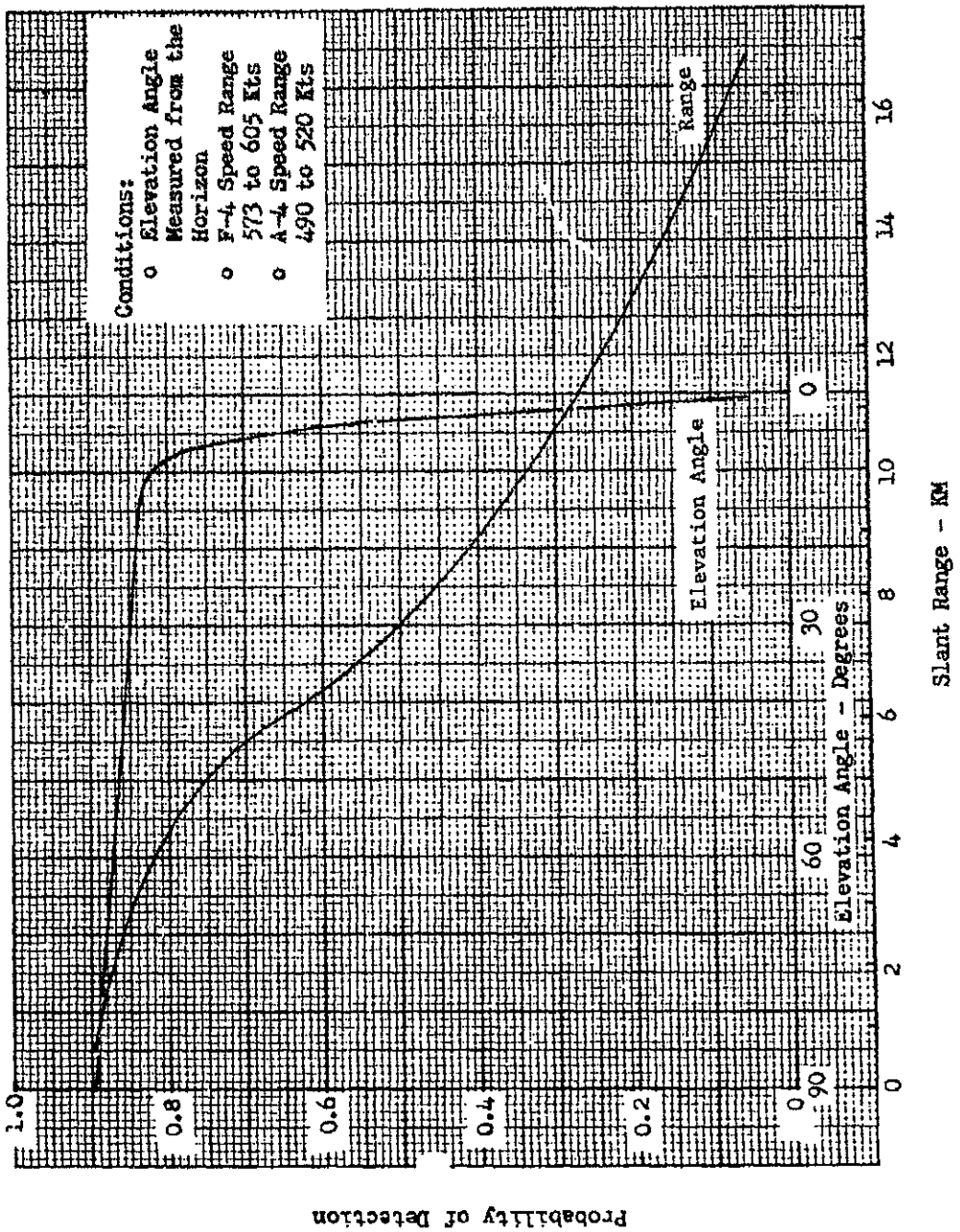

(U) Frankford Arsenal conducted tests measuring the potential of a ground based FLIR system to detect low flying aircraft. The tests, Reference (30), consisted of detecting A-4, F-4 and A-6 aircraft, flying at an altitude of 500 to 1000 feet, with an 8 to 14 micron spectral band FLIR system. One point observed in these tests was that a detected aircraft could be lost on the FLIR display if it flew from a clear sky into a cloud background. This implies that the probability of detecting an airborne aircraft by FLIR is diminished with a cloud cover.

8.3 FLIR DETECTION CAPABILITY ANALYSIS

(U) The data available on detection of aircraft in the 8-14 micron band led to the decision to construct an analytical model of a typical FLIR, the AAS-28A, and to use this to assess the detectability of the QAA. The analysis of the atmosphere effects, the FLIR model, and the QAA signature are discussed in this section, as well as the detection results.

8.3.1 (U) ATMOSPHERIC RADIANCE - Atmospheric radiance is the radiant energy that would be received by the FLIR system when no target is present. It can consist of atmospheric constituent emissions, reflected terrain emissions, and diffused sunlight. A computer simulation, used to calculate the atmospheric radiance levels, requires knowledge of the atmospheric conditions. These are:

- o ground level temperatures
- o temperature gradient
- o ground level pressure
- o pressure gradient
- o carbon dioxide content
- o water vapor content

The carbon dioxide content and water vapor content are needed because they are the primary sources of atmospheric emissions within the 8 to 14 micron spectral band. These data and measured atmospheric radiance data can be combined to predict the atmospheric radiance levels.

(U) Time of day is another needed parameter but it can be segmented into "Night," "Day" and "Twilight." Thus, the atmospheric radiance levels can be classified in the same fashion to obtain the notation

- o Nighttime Radiance
- o Twilight Radiance
- o Daytime Radiance

Nightime radiance is most important because of it having the lowest value.

(U) Nighttime Radiance - The data selected to represent the nighttime atmospheric radiance was measured by Bell, et. al., Reference (31), at Cocoa Beach, Florida. These measurements for the 27°C humid atmosphere have been reproduced in Figure 8-8. Using these data and the 27°C blackbody spectral radiance data, Figure 8-9, the spectral emissivity of the atmosphere can be computed and is shown in Figure 8-10. The difficulty experienced here is the term "humid atmosphere" which can only be interpreted as an atmosphere having a relative humidity between

(U) FIGURE 8-8
27°C HUMID, NIGHTTIME CLEAR ATMOSPHERE RADIANCE

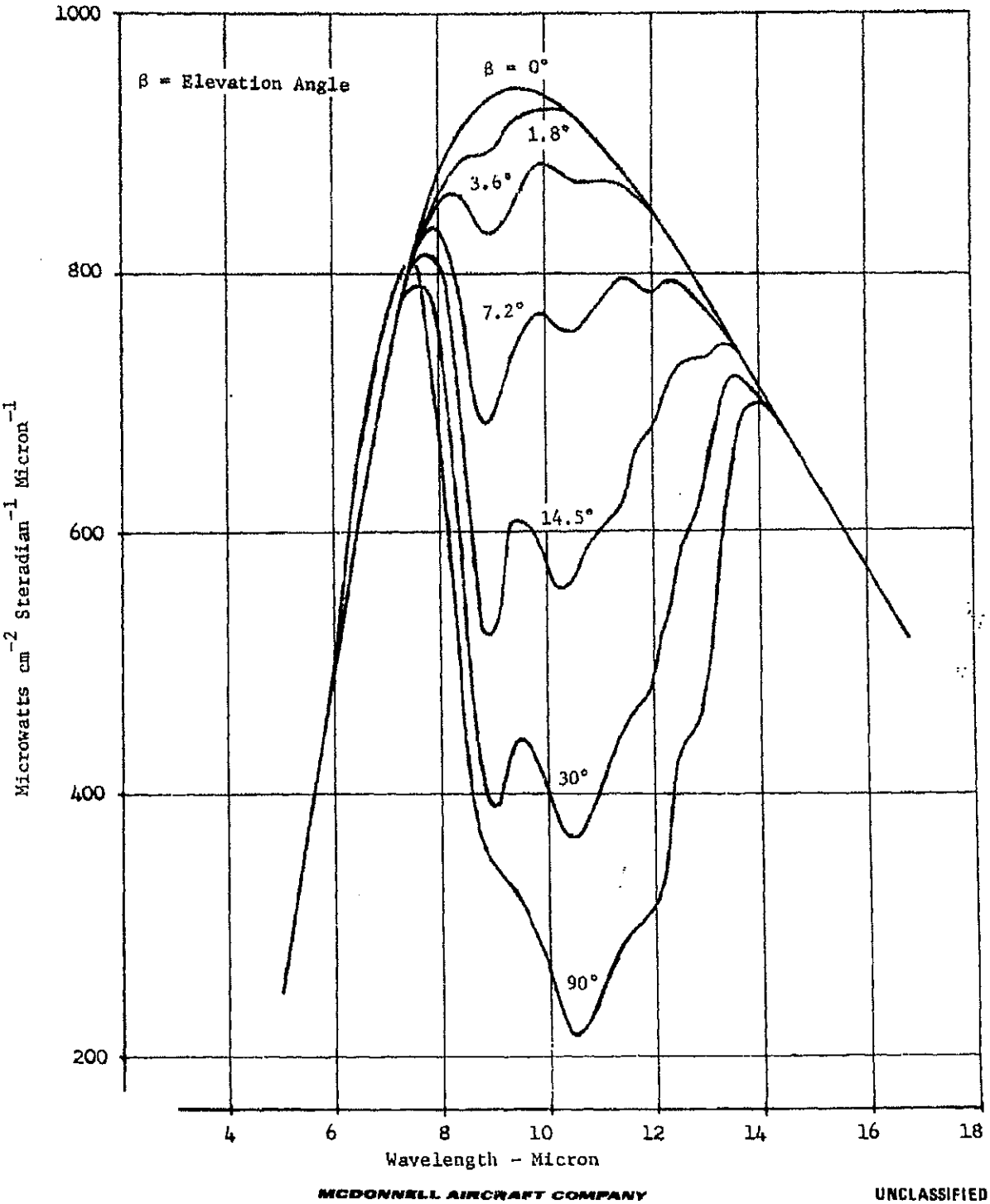

MCDONNELL AIRCRAFT COMPANY

UNCLASSIFIED

(U) FIGURE 8-9
BLACKBODY RADIANCE

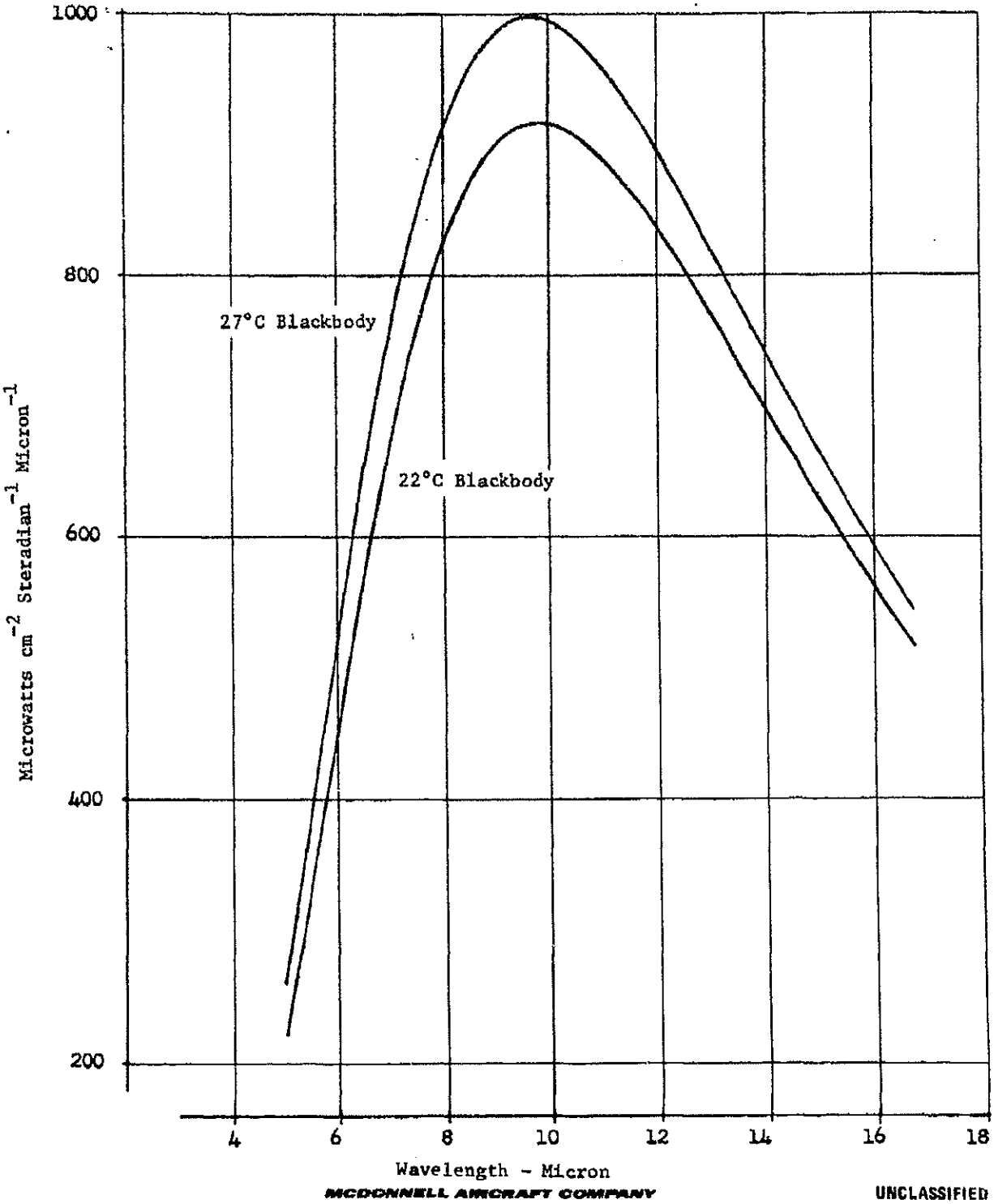

(U) FIGURE 8-10
NIGHTTIME CLEAR ATMOSPHERE EMISSIVITY
(Based on Figure 8-8 Data)

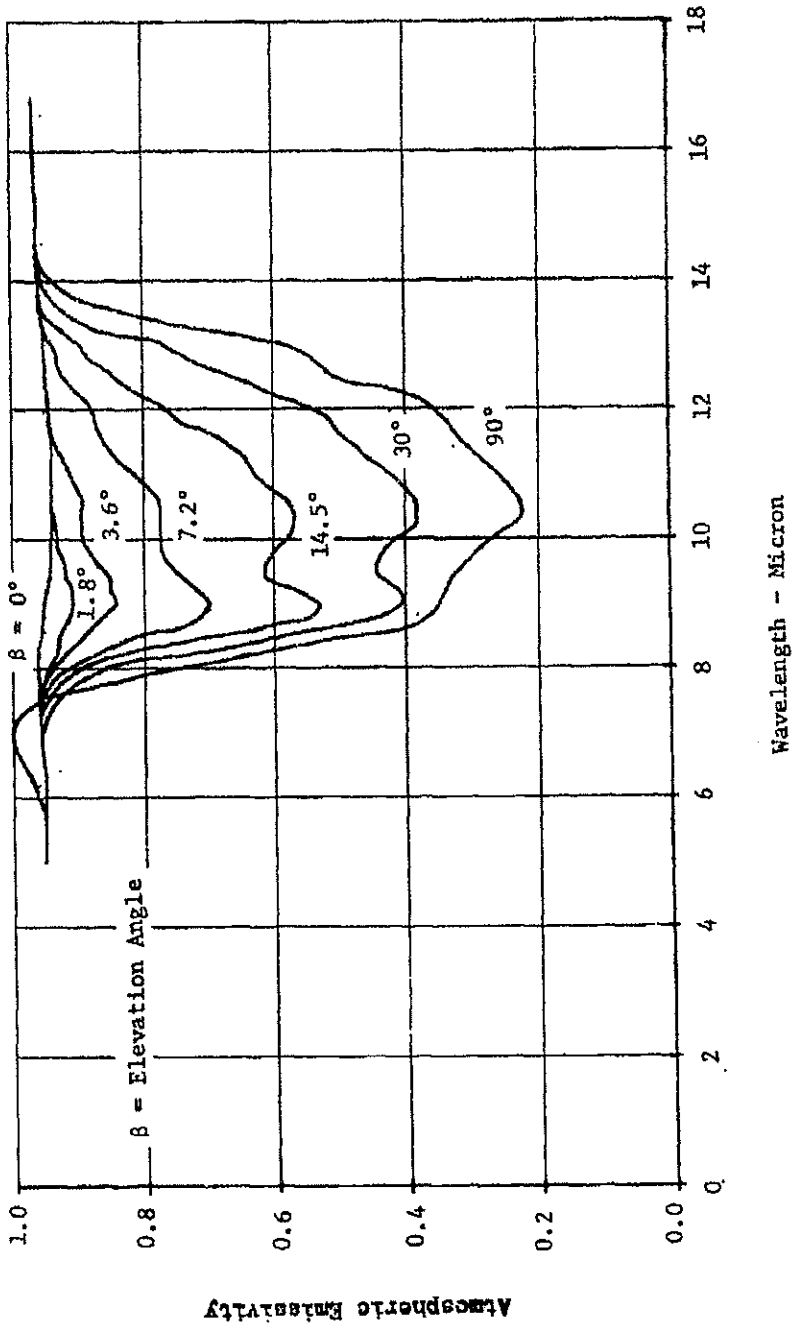

80% and 100%. Nevertheless, these data have been encoded for use with the ground to air FLIR model. Additional atmospheric radiance data would be beneficial and will be added to the ground to air FLIR model when available.

(U) Twilight Radiance - The spectral radiant intensities under the twilight condition is a sum of atmospheric emissions, reflected terrain and diffused sunlight. The amount attributed to diffused sunlight is related to the relative orientation of the FLIR system with respect to the sun. Twilight radiation was not considered in this study due to its complexity.

(U) Daytime Radiance - Diffused sunlight is the predominant source during the day. Its relative importance is still dependent upon the relative orientation of the FLIR system with respect to the sun and the sun's position relative to its zenith. Daytime radiation was not considered in this study due to its complexity.

(U) Clouds - The effect clouds have on the atmospheric radiance is to increase the radiance levels above the clear sky values, Reference (31). The variety of cloud conditions that can occur makes this an extremely difficult problem to simulate. In fact, the most likely simulation procedure is to determine the FLIR system performance for a specific cloud cover. Bell, et. al. data measurements for nighttime cumulus and cirrus cloud cover conditions are shown in Figure 8-11. These data are readily converted to atmospheric emissivity, Figure 8-12, with the note that these data are based upon a humid atmosphere.

(U) FIGURE 8-11
NIGHTTIME CLOUD COVER RADIANCE

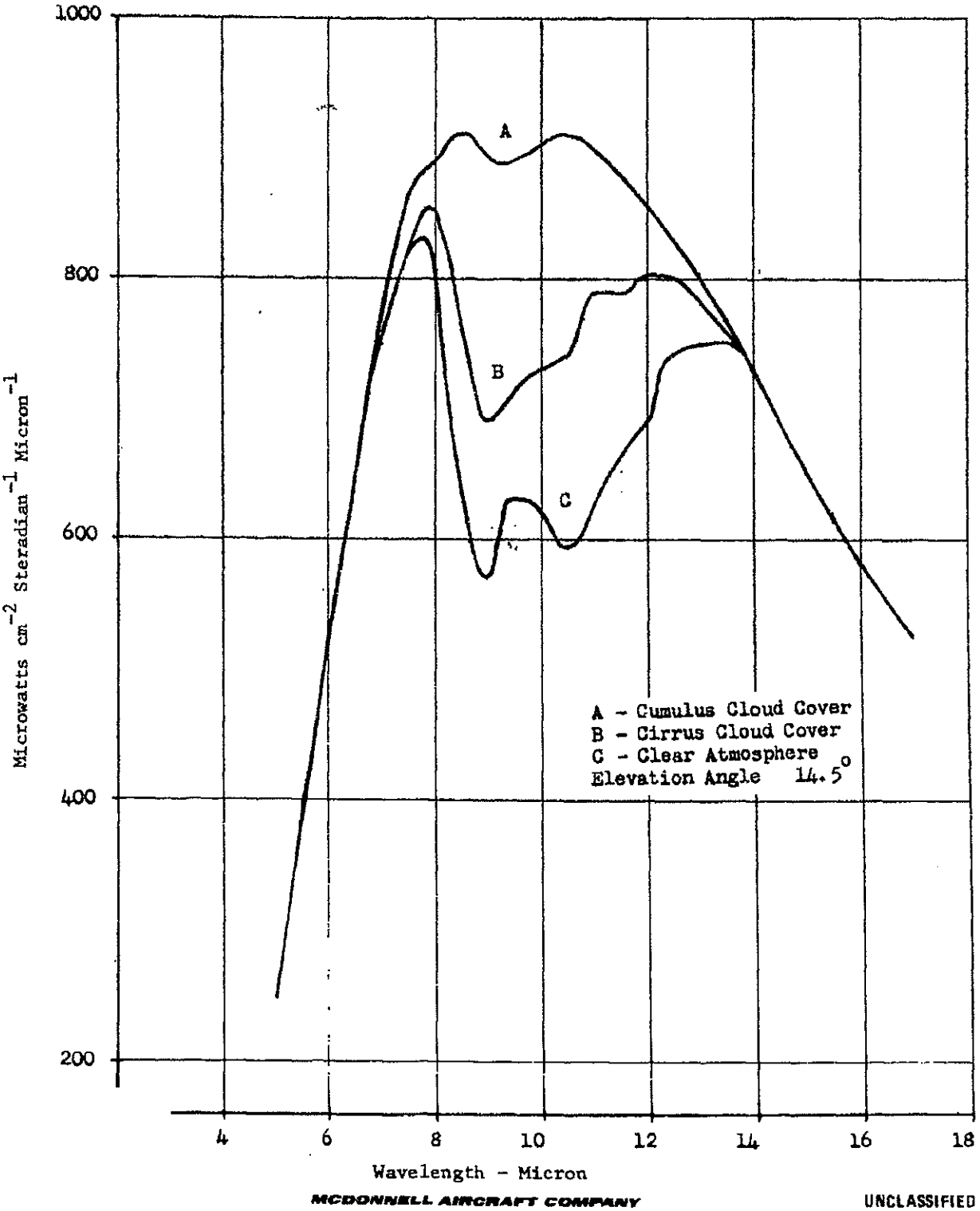

(U) FIGURE 8-12
NIGHTTIME CLOUD COVER ATMOSPHERE EMISSIVITY

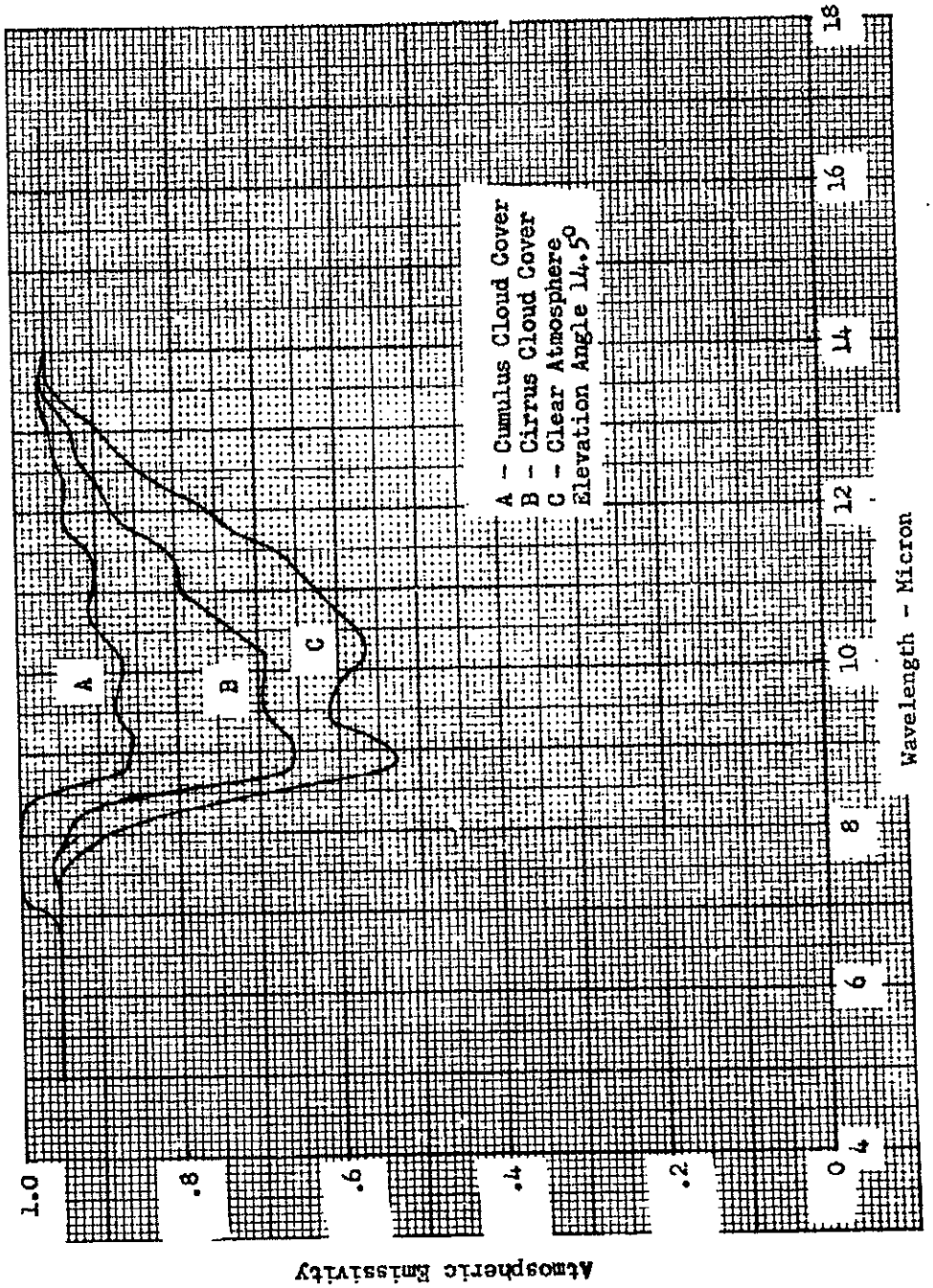

8.3.2 (U) GROUND TO AIR FLIR MODEL - The objective of this section is to review the relationships employed to describe the operational performance of the forward looking infrared system in a ground to air mode. These include the transfer of scene data through the atmosphere, the transfer of the atmospheric modified scene data through the FLIR system and the final displayed scene on the observer's display.

(U) FLIR System Modulation Transfer Functions (MTF) - Figure 8-13 illustrates the basic FLIR system building blocks. Each can be described, using modulation transfer theory, in solving for the transfer of the atmospheric modified scene.

(U) FIGURE 8-13
FLIR SYSTEM BUILDING BLOCKS

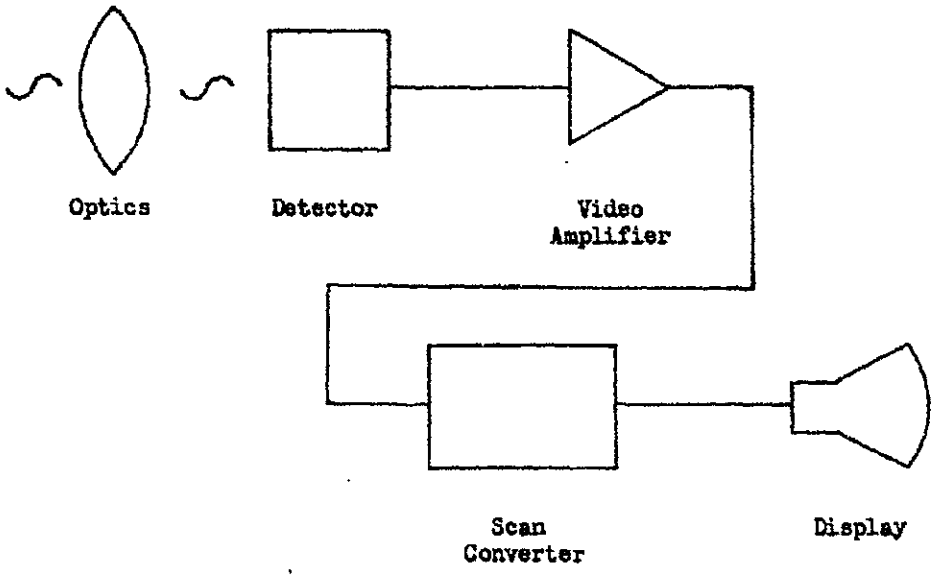

(a) (U) Diffraction Limited, Circular Optics MTF - This MTF is

$$T_a(\Omega) = \frac{2}{\pi}\left[\cos^{-1}(\Omega) - \Omega(1-\Omega^2)^{1/2}\right];\ 0 \leq \Omega \leq 1 \qquad (1)$$

where

$$\Omega = 1000\,\frac{R\lambda}{d} \qquad (2)$$

with R = spatial frequency in cycles/milliradian
λ = wavelength in millimeters
d = lens diameter in millimeters

(U) This MTF is symmetric and as such the spatial frequency R can be written in terms of the orthogonal spatial frequencies

$$R = \sqrt{(R_s)^2 + (R_{\underline{s}})^2} \tag{3}$$

Where

R_s = spatial frequency vector in the scan direction
$R_{\underline{s}}$ = spatial frequency vector in the nonscanning direction

and the inner product

$$R_s \cdot R_{\underline{s}} = 0 \tag{4}$$

(b) (U) Detector Aperture MTF - The detector aperture is a combination of the optics aperture and the detector shape. Here the detector shape is considered as the limiting factor and is assumed to be rectangular. With this

$$T_b(R_s, R_{\underline{s}}) = \frac{\sin(\pi\gamma_s R_s)\sin(\pi\gamma_{\underline{s}} R_{\underline{s}})}{(\pi\gamma_s R_s)(\pi\gamma_{\underline{s}} R_{\underline{s}})} \tag{5}$$

where

γ_s = detector field of view in the scan direction and measured in milliradians

$\gamma_{\underline{s}}$ = detector field of view in the nonscanning direction and measured in milliradians

(c) (U) Detector Electrical MTF - The electrical response of the detector, to time varying levels of input radiation, affects only the transfer of scene data along the scan direction. This electrical transfer function can have the form

$$E_c(f) = \left|1 + (2\pi T_d f)^2\right|^{-1/2} \tag{6}$$

where

f = temperal frequency in Hz
T_d = detector time constant in seconds

This is converted to a MTF by considering that

$$R_s = \frac{f}{w} \tag{7}$$

with

w = scanning rate in milliradian/second

yielding

$$T_c(R_s, \underset{s}{R}) = \left[1 + (2\pi T_d w R_s)^2\right]^{-1/2} \delta(\underset{s}{R}) \tag{8}$$

The impulse function is needed to illustrate that the only spatial frequency transferred by a single detector in the nonscanning direction is $\underset{s}{r} = 0$, since

$$\delta(\underset{s}{R}) = \begin{cases} 1; & \underset{s}{R} = 0 \\ 0; & \text{otherwise} \end{cases} \tag{9}$$

There is a phase shift associated with each detector scan line and this can be seen in Appendix B.

(d) (U) Video Electrical MTF - The amplifying circuit associated with each detector is considered to be a shunt peaking amplifier. This amplifier's transfer function, with a damping coefficient Q, is

$$E_d(f) = \left[\frac{1 + Q^4 (f/f_o)^2}{\left\{1 - Q^2 (f/f_o)^2\right\}^2 + \quad ^2}\right]^{1/2} \tag{10}$$

f_o = video amplifier 3dB ban · in Hz.

Using the conversion in Eq. (7), the MTF i.

$$T_d(R_s, \underset{s}{R}) = \left[\frac{1 + Q^4 \left[\frac{R_s w}{\quad}\right]^2}{\left\{1 - Q^2 \left[\frac{R_s w}{f_o}\right]^2\right\}^2 + \left[\frac{R_s w}{f_o}\right]^2}\right]^{1/2} \delta(\underset{s}{R}) \tag{11}$$

(e) (U) Scan Converter MTF - The scan converter is needed in the FLIR system in order to convert the multiple scanning detecto outputs into a format suitable to the display scanning format. At the present, i·t

$$T_e(R_s, \underset{s}{R}) = \tag{12}$$

(f) (U) Display MTF - This MTF is represented as

$$T_f(R_s,\underset{s}{R}) = G_1(\underset{s}{R})G_2(R_s) \tag{13}$$

$$G_1(\underset{s}{R}) = \begin{cases} 1 - 2\gamma_s \underset{s}{R}\,\underset{s}{R}\,; & 0 \le \underset{s}{R} \le \dfrac{1}{2\gamma_s} \\ 0 & ; \text{otherwise} \end{cases} \tag{14}$$

$$G_2(R_s) = \begin{cases} 1 & ; 0 \le R_s < \dfrac{1}{2\gamma_s} \\ 2(1 - \gamma_s R_s); & \dfrac{1}{2\gamma_s} \le R_s \le \gamma_s \\ 0 & ; \text{otherwise} \end{cases} \tag{15}$$

(g) (U) FLIR System MTF - The FLIR system MTF is the product of the building block MTFs.

$$T_S(R_s,\underset{s}{R}) = \prod_{\alpha\varepsilon\phi} T_\alpha(R_s,\underset{s}{R}) \; ; \; \phi = \{a,b,c,d,e,f\} \tag{16}$$

8.3.3 EARTH RELATED FUNCTIONS

(a) (U) Spherical Earth - The terrain scenario will affect the QAA's probability of being detected during its penetration run in. The infinite variety of possible scenarios must necessarily be limited. Herein only a spherical earth is considered, as shown in Figure 8-14 with the slant range to the aircraft:

$$S = \sqrt{(R_e+h)^2 - R_e^2\cos^2\beta} - R_e\sin\beta \tag{17}$$

where

h = aircraft altitude in feet
R_e = earth's radius in feet = 20,902,957
β = elevation angle measured from the horizon

(U) The elevation aspect at which the ground observer sees the aircraft is computed from

$$\beta+\Delta = \cos^{-1}\left\{\frac{R_e\cos\beta}{R_e+h}\right\} \tag{18}$$

(U) FIGURE 8-14
SPHERICAL EARTH PARAMETERS

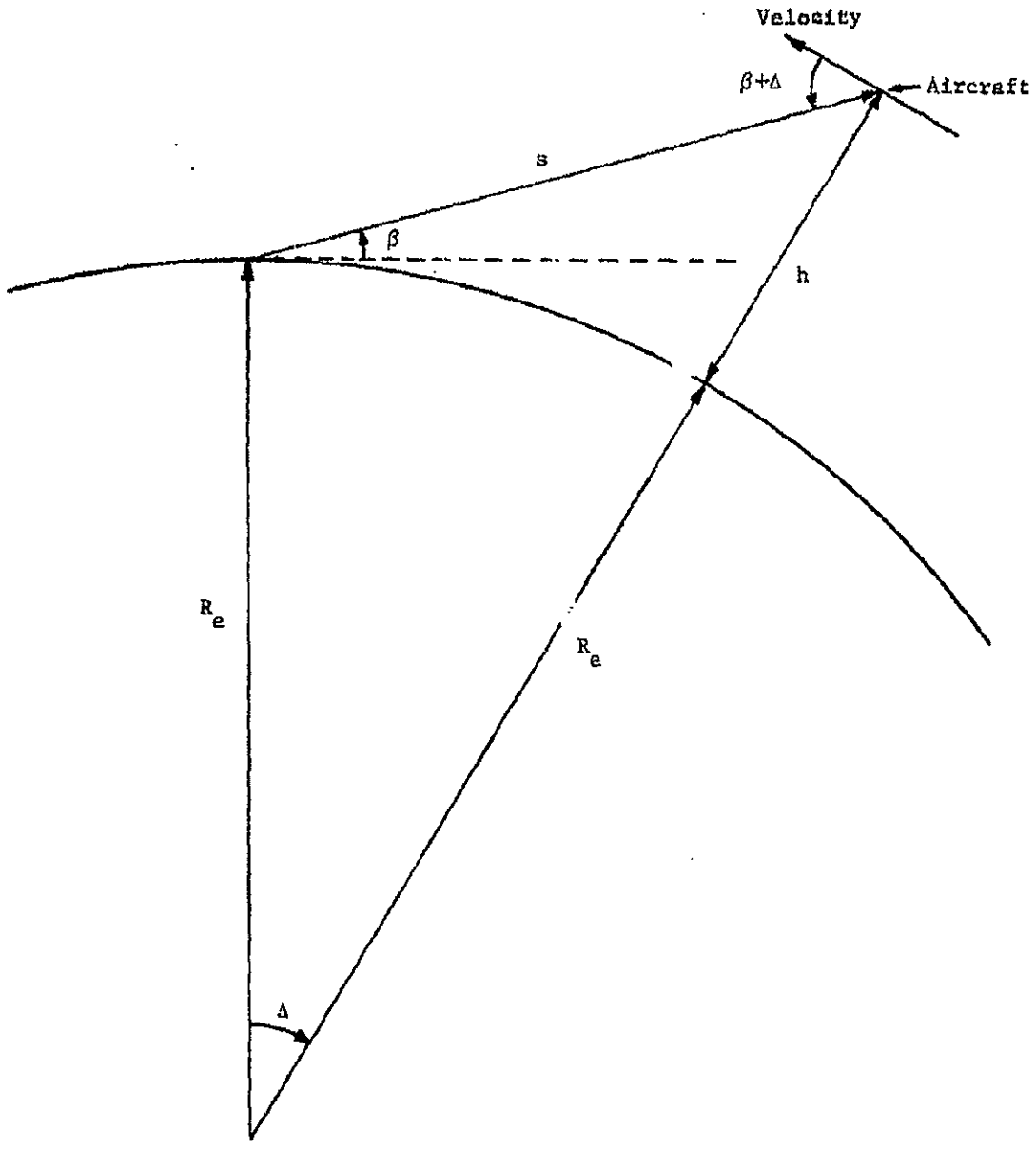

At each elevation aspect the aircraft presents a distinctive view to the ground observer, which will affect his ability to detect the QAA in the FLIR display image. Appendix C contains the projected QAA views at selected elevation aspect angles; each view is drawn with the QAA flying directly toward or above the ground observer.

(b) (U) Altitude Correction of Atmospheric Transmission - A segmentation of the atmosphere into 500 foot layers is employed here to correct for temperature, pressure and gas density variations. The correction factor for the carbon dioxide and water vapor transmission are normally given for the standard atmosphere and a horizontal slant path, Reference (32), as shown in Figure 8-15. These data can be generated using

$$\alpha_{H_2O}(h) = \exp\{-1.99612\times10^{-5}h\} \; ; \; 0 \leq h \leq 2500 \text{ ft} \tag{19}$$

$$\alpha_{CO_2}(h) = \exp\{-5.99014\times10^{-5}h\} \; ; \; 0 \leq h \leq 2500 \text{ ft} \tag{20}$$

for the standard atmosphere. The variation of the water vapor density with altitude uses the standard atmosphere temperature gradient

$$\alpha_T = -0.0019812 \; ^{o}C/\text{ft}; \; 0 \leq h \leq 2500 \text{ ft} \tag{21}$$

and considers uniformly mixed gases (constant relative humidity for all altitudes). Water vapor density at a given temperature, Figure 8-16, can be converted to precipitable millimeters of water vapor per foot (prmm) using

$$\Gamma(h) = .3048\times10^{-3}\rho_s(T_h)r \tag{22}$$

where

T_h = atmospheric temperature at altitude h
r = relative humidity

The equivalent horizontal sea level path length for a horizontal path at altitude h is

$$S_{H_2O}(0) = \alpha_{H_2O}(h)S(h) \tag{23.a}$$

$$S_{CO_2}(0) = \alpha_{CO_2}(h)S(h) \tag{23.b}$$

The equivalent precipitable millimeters of water vapor for the horizontal path is

$$\hat{\Gamma} = \Gamma(h)\,\alpha_{H_2O}(h)S(h) \tag{24}$$

(U) FIGURE 8-15
ALTITUDE CORRECTION FACTORS FOR REDUCTION TO EQUIVALENT SEA-LEVEL PATH

Altitude h (FT)	Altitude Correction Factor	
	$\alpha_{H_2O}(h)$ Water Vapor	$\alpha_{CO_2}(h)$ Carbon Dioxide
0	1.	1.
1000	.981	.941
2000	.961	.888
3000	.942	.836
4000	.923	.786
5000	.904	.742
6000	.886	.698
7000	.869	.658
8000	.852	.619
9000	.835	.582
10000	.819	.549

(U) FIGURE 8-16
SATURATION VAPOR DENSITY OF WATER vs TEMPERATURE

T - Temperature (°C)	$\rho_s(T)$ - density (gm/m^3)
-10	2.36
0	4.85
10	9.40
20	17.3
30	30.4
40	51.2

Now using the layered atmosphere concept, the equivalent values for a slant path are

$$\text{prmm} = \sum_{n=0}^{N} \Gamma_n \, \alpha_{H_2O,n} \, \hat{S}_n \tag{25.a}$$

$$CO_2\text{path length} = \sum_{n=0}^{N} \alpha_{CO_2,n} \, \hat{S}_n \tag{25.b}$$

Where

Δ = atmosphere layer height (500 ft)

n = the n^{th} layer; $n\Delta \leq h < (n+1)\Delta$, $n = \{0,1,2,\ldots,N\}$

$\alpha_{CO_2,n}$ = mean value of $\alpha_{CO_2}(h)$ for the n^{th} layer

$\hat{S}_n$ = slant path through the n^{th} layer

Γ_n = mean value of $\Gamma(h)$ for the n^{th} layer

$\alpha_{H_2O,n}$ = mean value of $\alpha_{H_2O}(h)$ for the n^{th} layer

8.3.4 AIRCRAFT RELATED FUNCTIONS

(a) (U) Aircraft Motion MTF - The combination of aircraft motion, FLIR scanning rate and FLIR image transfer yields a problem which remains to be expressed in analytical form. A general approximation can be made by

$$T(R_s,\underset{s}{R}) = \frac{\text{Sin}(\pi R_s \beta_s)}{(\pi R_s \beta_s)} \frac{\text{Sin}(\pi \underset{s}{R} \underset{s}{\beta})}{(\pi \underset{s}{R} \underset{s}{\beta})} \tag{26}$$

Where

$\beta_s, \underset{s}{\beta}$ = aircraft angular motion in milliradians per Δt seconds

Δt = 0.2 seconds, the integration time of the eye, Reference (33)

The aircraft motion induced flicker, induced into the displayed image, will affect the observer's cummulative probability of detecting the aircraft.

(b) (U) Aerodynamic Heating - The approximation to be employed in computing the aircraft skin surface temperature rise, Reference (34), is

$$T_s = T_o \left(1 + \frac{\eta-1}{2} M_o^2\right) \tag{27}$$

Where

T_o = aircraft ambient air temperature, ^oK

M_o = aircraft mach number

η = 1.4 for air

This is only an estimate; nevertheless, the data in Figure 8-1 and Figure 8-2 appear to be consistent with this expression.

8.3.5 (U) QAA SIGNATURES - The utilization of a ground based FLIR system for the detection of airborne aircraft necessarily required that both the spectral and spatial signatures of the QAA by evaluated. The spectral signature involves temperature and emissivity of the aircraft, while the spatial signature is concerned with the projected view of the aircraft seen by the FLIR.

(U) 8 to 14 Micron Spectral Band Signature - The QAA design is such that it can be segmented into three radiating elements. These are the aircraft outer surface (aerodynamic heating), engine exhaust cavity and engine exhaust plume.

(U) The temperature of the aircraft outer surface can be limited to aerodynamic heating with the provision that the heat transfer from the internal heat sources is negligible. The surface can be treated as a graybody Lambertian radiator at the temperature level given by Eq. (27). At the 2500 ft altitude and velocity of 110 kts used in this analysis, the QAA surface should be approximately 1.7°C above an ambient air temperature of 22°C.

(U) The engine exhaust cavity can be considered as a blackbody cavity at the exhaust gas temperature, when looking directly into the exhaust duct. Its radiance at this center line aspect would be:

$$N_o(\lambda_1,\lambda_2) = \frac{1}{\pi} \int_{\lambda_1}^{\lambda_2} \frac{C_1}{\lambda^5} \left[\exp\left(C_2/\lambda T\right) - 1\right]^{-1} d\lambda \tag{28}$$

Where

C_1 = 37400. watts micron ^{4} cm^{-2}
C_2 = 14380. micron ^oK
T = exhaust gas temperature at the exit (^oK)
λ = wavelength (microns)

Specifying a fixed cavity area, in this case the exhaust duct cross section area, the QAA exhaust cavity radiance can be normalized to the center line aspect. Employing the angle notation illustrated in Figure 8-17, this normalized exhaust cavity radiance for a given elevation angle θ and azimuth angle γ from exhaust center line is:

$$N(\lambda_1,\lambda_2,\theta,\gamma) \approx \begin{cases} N_o(\lambda_1,\lambda_2)\{\tan(39^o)-\tan(\theta-90^o)\}\cos(\theta-90^o)\cos\gamma; & 90^o<\theta\leq 129, |\gamma|\leq 90^o \\ N_o(\lambda_1,\lambda_2)\{\cos^4\theta\cos^4\gamma+\tan(39^o)\sin\theta\cos\gamma\} & ; 0^o\leq\theta\leq 90^o, |\gamma|\leq 90^o \\ N_o(\lambda_1,\lambda_2)\{1-\tan(39^o)\tan\theta\}\cos^4\theta\cos\gamma & ; -51^o\leq\theta<0, |\gamma|\leq 90^o \\ 0 & ; \text{otherwise} \end{cases} \quad (29)$$

(U) The exhaust plume conditions during the QAA penetration run in should be approximately at the same level as the F-8 at idle power. Thus the QAA's plume radiation in the 8 to 14 micron spectral band is negligible.

(U) Spatial Signature - The QAA's spatial signature is its visible projected image, Appendix C. Furthermore the most important consideration is the spatial signature on the display, since the observer will use this to detect the airborne aircraft. Appendix B contains the information relating the transfer of the QAA visible projection through the FLIR system and the resultant image on the display.

(U) FIGURE 8-17
QAA NOZZLE ASPECT ANGLE

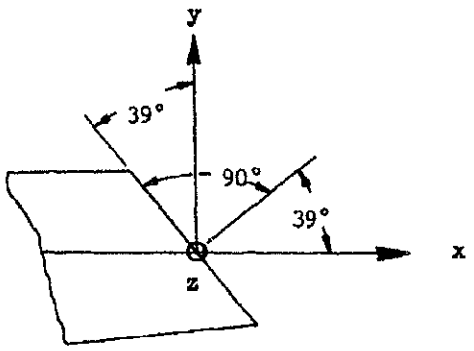

side view of QAA engine exhaust nozzle

8.4 SIMULATION USING AN AAS-28A FLIR

(U) A complete list of the data, needed to analyze the capability a ground based FLIR system would have against the QAA, is shown in Figure 8-18. Each parameter can be readily decoded by referring to Appendix D. These data are comprised of aircraft parameters, atmosphere parameters and FLIR system parameters. It must be noted that the atmospheric radiance is limited to the nighttime clear atmosphere radiation level.

(U) An infinite number of simulations are possible in describing the performance a ground based AAS-28A FLIR system would have in the detection of an airborne QAA. Thus the simulation must necessarily be restricted to the most logical flight path. Here the QAA is flying a penetration run in at 2500 ft and 110 knots, and the flight path is such that the QAA would fly directly over the ground based AAS-28A FLIR system. The visible area projections for this flight path would be as shown in Appendix C, and the exhaust cavity would not be visible so there would be no IR radiation detectable from it.

8.4.1 (U) OUTPUT - Each MTF described in Section 8.3.2 is available as an output; however, each is computed only for its values along the coordinate axes (i.e., $T_b(R_S,0)$ and $T_b(0,R_S)$). The characteristics of each MTF can be readily observed in Figure 8-19, in which all of the AAS-28A system MTF's have been plotted. There exists one conclusion that can be made from these plots, which is that the limiting MTF in the system's performance is the number of detector scan lines.

(U) Figure 8-20 is a plot of the equivalent sea level values of precipitable millimeters of water vapor and carbon dioxide path length as a function of aircraft altitude, up to the input altitude (parameter AH in Figure 8-18). In this figure, the output data are plotted for elevation angles of 0° (the horizon) and 90° (the zenith) to specifically show the variation. These data were computed based upon the standard atmosphere characteristics illustrated in Figure 8-21, which shows the altitude correction factors and altitude dependent atmospheric temperature.

(U) The spherical earth affect is primarily seen at elevation angles less than 3.6° from the horizon. At this elevation angle the atmospheric transmission is approximately zero for the selected atmospheric conditions of 80% relative humidity (RH) and 27°C sea level temperature (SLT). Elevation aspect angle differences do exist, as shown in Figure 8-22; however, combining the tabulated elevation aspect data with Appendix C, finds that the difference in the projected visible QAA surface area are quite negligible for the simulation flight path.

8.4.2 (U) FLIR PERFORMANCE - The spectral passband of the AAS-28A FLIR system was limited to the 8 to 14 micron spectral band with unity spectral response at all wavelengths within the spectral band. As such, the best possible performance obtainable with the AAS-28A is shown in Figure 8-23. The 0.7 emissivity is a representative value for most aircraft. These data are under the stipulation that the detector instantaneous field of view is filled by the aircraft, otherwise the condition where the field of view contains some background would yield lesser values. A direct relationship does exist between the differential received power (DPR), which is the difference in brightness between the aircraft and the sky, and the percentage of the instantaneous field of view filled by the aircraft. The obvious question needing an answer is the elevation angle at which the aircraft first just fills the

(C) FIGURE 8-18
AAS-28A FLIR GROUND-TO-AIR PERFORMANCE ANALYSIS DATA

Parameter	Value	Units
AH	2500.	Feet
AV	110.	Knots
AT	23.7	Degrees C
AE	0.7	Unitless
SLT	27.	Degrees C
RH	80.	Percent
VIS	10.	Nautical Miles
ZF	1.	Unitless
COT	1.	Unitless
COAD	7.	Inches
WLC	0.0008	Centimeters
WUC	0.0014	Centimeters
DS	400.	Unitless
DSTAR	0.270E 09	CM*SQRT (Hz)/Watt
DTC	0.100E-04	Seconds
SMRS	60.	Scans/Second
SIR	1.	Unitless
FOVELI	0.00048	Radians
FOVAZI	0.00048	Radians
FOVEL	11.	Degrees
FOVAZ	14.4	Degrees
BW	0.400E 05	Hz
Q	0.5	Unitless
VNF	1.14	Unitless
ADET	0.134E-04	CM^2
OVD	20.	Inches
DW	9.	Inches
DH	7.5	Inches

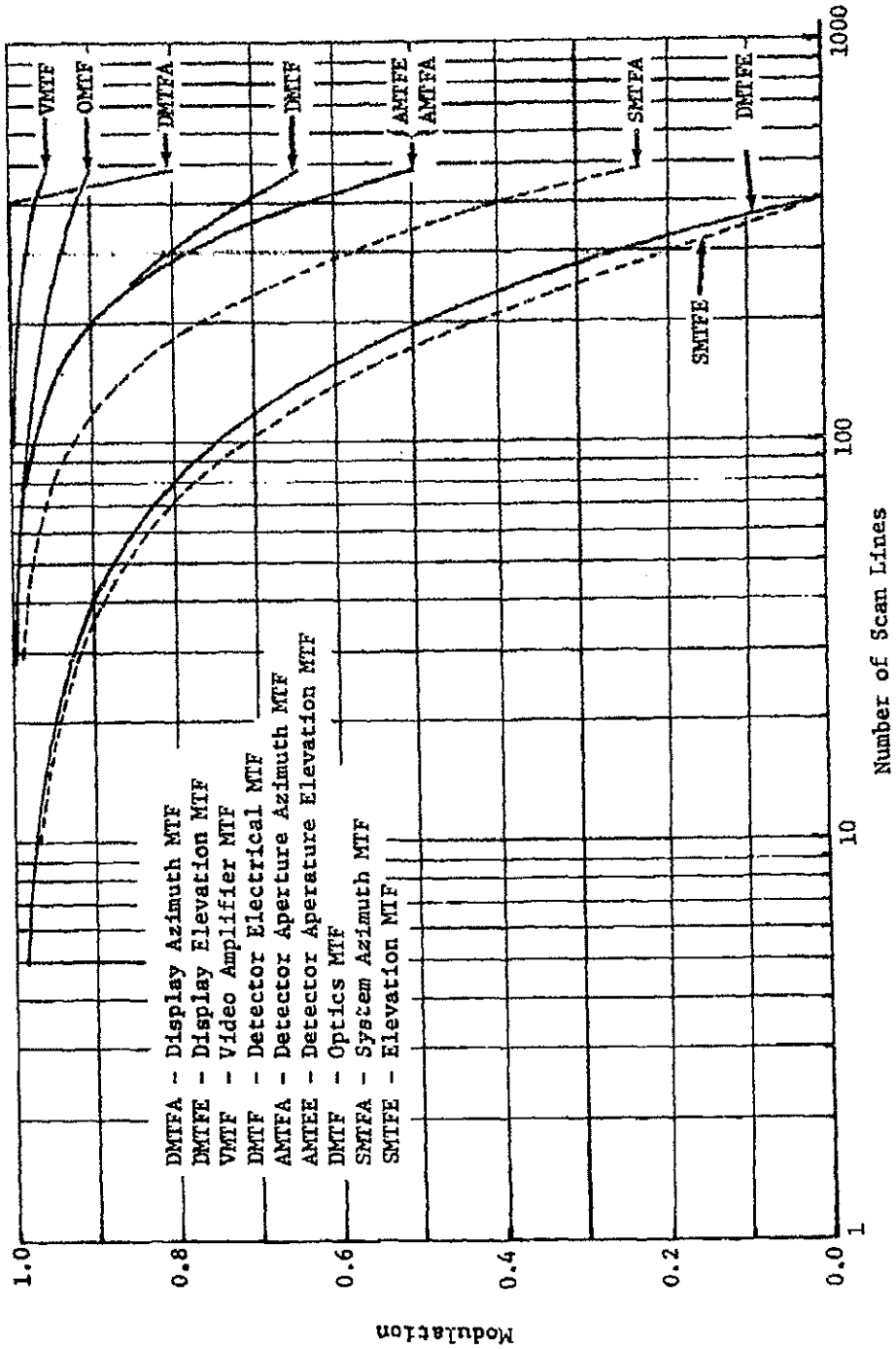

~~(C)~~ FIGURE 8-19
AAS-28A SYSTEM MODULATION TRANSFER FUNCTIONS

(U) FIGURE 8-20
ATMOSPHERE SLANT PATH PARAMETER VARIATION

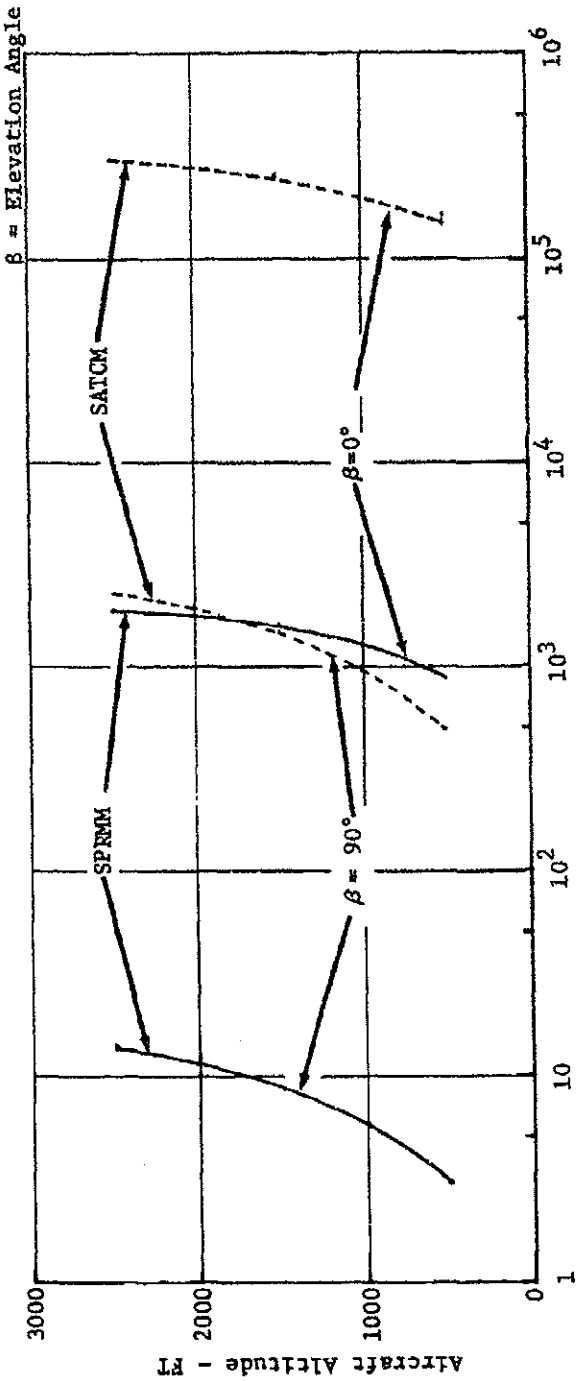

SPRMM - Precipitable Millimeters of Water
SATCM - Carbon Dioxide Path Length in Feet

(U) FIGURE 8-21
SIMULATION ATMOSPHERE DATA

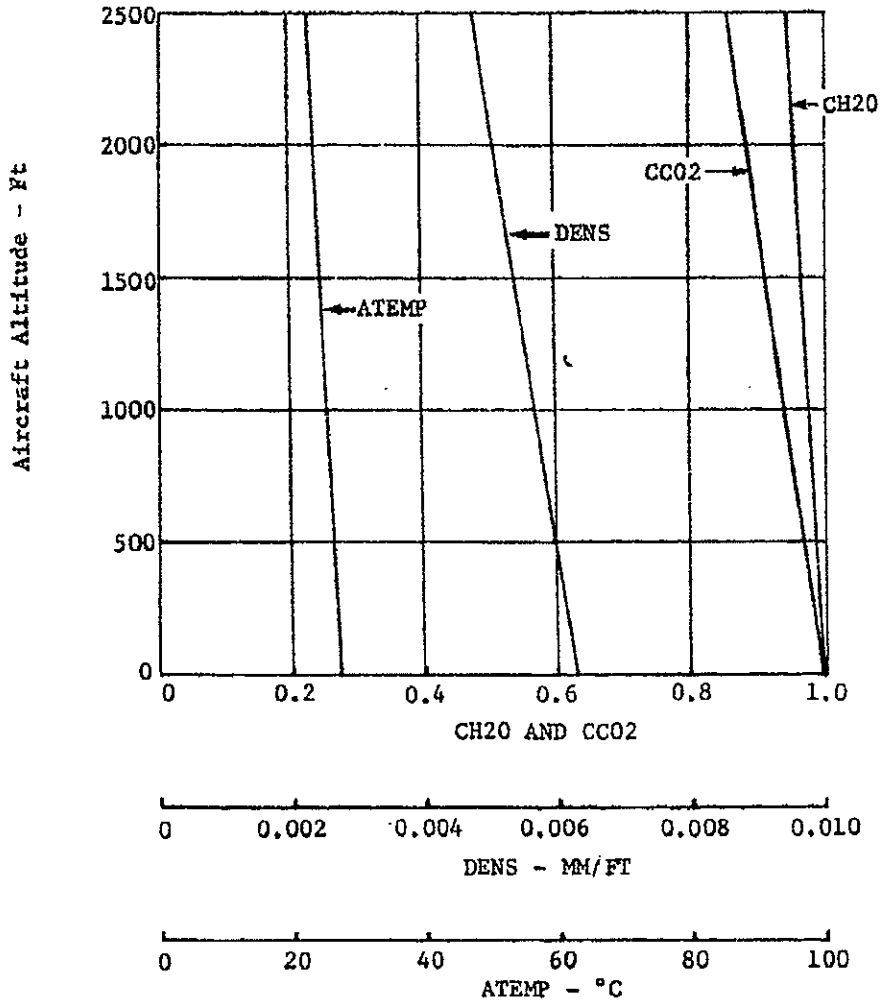

CH20 - Correction Factor for Water Vapor
CCO2 - Correction Factor for Carbon Dioxide
DENS - Saturated Air Precipitable Millimeters of Water per Foot
ATEMP - Atmosphere Temperature

(U) FIGURE 8-22
SIMULATION ASPECT AND SLANT PATH DATA

β Elevation Angle	β + Δ Aircraft Elevation Aspect Angle	S Slant Range (ft)	Equivalent Sea Level Values	
			Precipitable Millimeters of Water	Carbon Dioxide Path Length (Km)
0.00°	0.89°	323143.	1816.8	93.54
1.80°	2.01°	75405.	405.0	21.38
3.60°	3.71°	39249.	210.3	11.11
7.20°	7.25°	19925.	106.8	5.64
14.50°	14.53°	9969.	53.4	2.82
30.00°	30.01°	5024.	26.9	1.42
45.00°	45.01°	3529.	18.9	1.00
60.00°	60.01°	2896.	15.5	0.82
90.00°	90.00°	2500.	13.4	0.71

~~(C)~~ FIGURE 8-23
AAS-28A FLIR SYSTEM BEST POSSIBLE PERFORMANCE
WITH A 0.7 AIRCRAFT SURFACE EMISSIVITY

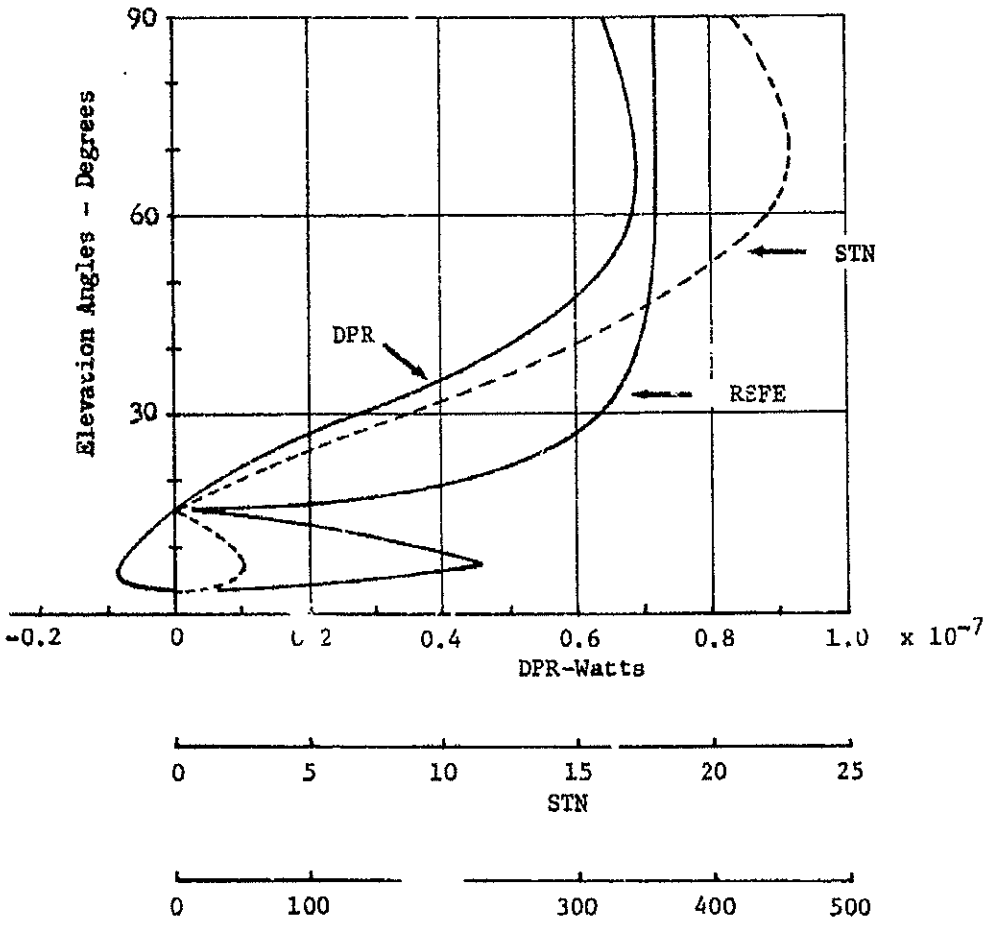

DPR - Differential Received Power
STN - Signal to Noise ratio
RSFE - Resolvable Number of Lines in Elevation

instantaneous field of view. This occurs when the peak signal to noise ratio increases to the same value as the maximum signal to noise ratio. A combination of the data in Figure 8-18, Figure 8-22 and Appendix C finds that this occurs when the elevation angle β is between 7.2° and 14.5°, as shown in Figure 8-24.

(a) (U) Spectral Signature - A differential received power inversion is shown to exist for this simulation (Figure 8-23) at approximately β = 16°. The position and existence of this inversion is dependent upon the atmosphere conditions, aerodynamic heating and surface emissivity. Its effect would be to increase the diffifulty the observer would have in detecting the QAA during its penetration run in. Figure 8-25 is a plot of the spectral differential received power distribution for the 0.7 aircraft surface emissivity, which can be integrated over the spectral band to provide DPR. This figure definitely illustrates two points concerning the detection of the airborne QAA, one relating to an optimum FLIR system spectral passband and the other to an optimum aircraft surface emissivity. The optimum FLIR system spectral passband, depicted by Figure 8-25, is approximately 8.5 to 11.5 micron. A FLIR system, such as the PINE FLIR, having this spectral passband would achieve a maximum utilization of the spectral differential received power, since it would have nearly the same sign over the spectral passband. This optimality, in addition to the atmospheric conditions, would explain the ability of the PINE FLIR to detect the airborne aircraft near the horizon in the field tests. Figures 8-26, 8-27 and 8-28 are included here to show the specific effect the aircraft surface emissivity has on the spectral differential received power. These data are for a 27°C, 80% relative humidity atmosphere; however, they are consistent in depicting the 8.5 to 11.5 micron spectral passband as being the optimum. A less humid atmosphere would yield different spectral differential received power values, but this difference would be a spectrally dependent positive shift in the zero axis with the predominant value existing in the 8.5 to 11.5 micron spectral band.

~~(C)~~ The data in Figure 8-24 and Figure 8-25 do present the implication that an optimum aircraft surface emissivity exists. Its existence would be to minimize the differential received power and in turn the signal to noise ratio. With this, Figure 8-29 contains data for several aircraft surface emissivity values. These data can be utilized to study the emissivity values which would minimize the QAA's probability of detection. Rosell and Willson, Reference (35), have formulated a relationship between the video signal to noise ratio and the target image size on the display in arriving at a parameter identified as display signal to noise ratio. This relationship for stationary target images is:

$$(S/N)_{display} = \left(\frac{\Delta f\ a\ t}{A}\right)^{1/2} (S/N)_{video} \qquad (30)$$

and can be employed here in determining the optimum emissivity. Where

$(S/N)_{display}$ = display signal to noise ratio

Δf = video bandwidth

a = target area on the display

t = eye integration time

A = display area

$(S/N)_{video}$ = video signal to noise ratio

CONFIDENTIAL
(This Page is UNCLASSIFIED)

(U) FIGURE 8-24
IMAGE EVALUATION, 0.7 AIRCRAFT SURFACE EMISSIVITY

Elevation Angle	Instantaneous Field of View Width in Feet	Maximum Signal to Noise Ratio (STN)	QAA Display Image Evaluation
0	155.10	0	
1.8	36.19	0	
3.6	18.84	0.00	
7.2	9.56	2.55	Either one or two scan lines across QAA. Peak signal to noise ratio of 1.28. Image limited to fuselage.
14.5	4.79	0.355	Between three and five scan lines across QAA. Peak signal to noise ratio of 0.355. Approximately 50% of wing should appear in image.
30	2.41	8.74	Between nine and eleven scan line across QAA. Peak signal to noise ratio of 8.74. All of wing and tail should appear in image.
45	1.69	17.0	Between nineteen and twenty-one scan lines across QAA. Peak signal to noise ratio of 17.0. All of the QAA should appear in the image.
60	1.39	22.1	Between twenty-eight and thirty scan lines across QAA. Peak signal to noise ratio of 22.1. All of the QAA should appear in the image.
90	1.20	20.7	Between thirty-seven and thirty-nine scan lines across QAA. Peak signal to noise ratio of 20.7. All of the QAA should appear in the image.

~~(C)~~ FIGURE 8-25
AAS-28A SIMULATION OF SPECTRAL DIFFERENTIAL RECEIVED POWER,
0.7 AIRCRAFT SURFACE EMISSIVITY

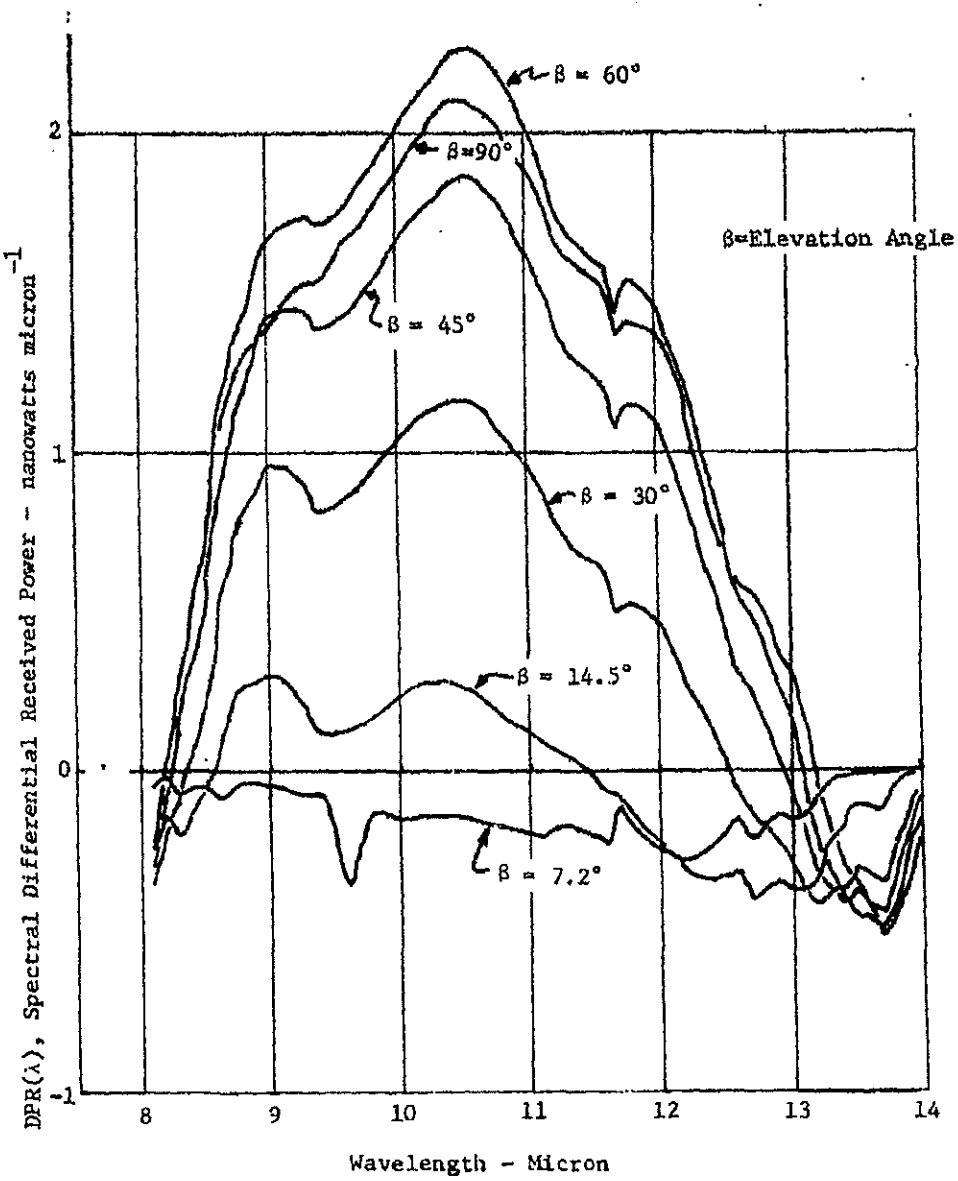

(C) FIGURE 8-26
AAS-28A SIMULATION OF SPECTRAL DIFFERENTIAL RECEIVED POWER,
7.2° ELEVATION ANGLE

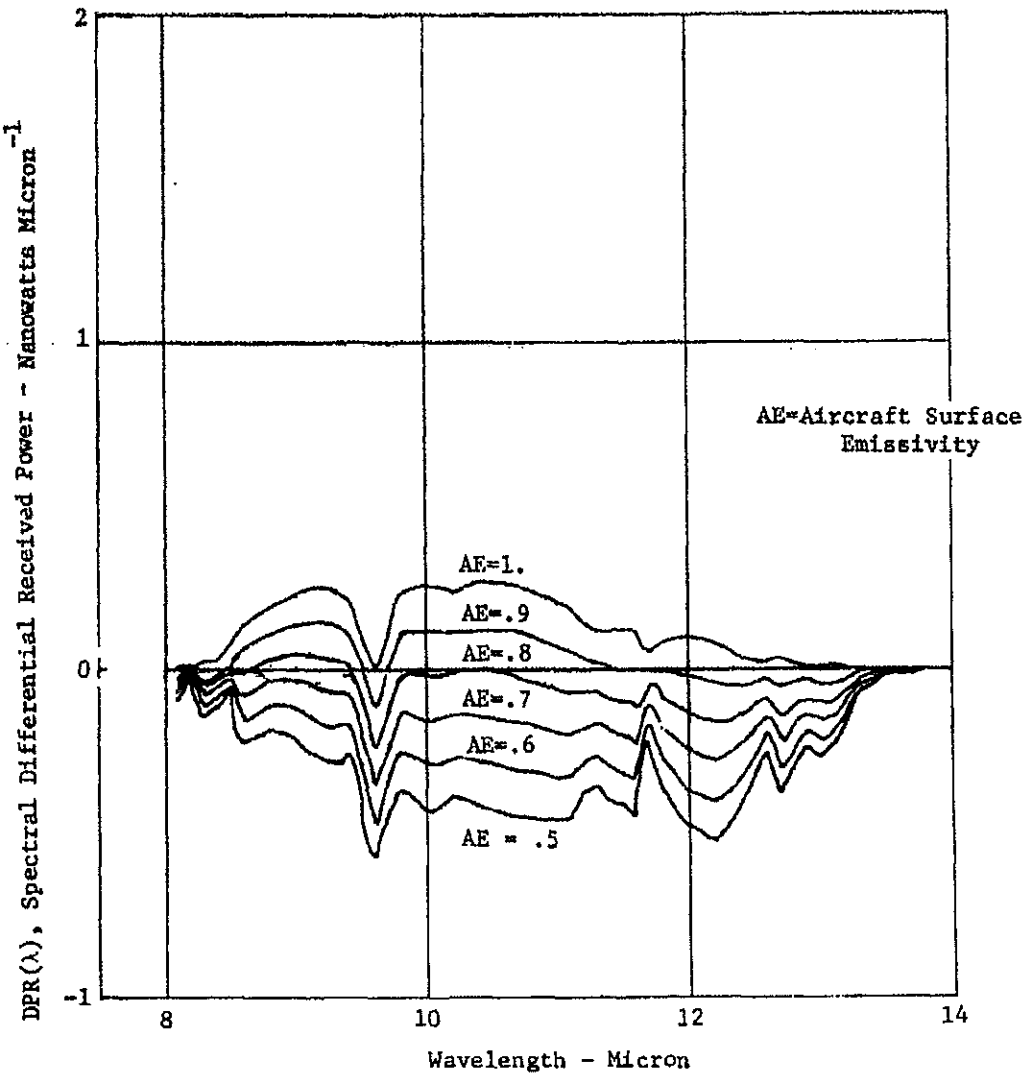

~~(C)~~ FIGURE 8-27
AAS-28A SIMULATION OF SPECTRAL DIFFERENTIAL RECEIVED POWER, 14.5° ELEVATION ANGLE

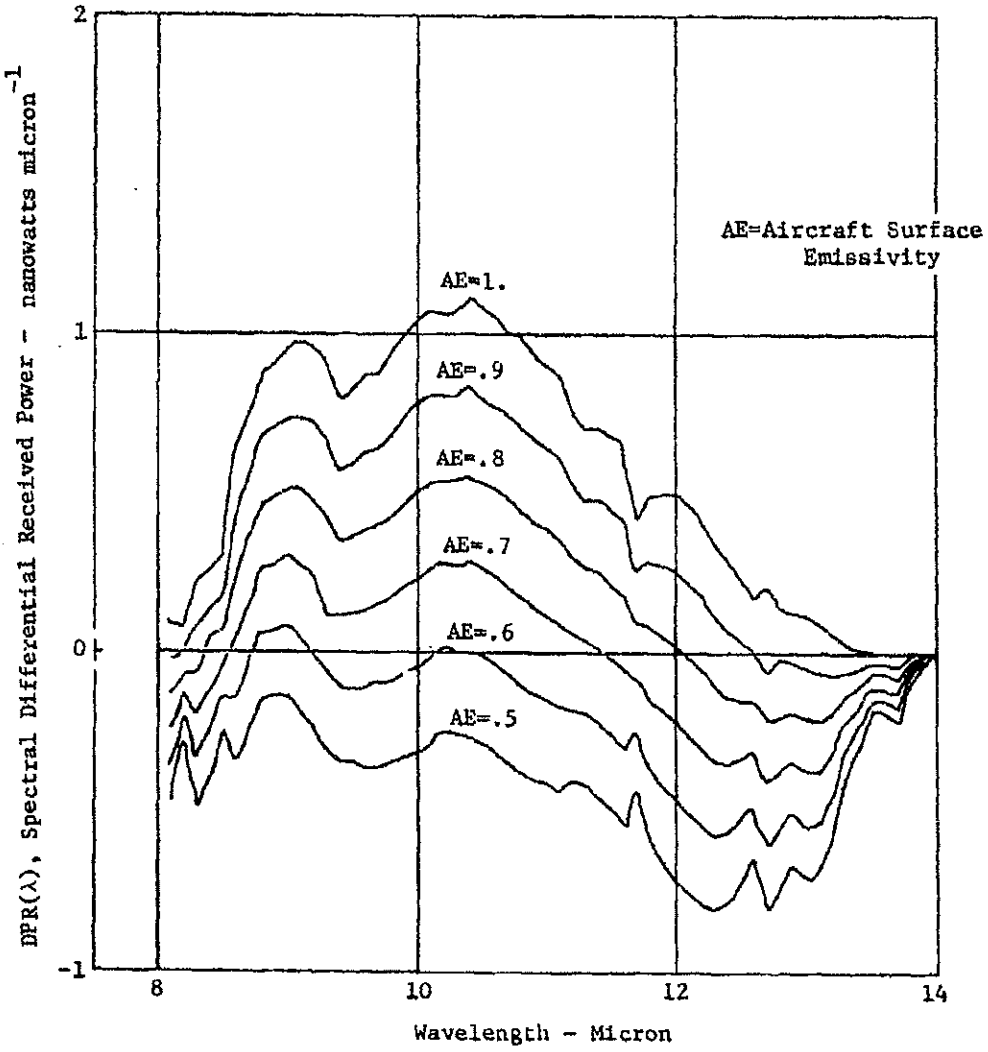

~~(C)~~ FIGURE 8-28
AAS-28A SIMULATION OF SPECTRAL DIFFERENTIAL RECEIVED POWER,
30° ELEVATION ANGLE

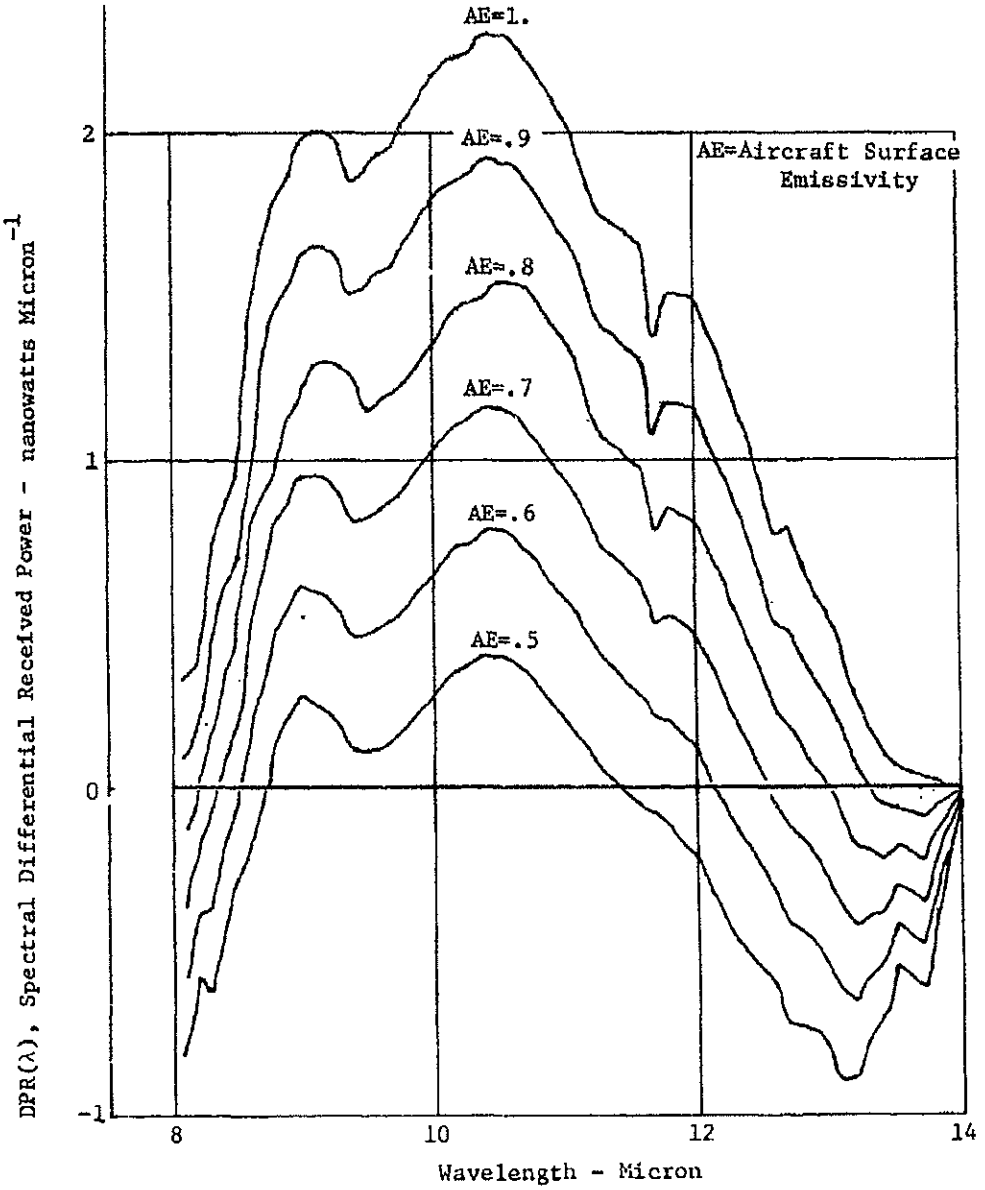

~~(C)~~ FIGURE 8-29
AIRCRAFT SURFACE EMISSIVITY STUDY, AAS-28A SIMULATION

Elevation Angle (Degrees)	Aircraft Surface Emissivity Values											
	$\epsilon = .5$		$\epsilon = .6$		$\epsilon = .7$		$\epsilon = .8$		$\epsilon = .9$		$\epsilon = 1.0$	
	DPR	S/N	DPR	S/N	DPR	S/N	DPR	S/N	DPR	S/N	DPR	S/N
0.0	-	-	-	-	-	-	-	-	-	-	-	-
1.8	-	-	-	-	-	-	-	-	-	-	-	-
3.6	-	-	-	-	-	-	-	-	-	-	-	-
7.2	$-.177 \times 10^{-7}$	5.72	$-.128 \times 10^{-7}$	4.14	$-.789 \times 10^{-8}$	2.55	$-.300 \times 10^{-8}$	0.970	$.189 \times 10^{-8}$	.613	$.679 \times 10^{-8}$	2.20
14.5	$-.243 \times 10^{-7}$	7.85	$-.127 \times 10^{-7}$	4.10	$-.110 \times 10^{-8}$	.355	$.105 \times 10^{-7}$	3.39	$.221 \times 10^{-7}$	7.19	$.336 \times 10^{-7}$	10.9
30.	$-.894 \times 10^{-8}$	2.89	$.904 \times 10^{-8}$	2.92	$.270 \times 10^{-7}$	8.74	$.450 \times 10^{-7}$	14.6	$.630 \times 10^{-7}$	20.4	$.810 \times 10^{-7}$	26.2
45.	$.114 \times 10^{-7}$	3.68	$.320 \times 10^{-7}$	10.3	$.526 \times 10^{-7}$	17.0	$.732 \times 10^{-7}$	23.7	$.938 \times 10^{-7}$	30.3	$.114 \times 10^{-6}$	37.0
60.	$.245 \times 10^{-7}$	7.91	$.464 \times 10^{-7}$	15.0	$.683 \times 10^{-7}$	22.1	$.903 \times 10^{-7}$	29.2	$.112 \times 10^{-6}$	36.3	$.134 \times 10^{-6}$	43.4
90.	$.184 \times 10^{-7}$	5.96	$.413 \times 10^{-7}$	13.3	$.641 \times 10^{-7}$	20.7	$.870 \times 10^{-7}$	28.1	$.110 \times 10^{-6}$	35.5	$.133 \times 10^{-6}$	42.9

DPR in watts

These parameters have the following values in the AAS-28A simulation.

Δf = 40000 Hz

a = refer to Figure 8-30

t = 0.2 seconds

A = (9 inches) (7.5 inches) = 67.5 $in.^2$

Rosell and Willson found that a value of (S/N) display = 3 yields an approximate probability of detection of 50% on the display; whereas, a (S/N) display = 4 would correspond to a 85% probability of detection. With this, the video signal to noise ratio can be computed that will yield the corresponding (S/N) display value. This has been done and the data is shown in Figure 8-30.

~~(C)~~ For the simulated atmospheric condition and aircraft flight 2500 ft. AGL, Figure 8-31 illustrates the effect of aircraft surface emissivity AE on the elevation angles, and thus slant range, where 50% and 85% probability of detection occur for a specific elevation angle. The video signal to noise ratios from Figure 8-30 have been converted to DPR and shown as dotted lines on Figure 8-31 for the two probabilities. Negative values of DPR indicate that the aircraft radiation received by the FLIR detector is less than the radiation received from the background sky, and vice versa for positive DPR values. Thus, there are two sets of probability curves because, as long as there is sufficient difference in received radiation or contrast between the aircraft and the sky, it makes no difference which is hotter. Obviously, when the differential received power DPR is zero there is zero contrast between the aircraft and background sky, and the probability of detection is also zero. This condition is approached, for all AE values, at long ranges where the elevation angle of the aircraft above the horizon is less than 10^o. The optimum emissivity is seen to be 0.6, which delays the 50% probability of detection until the aircraft has approached to an elevation angle of 28^o, corresponding to a slant range of 5300 ft. A lower emissivity of 0.5 is seen to be even worse than an emissivity of 1.0 because 50% probability first occurs at an elevation angle of 11.5^o (12,500 ft. slant range), after which the % probability reaches a peak at 20^o to 25^o, then declines to 0% at 36^o, and then increases again to 50% at 39^o. The spectrally dependent positive shift in the differential received power, for a less humid atmosphere, would yield a corresponding positive shift in the zero axis in Figure 8-31. Such a positive shift would force the 0.6 emissivity curve to cross the 50% probability of detection at a lower elevation angle, say $\beta = 20^o$.

(b) (U) Spatial Signature - The QAA's spatial signature, involving its apparent size and shape as seen by the FLIR, must necessarily be limited to the data given in Figure 8-24 and Appendix C. Figure 8-24 consists of the number of scan lines across the aircraft and the peak signal to noise ratio values; whereas, Appendix C is the projected visible surface as a function of selected elevation aspect angles with a zero azimuth aspect. Appendix B also needs to be incorporated into the ground to air FLIR model to compute the most probable QAA image on the display as a function of the elevation angle, because of smearing of the Appendix C image by the scanning mechanism. At this time, Appendix B is too complex to be incorporated into the mathematical model, and this is conservative because incorporating Appendix B would reduce the probability of detection.

(U) FIGURE 8-30
SIGNAL TO NOISE VALUES YIELDING 50% AND 85% PROBABILITY OF DETECTION

Elevation Angle β	x Approximate Aircraft Surface Area (Ft^2)	y Instantaneous Field of View Area (ft^2)	$1 \leq (\frac{x}{y})$	$a = (\frac{x}{y})\ b$ *	$(S/N)_{Video}$ with $(S/N)_{display}=3$	$(S/N)_{Video}$ with $(S/N)_{display}=4$
0°	90	24058.7	1	.0003516	14.7	19.6
1.8°	92	1310.0	1	.0003516	14.7	19.6
3.6°	100	354.9	1	.0003516	14.7	19.6
7.2°	110	91.5	1.20	.0004219	13.4	17.9
14.5°	180	22.9	7.86	.002763	5.24	7.00
30°	360	5.82	61.9	.02176	1.87	2.49
45°	500	2.87	174.	.06117	1.11	1.49
60°	610	1.93	316.	.1111	.827	1.10
90°	720	1.44	500.	.1758	.657	.876

* b = .0003516 in^2 per square scan line element

(C) FIGURE 8-31
AIRCRAFT SURFACE EMISSIVITY AND PROBABILITY OF DETECTION THRESHOLDS

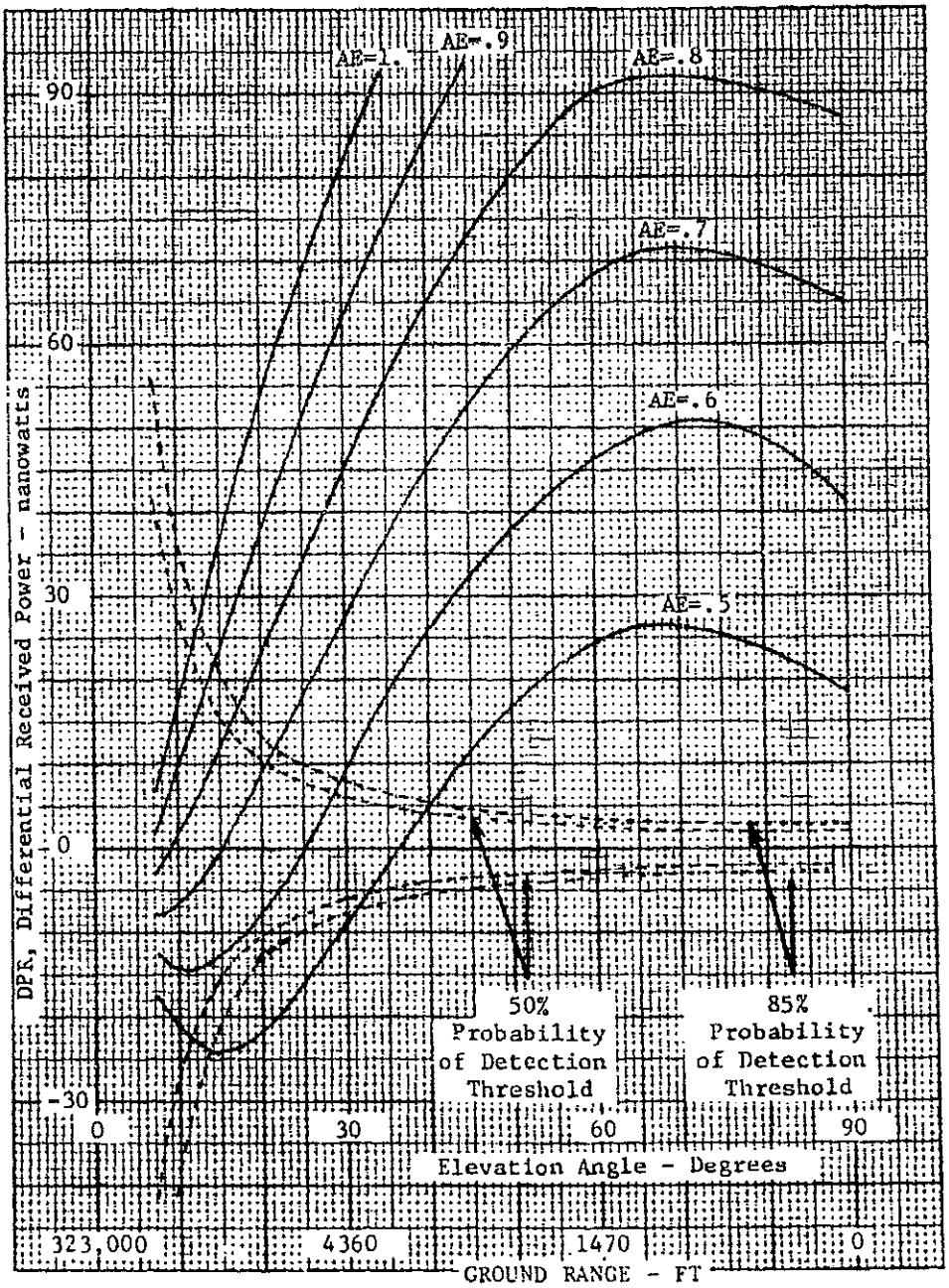

8.5 CONCLUSIONS

(U) The experimental work already performed shows that conventional aircraft have adequate signal level to be detected by current 8-14 micron FLIR systems. The sources of the signals have not been adequately defined by tests to make clear where the aircraft modification work needs to be concentrated.

(U) Modeling the airframe temperature contrasted with the background (sky) shows that at quiet speed the aircraft can be made to have the same output level as the background. This occurs with an achieveable surface emissivity of 0.6 and typical atmospheric conditions. For these typical conditions, a contrast level low enough for detection probability to be below 0.5 can be maintained down to ground ranges of less than 5000 ft. This ground range for detection could place severe constraints on the defending system using an airplane detection system of a FLIR type.

(U) The model is considered to be valid. However, specific additional tests would be necessary for final validation.

9. ACOUSTIC NOISE

(U) In Reference (1) the techniques for predicting the aerodynamic and propulsion noise generated by the aircraft were discussed, along with the acoustic detection range for an observer surrounded by different kinds of background noise when the aircraft is flying at quiet speed. At that time the aircraft, Model 226-454A, had two tip driven fans powered by a scaled GE1/10 gas generator, and quiet speed was based on a nominal wing lift coefficient of 0.8.

(U) The current quiet attack aircraft, Model 226-458 described in Section 2, has a General Electric TF-34 core gas generator driving two 23 inch tip driven fans of revised design, a higher weight, and higher lift coefficients. Since these changes affect both the aerodynamic and the propulsion noise, it has been necessary to recalculate noise and acoustic detection ranges. These new estimates of noise and detection range are still based on a clean aircraft carrying only internal bombs, but noise and detection ranges have been evaluated for the complete speed range from 1.2 V_{STALL} to maximum speed at 2500 ft altitude. An attempt was also made, without success, to predict the noise spectrum generated by external stores such as bombs and pylons. The lack of test data allows a theoretical development only. As was the case previously, propulsion noise has been suppressed, by the use of tip driven fans and duct acoustic treatment, to the point where it is less dominant than aerodynamic noise in determining acoustic detection range under any condition of speed or background noise.

(U) In this program, the prediction of source noise generated by the aircraft is based on empirical methods and data correlation of sound measurements for a large number of full scale aircraft and glider flyovers and by propulsion system ground tests. Since aerodynamic noise is dominant, minimum noise and detection range occur when the aircraft flies at minimum speed (1.2 V_{STALL}). At this condition Model 226-458 produces less noise than that previously shown in Reference (1) for Model 226-454A.

(U) The conclusions are that a practical carrier based attack aircraft can also be acceptably quiet when flown at low speed at low altitude. In extreme cases when there is little or no background noise around the ground observer the aircraft might be detected, but under typical conditions of background noise and observer activity the aircraft will be inaudible.

9.1 NOISE PREDICTION

(U) The unit of noise level in this study program is the decibel (dB) referenced to 10^{-13} watts for sound power level and .0002 dynes/cm^2 for sound pressure level. Other units, such as perceived noise decibels (PNdB) and effective perceived noise decibels (EPNdB), are generally measures of noise annoyance and are not applicable.

9.1.1 AERODYNAMIC NOISE - (U) Aircraft aerodynamic noise is composed of four significant sources: discrete frequency noise which contains cavity, protrusion and flow noise, wing vortex noise (the result of vortex shedding from the trailing edge of the airfoil), radiated boundary layer noise (the result of random fluctuating pressures caused by the turbulent boundary layer), and wake noise (the shearing effects between wake velocity air aft of a body and the freestream).

(U) Discrete frequency or tone noise is very critical since it may occur in the higher frequency range (frequencies above 500 Hz) at which the ear is most sensitive, and because it may be of high magnitudes. For an aircraft to be classed as aerodynamically quiet, it is essential that no tone noise from cavities and protrusions (antennas, wires, etc.) exist. Reference (36) points out that laminar flow at low angles of attack (less than 10^{o}) also creates tones as a result of vortices being shed from the airfoil trailing edge at a periodic or near periodic rate. These tones, which may extend up to 20 dB above the broadband noise level and are very difficult to predict, may be reduced or eliminated, without adverse aerodynamic effects, by attaching properly designed and located serrated strips near the lower leading edge of the airfoil to create turbulent instead of laminar boundary layer flow with random instead of periodic vortex shedding.

(U) A general equation was developed from measured data by Reference (37) to predict the aerodynamic overall sound pressure level (OASPL) from all sources excluding pure tone components. Wing trailing edge vortex shedding and the associated fluctuating lift are thought to be the primary noise sources, according to Reference (38). This prediction method in Reference (37) generally agrees within ± 5 dB with other measured data in References (38) and (39) for clean aircraft having no external stores or protrusions. The equation is as follows:

$$OASPL = 10 \log \left[\frac{V_{kt}^4}{h^2} \times \frac{W}{C_L} \times \frac{\bar{c}}{b} \right] + 6.4$$

With $\bar{c}/b = 1/AR$ this can also be expressed as:

$$OASPL = 40 \log V_{kt} - 20 \log h + 10 \log (W/C_L) - 10 \log AR + 6.4$$

For any given aircraft in level flight, the OASPL can be obtained by substituting for C_L and expressing speed in feet per second instead of knots which reduces the equation to:

$$OASPL = 60 \log V + 10 \log S - 20 \log h - 10 \log AR - 32$$

Where: V_{kt} = Velocity in knots V = Velocity in fps

$\bar{c}$ = Mean chord in ft S = Wing Area in ft^2

W = Weight in lb h = Distance from an observer in ft

C_L = Coefficient of lift AR = Aspect Ratio

b = Span in ft

Figure 9-1 shows the aerodynamic noise OASPL for an arbitrary wing area of 600 ft^2 and aspect ratio of 8 as a function of aircraft velocity for various distances between the aircraft and ground observer. A uniform directivity pattern is assumed. Noise is reduced 6 dB each time the distance is doubled for distances within several thousand feet, and increased 18 dB each time speed is doubled.

(U) FIGURE 9-1
TOTAL AERODYNAMIC NOISE OASPL

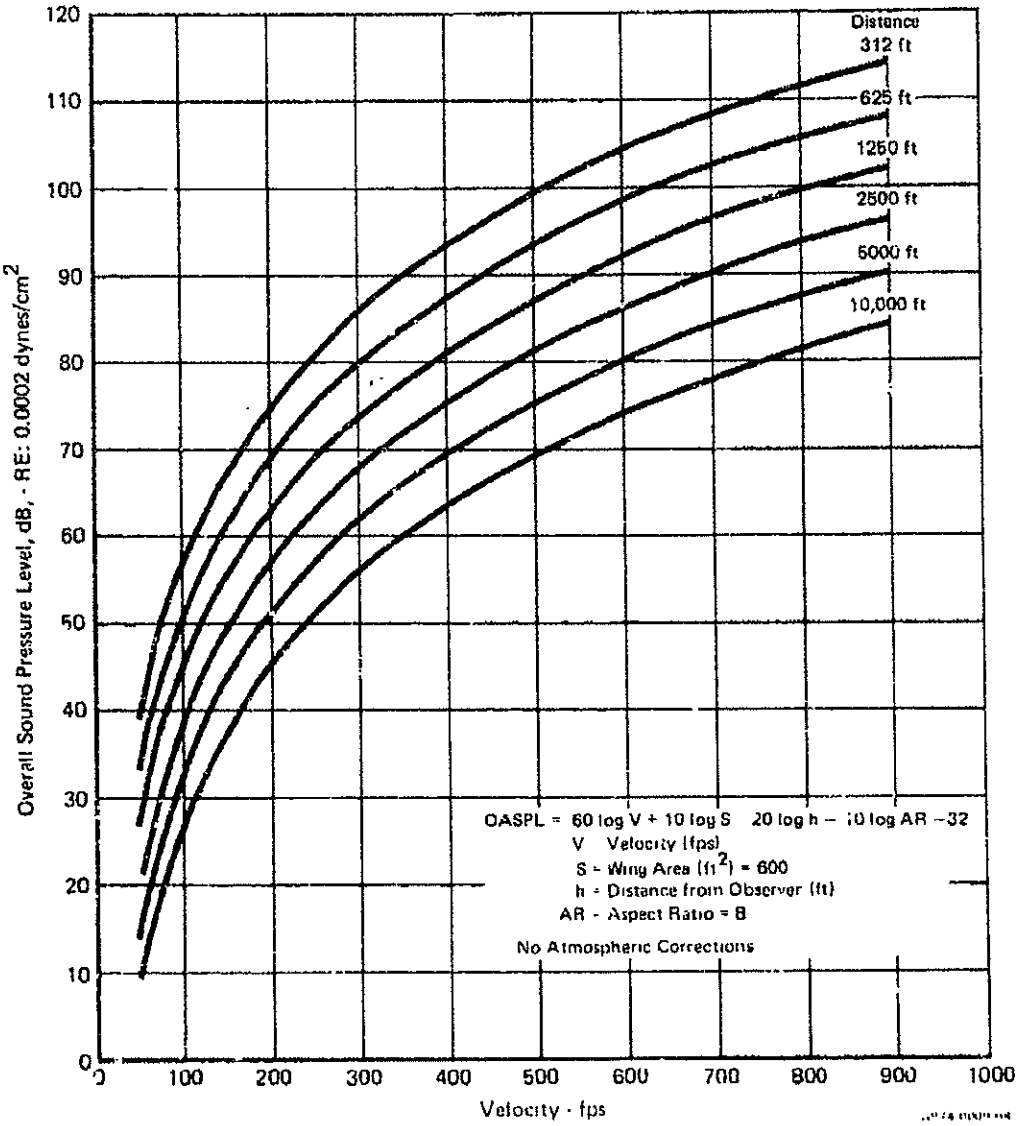

(U) The method for predicting the total aerodynamic noise spectrum was also developed from Reference (37). This method involves, first, calculating a prime frequency determined as:

$$f_{prime} = 1.1\ V/t$$

Where: f_{prime} = prime frequency

t = mean wing thickness in ft.

V = aircraft velocity in fps

Then the one-third octave band sound pressure levels (SPLs) are calculated according to the non-dimensional aerodynamic noise spectrum shown in Figure 9-2. This figure exhibits the relation between OASPL and the one-third octave band SPL for commercial and military aircraft and a low drag glider type aircraft. The spectrum are based on Reference (37), but the commercial and military aircraft spectrum is a modification to more accurately reflect the measured noise data.

(U) The prediction method also requires further correction of the spectrum for atmospheric attenuation as explained in Reference (40).

9.1.2 TIP DRIVEN FAN PROPULSION NOISE - (U) The prediction of propulsion noise at low power settings created considerable problems since the majority of engine test data, directivity index (DI) curves, and propulsion noise prediction methods are based on operation at full power.

(U) FIGURE 9-2
NONDIMENSIONAL AERODYNAMIC NOISE SPECTRUM

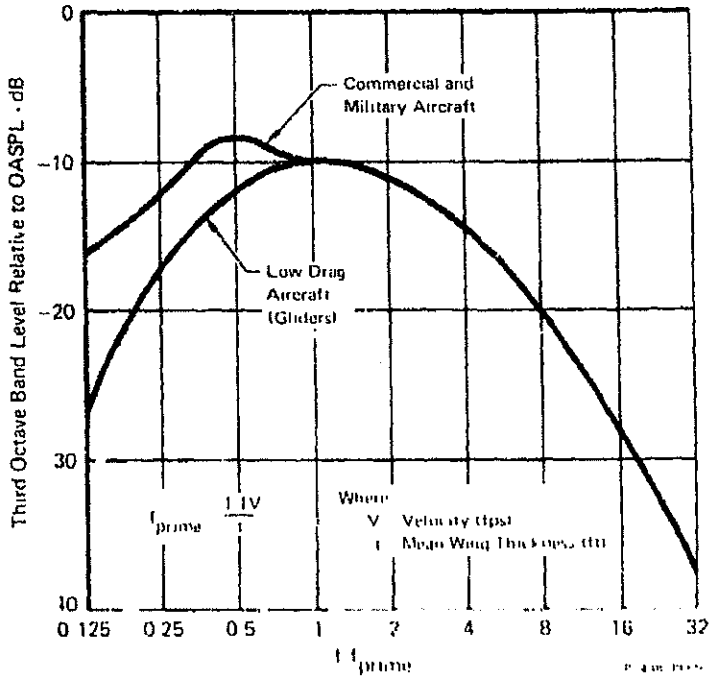

(U) After a comprehensive literature search, a method for predicting the spectrum shape of tip driven fans at low power settings was developed. The method calculates the fan and jet noise separately and then adds them logarithmically to produce the total tip driven fan spectrum. The steps are as follows:

(1) (U) The prediction method of H. D. Sowers, References (41) and (42), is used to predict the 100% RPM overall sound power level (OAPWL) source noise of the fan, based on no internal design features to reduce noise. This method is based on energy flux and other fan parameters as noted in Figure 9-3. Different type fans and compressors are spotted on the curve and show good correlation with the analytical curve.

(U) FIGURE 9-3
FAN AND COMPRESSOR NOISE
100% Static Thrust

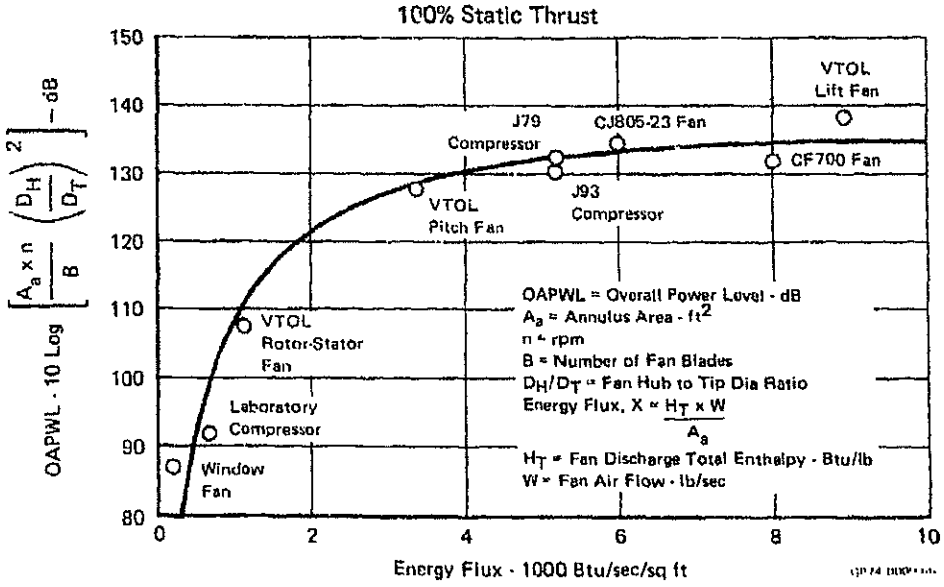

(2) (U) To this OAPWL, a correction factor of +6 dB is added which corresponds to measured data of tip driven fans having no internal design acoustic optimization (rotor-stator spacing, stator lean and number of blades and vanes) at 100% power.

(3) (U) This OAPWL is next corrected for operation at other than 100% RPM by utilizing the OAPWL vs Percent RPM curve of Figure 9-4 which is based on measured data.

(U) FIGURE 9-4
OVERALL SOUND POWER LEVEL vs PERCENT THRUST AND RPM
For Tip Driven Fan and Turbofan Power Plants

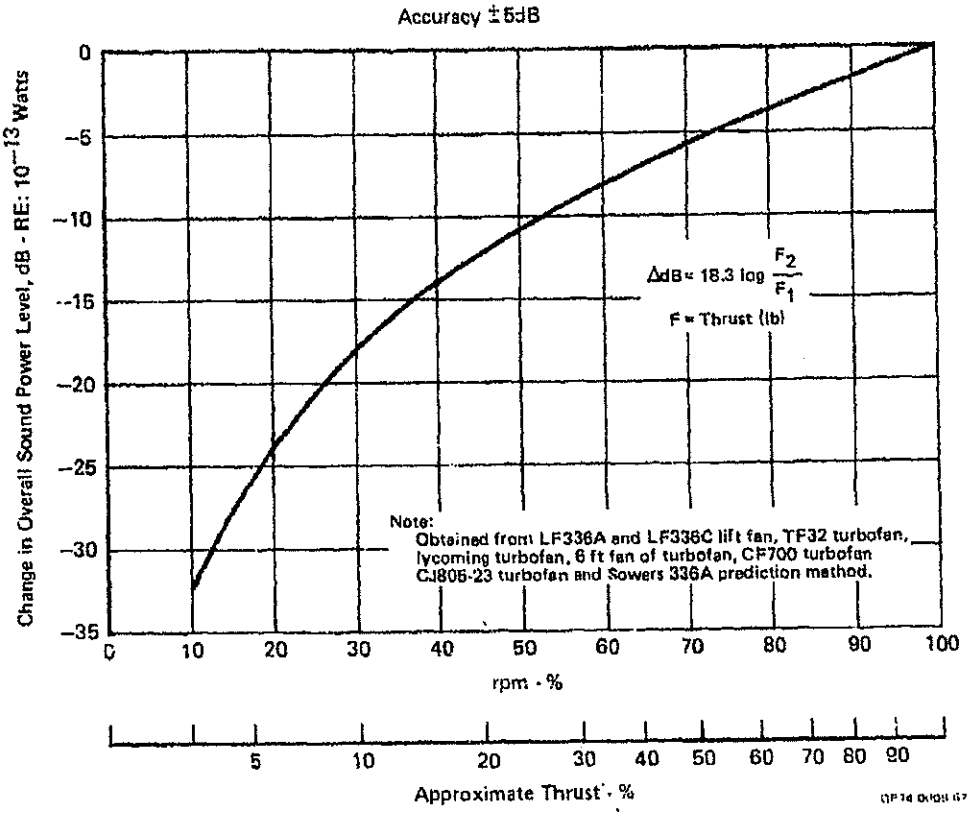

(4) (U) In order to determine the fan OASPL at any distance and azimuth angle, the OAPWL is corrected for spherical spreading, directivity index, number of fans and internal design optimization. Atmospheric attenuation will be applied later to the actual spectrum. The dB correction for spherical spreading is defined as $-10 \text{ Log}(4\pi h^2)$, where h is the distance in ft to the observer. The directivity index correction was developed from measured data, Figure 9-5, and represents power settings between 43 and 100% RPM. The dB correction for the number of fans is +10 log E, where E is the number of fans. The corrections, based on measured data, for optimum rotor-stator spacing, stator vane lean and number of blades and vanes are -4, -3.5 and -1.5 dB respectively. Thus, total internal optimization results in a -9 dB correction. Now, the absolute fan OASPL at reduced power for any distance and azimuth angle is available, excluding atmospheric attenuation.

(U) FIGURE 9-5
FAN DIRECTIVITY INDEX CURVES
Accuracy ± 1.5 ΔdB

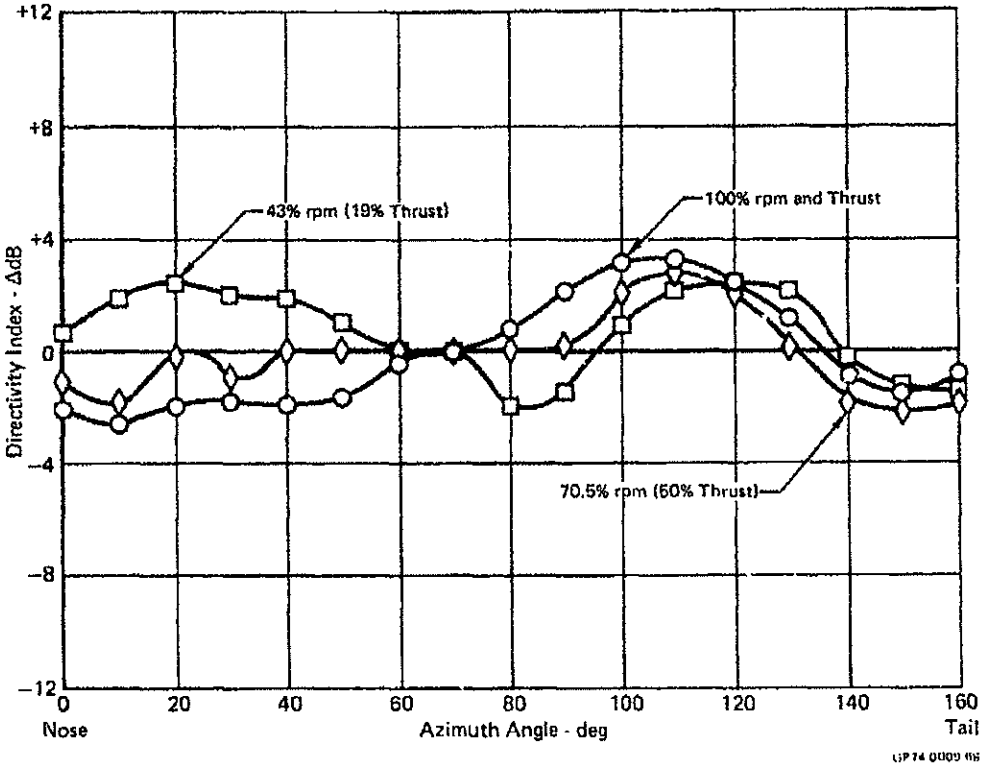

(5) (U) Optimum internal configuration tip-driven fan spectrums for the minimum power setting (43% RPM) used at quiet speed and various azimuth angles are shown in Figure 9-6. They are based on measured data, Reference (43), and are shown for a fan with a fundamental blade passage and second harmonic frequency of approximately 4000 and 8000 Hz respectively. Additional data indicates that at low power settings, the intensities at the fundamental and second harmonic frequencies attributed to blade passage are not significant. Therefore, no correction needs to be applied for other fans with different fundamental and second harmonic frequencies at these low power settings. The spectrum for fan noise only is given absolute levels by assigning the calculated OASPL in Step (4) above to the appropriate azimuth OASPL level noted in Figure 9-6.

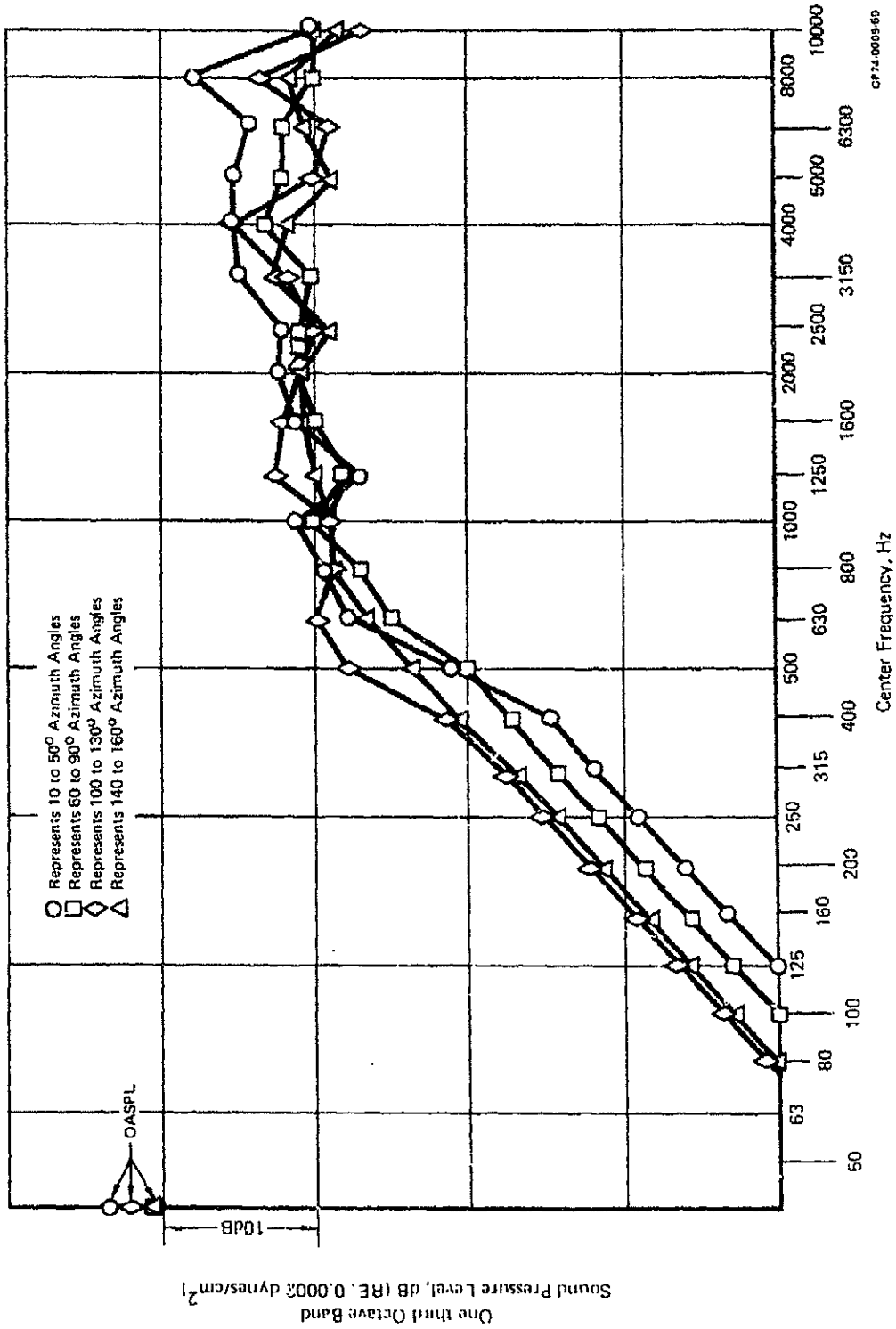

(U) FIGURE 9-6
FAN NOISE SPECTRUMS
Optimum Internal Configuration (Lean, Rotor-Stator Spacing, and Number of Blades and Vanes)
43% to 46% rpm

(6) (U) Next, the jet noise from the fan exhaust is determined, based on References (44) and (45). Reference (44) predicts the maximum jet noise of hot jets at a sideline distance of 200 ft (equivalent to a slant range of 400 ft) and an azimuth angle of approximately 150°. A line representing the term OASPL -10 $\log(\rho^2 A)$ is shown in Figure 9-7 as a function of jet relative velocity V_R (jet exit velocity minus flight speed) for the range 1000 to 4000 fps. The jet density (ρ) is calculated from:

$$\rho = W/AV_J$$

Where: W is the flow rate in lb/sec
A is the jet nozzle area in ft^2
V_J is the jet exit velocity in fps

(U) FIGURE 9-7
NORMALIZED JET NOISE vs JET RELATIVE VELOCITY
Jet Noise = Maximum Passby OASPL

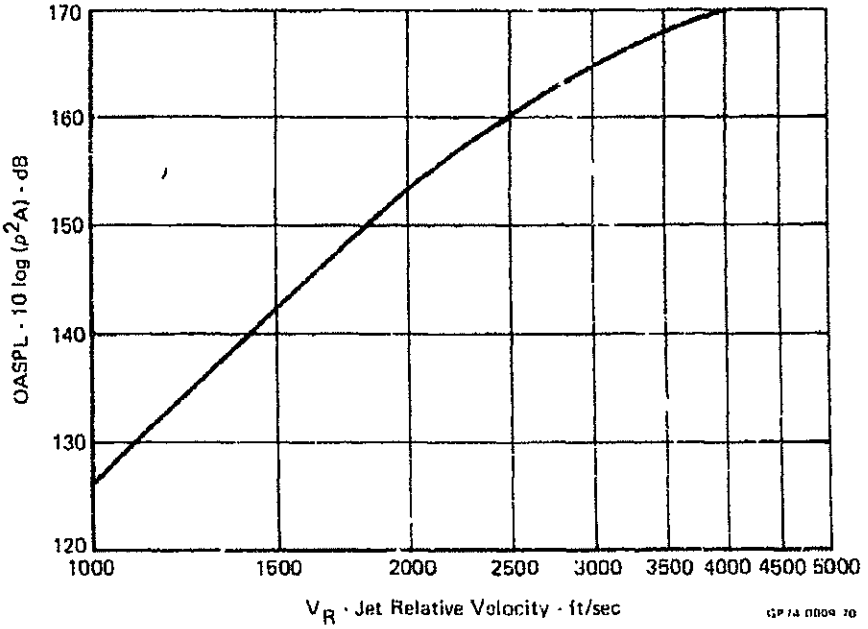

(U) Reference (45) predicts the noise of cold jets (which reflects jet density changes) and compares it to that of hot jets at a shorter sideline distance of 100 ft, equivalent to a slant range of 200 ft., and an azimuth angle of approximately 150°. Figure 9-8 represents the jet noise as a function of jet relative velocity for the lower range of 400 to 1000 fps. The SAE curve shown in Figure 9-8 is a linear extrapolation of the curve shown in Figure 9-7 with an adjustment of +6 dB to account for the shorter distance. The jet density curves are not extended above a relative velocity of 1000 fps because most tip driven fan jet relative velocities do not exceed this value. Therefore, the tip driven fan jet density is calculated as shown above for the selected fan RPM, and the line on Figure 9-8 representing a jet density closest to this calculated density is used to determine OASPL at a distance of 200 ft. and 150° azimuth. This OASPL is converted to Overall Sound Level at the source by adding 57 dB to account for the 200 ft. distance, and 0 dB to account for the directivity index for 150° azimuth at low power settings.

(U) FIGURE 9-8
SOUND LEVEL AS FUNCTION OF JET VELOCITY

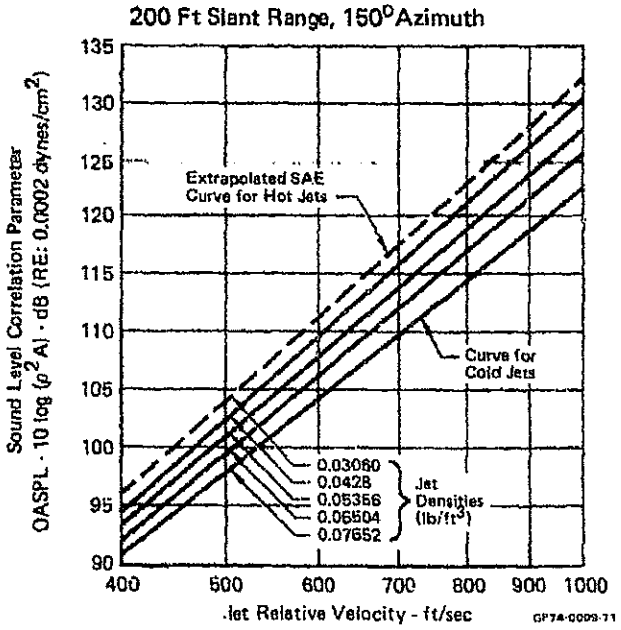

(7) (U) The jet noise OASPL at any other distance and azimuth angle may now be calculated by correcting the OAPWL for spherical spreading by subtracting 10 log ($4\pi h^2$). The correction for azimuth angle is obtained from the 30% thrust curve of Figure 9-9, taken from Reference (46).

(8) (U) The octave band spectrum of the jet noise is calculated by the procedure described in Reference (44). This technique requires the calculation of the Strouhal number for each octave band, (SN_n), from:

$$SN_n = \frac{f_n}{V_R / D_e}$$

Where: f_n is the geometric mean frequency in Hz for the particular octave band

V_R is the jet relative velocity in fps

D_e is the effective diameter of the jet exhaust (nozzle diameter in ft.).

(U) The jet noise absolute octave band SPL is determined by adding the flight spectrum f(SN) shown in Figure 9-10 from Reference (44) for each octave band, to the OASPL calculated in Step (7). The one-third octave band is obtained by subtracting 5 dB from each octave band.

(U) FIGURE 9-9
JET DIRECTIVITY INDEX

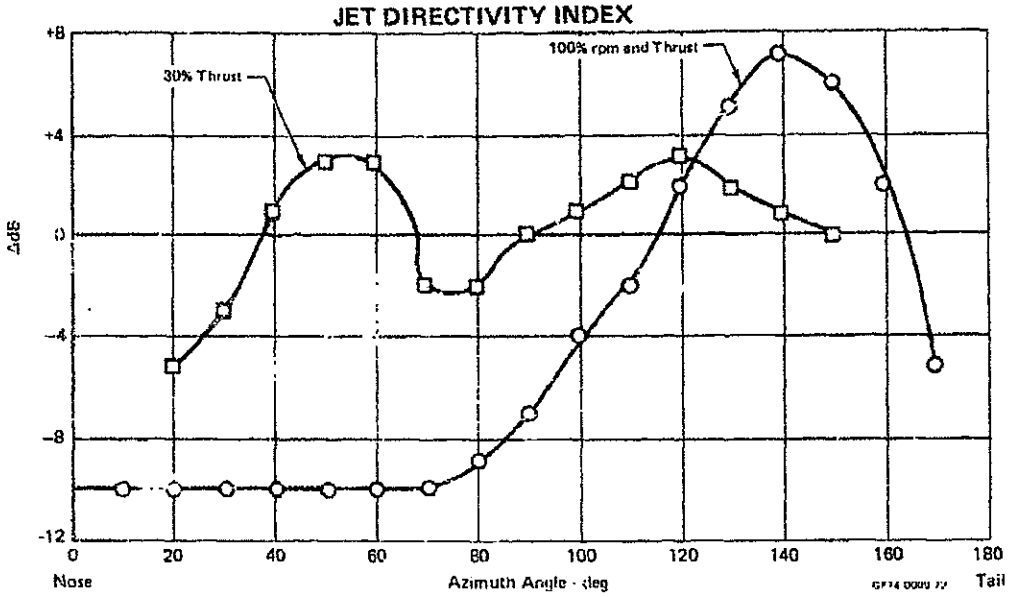

(U) FIGURE 9-10
OCTAVE-BAND JET NOISE vs STROUHAL NUMBER

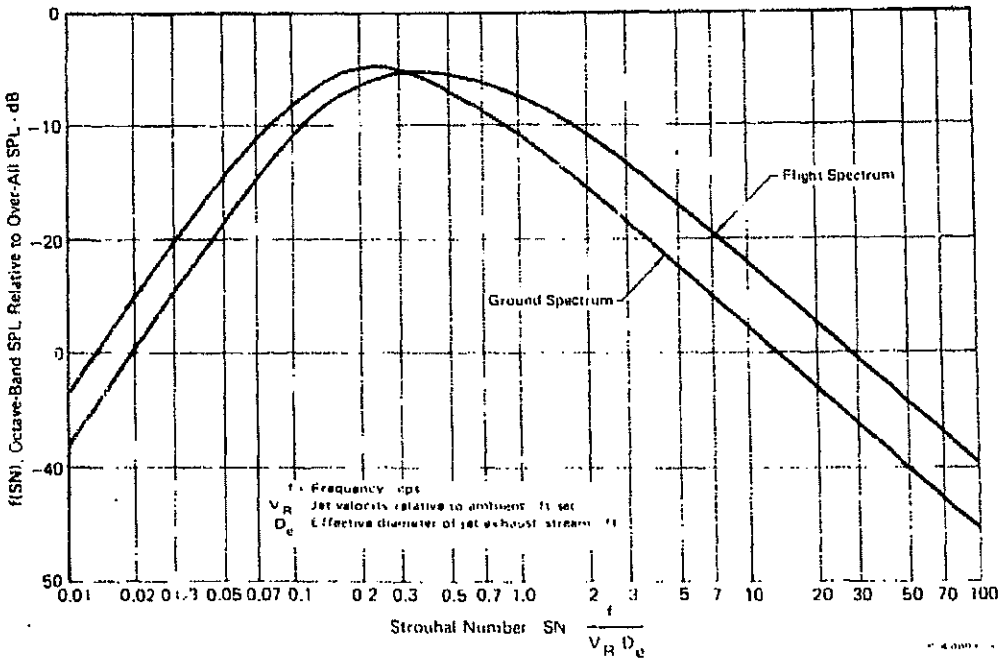

(9) (U) The separate spectra of fan and jet noise for the same fan RPM, distance, and azimuth are now added logarithmically to obtain the combined tip driven fan spectrum. This is then corrected for atmospheric attenuation as described in Reference (40).

9.1.3 INTAKE DUCT ATTENUATION OF PROPULSION NOISE - (U) A literature search, References (47) through (52), was made to evaluate the attenuation provided by unlined (no acoustic treatment) metal ducts with and without bends. The total attenuation provided by unlined ducts is a function of: (1) the transfer of acoustical energy to the duct walls, (2) the sound reflected by bends, and (3) the reflection of sound at the open end of the duct.

(U) Duct attenuation is provided by energy absorption due to damping in the walls. In general, soft-walled or flexible ducts absorb more acoustic energy and provide more attenuation than stiff walls. The walls of rectangular ducts tend to be less rigid than circular ducts. The attenuation provided by rectangular sheet metal duct walls may be estimated by Figure 9-11 from Reference (47). An illustration of attenuation for circular ducts of 4 to 12 inch diameter is shown in Figure 9-12 from Reference (48).

(U) FIGURE 9-11
APPROXIMATE ATTENUATION IN BARE RECTANGULAR SHEET METAL DUCTS

Duct	Size, in.	Frequency, Hz			
		20-75	75-150	150-300	Above 300
		Attenuation, dB/ft			
Small	6 x 6	0.2	0.2	0.15	0.1
Medium	24 x 24	0.2	0.2	0.1	0.05
Large	72 x 72	0.1	0.1	0.05	0.01

GP 74 0009 74

(U) FIGURE 9-12
APPROXIMATE ATTENUATION IN BARE ROUND RIGID METAL DUCTS

Duct	Diameter Size, in.	Frequency, Hz	
		Below 1000	Above 1000
		Attenuation, dB/ft	
Small	4 to 12	0.03	0.1

GP74 0009 75

(U) The attenuation provided by unlined 90° bends is also small, as shown in Figure 9-13 from Reference (49), since in the absence of any sharp mismatch of impedance which would reflect sound energy, there is little to prevent the sound from flowing around the bend. Although little data exists regarding the attenuation of bends less than 90°, as an approximation one may assume that the attenuation is proportional to the angle, see Reference (50). For example, one may estimate the attenuation of a 30° bend to be one-third that of a 90° bend.

(U) FIGURE 9-13
APPROXIMATE ATTENUATION OF ROUND ELBOWS

Diameter or Dimensions, In.	Octave Band Center Frequency, Hz							
	63	125	250	500	1000	2000	4000	8000
	Attenuation, dB							
5-10	0	0	0	0	1	2	3	3
11-20	0	0	0	1	2	3	3	3
21-40	0	0	1	2	3	3	3	3
41-80	0	1	2	3	3	3	3	3

GP74 0009 76

(U) End reflection losses occur when a duct opens abruptly into a large space, and vary with the frequency of sound and with the size and shape of the duct opening. These losses occur because the sudden enlargement of the duct to space acts as a sound reflecting barrier. These losses are explained in Reference (49) and are shown in Figure 9-14. The duct size used to calculate the end-reflection losses is that which exists several wave lengths before the opening.

(U) FIGURE 9-14
END REFLECTION ATTENUATION

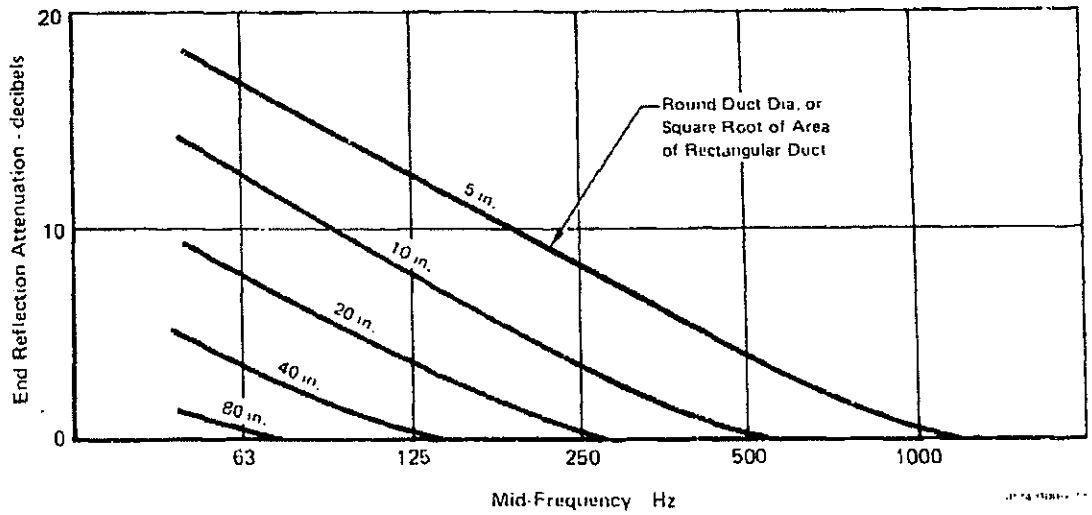

9.2 NOISE OF FLAPS AND STORES

(U) The predominant source of noise of the Quiet Attack Aircraft at quiet speed is aerodynamic noise. For minimum noise, an aerodynamically clean aircraft is required - one that eliminates or minimizes noise-inducing separated airflow. This would indicate no use of high lift devices (flaps) and no external stores. However, flaps may eventually be added to improve takeoff and landing performance with external stores, in which case the flaps could also be used to reduce quiet speed if the flap noise is not excessive. External bomb carriage is most desirable to greatly increase the payload over what can be carried in the fuselage internal bomb bay. Thus, there is a definite need of prediction methods to accurately estimate flap and external stores noise spectrums which can then be added to the clean aircraft spectrum to determine detection range. Radiated aerodynamic noise data of flaps and external stores are either very limited or nonexistant. Development of accurate prediction techniques for the noise spectrums of flaps and stores is a complex task which will probably require extensive measured data for correlation.

9.2.1 FLAPS - (U) The noise of flaps is similar to that which occurs when airflow impinges on an oblique surface. An extensive literature search of blown flap noise, References (53) through (68), and jet impingement noise, References (69) through (75), was made. It appears that OASPL flap noise is a function of the sixth power of the velocity, is highly directional and contains considerable low frequency (less than 1000 Hz) energy.

(U) Data on radiated aerodynamic noise generated by deflected flaps are presently limited to the following:

o Effective perceived noise level (EPNdB) data, Reference (68), of the Boeing 727 and Boeing 747 commercial aircraft with flaps and landing gear extended. Increases in noise of 10 to 12 EPNdB over that produced by a clean aircraft were stated. Boeing has spectral data but has not published it. Effective perceived noise level is a single number of rating "noisiness" or "annoyance" of an aircraft flying overhead, and is based on the calculated loudness level of the noise plus an adjustment for duration and pure-tone content. The problem is that there is no way to start with a single number for noise such as EPNdB or PNdB and work back to determine the corresponding noise spectrum. Besides being a one-number rating unit, the increase in EPNdB stated in Reference (68) included both flap and gear effects but not flap effects alone.

o EPNdB data, Reference (38), of the Lockheed C-5A aircraft. The test results indicate an increase of approximately 9 EPNdB with both flaps and gear extended. Tests of each of these items extended individually indicate that most of the noise increase is a result of the gear and not the flaps. Lockheed postulates that the inherent geometry of the C-5A's flaps may limit flap noise generation.

(U) The NASA Flight Research Center at Edwards Air Force Base is currently measuring the aerodynamic noise of airplanes with their engines throttled back or turned off, and with their flaps and landing gear in various positions. The tests are to include a twin-engine propeller-driven aircraft, a four-engine jet executive aircraft and a four-engine jet transport. The program is aimed at distinguishing the various sources of aircraft aerodynamic noise. Test results are not available yet.

(U) Limited available data of noise generated by flaps of aircraft indicate that the flaps could increase the total radiated OASPL noise by very little to as much as 12 dB. Until additional data of flaps of various size and type become available and is correlated with data of blown flaps and jet impingement noise, accurate prediction methods of aircraft with any type of flap will be quite difficult.

9.2.2 STORES - (U) Aerodynamic radiated noise spectrum data of bombs and of aircraft with external bombs installed are nonexistent. Bomb related data, References (76) through (86), is limited to surface measurements of the boundary layer fluctuating pressure on bombs at transonic rather than low subsonic Mach numbers. The approximate surface noise of fully turbulent boundary layers that contain no separated regions has been defined by most theoretical and experimental investigators, References (87) through (102), at high subsonic (greater than Mach 0.8) and transonic Mach numbers as:

$$OASPL = 20 \log q + 83 = 10 \log q^2 + 83$$

Where: OASPL is the surface overall sound pressure level in dB and q is the dynamic pressure in lb/ft^2

It has been found that local surface boundary layer pressure fluctuations on bombs may be as much as 25 dB greater if the flow is separated. The above expression for unseparated flow shows the surface OASPL to be proportional to the fourth power of velocity at Mach numbers greater than about 0.8. On the other hand radiated aerodynamic noise of aircraft, airfoils and bodies has been found to be proportional to the sixth power of velocity for Mach numbers less than 0.3. This suggests the possibility of a situation similar to that for jet noise in which low velocity jet noise is proportional to V^8 and high velocity jet noise is proportional to V^3. An obvious technique for predicting radiated aerodynamic noise from external bombs would then be to allow a dependence upon velocity to vary from V^6 to V^4 with increase in Mach number, and to follow the method postulated in a previous Technical Report, Reference (103). This is to determine the surface noise per unit area for each section of the store, integrate the noise over the section, logarithmically add the noise of each section, and then apply spherical spreading and atmospheric attenuation. Such a technique, however, may not cover interference noise between the bomb suspension system and the wing unless there is separated flow on the bomb. In any event, lack of measured data for correlation prevents the establishment of a high degree of confidence in any current prediction technique.

(U) An attempt was made to relate the radiated aerodynamic noise of "dirty" aircraft having protuberences other than bombs (landing gear, sensor housings, etc.) to an aircraft with bombs attached. Reference (37) contains measurements of airframe noise of a Cessna 150 with fixed landing gear. The noise of this "dirty" aircraft was approximately 5 dB higher for all frequencies over that predicted for a clean aircraft. The geometry of this gear structure, however, is not similar to bombs and, consequently, it is difficult if not impossible to relate this noise to an aircraft with bombs. Measured data of the YO-3A aircraft, Reference (104), indicates an increase in noise of several dB for most frequencies when the mission equipment (illuminator and periscope) is installed. However, the radiated noise of the clean aircraft is controlled by propulsion noise, and the addition of the mission equipment imposes an approximate 20% increase in horsepower requirement of the engine. Since the propulsion system dominates part or possibly all of the noise spectrum

for both configurations, the actual effect of the mission equipment on aerodynamic noise cannot be determined.

(U) It is apparent that the radiated noise of stores is very complex. Lack of measured radiated aerodynamic noise data of bombs slows development of a prediction method. It is probable that a drag term needs to be incorporated into the empirical radiated aerodynamic noise prediction equation in order to estimate the effects of "dirty" aircraft.

9.3 ACOUSTIC DETECTION RANGE

(U) As the distance between the aircraft and observer increases, the spectrums for aerodynamic and propulsion noise reaching the observer become progressively weaker, in terms of dB for each one-third octave band, due to the combined attenuation from distance and atmospheric absorption. The acoustic detection range is defined as the slant range at which the received spectrums from the aircraft both fall completely below the spectrum used as the detection criteria. This condition is illustrated by Figure 9-15, where the dotted spectrum is the nominal detection criteria used in this study and represents the hearing threshold of an average soldier with no background noise around him.

(U) When there is background noise heard by the observer the background noise spectrum is higher than the observers threshold of hearing spectrum, and this is illustrated by Figure 9-16 for different background noises. The "Virginia Coast" spectrum represents light surf breaking on a seashore 175 ft. away from the observer. The "Typical Wet Day Jungle" represents the noise of insects and dripping moisture on the floor of a tropical jungle in Panama. Although this jungle spectrum is sometimes advocated as a detection criteria, it is not considered valid since most of it lies below the average hearing threshold and thus could not be heard by an average observer. Audible background noise reduces the acoustic detection range because the aircraft must be closer and therefore noisier, to be heard over the background noise.

(U) There are a number of other factors which act to reduce the acoustic detection range, but which have been conservatively neglected in this study. One is the aircraft noise attenuation due to deep grass or foliage, which is most effective when the aircraft is at a low elevation angle from the observer. Another is the turbulent boundary layer of the earth, extending up to about 1500 ft. above ground level. Still another is a whole class of psychological factors such as the observer being under stress, concentrating on some work task instead of listening intently, or the similarity between the dominant aerodynamic noise and the sound caused by the wind blowing.

9.4 NOISE ANALYSIS OF QUIET ATTACK AIRCRAFT MODEL 226-458

~~(C)~~ Due to the new propulsion system characteristics and quiet speed, the aerodynamic and propulsion noise and detection distances previously determined for Model 226-454A were recalculated for Model 226-458 for a clean aircraft with internal bombs only.

(U) FIGURE 9-15
ACOUSTIC DETECTION CRITERIA

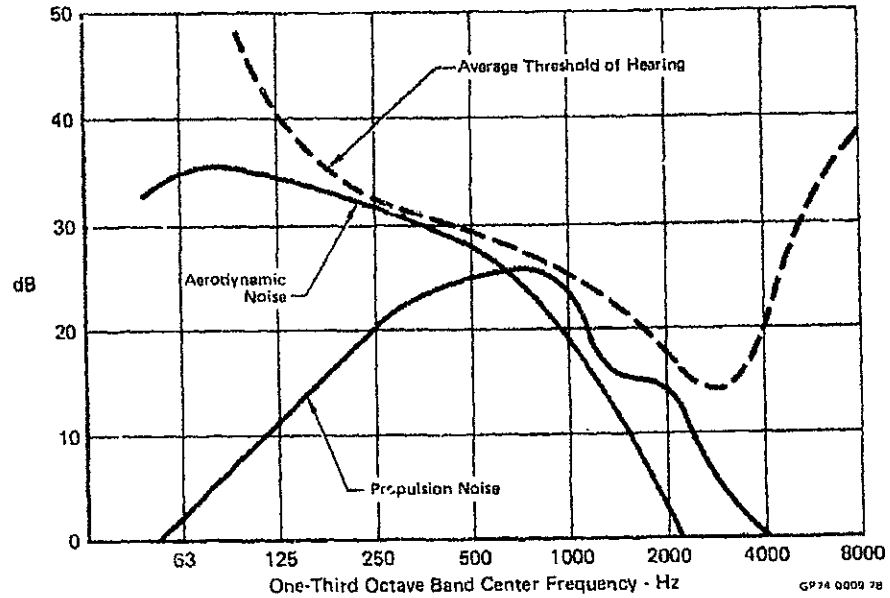

(U) FIGURE 9-16
THRESHOLD OF HEARING AND BACKGROUND NOISE

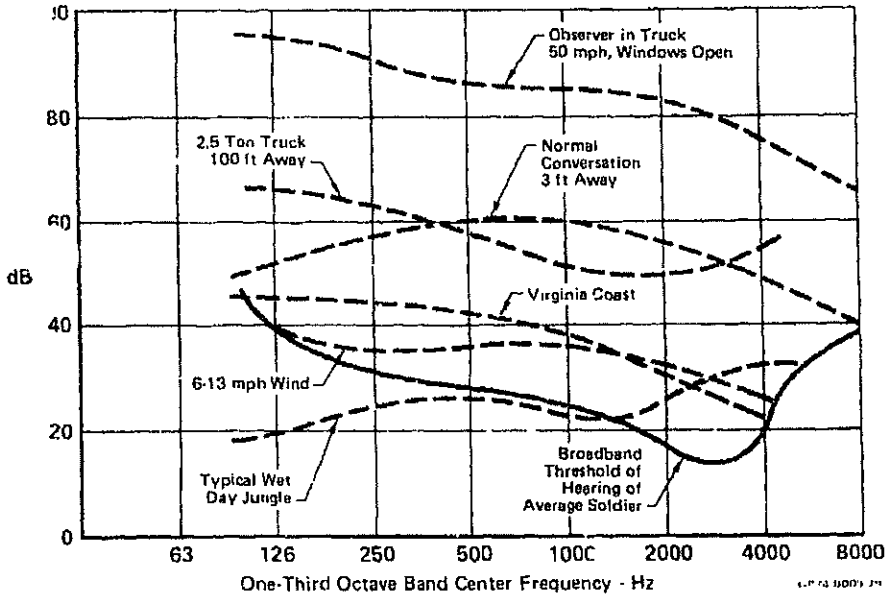

~~(S)~~ The aerodynamic noise parameters of this aircraft, Model 226-458, are: combat weight (W) - 14223 lb., wing area (S) - 400 ft^2, wing aspect ratio (AR) - 8, and mean wing thickness (t) - 1.06 ft. The aircraft was evaluated at velocities ranging from 98 to 445 knots corresponding to coefficients of lift (C_L) of 1.165 to 0.057, respectively. 98 knots is 1.2 V_{STALL} and 445 knots is top speed at 2500 ft. The calculated aerodynamic OASPL's and prime frequencies, and corresponding aircraft speeds and coefficients of lift are compared in Figure 9-17 for a distance of 5000 ft. The resultant aerodynamic noise spectrums, as well as the propulsion noise spectrums, at a distance of 5000 ft and azimuth angle of 30° are shown in Figure 9-18. It should be noted that measured data of radiated aerodynamic noise has been measured only up to approximately 200 knots, but for lack of anything better the same prediction method has also been used for higher speeds.

~~(S)~~ FIGURE 9-17
AERODYNAMIC NOISE AND PRIME FREQUENCY
2500 Ft Altitude 5000 Ft Distance

Velocity Knots	Coefficient of Lift	OASPL dB	Prime Frequency Hz
98	1.165	44	173
115	0.857	48	202
150	0.503	55	264
250	0.181	68	459
350	0.092	77	613
445	0.057	84	781

0P74 0009 99

~~(C)~~ The spectrums in Figure 9-18 include the effects of atmospheric absorption and show that aerodynamic noise is the predominant source that controls detectability. The aerodynamic noise varies with the sixth power of the flight velocity and increases approximately 40dB as the flight speed increases from 98 to 445 knots. The fan portion of propulsion noise is dependent on the power setting of the engine. Flight speeds from 98 to 445 knots require power settings of 50 to 97% fan RPM respectively, which result in a fan noise increase of 10 dB. The jet exhaust velocity of the tip driven fan for the same speed range increases from 450 to 850 fps; however, the relative jet velocity, which determines the jet portion of the propulsion noise, decreases from 284 to 98 fps and results in a jet noise reduction of 37 dB. The horizontal dotted lines for propulsion noise at 98 and 115 knots represent jet noise, which effectively disappears at higher speeds.

~~(C)~~ The propulsion noise of this aircraft is generated by the two tip driven fans. The propulsion system noise parameters that are independent of aircraft speed are: design pressure ratio - 1.5, number of blades - 41, annulus area - 2.18 ft^2, tip diameter - 23 in, hub diameter/tip diameter - 0.5 and internal design optimization. The fan noise prediction method requires calculating the noise at full power and correcting for operation other than 100% RPM. At full power the remaining design parameters are fan airflow - 85 lb/sec per fan and fan enthalpy - 140 Btu/lb.

~~(C)~~ FIGURE 9-18
AERODYNAMIC AND PROPULSION NOISE SPECTRUMS
Model 226-458 at 5000 Ft Slant Range

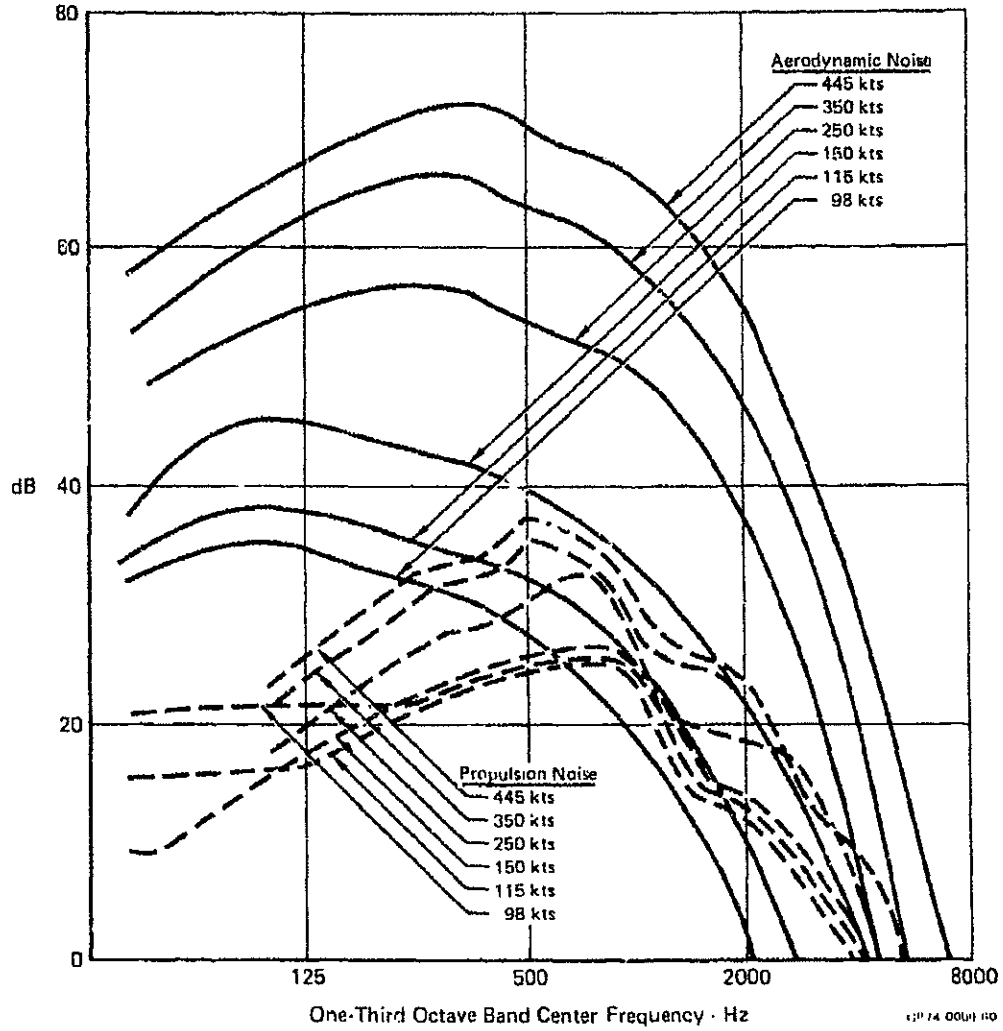

~~(C)~~ Fan RPM and relative jet parameters that are dependent on aircraft speed, and the corresponding fan and jet propulsion noise at a distance of 5000 ft. and an azimuth angle of 30° are shown in Figure 9-19. The method in Section 9.1.2 was used exclusively to determine the propulsion noise at low power settings (fan RPM 51% and less). At fan RPM greater than 51%, revised spectrum shapes similar to those in Figure 9-6 were developed. Figure 9-20 shows these revised fan spectrums for azimuth angles 10 to 50° at different ranges of fan RPM. They are based on measured data from Reference (47), and the spectrum at the low RPM range is the same as the 10 to 50° azimuth angle spectrum shown in Figure 9-6. The 86 to 100% RPM spectrum represents a fan with a fundamental blade passage and second harmonic frequency of 4000 and 8000 Hz respectively.

~~(C)~~ FIGURE 9-19
PROPULSION SYSTEM PARAMETERS AND NOISE

Aircraft Velocity (knots)	Percent Fan rpm	Fan rpm	(2) Fan OASPL (dB)	Jet Relative Velocity (fps)	(2) Jet OASPL (dB)
98	50	6,225	61	284	32
115	47.5	5,910	60	236	25.5
150	51	6,350	61.5	196	19
250	69	8,600	65.5	178	16
350	86	10,700	69.5	158	12
445	97	12,070	71	98	0

(U) FIGURE 9-20
REVISED FAN NOISE SPECTRUMS
Optimum Internal Configuration (Lean, Rotor-Stator Spacing, and Number of Blades and Vanes)
Represents 10 to 50° Azimuth Angles

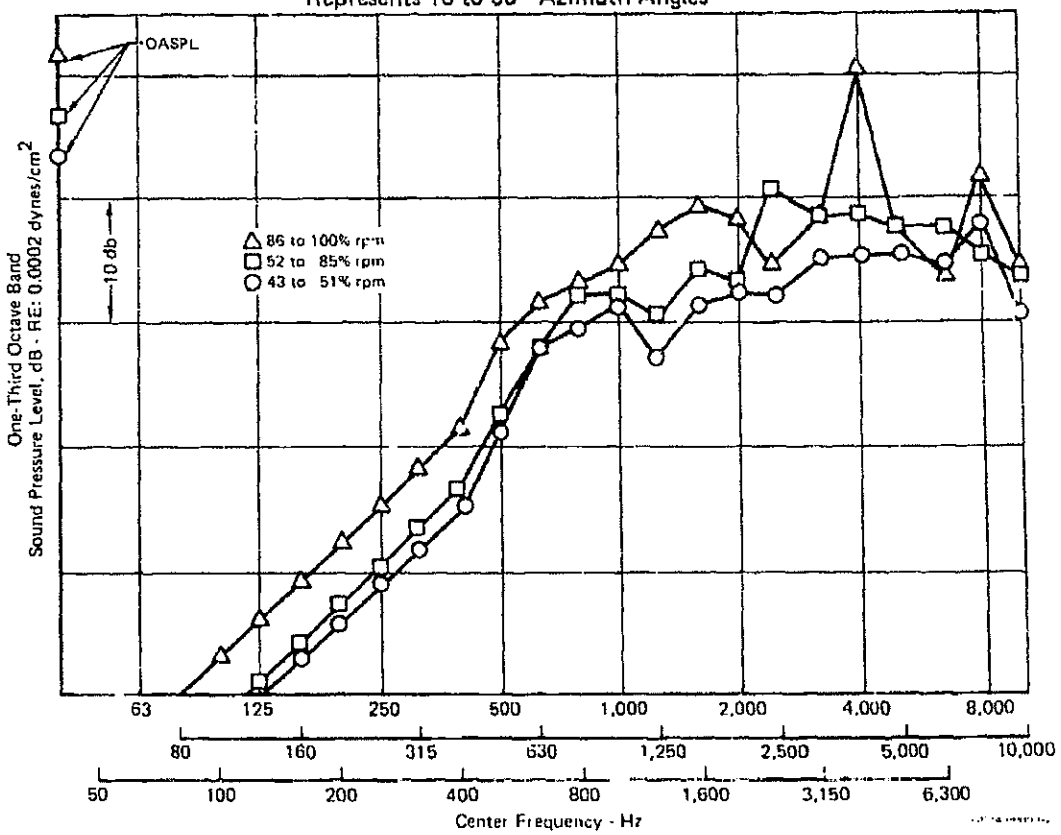

(C) The attenuation provided by the relatively long (14 ft.) inlet ducts before using acoustic treatment was estimated to be less than 1 dB for frequencies between 250 and 1000 Hz and less than 3 dB for frequencies greater than 1000 Hz. With the addition of acoustic treatment, the resultant propulsion noise spectrums at a distance of 5000 ft. and an azimuth angle of 30° are as previously shown in Figure 9-18. The attenuation due to duct acoustic treatment is equivalent to the same amount shown in Figure 9-21 taken from Reference (1). This amount of treatment is nearly optimum at quiet speed operating conditions, where a configuration is defined as optimum when the propulsion noise is no more detectable than aerodynamic noise.

(C) FIGURE 9-21
PROPULSION NOISE REDUCTION BY ACOUSTIC TREATMENT
5000 Ft Distance

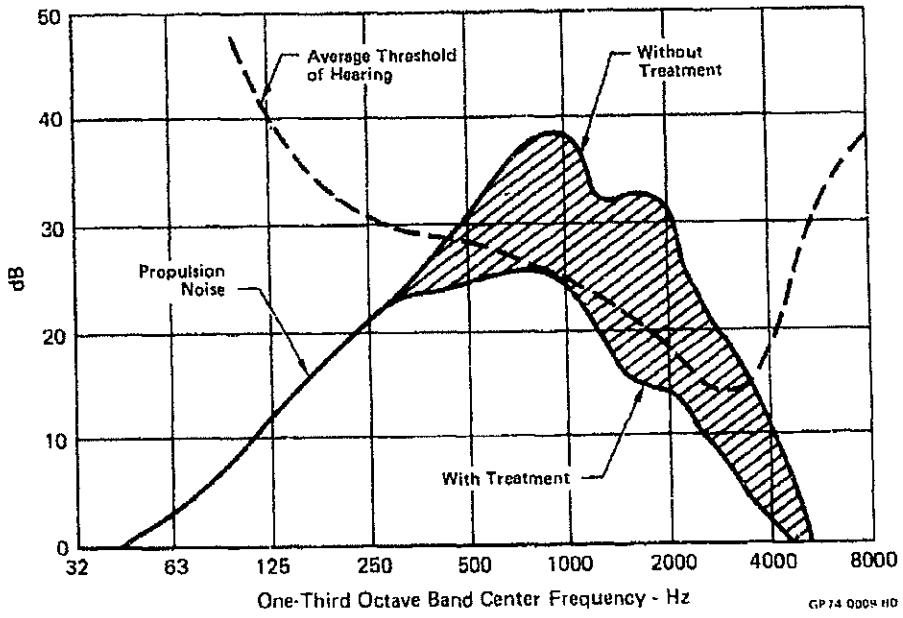

9.5 NOISE ANALYSIS SUMMARY

(U) Aerodynamic noise is the prime concern in regard to acoustic detectability, since noise from the fans of the propulsion system can be suppressed with sufficient acoustic treatment. The aerodynamic noise generally most critical is in the frequency range of 100 to 400 Hz.

~~(C)~~ Figure 9-22 compares the detection slant and ground ranges for the Quiet Attack Aircraft (Model 226-458) at various flight speeds and background noise levels. All data are based on a clean approaching aircraft at 2500 ft. above ground level.

~~(C)~~ FIGURE 9-22
SPEED AND BACKGROUND NOISE EFFECTS ON ACOUSTIC DETECTION RANGE
Slant Range/Ground Range (Ft) for Model 226-458 at 2500 Ft AGL

Aircraft Speed (Knots)	Background Noise Criteria					
	None (Average Threshold of Hearing)	6-13 mph Wind	Early Morning Surf 175 ft Away	Conversati... 3 ft Away	Truck 100 ft Away	Observer in Truck at 50 mph, Window Open
98	5,400/4,790	3,870/2,960	1,590/0	933/0	125/0	17/0
115	8,100/7,700	5,600/5,000	2,580/642	1,480/0	204/0	26/0
160	14,500/14,300	11,000/10,700	5,200/4,570	2,750/1,150	513/0	47/0
250	*	27,500/27,400	15,500/15,300	6,600/6,100	2,480/0	142/0
350	*	*	26,000/25,850	13,500/13,300	5,200/4,560	364/0
445	*	*	*	21,000/20,800	9,500/9,150	660/0

*Detection ranges greater than 35,000 ft are not shown here because prediction techniques can be particularly inaccurate as a result of the appreciable temperature and wind gradients, atmospheric turbulence, and ground effects at such large slant ranges.

GP J4 0000 03

~~(C)~~ The acoustic detection ranges vary significantly with aircraft speed and as the background noise rises above the average threshold of hearing spectrum. All the background noises, except for the 6-13 MPH wind and the early morning surf, make the aircraft inaudible at flight speeds ranging from 98 to 115 knots. As the speed of the aircraft increases, higher background noise levels are required to make the aircraft inaudible at the same flight altitude.

~~(C)~~ Slant ranges shown greater than about 7800 ft. in Figure 9-22 are somewhat conservative because excess ground attenuation, References (105) and (106), at low angles of elevation between the observer and the aircraft was not included. The excess ground attenuation is a result of the scattering of the noise signal in the turbulent boundary layer near the ground and the ground absorption as the signal passes over the ground. The smaller the elevation angle, the greater the attenuation and the greater the effect on the detection distance. Excess ground attenuation effects were not included because of the limited available data and the large variation of existing data at the distances involved.

10. REFERENCES

1. C. A. Mohr, "Quiet Attack Aircraft, Technical Report," MDC A1659, Volume II, 15 March 1973 (SECRET)

2. R. H. Liebeck, "Wind Tunnel Tests of Two Airfoils Designed for High Lift Without Separation in Incompressible Flow," MDC J5667/01, August 1972

3. R. H. Liebeck and A. I. Ormsbee, "Optimization of Airfoils for Maximum Lift," AIAA Journal of Aircraft, Vol. 7 No. 5, September-October 1970

4. Bernard Spencer, "Low Speed Longitudinal Aerodynamic Characteristics Associated with Variations in the Geometry of the Fixed Portion of a Variable-Wing-Sweep Airplane Configuration having an Outboard Pivot," NASA TMX-625, January 1962

5. NAVAIR 01-245FDB-1T "Tactical Manual, Navy Model F-4B, F-4J and F-4N Aircraft," dated 1 September 1972 (CONFIDENTIAL)

6. M. Luckiesh, "The Visibility of Aircraft," Journal of the Franklin Institute, Volume 187, March-April 1919.

7. A. D. Wright, "The Performance of Ground Observers Detecting, Recognizing, and Estimating Range to Low Altitude Aircraft," George Washington University, December 1966.

8. E. W. Frederickson, et. al., "Aircraft Detection Range Estimation, and Auditory Tracking Tests in a Desert Environment," George Washington University, March 1967.

9. W. Wokoun, "Detection of Random Low Altitude Jet Aircraft by Ground Observers," U. S. Army Ordnance Human Engineering Laboratory, Aberdeen Proving Ground, Maryland, June 1960.

10. Commander Operational Tests and Evaluation Force, "Evaluation of High Reflectance Paint and Visual Acquisition of the F-4 Airplane by Ground Observers," Thirteenth Partial Report on Project F/0210, Air Test and Evaluation Squadron 4, Echo Range Naval Weapons Center, China Lake, October 1969 (SECRET)

11. F. B. Barrett, "Visual Detection of F-4 Aircraft as a Function of Paint Color," Naval Missile Center, Point Mugu, California, Technical Report TP-73-39, July 1973 (CONFIDENTIAL)

12. Institute of Optics, "A Series of Measurements of the Brightness of the Night Sky," University of Rochester, New York (AD 895347), 1942.

13. E. O. Hulburt, "Measurements and Estimates of the Sky Brightness for all Attitudes of the Sun for Various Altitudes of the Observer Above the Earth," Navy Research Laboratory 4870, February 1957.

14. L. M. Biberman, et. al., "Levels of Nocturnal Illumination," Research Paper P232, Institute of Defense Analysis, Arlington, Virginia, January 1966.

15. S. Q. Duntley, "Airborne Measurements of Optical Atmospheric Properties at Night," Scripps Institute of Oceanography, Final Report S10 70-7 (also AFCRL-70-0137), May 1970.

16. A. R. Boileau, "Atmospheric Properties," Applied Optics, Vol. 3, No. 5, pp. 570-581, May 1964.

17. R. E. Dayton Brown, "Natural Illumination Charts," Report No. 374-1, Bu Ships, Department of the Navy, September 1952.

18. H. R. Blackwell, "Contrast Thresholds of the Human Eye," Journal of the Optical Society of America, Vol. 36, No. 11, 1946.

19. J. H. Taylor, "Use of Visual Performance Data in Visibility Prediction," Applied Optics, Vol. 3, No. 5, 1964

20. S. Q. Duntley, "The Reduction of Apparent Contrast by the Atmosphere," Journal of the Optical Society of America, Vol. 38, No. 2, February 1948.

21. W. E. Knoles Middleton, "Vision Through the Atmosphere," University of Toronto Press, 1958.

22. S. Q. Duntley, et. al., "Image Transmission by the Troposphere I, "Journal of the Optical Society of America, Vol. 47, No. 6, pp. 499-506, June 1957.

23. Grahm (Editor), Vision & Visual Perception, John Wiley, 1965.

24. Edward S. Lamar, et. al., "Shape, Size and Contrast Detection of Targets by Daytime Vision, I Data & Analytic Description," Journal of the Optical Society of America, Vol. 37, No. 7, July 1947.

25. S. Rodak, "F-8 Equivalent Blackbody Temperatures in the 8-14 Micrometer Spectral Band," unpublished data, Army Night Vision Laboratories ~~(CONFIDENTIAL)~~

26. S. Rodak, "F-105 Equivalent Blackbody Temperatures in the 8-14 Micrometer Spectral Band," unpublished data, Army Night Vision Laboratories ~~(CONFIDENTIAL)~~

27. Rugari, et. al., "Ground-Air Performance Analysis of Thermal Imaging Systems 'Pax I', "USA (ECOM), September 1972 ~~(CONFIDENTIAL).~~

28. T. B. Farris, "Chaparral Degraded Visibility Demonstration Program," U.S. Army Missile Command, Redstone Arsenal, Report No. RT-TR-71-2, January 1971 ~~(CONFIDENTIAL)~~

29. R. W. Kotter and F. R. Damon, "The AN/AAS-25 (PINE)/Chaparral Night Vision Sight Degraded Visibility Evaluation Program conducted at San Clemente Island, California and Fort Bliss, Texas," Hughes Aircraft Company, C1226, Vol. I, August 1970 (CONFIDENTIAL).

30. Pontelandolfo and Popko, "Des-Val IR Air Defense Test," Frankford Arsenal unpublished data ~~(CONFIDENTIAL)~~

31. Bell, et. al., "Infrared Techniques and Measurements," Ohio State University, Final Report 659, October 1957.

32. R. D. Hudson, "Infrared System Engineering," John Wiley & Sons, 1969.

33. Tisdale, et. al., "Detection of TV Imagery by Humans vs. Machines," Applied Optics, Vol. 11, May 1972.

34. N. K. Hild, unpublished data, McDonnell Aircraft Company, St. Louis, 4 September 1973.

35. F. A. Rosell and R. H. Willson, "Performance Synthesis (Electro-Optical Sensors)," Westinghouse Defense & Space Center, Technical Report AFAL-TR-71-137, May 1971.

36. A. S. Hersh, "Aerodynamic Sound Radiation from Lifting Surfaces With and Without Leading Edge Serrations," BBN Report No. 71A01, NASA CR-114370, 1971.

37. M. Bodner, J. B. Gibbs, and G. J. Healy, "Far Field Aerodynamic Noise Measurement Program," Lockheed-California Company, LR 23640, 22 June 1970.

38. J. S. Gibson, "Non-Engine Aerodynamic Noise: The Limit to Aircraft Noise Reduction," INTER-NOISE 73 Presentation, August 1973.

39. D. L. Smith, "Measurements of the Radiated Noise from Sailplanes," TM-70-3-FDDA, 1970.

40. SAE ARP 866, "Standard Values of Atmospheric Absorption as a Function of Temperature and Humidity for Use in Evaluating Aircraft Flyover Noise," 31 August 1964.

41. H. D. Sowers, "Investigation of Methods for Prediction and Alleviation of Lift Fan Noise," USATRECOM TR 65-4, April 1965, (General Electric).

42. J. E. Marte and D. W. Kurtz, "A Review of Aerodynamic Noise from Propellers, Rotors and Lift Fans," NASA TR 32-1462, January 1, 1970, Jet Propulsion Laboratory.

43. "LF 336/C Modification and Acoustic Test Program Data Report," General Electric, Volumes 1 through III, September 1970.

44. SAE AIR 876, "Jet Noise Prediction," July 1965.

45. G. L. Minner and C. E. Feiler, "Low-Speed Jet Noise From a 1.83-Meter (6 Ft.) Fan for Turbofan Engines," NASA TN D-6314, April 1971.

46. S. L. Bragg, "Noise from Turbojet Compressors," Journal of Royal Aeronautical Society, January 1964.

47. J. B. Chaddock, T. L. Moore, H. H. Bell and J. K. Nunnely, "Sound Attenuation in Straight Ventilation Ducting," Refrigeration Engineering, January 1959.

48. L. L. Beranek, Noise Reduction, McGraw-Hill Book Company, Inc., pp. 554-556, 1960.

49. "Sound and Vibration Control," Chapter 31 of Heating, Ventilating and Air Conditioning Guide, American Society of Heating, Refrigeration and Air Conditioning Engineers, Inc., 1967.

50. L. L. Beranek, Noise and Vibration Control, McGraw-Hill Book Company, Inc., pp. 390-391, 1971

51. "Sound Control," Chapter 40 of Heating, Ventilating and Air Conditioning Guide, American Society of Heating, Refrigeration and Air Conditioning Engineers, Inc., 1957.

52. W. L. Copeland, "Inlet Noise Studies for an Axial-Flow Single-Stage Compressor," NASA TN D-2615, February 1965.

53. R. G. Dorsch, E. A. Krejsa and W. A. Olsen, "Blown Flap Noise Research," NASA TM X-67850, June 1971.

54. T. G. Ganger, "Results of Prop-Fan/STOL Wing Acoustic Tests," NASA CR-111956, July 1971.

55. T. W. Putnam and P. L. Lasagna, "A Full-Scale Investigation of Externally Blown Flap Impingement Noise," NASA FWP-25, August 1971.

56. W. A. Olsen, R. G. Dorsch and J. H. Miles, "Noise Produced by a Small-Scale Externally Blown Flap," NASA TN D-6636, March 1972.

57. J. F. Groeneweg and G. L. Minner, "Measured Noise of Model Fan-Under-Wing and Flap-on-Flap Jet Flap Configurations," NASA TN D-6781, May 1972.

58. F. W. Gibson, "Noise Measurements of Model Jet-Augmented Lift Systems," NASA TN D-6710, April 1972.

59. F. W. Gibson, "Noise Measurement Studies of Several Model Jet Augmented Lift Systems," NASA LWP-981, August 1971.

60. R. E. Hayden, Y. Kadman and R. C. Chanaud, "A Study of the Variable Impedance Surface Concept as a Means for Reducing Noise from Jet Interaction with Deployed Lift-Augmenting Flaps," NASA CR-112166, July 1972.

61. R. G. Dorsh, W. J. Kreim and W. A. Olsen, "Externally Blown Flap Noise", AIAA Paper 72-129, January 1972.

62. M. P. Fink, "Aerodynamic Characteristics, Temperature, and Noise Measurements of a Large Scale External-Flow Jet-Augmented-Flap Model with Turbojet Engines Operating," NASA TN D-943, September 1961.

63. D. Chestnutt, W. L. Copeland and L. R. Clark, "Noise Generation by Plates in the Presence of Jets," NASA LWP-989, Part D, September 1971.

64. M. D. Falarski, "Large-Scale Wind Tunnel Investigation of the Noise Characteristics of a Semispan Wing Equipped with an Externally Blown Jet Flap," NASA TM X-62154, May 1972.

65. A. Chamay, D. P. Edkins, R. B. Mishler and W. S. Clapper, "Design of a TF34 Turbofan Mixer for Reduction of Flap Impingement Noise," NASA CR-120916, Feb 1972.

66. D. L. Hughes, "Pressures and Temperatures on the Lower Surfaces of an Externally Blown Flap System During Full Scale Ground Tests," NASA TN D-7138, January 1973.

67. E. E. Ungar, K. L. Chandiramani and J. E. Barger, "Excitation, Response and Fatigue Life Estimation Methods of the Structure Design of Externally Blown Flaps," NASA CR-112216, October 1962.

68. V. L. Blumenthal, J. M. Streckenbach and R. B. Tate, "Aircraft Environmental Problems," AIAA Paper 73-5, January 1973.

69. L. C. Sutherland and D. Brown, "Methods for Near Field Noise Environments of VTOL Aircraft," AFFDL-TR-71-180, May 1972.

70. A. H. Marsh, "Noise Measurements Around a Subsonic Jet Impinging on a Plane Rigid Surface," Journal of the Acoustical Society of America, Volume 33, No. 8, August 1961.

71. J. N. Cole, R. T. England and R. G. Powell, "Effects of Various Exhaust Blast Deflectors on the Acoustic Noise Characteristics of 100 Pound Thrust Rockets," WADD TR 60-6, September 1960.

72. F. R. Wagner, "The Sound and Flow Field of an Axially Symmetric Free Jet Upon Impact on a Wall," NASA TT F13, 942, 1971.

73. R. C. Potter and M. J. Crocker, "Acoustic Prediction Methods for Rocket Engines Including the Effects of Clustered Engines and Deflected Exhaust Flow," NASA CR-566, October 1966.

74. W. A. Olsen, J. H. Miles and R. C. Dorsch, "Noise Generated by Impingement of a Jet Upon a Large Flat Board," NASA TN D-7075, December 1972.

75. O. A. Gutierrez and J. R. Stone, "Preliminary Experiments on the Noise Generated by Target Type Thrust Reverser Models," NASA TM X-2553, May 1972.

76. J. F. Dreher, "Aircraft Equipment Random Vibration Test Criteria Based on Vibrations Induced by Turbulent Airflow Across Aircraft External Surfaces," Shock and Vibration Bulletin, No. 43, 1973.

77. A. Burkhard, "Captive Flight Acoustic Test Criteria for Aircraft Stores," Shock and Vibration Bulletin, No. 43, 1973.

78. A. G. Pierson, "Vibration and Acoustic Test Criteria for Captive Flight of Externally Carried Aircraft Stores," AFFDL-TR-71-158, December 1971.

79. J. F. Dreher, "Effects of Vibration and Acoustic Noise on Aircraft/Stores Compatibility," Proceedings of Aircraft Compatibility Symposium, Vol. 6, pp. 245-272, November 1969.

80. J. F. Dreher, "The Effect of Tailfins on the Vibracoustic Environment of Externally Carried Aircraft Stores," Shock and Vibration Bulletin, No. 41, 1970.

81. J. F. Dreher and W. D. Hinegardner, "RF-4C Vibration and Acoustic Environment Study," Shock and Vibration Bulletin, No. 37, 1968.

82. J. F. Dreher, E. D. LaKin and E. A. Tolle, "Vibracoustic Environment and Test Criteria for Aircraft Stores During Captive Flight," Shock and Vibration Bulletin, No. 39, 1969.

83. R. W. Peverley, "Vibracoustic Test Methods for Vibration Qualification of Apollo Flight Hardware," Shock and Vibration Bulletin, No. 37, 1968.

84. T. R. Brice, "Determination of Flow Field Characteristics Around Generalized and Specific Protuberances at Mach Numbers 0.60 through 1.60," USAF (AEDC) TR-68-166, September 1968.

85. J. C. Westkaemper, "Protuberance and Vortex Generator Studies at ARL," ARL-TR-70-43, Part III, 25 January 1971.

86. J. E. Roberson, "Prediction of In-Flight Fluctuating Pressure Environments Including Protuberance Induced Flow," Wyle Lab. Report WR-71-10, March 1971.

87. W. W. Willmarth, "Space-Time Correlations and Spectra of Wall Pressure in a Turbulent Boundary Layer," NASA 3-17-59W, March 1959.

88. M. Harrison, "Pressure Fluctuations on the Wall Adjacent to a Turbulent Boundary Layer," Armed Services Technical Information Agency (ASTIA) 1260, December 1958.

89. R. H. Kraichnan, "Pressure Fluctuations in Turbulent Flow over a Flat Plate," Journal of the Acoustical Society of America, May 1956.

90. R. H. Kraichnan, "Noise Transmission from Boundary Layer Pressure Fluctuation," Journal of the Acoustical Society of America, January 1957.

91. H. S. Ribner, "Boundary Layer-Induced Noise in the Interior of Aircraft," University of Toronto, Institute of Aerophysics (UTIA) No. 37, April 1956.

92. N. J. McLeod and G. H. Jordan, "Boundary Layer Noise at Subsonic and Supersonic Speeds," Published in NACA Symposium Proceedings, Langley, 1959.

93. N. J. McLeod and G. H. Jordan, "Preliminary Flight Survey of Fuselage and Boundary Layer Sound Pressure Levels," NACA RM H58B11, 13 May 1958.

94. F. J. Leech, "Boundary Layer Noise Measurements on the F102A Aircraft," Medical Research Laboratory Report No. MDL-TDR-62-71, August 1962.

95. W. L. Nelson and C. M. Alaia, "Aerodynamic Noise and Drag Measurements on a High-Speed Magnetically-Suspended Rotor," WADC TR 57-339, ASTIA No. Ad 142153, January 1958.

96. H. R. Mull and J. S. Algranti, "Preliminary Flight Survey of Aerodynamic Noise on an Airplane Wing," NACA RM E55K07, 2 March 1956.

97. K. Eldred, W. Roberts, and R. White, "Structural Vibrations in Space Vehicles," WADD Technical Report 61-62, December 1961.

98. L. L. Beranek, Noise Reduction, McGraw-Hill Book Company, Inc., pp. 681-683, 1960.

99. P. A. Franken and E. M. Kerwin, Jr., "Methods of Flight Vehicle Noise Prediction," WADC TR 58-343, Vol. I, November 1958.

100. J. A. Hay, "Problems of Cabin Noise Estimation for Supersonic Aircraft," Journal of Sound and Vibration, Vol. 1, No. 2, April 1964.

101. D. A. Bies, "A Review of Flight And Wind Tunnel Measurements of Boundary Layer Pressure Fluctuations and Induced Structural Response," NASA CR-626, October 1966.

102. M. V. Lowson, "Prediction of Boundary Layer Pressure Fluctuations," AFFDL-TR-67-167, April 1968.

103. Report MDC A1658-16, "Quiet Attack Aircraft, Technical Report (U)," dated 29 June 1973 (SECRET).

104. Y. Morimoto and D. Paul III, "Acoustic Qualification Flight Test Report YO-3A Observation Aircraft (U)," Lockheed Missiles and Space Company Report LMSC-695189, January 1970 (CONFIDENTIAL)

105. L. L. Beranek, Noise and Vibration Control, McGraw-Hill Book Company, Inc., pp. 182-184 and 537-538, 1971.

106. SAE AIR 923, "Method for Calculating the Attenuation of Aircraft Ground to Ground Noise Propagation During Takeoff and Landing," August 1966.

APPENDIX A
ATMOSPHERIC CONTRAST TRANSMITTANCE

(U) The material in this section is concerned only with the development of Equation (1) in Section 7 defining atmospheric contrast attenuation when the attenuation length and background sky luminance are constant over the path of sight.

(U) As was mentioned previously, the apparent luminance (brightness) of a distant object is the sum of two independent components: (1) the residual image forming light from the object that has traversed the atmospheric path without having been scattered or absorbed, and (2) the additional light arriving at the observer that is attributed to the scattering of ambient light throughout the path of sight, including sunlight, moonlight, skylight, earth-shine, etc. The first component of light contains information concerning the object whereas the second component, depending on scattering and absorbing processes throughout the path of sight, is independent of the nature of the object.

(U) The apparent luminance of an object when viewed at a distance is thus:

$$ {}_tB_r(z,\theta,\phi) = T_r(z,z_t,\theta)\,{}_tB_o(z_t,\theta,\phi) + B^*_r(z,z_t,\theta,\phi) \qquad (A1) $$

where the notation is explained in the footnote.*

(U) *The symbol for luminance is B and the symbol for the direct atmospheric transmission of a light beam is T. We assume herein that T is independent of azimuth angle. The altitude of the observer is denoted by z. The direction of any path of sight is specified by a zenith-angle θ and an azimuth angle ϕ, the direction of view being directed upward when $0 \leq \theta \leq \pi/2$ RADIANS. The subscripts t, z, θ, and ϕ are always written as parenthetic attachments to the parent symbol. When the post subscript r is appended to any symbol, it denotes that the quantity pertains to a path of length r. The subscript letter o always refers to the hypothetical concept of an observer located at zero distance from the object as, for example, in denoting the inherent brightness of a surface. Pre-subscripts identify the object, thus the pre-subscript b refers to background, and t to object or visual target. Thus, the inherent brightness of an object t at altitude z_t as viewed in the direction (θ,ϕ) is ${}_tB_o(z_t,\theta,\phi)$ and the corresponding apparent luminance of the object as observed in the same direction (θ,ϕ) at the observer altitude z is ${}_tB_r(z,\theta,\phi)$ where $z_t = z + r\cos\theta$. A post-superscript * is attached to the path luminance terms as a symbol signifying that the brightness has been generated by the scattering of ambient light reaching the path from all directions. Thus $B^*_r(z,z_t,\theta,\phi)$ is used to denote sky luminance along path length r between altitudes z and z_t.

(U) The inherent contrast of an object and its background is, by definition:

$$C_o(z,\theta,\phi) = \frac{{}_tB_o(z,\theta,\phi) - {}_bB_o(z,\theta,\phi)}{{}_bB_o(z,\theta,\phi)} \tag{A2}$$

(U) The corresponding definition for apparent contrast is:

$$C_r(z,\theta,\phi) = \frac{{}_tB_r(z,\theta,\phi) - {}_bB_r(z,\theta,\phi)}{{}_bB_r(z,\theta,\phi)} \tag{A3}$$

(U) The apparent and inherent background luminances are related by:

$${}_bB_r(z,\theta,\phi) = T_r(z,z_t,\theta)\,{}_bB_o(z_t,\theta,\phi) + B_r^*(z,z_t,\theta,\phi) \tag{A4}$$

where

$$T_t(z,z_t,\theta) = \exp\left[\int_{z_t}^{z} \frac{\sec\theta\, dz}{L(z)}\right] \tag{A5}$$

where $L_{(z)}$, the attenuation length, is a function of altitude. If Equation (A4) is subtracted from Equation (A1), the difference divided by ${}_bB_r(z,\theta,\phi)$ and the result combined with Equation (A3), the following result is obtained:

$$C_r(z,\theta,\phi) = \frac{T_r(z,z_t,\theta)\;{}_bB_o(z_t,\theta,\phi)}{{}_bB_r(z,\theta,\phi)}\; C_o(z_t,\theta,\phi) \tag{A6}$$

(U) Equation (A6) is the basic equation defining atmospheric contrast transmittance. The values for intrinsic background luminance, ${}_bB_o(z_t,\theta,\phi)$, apparent background luminance, ${}_bB_r(z,\theta,\phi)$, and atmospheric transmittance, $T_r(z,z_t,\theta)$ are inputs needed to calculate atmospheric contrast transmittance. The input values are usually obtained directly from atmospheric measurements or from atmospheric models based on direct measurements.

(U) In the special case where the attenuation length and background luminance are constant over the path of sight, such as for horizontal paths of view, Equation (A5) becomes:

$$C_r(z,\theta,\phi) = C_o(z_t,\theta,\phi)\,\exp\left[\frac{-(z-z_t)\sec\theta}{L(z)}\right] \tag{A7}$$

In other words, for this special case, the atmospheric contrast transmittance is the same as the direct atmospheric transmission of a light beam.

APPENDIX B

FLIR SPATIAL FREQUENCY ANALYSIS

(U) Development of the spatial frequency analysis will be based upon the notion that the FLIR imagery can be represented by Figure B-1. Here the imagery is such that it can be considered to be a periodic scene along the scanning axis, Figure B-2. Let

$$f(x,y) = \text{scene intensity at each point } (x,y) \tag{B1}$$

Assuming a definite detector shape, the integrated scene intensity for the detector at a given time "t" is

$$i(\dot{x}t,k\Delta) = \int_{-\infty}^{\infty}\int_{-\infty}^{\infty} h(\dot{x}t-x,k\Delta-y)f(x,y)dxdy \tag{B2}$$

Where

$$h(x,y) = \text{detector scanning aperture point spread function} \tag{B3}$$

$\dot{x}$ = scan velocity in radians/second

t = time in seconds

Δ = center to center detector separation (this would allow over and underscan)

Eq. (B2) can be written as

$$i(\dot{x}t,k\Delta) = \mathcal{F}^{-1}_{R_s,R_{\bar{s}}}\left\{H(R_s,R_{\bar{s}})\ F(R_s,R_{\bar{s}})\right\} \tag{B4}$$

With the notation that

R_s = spatial frequency vector in the scan direction

$R_{\bar{s}}$ = spatial frequency vector in the nonscanning direction

(U) FIGURE B-1
FLIR PERIODIC SCENE

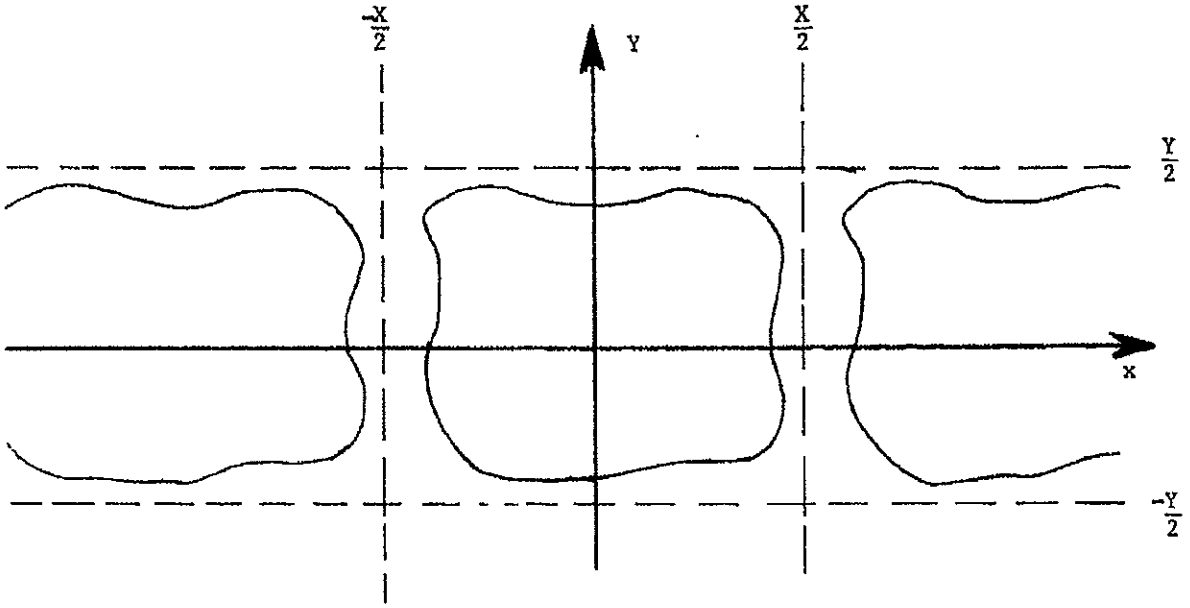

(U) FIGURE B-2
SCANNING ARRAY

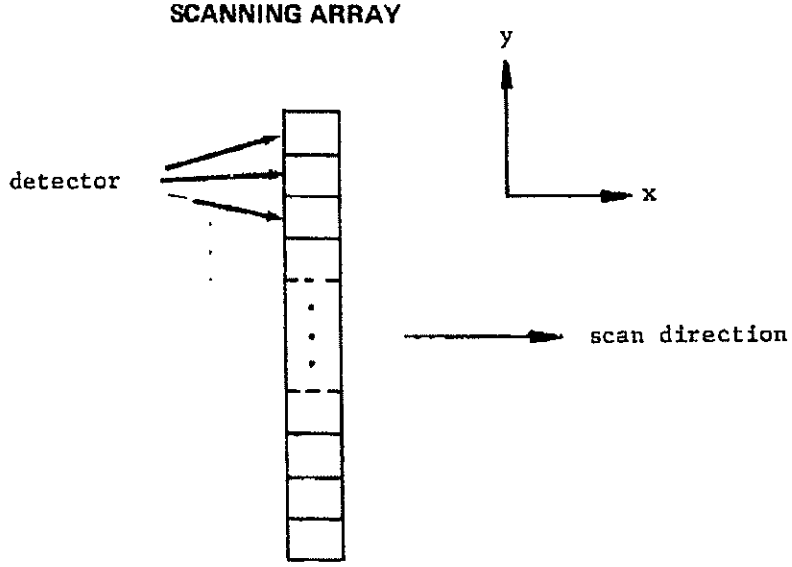

Where

$$\mathfrak{F}_{x,y}\{\quad\} = \text{two dimensional Fourier transform} \tag{B5}$$

$$\mathfrak{F}^{-1}_{R_s,\,R_{\bar{s}}}\{\quad\} = \text{inverse two dimensional Fourier transform} \tag{B6}$$

and

$$H(R_s, R_{\bar{s}}) = \int_{-\infty}^{\infty}\int_{-\infty}^{\infty} h(x,y)\, e^{-j2\pi R_s x - j2\pi R_{\bar{s}} y}\, dxdy \tag{B7}$$

$$F(R_s, R_{\bar{s}}) = \frac{1}{X}\int_{-\frac{X}{2}}^{X/2}\int_{-\infty}^{\infty} f(x,y)\, e^{-j2\pi R_s x - j2\pi R_{\bar{s}} y}\, dydx \tag{B8}$$

The spatial content of the k^{th} detector scan line can be arrived at by considering the scanning mechanism. With scanning only in the x direction, the waveform being an impulse along the y axis, the spectrum has the form

$$I(R_s, R_{\bar{s}}) = I_k(R_s)\,\delta(R_{\bar{s}}) \tag{B9}$$

Here

$$I_k(R_s) = \mathfrak{F}_x\left\{i(\dot{x}t, k\Delta)\right\} \tag{B10}$$

$$= \mathfrak{F}^{-1}_{R_{\bar{s}}}\left\{H(R_s, R_{\bar{s}})\, F(R_s, R_{\bar{s}})\right\} \tag{B11}$$

$$= \int_{-\infty}^{\infty} H(R_s, R_{\bar{s}})\, F(R_s, R_{\bar{s}})\, e^{j2\pi R_s k\Delta}\, dR_{\bar{s}} \tag{B12}$$

Let

$$i_k(t) = i(\dot{x}t, k\Delta) \tag{B13}$$

in order to simplify the notation. This function is now modified by the electrical impulse response to obtain the output video signal for the k^{th} detector.

$$v_k(\tau) = \int_{-\infty}^{\tau} e(\tau - t)\, i_k(t)\, dt \qquad \text{(B14)}$$

$$e(t) = \text{electrical impulse response} \qquad \text{(B15)}$$

In order to continue, let each video channel (detector) be reproduced without sampling. Furthermore, the time period for the periodic video channel waveform is

$$T = \frac{X}{\dot{x}} \qquad \text{(B16)}$$

With this, the conversion existing between the spatial frequency, R_s, and the temporal frequency, f_t, is

$$f_t = R_s \dot{x} \qquad \text{(B17)}$$

Continuing, the spatial spectrum is modified by the electrical response for which

$$V_k(f_t) = E(f_t)\, I_k(f_t) \qquad \text{(B18)}$$

Using Eq. (B17) and (B18), the spatial spectrum to this point has the form

$$V_k(R_s, \underline{R_s}) = E\left(\frac{f_t}{\dot{x}}\right) I_k(R_s)\, \delta(\underline{R_s}) \qquad \text{(B19)}$$

The image produced upon the display by a single scan line can be represented as

$$s_k(x, y) = \int_{-\infty}^{\infty} \int_{-\infty}^{\infty} w(x-\xi, y-\eta) v_k(\xi, \eta)\, d\xi d\eta \qquad \text{(B20)}$$

$$w(x, y) = \text{display scanning spot point spread function} \qquad \text{(B21)}$$

This is the integrated intensity observed at each point (x, y) on the display for the k^{th} scan line. Rewriting this

$$s_k(x, y) = \int_{-\infty}^{\infty} \int_{-\infty}^{\infty} W(R_s, \underline{R_s})\, V_k(R_s, 0)\, e^{j2\pi R_s x + j2\pi \underline{R_s} y}\, dR_s\, d\underline{R_s} \qquad \text{(B22)}$$

Substituting in Eq. (19)

$$s_k(x, y) = \int_{-\infty}^{\infty} \int_{-\infty}^{\infty} W(R_s, R_{\bar{s}})\, E(R_s)\, I_k(R_s) \cdot e^{j2\pi R_s x + j2\pi R_{\bar{s}} y}\, dR_s\, dR_{\bar{s}} \tag{B23}$$

Extending this to a total of 2N + 1 scan lines, all of which are considered to be evenly spaced along the y-axis, finds the displayed image is

$$g(x, y) = \sum_{k=-N}^{N} s_k(x, y) \tag{B24}$$

The spatial spectrum of this image is

$$G(R_s, R_{\bar{s}}) = \sum_{k=-N}^{N} S_k(R_s, R_{\bar{s}})\, e^{-j2\pi R_{\bar{s}} k\Delta} \tag{B25}$$

Where

$$S_k(R_s, R_{\bar{s}}) = W(R_s, R_{\bar{s}})\, E(R_s)\, I_k(R_s) \tag{B26}$$

Continuing

$$G(R_s, R_{\bar{s}}) = W(R_s, R_{\bar{s}})\, E(R_s) \left\{ \sum_{k=-N}^{N} I_k(R_s) \cdot e^{-j2\pi R_{\bar{s}} k\Delta} \right\} \tag{B27}$$

$$G(R_s, R_{\bar{s}}) = W(R_s, R_{\bar{s}})\, E(R_s) \left\{ \sum_{k=-N}^{N} \left[\int_{-\infty}^{\infty} H(R_s, \hat{R}_{\bar{s}})\, F(R_s, \hat{R}_{\bar{s}}) \cdot e^{j2\pi (\hat{R}_{\bar{s}} - R_{\bar{s}}) k\Delta}\, d\hat{R}_{\bar{s}} \right] \right\} \tag{B28}$$

Note that $F(R_s, \hat{R}_{\bar{s}})$ is the spatial spectrum of the scene and $G(R_s, R_{\bar{s}})$ is the spatial spectrum of the displayed scene.

 (Page B-6 is blank)

APPENDIX C

QAA VISIBLE SURFACE PROJECTIONS

(U) The QAA visible surface projections were constructed from the QAA cross section at the stations shown in Figure 2-2. These projections were based upon the following restrictions:

- Zero azimuth aspect from the QAA nose
- Elevation aspect angles of 0°, 1.8°, 3.6°, 7.2°, 14.5°, 30°, 45°, 60° and 90° below the QAA nose.

(U) FIGURE C-1
QAA LEFT SIDE VISIBLE AREA PROJECTION AT 0° ELEVATION ASPECT ANGLE

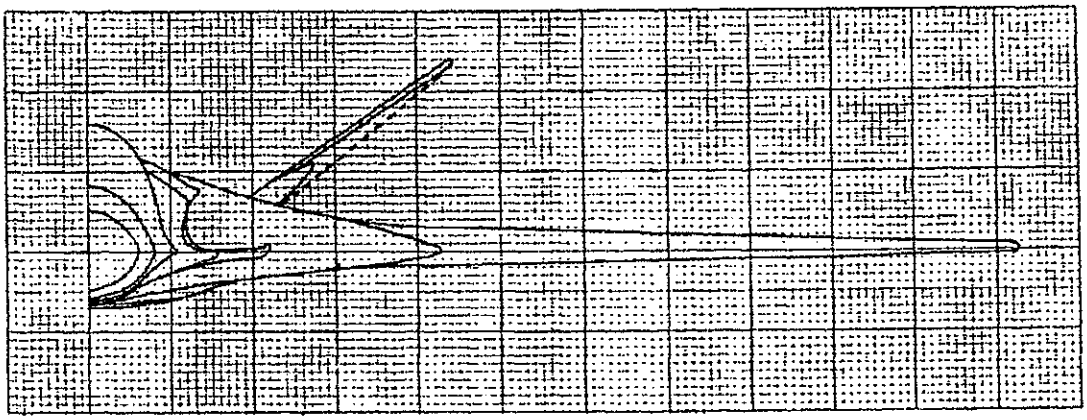

(U) FIGURE C-2
QAA LEFT SIDE VISIBLE AREA PROJECTION AT 1.8° ELEVATION ASPECT ANGLE

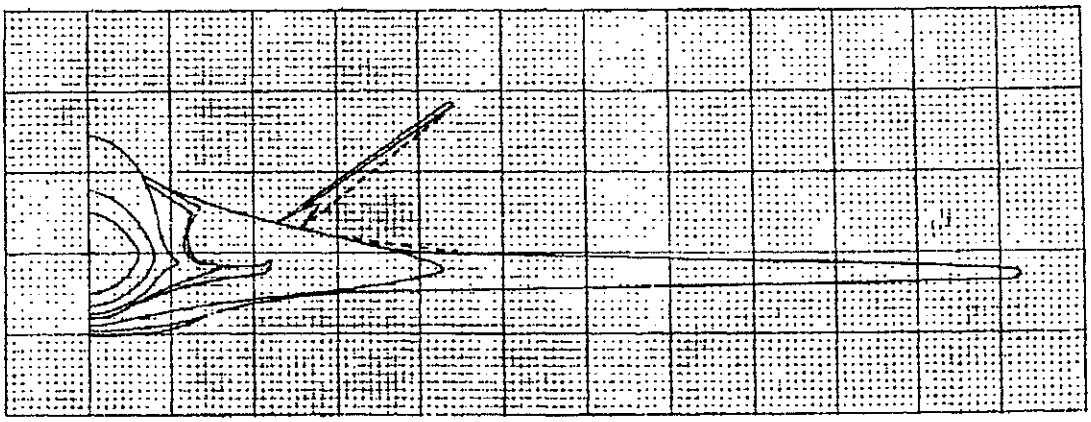

(U) FIGURE C-3
QAA LEFT SIDE VISIBLE AREA PROJECTION AT 3.6° ELEVATION ASPECT ANGLE

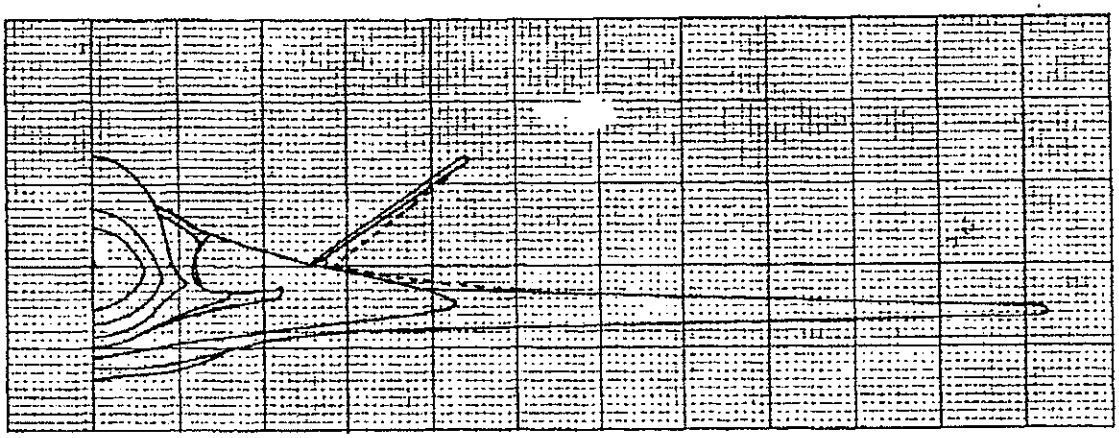

(U) FIGURE C-4
QAA LEFT SIDE VISIBLE AREA PROJECTION AT 7.2° ELEVATION ASPECT ANGLE

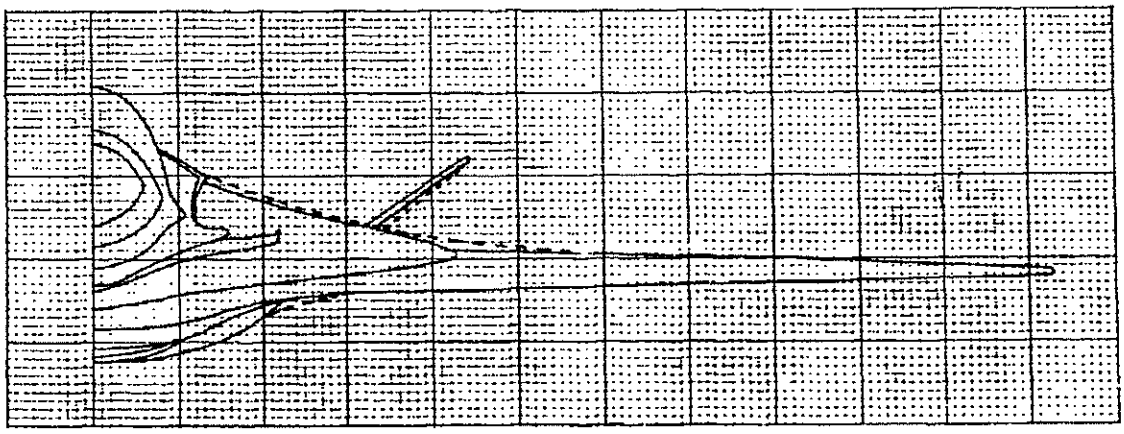

(U) FIGURE C-5
QAA LEFT SIDE VISIBLE AREA PROJECTION AT 14.5° ELEVATION ASPECT ANGLE

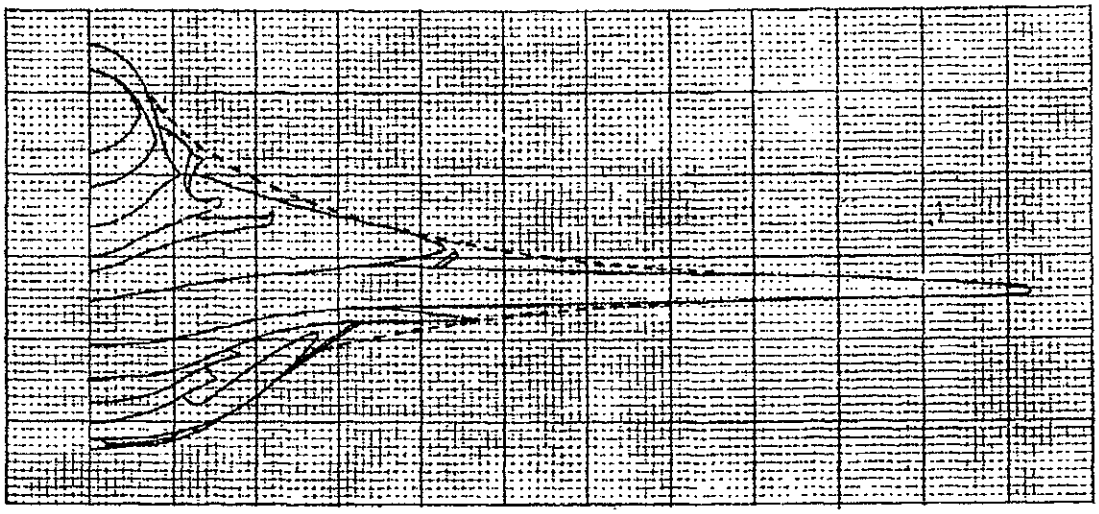

(U) FIGURE C-6
QAA LEFT SIDE VISIBLE AREA PROJECTION AT 30° ELEVATION ASPECT ANGLE

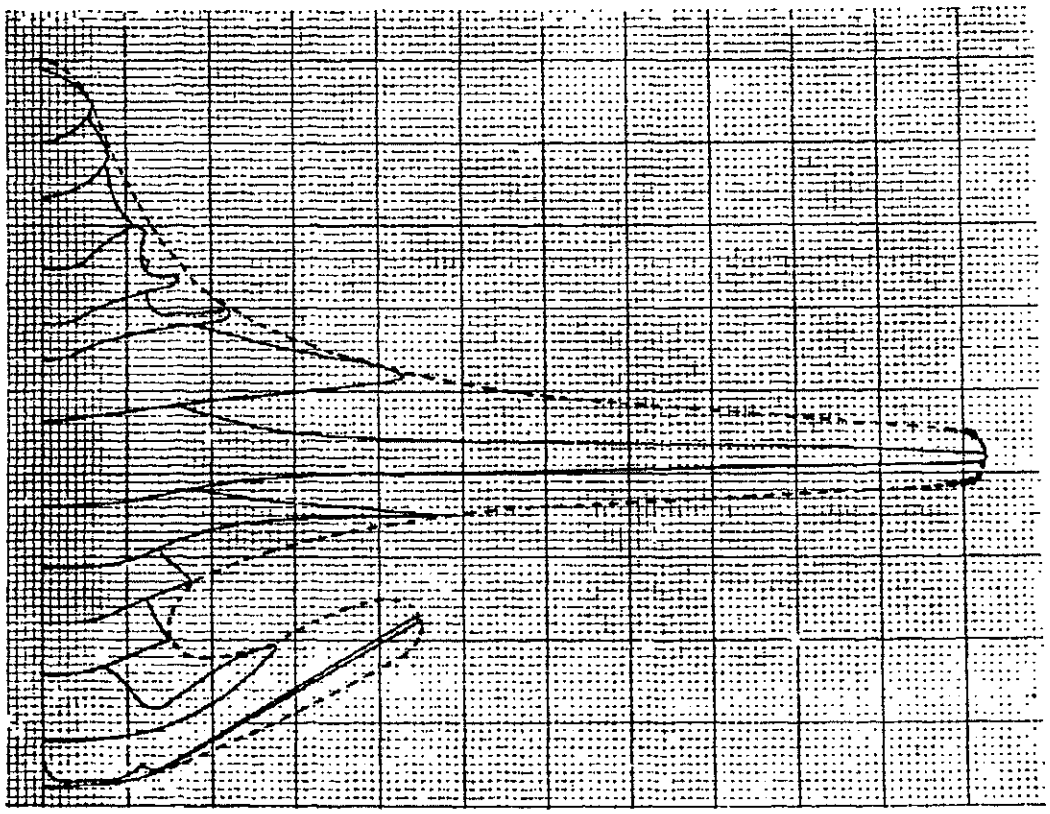

(U) FIGURE C-7
QAA LEFT SIDE VISIBLE AREA PROJECTION AT 45° ELEVATION ASPECT ANGLE

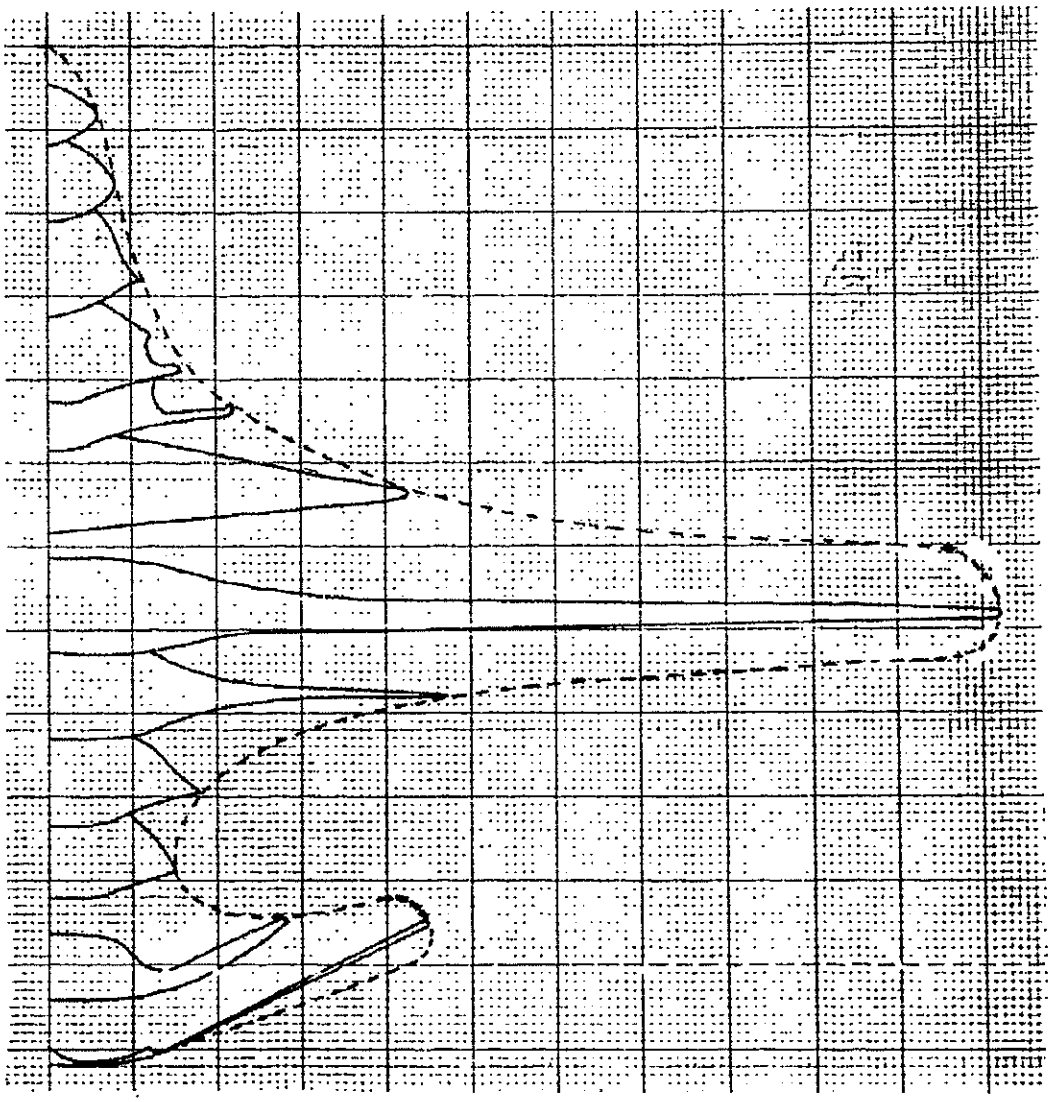

(U) FIGURE C-8
QAA LEFT SIDE VISIBLE AREA PROJECTION AT 60° ELEVATION ASPECT ANGLE

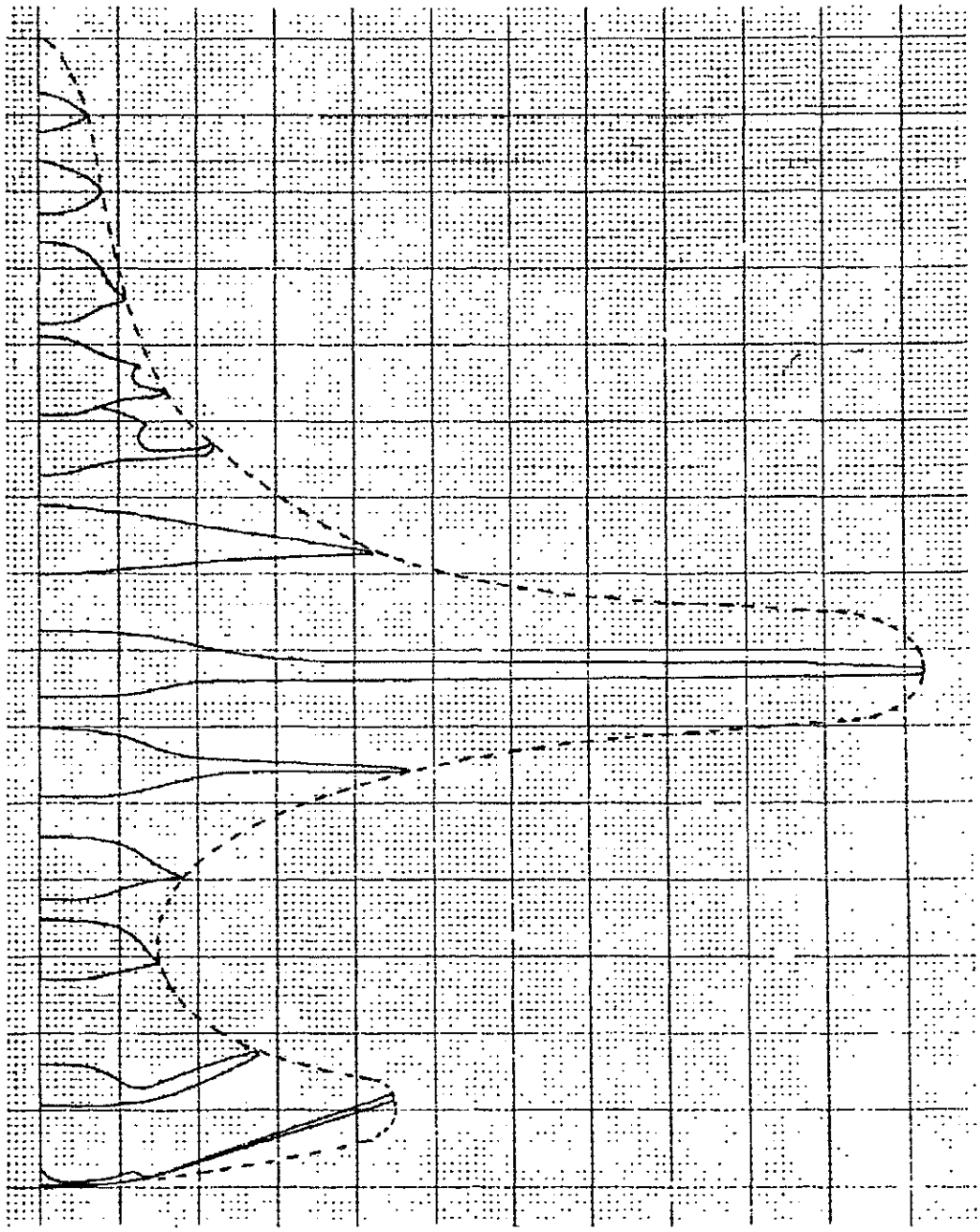

(U) FIGURE C-9
QAA LEFT SIDE VISIBLE AREA PROJECTION AT 90° ELEVATION ASPECT ANGLE

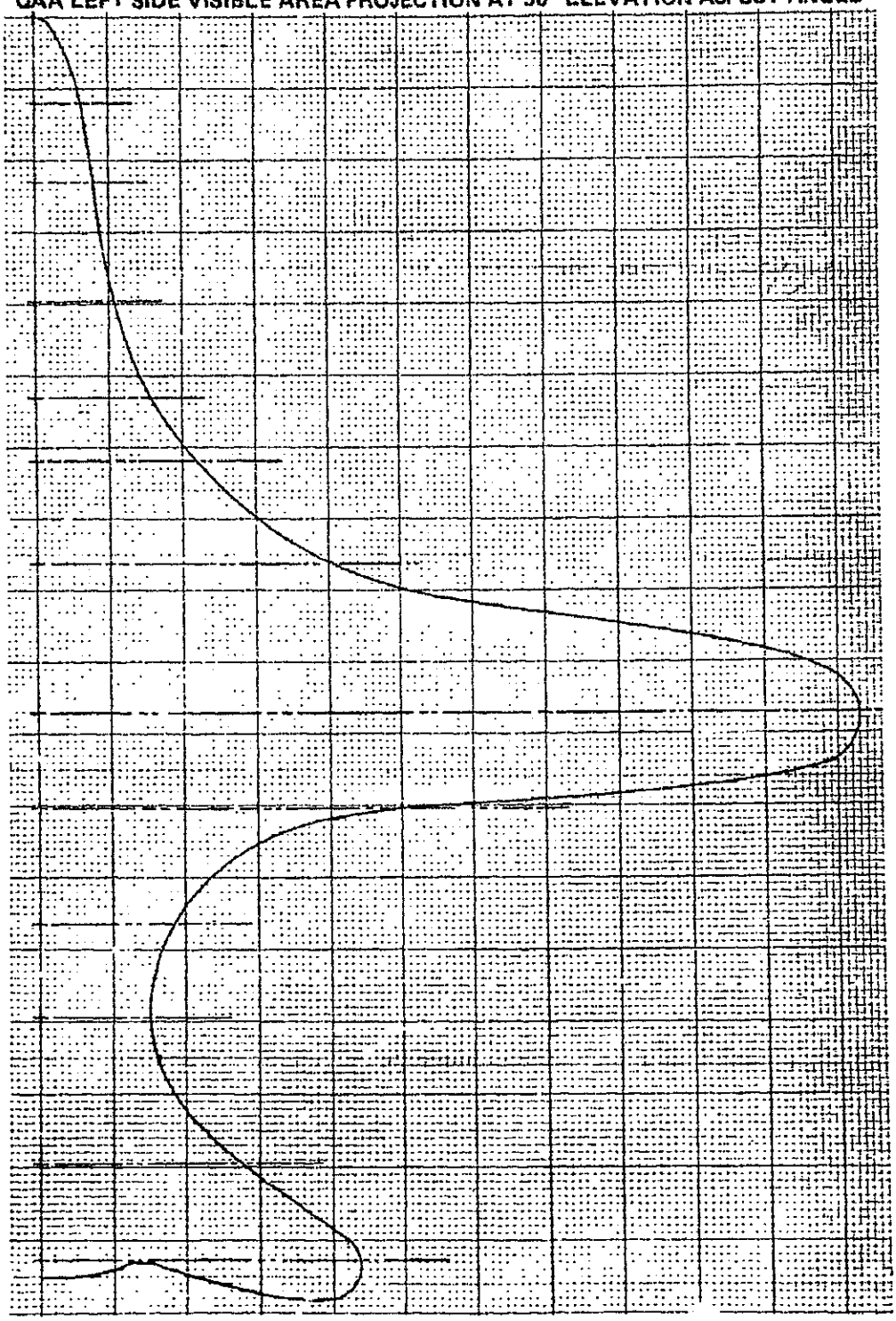

(Page C-8 is blank)

APPENDIX D

(U) GROUND-TO-AIR FLIR MODEL PARAMETERS

Initial Inputs	Symbol	Units
Aircraft Parameters		
Altitude	AH	Feet
Velocity	AV	Knots
Temperature	AT	Degrees C
Emissivity	AE	Unitless
Atmosphere Parameters		
Sea Level Temperature	SLT	Degrees C
Relative Humidity	RH	Percent
Atmosphere Visual Range	VIS	Nautical Miles
FLIR Parameters		
Zoom Factor	ZF	Unitless
Collecting Optics Transmission	COT	Unitless
Collecting Optics Aperture Diameter	COAD	Inches
Wavelength, Lower Cutoff	WLC	Centimeters
Wavelength, Upper Cutoff	WUC	Centimeters
Detectors in a Scan	DS	Unitless
Detector Detectivity (D-Star)	DSTAR	CM*SQRT(HZ)/Watt
Detector Time Constant	DTC	Second
Scanning Prism Rotational Speed	SMRS	Scans/Second
Scan Interlace Ratio	SIR	Unitless
Detector Elevation Field of View	FOVELI	Radians
Detector Azimuth Field of View	FOVAZI	Radians
Total Scan Field in Elevation	FOVEL	Degrees
Total Scan Field in Azimuth	FOVAZ	Degrees
Preamp 3 dB Bandwidth	BW	Hertz
Preamp Damping Coefficient	O	Unitless
Video Noise Figure	VNF	Unitless
Area of Detector	ADET	Centimeters**2
Display Parameters		
Observer Viewing Distance	OVD	Inches
Display Width	DW	Inches
Display Height	DH	Inches

Notes:
1. Atmospheric Attenuation Tables, Pudson, Wiley, 1969.
2. Air Temperature versus Water Vapor Density, Selby and McClatchey, AFCRL-72-0745.
3. Cocoa Beach atmospheric Radiance, Bell et al, Josa, pp 1313-1320, December 1960.

(Page D-2 is blank)

DISTRIBUTION LIST

Commandant of the Marine Corps
ATTN: Aircraft Procurement Section (1)

Chief of Naval Research
Department of the Navy
Arlington, Virginia 22217
ATTN: CDR W. F. Greene, Code 411 (3)
CAPT G. J. Mischke, Code 411 (1)
Mr. D. C. Lauver, Code 411 (1)
Code 430C (1)
Code 410T (1)

Commander
Naval Air Systems Command
Washington, D. C. 20360
ATTN: Mr. E. D. Cooper, AIR-03P1 (1)
Mr. E. J. Paglianate, AIR-53013 (1)
Mr. W. T. Sparrow, AIR-03PA3 (1)
Mr. H. O. Hollenberg, AIR-03PA1 (1)
Mr. R. G. Perkins, AIR-3032H (1)
Mr. H. Andrews, AIR-53011 (1)
Mr. W. Koven, AIR-03PA (1)
Mr. S. W. Kerkering, AIR-5103 (1)
Mr. R. F. Siewert, AIR-320 (1)

Commanding Officer
Naval Weapons Center
China Lake, California 93555
ATTN: Flight Test, Weapons Div. (1)

Commander
Naval Air Test Center
Patuxent River, Maryland 20670
ATTN: Director, Flight Test (1)
Naval Test Pilot School

Director
Naval Research Laboratory
Washington, D.C. 20390
ATTN: Library, Code 2029 (ONRL) (6)
Technical Information Div. (6)

Chief of Naval Material
Department of the Navy
Washington, D. C. 20360
ATTN: Mr. W. H. Young, MAT-0334 (1)
Mr. D. E. Schwartz, PM7-9 (1)

Naval Ship Research & Development Center
Carderock Laboratory
Bethesda, MD 20034
ATTN: Dr. Harvey Chaplin (1)

Headquarters U. S. Marine Corps
Deputy Chief of Staff RD&S
Washington, D. C. 20380 (2)

Dr. A. L. Slafkosky, Scientific Advisor
Commandant of the Marine Corps
Code RD-1
Washington, D. C. 20380 (1)

Center for Naval Analysis
1401 Wilson Blvd.
Arlington, Virginia 22209 (2)

Chief of Naval Operations
Washington, D. C. 20360
ATTN: OPNAV 05 - Vol I Only (1)
OPNAV 50 - Vol I Only (1)
OPNAV 506F3 - Vol I Only (3)
OPNAV 506C4 Vol I and II (1)

Defense Documentation Center
Building 5
Cameron Station
Alexandria, Virginia 22314 (2)

Department of the Air Force
Air Force Flight Dynamics
Laboratory (AFSC)
Wright Patterson Air Force Base
Dayton, Ohio 45433
ATTN: Mr. C. B. Westbrook
Chief, Control Criteria Br. (1)
Mr. J. Lockenour (1)

U. S. Air Force Plant Representative
Office
McDonnell Aircraft Company
St. Louis, Missouri 63166 (1)

Office of Naval Research
Branch Office
1030 East Green Street
Pasedena, California 91101 (1)

Naval Air Development Center
Code STD-13
Warminster, Pennsylvania 18974
ATTN: Mr. W. K. Eagan, Jr. (1)

(Page E-2 is blank)